MASTER

Aging of semi-transparent mixed-halide perovskite solar cells
the effect of illumination and orientation on stability

Dirven, B.J.C.

Award date:
2021

Link to publication

Aging of semi-transparent mixed-halide perovskite solar cells: the effect of illumination and orientation on stability

Master Thesis

Brian Dirven

Supervisor TU/e:
Prof.dr.ir. René A.J. Janssen

Supervisor Solliance:
Dr.ir. Mehrdad Najafi

Committee members:
Dr.ir. Jan van Dijk
Prof.dr. Reinder Coehoorn

June 2021

Abstract

Perovskite solar cells have emerged as a promising photovoltaic technology due to their excellent optoelectronic properties. Despite this, their stability remains a bottleneck and prevents the technology from taking over the commercial market. This thesis reports on an aging study that focuses on the effect of light soaking for 1250 hours on the stability of inverted semi-transparent perovskite solar cells. The ability to age and measure both sides of the device allows for a unique investigation on its orientational dependence. Three different $Cs_{0.15}FA_{0.85}PbI_3$-based perovskite compositions are investigated to study the effect of a small bromide substitution and rubidium chloride doping on the performance and stability. The devices show an overall decrease of the figures of merit for both aging orientations, with no significant differences between the compositions. After storing the devices in an inert dark environment for two months, a clear difference emerged for the different orientations.

Devices aged from the superstrate side show a significant decrease in performance accompanied by a S-shaped current density-voltage curve. The performance can be (partially) regained by light soaking at maximum power point for a couple of hours. Using drift-diffusion simulations it is discovered that the light soaking causes ions, specifically charged donor defects, to migrate to and accumulate at the PTAA/perovskite interface. Subsequently, the internal electric field is screened resulting in an increase of non-radiative interface recombination.

For the substrate-aged devices the opposite effect is observed, since they almost fully recover their initial performance before light soaking. The recovery is attributed to an initially damaged perovskite/PCBM interface, which experiences a curing effect due to the light soaking. This thesis provides useful insights into the effect of light soaking and its orientation on the aging and recovery of semi-transparent perovskite solar cells as well as the simulation of perovskite solar cells using SCAPS.

Acknowledgements

First of all, I would like to thank Mehrdad for the opportunity to carry out my final graduation project in Solliance. You have taught me a lot on the fabrication processes and measurement techniques of perovskite solar cells and I have had a wonderful educational and enjoyable experience during my stay. Although it was shorter than expected, you have continued to support me by finishing the necessary measurements and helped me with the interpretation of the many results during our weekly meetings, for which I am very grateful.

I would also like to thank René for the supervision and guidance during my project. Your extensive knowledge always provided new insights, useful suggestions and greatly helped with the interpretation of the results. Your vision for the next steps in the project made sure that it continued heading in the right direction and your patience has allowed my to write a thesis that I am proud of.

A special thanks to Dong for the help with the simulations. This was the first time that I have used simulations in a project and your help was a great kick-start to my introduction of that part of the research field. Also, your selfless act to attend our weekly meetings in your own time is greatly appreciated and your advice and feedback have been essential for the interpretation of the simulation results.

I would like thank the M2N group members for the fun conversations during the lunch and coffee breaks. In particular, I want to show my appreciation and gratitude to Margot. Your empathy to help me went so far that you were willing to share your office with me so I could have a place to work at the university, which really helped boost my productivity.

Pap en mam, ik wil jullie heel graag bedanken voor alle liefde en steun die jullie mij geven. Het is altijd weer fijn om thuis te komen, wetende dat jullie er zijn met interesse in mijn week en project. Jullie staan altijd voor me klaar, zij het om een kopje thee te brengen terwijl ik aan het werk ben of een taxirit naar Eindhoven nodig heb. Dit alles maakt mij dankbaar om jullie als mijn ouders te hebben.

Lieve Heleen, door mijn "uitmuntend vermogen" in plannen heeft onze vakantie helaas iets langer op zich moeten laten wachten, maar nu is het dan eindelijk bijna zo ver. Ondanks dat mijn streven naar perfectie jouw geduld ook heeft getest heb je mij altijd volledig gesteund. Gedurende al die tijd heb je mij altijd weten te motiveren als ik het even moeilijk had, weten te kalmeren als ik gestrest was en weten te strikken voor een serie of bordspel als ik afleiding nodig had. Hier ben ik je ongelooflijk dankbaar voor en ik prijs me enorm gelukkig met zo'n lieve vriendin als jij.

Contents

List of Abbreviations

ALD	Atomic layer deposition
CBM	Conduction band minimum
DFT	Density functional theory
DLTS	Deep level transient spectroscopy
DMF	Dimethylformamide
DMSO	Dimethylsulfoxide
DOS	Density of states
EA	Electron affinity
ETL	Electron transport layer
FA	Formamidinium
FF	Fill factor
HTL	Hole transport layer
IE	Ionization energy
IQE	Internal quantum efficiency
IPA	Isopropylalcohol
ITO	Indium tin oxide
J_{SC}	Short-circuit current
J-V	Current density-voltage
LED	Light emitting diode
MA	Methylammonium
MPP	Maximum power point
PCBM	[6,6]-phenyl-C_{61}-butyric acid methyl ester
PCE	Power conversion efficiency
PTAA	Poly[bis(4-phenyl)(2,4,6-trimethylphenyl)amine]
QFLS	Quasi-Fermi level splitting
SCAPS	Solar cell capacitance simulator
SIMS	Secondary-ion mass spectrometry
SOC	Spin-orbit coupling
SRH	Shockley-Read-Hall
TSC	Thermally stimulated current
VBM	Valence band maximum
V_{OC}	Open-circuit voltage
XPS	X-ray photoelectron spectroscopy
XRD	X-ray diffraction

List of Symbols

Symbol	Description	Units
A	Monomolecular recombination coefficient	s^{-1}
$A(\lambda)$	Wavelength-dependent absorptance	%
A_{Aperture}	Area of the aperture of the mask	cm^2
A_{Device}	Active area of the solar cell	cm^2
B	Bimolecular recombination coefficient	cm^3 s^{-1}
C	Trimolecular recombination coefficient	cm^6 s^{-1}
E_{F}^0	Intrinsic Fermi level in the dark	eV
$E_{\text{F,min}}$	Quasi-Fermi level of the minority carriers	eV
E_{g}	Bandgap	eV
E_{IE}	Ionization energy	eV
E_{Urbach}	Urbach energy	eV
G	Charge carrier generation	cm^{-3} s^{-1}
I	Light intensity	mW cm^{-2}
h	Planck's constant	J s
J_0	Dark saturation current density	mA cm^{-2}
J_{MP}	Current density at maximum power point	mA cm^{-2}
J_{ph}	Photo-generated current density	mA cm^{-2}
k_{B}	Boltzmann constant	J K^{-1}
m^*	Effective mass	-
n	Charge carrier density	cm^{-3}
n_{id}	Ideality factor	-
n_{min}	Minority carrier density	cm^{-3}
N_{c}	Effective density of states in the conduction band	cm^{-3}
$N_{\text{D,A}}$	Doping concentration donors and acceptors	cm^{-3}
N_{T}	Defect density	cm^{-3}
N_{v}	Effective density of states in the valence band	cm^{-3}
P_{L}	Input power density	W cm^{-3}
P_{max}	Maximum power density	W cm^{-3}
q	Elementary charge	C
$R(\lambda)$	Wavelength-dependent reflectance	%
R_{s}	Series resistance	Ω cm^2
R_{sh}	Shunt resistance	Ω cm^2
R_{SRH}	Shockley-Read-Hall recombination rate	cm^{-3} s^{-1}
T	Temperature	K

Symbol	Description	Units
$T(\lambda)$	Wavelength-dependent transmittance	%
V_{MP}	Voltage at maximum power point	V
v_{th}	Thermal velocity	cm s^{-1}
X	Ratio of the mask aperture to the active area of the device	-
α	Power law factor	-
$\Delta E_{\mathrm{F,min}}$	Difference between $E_{\mathrm{F,min}}$ and E_{F}^0	eV
ϵ	Dielectric permittivity	F m^{-1}
ϵ_0	Vacuum permittivity	F m^{-1}
ϵ_{r}	Relative dielectric permittivity	-
$\epsilon_{\mathrm{r}}(0)$	Static dielectric constant	F m^{-1}
$\epsilon_{\mathrm{r}}(\infty)$	Optical dielectric constant	F m^{-1}
θ	Share of the minority carriers contribution to the total QFLS	-
λ	Wavelength	nm
μ	Mobility	cm^2 V^{-1} s^{-1}
$\sigma_{\mathrm{n,p}}$	Capture cross section electrons and holes	cm^2
$\tau_{\mathrm{m}}(T)$	Temperature-dependent mean scattering time	s
$\tau_{\mathrm{n,p}}$	Charge carrier lifetime electron and holes	s
χ	Electron affinity	eV

List of Figures

List of Tables

1. Introduction

As the global population continues to increase, so does the total amount of generated energy to meet the demand[1]. At present, fossil fuels are still the major sources for this energy, which emit tens of gigatonnes of greenhouse gases in the atmosphere each year[2]. All these gases contribute to the greenhouse effect, causing the average global temperature to rise with detrimental effects to ecosystem. To counteract this process over 190 countries have signed the Paris Agreements to reduce their emission over the next decades to limit the global warming[3]. In order to meet these requirements a switch to renewable energies is unavoidable. With the equivalent of over 7000 times the annual global energy consumption reaching earth each year, solar energy is a practically endless, free and carbon-free energy source[4]. At present, the vast majority of commercial solar cells available are based on crystalline silicon. Their cost per watt continues to decrease and they become an attractive solution for increasingly more people[5]. Despite this and other renewable sources, the global energy growth is still outpacing the targets set by the United Nations[6]. Hence, there is a need for new innovative solutions to help tip the scales in the other direction. Perovskite solar cells have emerged as next-generation photovoltaic solution with promising results for the future.

1.1 What is perovskite?

Perovskite owes its name to the mineral $CaTiO_3$ which was first discovered by Gustav Rose in 1839 and named after Lev Perovski[7]. Since then, materials with similar structure have been studied in different areas of research. The wide range of interesting properties lead to the integration of perovskites into various applications such as light emitting diodes (LEDs)[8], lasers[9], photodetectors[10], field-effect transistors[11], gas sensors[12] and resistive switch memory devices[13]. The very first solar cell based on perovskite was produced in 2009 by Kojima et al.[14] and had an efficiency of 3.8%. This triggered an explosion of research activity and in just over ten years the efficiency has risen to 25.6% [15]. This already brings it near the record for crystalline silicon solar cells and makes perovskite solar cells the fastest growing solar cell technology to date[16].

Metal-halide perovskites have a chemical formula which can be generalized to the form ABX_3 where A is a large monovalent cation, B is a smaller metal divalent cation and X is a halogen anion. A can be both an organic molecule such as methylammonium (MA) or formamidinium (FA) as well as inorganic ions such as cesium or rubidium, B is a heavy metal such as lead or tin and X is iodide, bromide or chloride. Additionally, multiple different molecules and ions with a corresponding lattice site can be combined in different ratios to create a mixed-perovskite structure. The basic schematic of the molecular structure of $CsFAPbI_3$

perovskite that is used in this project is shown in Figure 1.1. Each lead atom is enclosed in an octahedron consisting of six iodide anions. These octahedra are connected at the edges which form the crystal lattice. The remaining empty position within eight octahedra is filled by a cesium or formamidinium cation. Depending on the temperature the crystal will either have a cubic, tetragonal or orthorhombic crystal structure.
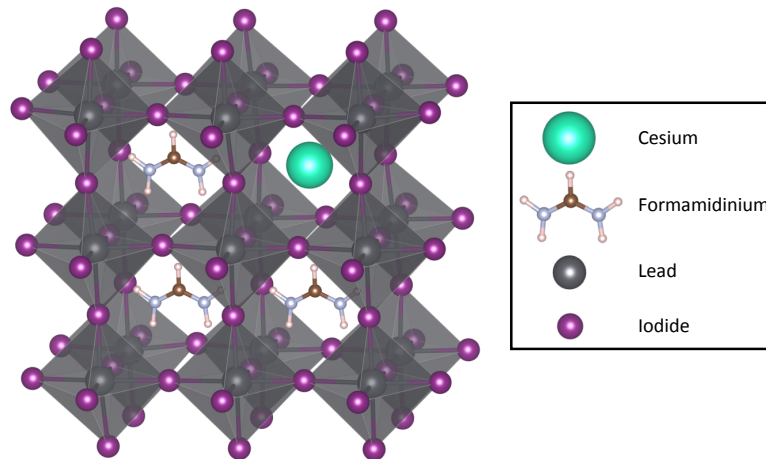
Figure 1.1: Crystal structure of perovskite
A schematic ABX_3 structure of the $CsFAPbI_3$ perovskite. Adapted from Szemjonov et al.[17].

Different cations and anions can be used which will result in different properties of the final material. However, there is a limit to the structural stability of the crystal, which can be determined using the Goldschmidt tolerance factor and is based on the lattice parameters. $FAPbI_3$ is a popular composition for its low bandgap, but converts to the photo-inactive yellow δ-phase at room temperature[18]. However, it was found that the perovskite could be stabilized by substituting cesium into the lattice resulting in the desired black α-phase[19]. Tuning the ratio of cesium and formamidinium can lead to a composition that is very stable and resistant to heat and moisture[18,20].

What makes these perovskites such excellent light converters is a combination of incredible parameters that are useful in solar cells. The material has a high absorption coefficient with a sharp onset[21], long diffusion lengths for electrons and holes[22] and low exciton binding energy[23]. Furthermore, there is the possibility to tune the bandgap[24,25], which makes it interesting for tandem applications where different layers are stacked on top of each other to capture different parts of the solar spectrum.

Besides interesting internal properties, the perovskite is also appealing with regards to the external factors. Contrary to the silicon solar cells, which need to be very thick due to its indirect bandgap, the perovskite has a direct bandgap and can thus be made very thin. This saves a significant amount of material, making perovskite solar cell modules lightweight and thus easier to install. Furthermore, the solar cell can be made thin enough such that it can be used on a flexible substrate[26]. Additionally, since the perovskite layer is processed from solution, it opens up opportunities to fabricate the solar cell using printing techniques[27].

1.2 Motivation

Even though perovskite solar cells show tremendous progress and have a large variety of applications, they are unfortunately still highly limited in their stability over time. Commercially available solar cells should last for at least 20 years, but the most stable laboratory perovskite devices only have a lifetime of up to one year[28], with most cells only lasting a few weeks. Hence, there is a high necessity for stability research and testing to determine the exact physicochemical mechanisms that cause degradation over time. Even though perovskites can already decrease in performance by simply storing them in a dark and inert environment, they deteriorate even more quickly in the presence of heat, moisture, oxygen and light. The focus of this research is solely on the effect of prolonged illumination. Measures are taken to make sure that the devices are only affected by light.

The practically infinite possible compositions all react slightly different to certain conditions[29], hence it is also important for aging studies to decipher which changes are beneficial for the stability of the perovskite. In this project, three different perovskite compositions are investigated for their stability, namely $Cs_{0.15}FA_{0.85}PbI_3$, $Cs_{0.15}FA_{0.85}Pb(I_{0.98}Br_{0.02})_3$ and $Cs_{0.15}FA_{0.85}Pb(I_{0.98}Br_{0.02})_3$ with 0.1 mole percent of RbCl. Throughout the thesis these compositions will be referred to as I (or iodide pure), IBr and RbCl, respectively. It has been observed that a small substitution of bromide for the iodide increases the stability under various (combined) aging conditions[30–33]. The process of doping the perovskite with alkali metal halides is still a relatively new concept and is found to improve the crystallinity and reduce defects[34–36]. Moreover, promising results are found regarding stability in ambient conditions and thermal stresses[37,38]. This project investigates whether the improved stability for these two alterations also hold under solely light soaking conditions.
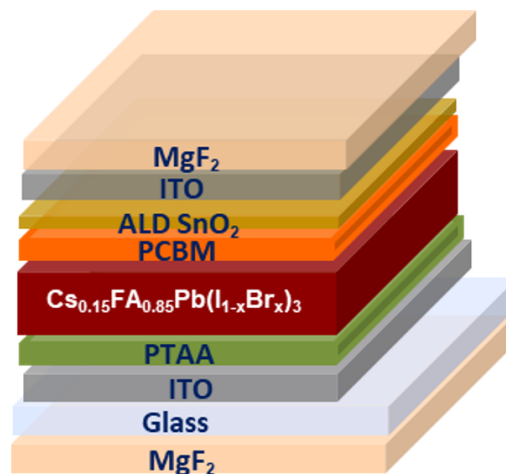
Figure 1.2: Device configuration used in the project.

The complete device stack used in this project is depicted in Figure 1.2. This particular structure is based on the so-called p-i-n or inverted configuration. The p refers to the hole

transport layer (HTL) which collects the positively charged carriers, i is the intrinsic perovskite layer and n is the electron transport layer (ETL) which collects the negatively charged carriers. In this configuration the Poly[bis(4-phenyl)(2,4,6-trimethylphenyl)amine] (PTAA) functions as the HTL and the [6,6]-phenyl-C_{61}-butyric acid methyl ester (PCBM) as the ETL.

This combination of layers results is a semi-transparent perovskite solar cell that allows the non-absorbed, higher wavelength part of the solar spectrum to pass through the device. Placing the perovskite solar cell on top of a silicon solar cell creates a perovskite-silicon tandem that can captured a larger part of the spectrum compared to a single junction solar cell. Another interesting application for semi-transparent solar cells is the use in windows, which could be a useful solution in dense urban environments[39]. The device could be designed such that the outside is optimized for absorption of sunlight and the inside is optimized for the artificial light of lamps. At present, the stability tests for semi-transparent perovskite solar cells are scarce and an investigation on the effect of orientation of the device could not be found in literature. This project is an investigation on the effects of prolonged illumination on the orientation of these types of perovskite solar cells in order to fill the absence of information in this part of perovskite research.

Chapter 2 introduces and discusses the theory of a number of important concepts that are needed for the explanation of the experimental results. Chapter 3 summarizes the fabrication process of the devices and briefly outlines the different measurement techniques used as well as the aging set-up. Simulations are performed to compare to the measurement results and also to see whether the effects of aging can be captured in a model. Both an optical and electrical simulation are optimized and their configuration and parameters are discussed in chapter 4. The experimental results are shown in chapter 5 and discussed for different moments during the aging process. The simulations are compared to the results, but are also deeper investigated themselves for an improved understanding of the physical concepts of the devices. Finally, the most important results are summarized in chapter 6 together with an outlook on open questions and future research.

2. Theory

This chapter explains the working principles of a solar cell together with the figures of merit that are used to characterize the performance. Additionally, it dives deeper into the theoretical background of a number of important phenomena that influence the performance.

2.1 Photovoltaics

The essence of a solar cell is the conversion of sunlight into electricity. Figure 2.1a shows a simplified schematic representation of the mechanisms that occur during this process, based on the device stack used in this project.
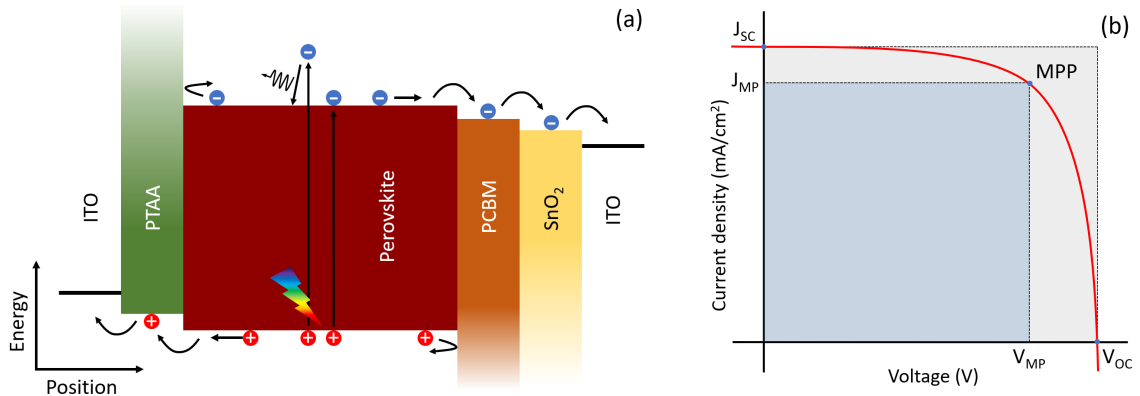
Figure 2.1: The inner workings of a solar cell and its performance indicators
(a) A simplified schematic representation of the generation, transport and extraction of the charge carriers in a perovskite solar cell. The electrons (holes) are indicated with blue (red) spheres and have a negative (positive) charge. (b) A typical current density-voltage curve with the important parameters indicated.

The horizontal direction shows the position in the device and the vertical direction represents the energy. First, a photon is absorbed by the perovskite which excites an electron from the top of the valence band, also known as the valence band maximum (VBM), to the bottom of the conduction band, also known as the conduction band minimum (CBM). This leaves behind an oppositely charged hole in the VBM. The difference between the VBM and CBM is defined as the optical bandgap of the material and places a limit on the range of light that can be absorbed. Only photons with an energy larger or equal to the bandgap can successfully excite an electron to the CBM. An electron that absorbs a photon with a higher energy compared to the bandgap is excited to a higher energy state in the conduction band. Subsequently, the electron relaxes to the CBM by dispensing its additional energy to the lat-

tice by means of a phonon, i.e., the energy is lost as heat. Using the internal electric field in the perovskite, the electron and hole are transported to their respective transport layer. Additionally, each transport layer also acts as an energetic blocking layer for the opposite carrier to prevent undesired recombination and thus loss of the carriers. Once the carriers have reached the interface, they are extracted from the absorber layer and transported to the electrode where they contribute to the generated electricity.

A general method for determining the performance of a solar cell is to measure the current density while externally applying a varying voltage to the device. This gives the so-called current density-voltage (J-V) curve as schematically depicted in Figure 2.1b. With no voltage applied, the device is short-circuited and the charge carriers are extracted via the electrodes. The current density measured at this point is called the short-circuit current density (J_{SC}). Increasing the voltage will lower the internal electric field and recombination of charge carriers will increase. At a certain voltage the device will be open-circuited, meaning that all carriers will recombine in the device and zero current density is measured. This particular point is called the open-circuit voltage (V_{OC}). The voltage for which the solar cell produces the maximum power density P_{max} is indicated by the maximum power point (MPP). The location of this point also defines the fill factor (FF) as given by the following equation:

$$FF = \frac{MPP}{J_{\text{SC}} \cdot V_{\text{OC}}} = \frac{J_{\text{MP}} \cdot V_{\text{MP}}}{J_{\text{SC}} \cdot V_{\text{OC}}}, \tag{2.1}$$

where J_{MP} and V_{MP} refer to the current density and voltage values at MPP, respectively. Another more intuitive method for explaining the MPP and FF is by using rectangles. In order to find the MPP, the area of the blue rectangle under the J-V curve in Figure 2.1b has to be maximized. Consequently, the FF is defined as the ratio of the blue area over the gray area. In other words, the FF is a measure of the 'squareness' of the the J-V curve. The power conversion efficiency (PCE) is defined as the final output power density divided by the total input power density P_{L} as determined by the illumination source, resulting in the following equation:

$$PCE = \frac{P_{\text{max}}}{P_{\text{L}}} = \frac{J_{\text{SC}} \cdot V_{\text{OC}} \cdot FF}{P_{\text{L}}}. \tag{2.2}$$

Hence, in order to enhance the efficiency of a solar cell, the J_{SC}, V_{OC} and FF all have to be optimized[40,41].

2.2 Recombination

After an electron and hole are generated, they have to travel to the contacts to be extracted during which various charge carrier recombination processes can occur that lead to undesirable losses. The change of charge carrier density n over time is described by the rate equation:

$$\frac{dn}{dt} = G - An - Bn^2 - Cn^3, \tag{2.3}$$

where G is the charge carrier generation rate, A the monomolecular recombination coefficient related to the Shockley-Read-Hall (SRH) recombination, B the bimolecular recombination

coefficient related to radiative recombination and C the trimolecular recombination coefficient related to Auger recombination[42]. The main difference between the recombination mechanisms is their reaction order as evident from the charge carrier density dependence in the equation. The different characteristics of the three recombination mechanisms are schematically depicted in Figure 2.2 and also reflect the dependence.

SRH (or defect-assisted) recombination is a first-order process where defect states are present in the material that act as non-radiative recombination centers. If their energy level lies within the bandgap it is possible for an electron or hole to be captured by a defect, followed by recombination with the oppositely charged carrier. During both processes the energy is lost as a emitted phonon as seen in the figure. In perovskites, there are three fundamental type of defects, which can be present in the bulk of the material or at the interface with the transport layers. Vacancy defects are atoms or molecules that are missing from their expected position in the crystal lattice, interstitial defects are atoms or molecules that occupy a position between the standard lattice sites and anti-site defects are atoms or molecules that occupy the wrong lattice site[43]. Radiative (or band-to-band) recombination is a second-order process where an electron and hole directly recombine and a photon with an energy equal to the bandgap is emitted. This photon can be reabsorbed by the material, which is known as photon recycling[44]. Auger recombination is a third-order process involving either two electron and a hole or two holes and an electron. The energy from the recombination of the two different carriers is passed on to a third carrier via a phonon, which will excite the carrier to a higher energetic state.
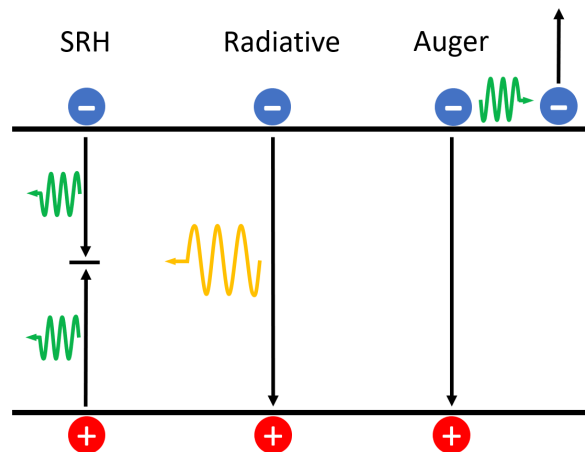
Figure 2.2: Different charge carrier recombination mechanisms in solar cells
Left: Shockley-Read-Hall (SRH) recombination, middle: radiative recombination and right: Auger recombination. The photon is indicated in yellow and the phonons in green.

Due to the relatively low charge carrier densities in solar cells compared to LEDs or lasers, SRH recombination is dominant in solar cells, while radiative and Auger recombination are more effective in LEDs and lasers[42,45]. Typical values for the coefficients of the recombination mechanisms in solar cells will be further discussed in section 4.2.2.

2.3 Hysteresis

An unusual phenomenon that is plaguing the electrical measurements of perovskite solar cells is the so-called hysteresis effect. Its presence is observed as a mismatch between the J-V curve recorded in the forward and reverse scan direction and this discrepancy complicates the correct determination of the performance of perovskite solar cells. In addition, the comparison between devices across literature is not straightforward anymore and thus it blurs the true progress over time. Ever since hysteresis was first discussed in 2014 [46] it has been a heavily debated topic in the research field[47,48]. There are various factors that influence the amount of hysteresis, such as the scan rate[49–51], preconditioning[52,53] and device architecture[54–56].

Over the years a number of mechanisms have been put forward as possible origin of the effect. These include capacitive effects[57,58], ferroelectricity[59,60] and charge trapping and de-trapping[61]. While these mechanisms can correctly predict aspects of the hysteresis, they all have certain parts that are in disagreement with theoretical or experimental observations[47,48].

The most promising and generally accepted explanation for hysteresis is based on the migration of ionic species[49,52,62–65]. Perovskites are known the be ionic conductors[66] and the application of an electric potential or light illumination further enhances the migration[67]. The interplay between the ions, charge carriers and internal field is shown in Figure 2.3 and works as follows.
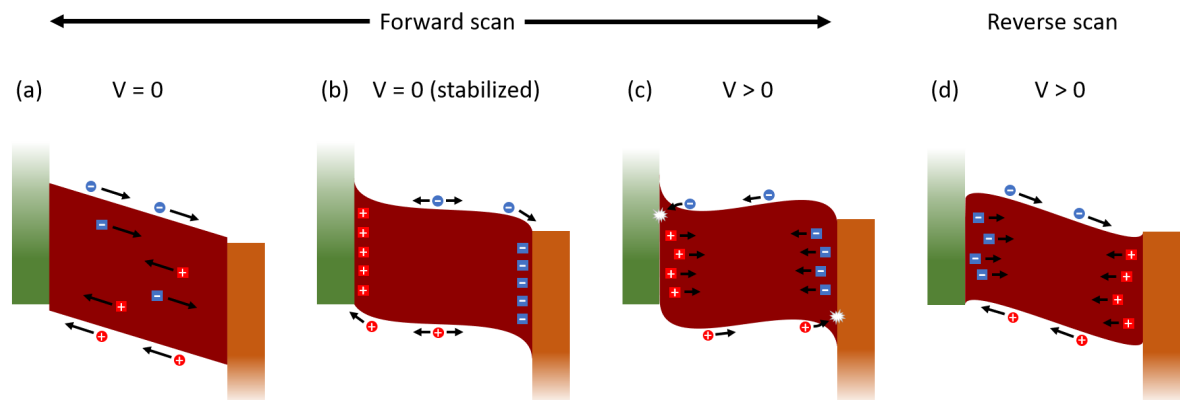
Figure 2.3: Effect of ion migration during the J-V scan
The circles are the charge carriers and the squares are the ions. (a) Both the charge carriers and ions are accelerated by the built-in electric field. (b) The accumulation of ions at the interface screens the built-in field. (c) A large positive bias reverses the built-in field and carriers recombine at the wrong interface. (d) Voltage prebiasing redistributed the ions resulting in an enhanced internal field and effective charge extraction.

Under short-circuit conditions, the ions in the perovskite are redistributed due to the built-in electric field created by the contacts (Figure 2.3a), leading to accumulation of the positively (negatively) charged ions at the HTL (ETL) interface. As a consequence, the internal electric field is partially screened (Figure 2.3b). When applying a positive bias during the forward scan, the already reduced internal electric field will be lowered more, such that the charge carriers

are mostly driven by diffusion, which leads to more recombination and thus a decreased FF. Further increase of the bias will at some point reverse the internal field and the charge carriers will be accelerated towards the wrong transport layers where they will recombine, resulting in a decreased FF and V_{OC} (Figure 2.3c). Since the diffusion of ions is a relatively slow process compared to the scan speed the ions have only just started moving to the other interface, which means that the reverse internal field is mostly maintained during the forward scan. After the forward scan the device is typically held at a voltage higher than V_{OC} for some time, which allows the ions to diffuse towards the other interface and reinforce the built-in field. The charge carriers are efficiently drifting to their corresponding transport layer, resulting in less recombination and thus improved performance.[40,68,69].

Knowing that hysteresis affects the performance, it is crucial to eliminate the effect if long-term stable performance is to be achieved. Various strategies have been successfully employed on different layers and interfaces to suppress hysteresis[70] of which one is alkali metal doping that is also investigated in this project[71,72]. The fact that such a large variety of strategies reduce hysteresis raises questions whether they actually tackle the ion migration itself or alter different properties of the device. Interestingly, there appears to be a trend for devices with less hysteresis to also have improved performance[69,73]. Hence, the strategies most likely reduce the non-radiative recombination in the bulk or at the interface rather than limiting the migration of ions. Indeed, Calado et al.[74] showed that devices with negligible hysteresis still exhibit ion migration. Thus, hysteresis does not originate from a single mechanism, but is the combination of ion migration and defect-assisted recombination, influenced by a whole array of internal and external factors[69,75].

2.4 Light intensity

A large part of the measurements in this project focus on the light intensity dependence of the solar cells. By measuring the J-V curve at various illumination intensities, information can be extracted about the recombination and transport properties of the device. This is a well-established technique in organic solar cells[76–78], but is only sporadically used as an elaborate analysis method for perovskite solar cells. It is common practice to convert the J-V data to plots of the figures of merit as function of light intensity. This method of visualization helps to understand the effects of different illumination intensities on the PCE and FF, which cannot easily be interpreted from the original J-V curves. Furthermore, the graph of the V_{OC} and J_{SC} can be fitted linearly to obtain the so called ideality factor and power law dependence, respectively, which are useful in determining the contribution of the various recombination mechanisms. It is important to note that these variables only give an indication of the dominant recombination mechanisms and not the actual total amount of recombination.

2.4.1 Ideality factor

The ideal solar cell is described by the well-known diode equation and assumes only bimolecular recombination as a recombination process. In reality, there are additional (non-radiative) recombination mechanisms which are captured in the Shockley diode equation by incorporation of the ideality factor n_{id} as shown below:

$$J(V) = J_{ph} - J_0 \left(\exp \left(\frac{qV}{n_{id}k_BT} \right) - 1 \right),$$ (2.4)

where J_{ph} is the photo-generated current density under illumination, J_0 the dark saturation current density, q the elementary charge, k_B the Boltzmann constant and T the temperature[79]. It is often stated that $n_{id} = 1$ implies that bimolecular recombination is dominant with an absence of trap-assisted recombination, while $n_{id} = 2$ refers to monomolecular i.e. SRH recombination being dominant[80–82]. Values in between 1 and 2 describe the relative strengths of the recombination mechanisms. Hence, it is thus often concluded that an ideality factor of 1 is desired and subsequently correlated to a lack of defects that could cause non-radiative recombination[83–85]. While this could certainly be the case, this conclusion is not always correct as shown by Caprioglio et al.[86]. The presence of defects at the interface can in fact reduce the ideality factor as is also shown in this thesis using simulations. Furthermore, there are other more specific conditions that influence the ideality factor, such as the carrier densities of both charge types and their ratio as well as the energy level of the defects within the bandgap[80,87].

There are various methods for determining the ideality factor of a solar cell, each with its own advantages and disadvantages[88]. The most popular methods for perovskite solar cells are fitting of the dark J-V curve in the diffusion-dominated, exponential region using the Shockley diode equation or linear fitting of the light intensity dependent V_{OC}, also known as the Suns-V_{OC} method. The drawback of the dark J-V method is that the parasitic resistances are not taking into account, which can lead to incorrect fits. It is possible to account for the shunt and series resistance by adjusting the Shockley equation, but the introduction of additional parameters makes the fit more error prone[89]. An advantage of the Suns-V_{OC} method is that no current is extracted from the device, which means that the series resistance does not affect the measurement. One could expect the same to be true for the shunt resistance, but this is not actually the case. For very low light intensities it is observed that a shunt path can manifest itself as a recombination mechanism, leading to a fast decrease of the V_{OC}[89,90]. The information given above is all based on the classical diode theory, which is founded on a series of assumptions that not necessarily hold for perovskite solar cells[86,91]. The presence of ion migration leads to changes in the internal electric field over time and thus also to the spacial distribution of charge carrier density. Since the charge density is associated with the determination of the V_{OC} of the device, it means that the changes will be reflected in the measurements[87]. As a result, the steady-state ideality factor as obtained from the classical analysis is not sufficient to accurately describe the dominant recombination mechanisms in a perovskite solar cell. Additional information can be extracted from the Suns-V_{OC} measurements by calculating the differential ideality factor as function of light intensity

(I) using the following equation:

$$n_{\mathrm{id}}(I) = \frac{q}{k_{\mathrm{B}}\mathrm{T}} \frac{\partial V_{\mathrm{OC}}}{\partial \ln(I)},$$ (2.5)

which shows that the value is actually not always constant over the entire light intensity range[89,90]. This could be an indication that different recombination mechanisms are dominant at different light intensities. Unfortunately, this method does not explain the effects of the ion migration on the ideality factor. Additionally, the ideality factor is voltage- and temperature-dependent[80,89,92] and using transient measurements can be beneficial to improve the understanding of the changes over time[87,93]. All in all, it is clear that a prediction solely based on a single ideality factor could lead to inaccurate interpretations of the dominant recombination mechanisms and hence should always be discussed with additional measurements[94].

2.4.2 Power law dependence

Another relation that can be used to learn about the underlying loss mechanisms of solar cells is the power law dependence of the J_{SC} as defined below:

$$J_{\mathrm{SC}} \propto I^{\alpha},$$ (2.6)

with α representing the correlation between the J_{SC} and light intensity. The method is popularized for organic solar cells and eventually adopted by the perovskite research community. This also holds for the physical interpretation of the α parameter, even though the electrochemical properties of the two types of solar cells are signifcantly different. To the best of my knowledge, there is no elaborate study on the power law dependence in perovskite solar cells, hence it is unclear whether the interpretations remain valid.

A value of $\alpha = 1$ implies that the charge collection efficiency at short-circuit is independent of light intensity, which is the desired ideal case. A deviation from unity indicates a significant problem with the extraction of the charge carriers and this can have multiple causes. In general, there are two different explanations used for the sublinear behavior throughout literature. On the one hand there is the interpretation that a pure bimolecular recombination limited cell leads to a reduction of α to a value of 0.5, while dominant monomolecular recombination results in α close to 1 [83,95–100]. The origin of this theory is based on a simple zero-dimensional model that states that the linear dependence of both carrier concentrations on light intensity as a result of the absorption of photons can be linked to bimolecular recombination, which is proportional to the product of these carrier concentrations. Furthermore, there is a general belief that bimolecular recombination is the limiting factor is in organic solar cells[78,101]. This does raise the question whether this argument holds for perovskite solar cells, which are considered to be monomolecular recombination limited in the form of defects[102,103].

The other explanation is based on the presence of space-charge due to a charge carrier imbalance or interfacial barrier, limiting the current extraction and ultimately reducing α to

a proportionality of 0.75 [82,104–110]. Koster et al.[111] proposed that the space-charge stems from a large difference in carrier mobility and that the bimolecular recombination in fact cannot be the cause of the sublinear dependence. While the mobility in perovskites can vary quite significantly (as explained in section 4.2.2), the difference between the electron and hole mobility is found to be minimal[112,113] and thus it is unlikely to be a cause for sublinear dependence. However, the existence of space-charge in perovskites is possible and is the result of ions accumulating at the interfaces, which can lead to reduced charge carrier extraction[62,114,115].

Finally, there is also research referring to both arguments and in theory both should be able to coexist[116–118]. The limitation of the zero-dimensional model is that it assumes no spatial dependency of the charge carriers, which is exactly what the space-charge argument provides as part of the explanation. A recent paper by Hartnagel et al.[78] explores the light intensity dependence of J_{SC} comprehensively and found that only a combination of the mechanisms can correctly predict the behavior of α over a wide variety of circumstances. Hence, similarly to the ideality factor, additional information is needed to correctly determine the loss mechanisms at J_{SC}.

2.5 Aging of perovskite solar cells

The stability of perovskite solar cells is still the biggest hurdle to overcome in order to achieve commercial viability. There are many factors that can lead to aging over time. These include, but are not limited to, excessive heating leading to decomposition or crystal phase changes, moisture and oxygen reacting with any of the layers resulting in chemical degradation, illumination causing halide phase segregation as a result of activated ion migration as well as the UV part of the spectrum causing damage and finally internal mechanical stresses that accelerates aging during operation[119–125]. While there are many ways a perovskite solar cell can age, there are theoretically infinite options for addressing the issues. The most popular method to avoid extrinsic effects is encapsulation of the entire device, which protects it from moisture, oxygen and large thermal fluctuations[122,126,127]. The advantage of encapsulation is that it does not put restrictions on the device architecture and layer selection, but could lead to a slight reduction in light absorption. Regarding intrinsic methods, a few general strategies are highlighted. The most obvious change is to exchange any layer with a more stable alternative or adjust the perovskite composition, but this could come at a cost of performance[29,128]. Different deposition techniques could be used that result in a more compact and less chemically active layer[129,130]. Buffer layers could be added to prevent ions and molecules from penetrating other layers[131]. Additionally, a layer or interface could be passivated, which can have many effects depending on the layer and passivation material[132,133].

Since light soaking is the aging method of choice for this project it is useful to discuss its effect on stability and performance as reported in literature. Perovskite solar cells are often observed to have a changing PCE over time under constant illumination conditions,

which is known as the light soaking effect[134]. Contrary to most other aging conditions, performance can either increase[64,85,134–142] or decrease[89,99,143–151] over time. Interestingly, ion migration is by far the most inferred explanation independent of the final performance of the device. This means that the perovskite composition and the charge carrier transport layers are the decisive factors in determining whether light soaking is either beneficial or detrimental for the solar cell. A well-known example for mixed-halide perovskites is the Hoke effect, where a high enough bromide percentage leads to photo-induced phase segregation into iodide- and bromide-rich regions[152]. Similarly, enhanced light soaking degradation is found in $Cs_{0.15}FA_{0.85}Pb(I_{0.85}Br_{0.15})_3$, while the $Cs_{0.15}FA_{0.85}PbI_3$ composition remains fairly stable[143,153]. In contrast, another paper by Li et al[154] shows that the $Cs_{0.15}FA_{0.85}PbI_3$ composition in fact phase segregates into a Cs- and FA-rich phase under operation with illumination. Another important aspect of light soaking are the conditions at which the devices are held. It has been shown that the load applied to the device influences the amount of degradation, with aging at open-circuit voltage leading to the highest losses[149,155]. Furthermore, the preconditioning voltage can determine whether the light soaking will increase or decrease the performance[156].

Degradation is generally thought of as an irreversible process, but it is often the case that devices can recover their light soaking losses by storing them in a dark environment[75,89,148–151]. The opposite effect where the improvements gained by light soaking are lost again by placing the device in dark is also observed[85,142]. All in all, the combination of internal and external factors make it nearly impossible to predict beforehand whether a device will improve or degrade with prolonged light illumination. This adds a big uncertainty to the viability of perovskite solar cells in commercial applications, hence more research is needed into methods that can prevent these changes over time.

2.6 Masking of a solar cell

The J-V sweep is commonly the first measurement done on a solar cell to quickly and easily evaluate its performance. Its figures of merit serve as a benchmark for other researchers to compare their cells to. It is thus essential that the measurement conditions and settings are identical across the field, for example, by correctly calibrating the lamp's intensity and uniformity to the AM1.5G solar spectrum[157]. This is especially important for perovskite solar cells, which show significant different values depending on preconditioning, scan speed and scan direction[158].

Another important aspect is the masking of the solar cell to correctly measure the J_{SC}. The mask is used to cover all areas that are not supposed to absorb light and has a well-defined aperture to precisely define the active area. Without a mask, the J_{SC} is often overestimated due to edge effects and 'light piping', where light enters via other layers and is directed into the photoactive area[157,159].

There is however a downside to using a mask, as is shown by Kiermasch et al.[160]. While the

mask allows for an accurately measured J_{SC}, it actually causes the V_{OC} to be underestimated and the FF to be overestimated. This can lead to a erroneous PCE depending on the severity of the differences. The origin of the reduced V_{OC} has to do with the ratio of the generation-versus recombination current density. Using a mask reduces both the active area and amount of generated current, leaving the generation current density unchanged as expected. However, the area in which recombination can occur is defined by the overlap of the electrodes and is not altered. Hence, even the area that is not illuminated as a consequence of the mask will still contribute to the recombination and thus the recombination current density will be decreased. This prevents the quasi-Fermi levels from reaching their full splitting potential, lowering the V_{OC} compared to a measurement without mask. The expected underestimation can be calculated using the following equation[160]:

$$\Delta V_{\mathrm{OC}} = \frac{n_{\mathrm{id}}k_{\mathrm{B}}T}{q}\ln(X) \quad \text{with} \quad X = \frac{A_{\mathrm{Aperture}}}{A_{\mathrm{Device}}}, \tag{2.7}$$

where A_{Aperture} is the area of the mask opening and A_{Device} is the active area of the device defined by the overlap of the electrodes. From this equation it becomes apparent that the smaller the aperture of the mask, the greater the underestimation of the V_{OC} will be. In the case of the devices of this project it is approximately 20 meV.

Kiermasch et al. extend this notion further by hypothesizing and proving that masking has the same effect on the V_{OC} and FF as reducing the light intensity by the factor X. In other words, a solar cell that is masked is not actually illuminated with an 100 mW/cm^2 solar intensity, but instead to a intensity proportional to the aperture-to-cell area ratio X. Hence, to properly account for this effect, the light intensity curves have to be shifted to lower intensities according to the ratio X. The experimental and simulation data in this thesis is adjusted accordingly to account for this effect.

3. Fabrication and characterization

This chapter summarizes the material and process details of the device fabrication and explains the measurement procedures of the various measurement techniques. Also, the process of aging is elaborated on.

3.1 Materials

- The precursor solution for the 1.4M $Cs_{0.15}FA_{0.85}Pb(I_{1-x}Br_x)_3$ perovskite was prepared using the following commercial powders with their respective molar concentrations and without purification: lead iodide (PbI_2, 1.4M) (99.99%, TCI), formamidinium iodide (FAI, 1.19M) (99.99%, GreatCell Solar), cesium iodide (CsI, 0.21M for x=0, 0.126M for x=0.02) (99.999%, Sigma-Aldrich), cesium bromide (CsBr, 0.084M) (99.999%, Sigma-Aldrich), rubidium chloride (RbCl, 0.0014M) (99.975%, Puratronic). For solvents dimethylformamide (DMF) (99.8%, Sigma-Aldrich) and 1-methyl-2-pyrrolidinone (NMP) (99.5%, ACROS Organics) were used in a 9:1 volume ratio mixture. The final solution was stirred overnight at room temperature.
- The PTAA (Solaris M) is diluted in toluene to acquire a 2 mg mL^{-1} solution and stirred overnight at room temperature.
- The PCBM (99%, Solenne) solution of 20 mg mL^{-1} is prepared by dilution in chlorobenzene and stirred overnight at 60°C.

3.2 Device fabrication

A glass substrate with a patterned indium tin oxide (ITO) layer (Naranjo) of 170 nm thickness is scrubbed and cleaned with a diluted soap solution of Extran MA02 and demineralized water followed by 10 minutes sonication in the solution. After that, the samples are thoroughly rinsed with demineralized water and subsequently sonicated in demi water for 10 minutes. The samples are rinsed with isopropylalcohol (IPA) and sonicated in IPA for 10 minutes. The samples are dried using a nitrogen gun and treated in a UV/Ozone oven for 30 minutes.

The solar cells are prepared in a nitrogen glove-box with oxygen and moisture levels around 1 ppm. 100 μL of the PTAA solution is spin coated statically on top of the ITO at 6000 RPM with an acceleration of 2000 RPM/s for 35 seconds to create a ∼10 nm thick layer. Here, statically means that the solution is applied to the substrate just before the spin coater is turned on. Subsequently, the sample is placed on a hotplate of 100°C for 10 minutes as

post-treatment. Next, 150 µL of the perovskite precursor solution is dynamically spin coated using the gas quenching method[161] together with a two-step spin coating program to create a perovskite layer of around 600 nm. Here, dynamically means that the solution is applied to the substrate just after the spin coater is turned on, i.e., during the acceleration. The spin coater starts at 2000 RPM with 500 RPM/s for 10 seconds followed by 5000 RPM with 2000 RPM/s for 30 seconds. After 15 seconds the spin coated solution is gas quenched using an nitrogen gun for 15 seconds at 6 bar pressure held approximately 10 cm vertically above the substrate. After that, the sample is placed on a hotplate of 100°C for 10 minutes as post-treatment. The ETL is dynamically spin coated using 70 µL of the PCBM solution at 1500 RPM with 3000 RPM/s for 50 seconds resulting in layer thickness of ∼40 nm. The SnO_2 buffer layer is processed using atomic layer deposition (ALD)[162] using the metalorganic precursor tetrakis(dimethylamino)tin (TDMA-Sn) (99.9%, STREM Chemicals) and H_2O as coreactant. The OpAL (Oxford Instruments) ALD reactor is used and the chamber substrate tables are set to 100°C. The outer edge of the sample (∼5 mm) is cleaned under ambient conditions using a DMF:chlorobenzene solution with a 1:6 volume ratio to remove all spin coated layers. The top ITO layer is deposited using RF magnetron sputtering (AJA sputtering system) at room temperature resulting in a thickness of 180 nm. Gold contacts with a thickness of 180 nm are thermally evaporated on top of the top ITO contacts. Lastly, a 100 nm thick layer of magnesiumfluoride (MgF_2) is thermally evaporated on both sides of the sample. The final schematic layout of the ITO layers and gold contact is shown in Figure 3.1 below together with a photograph of an actual sample after fabrication. Each sample has four devices and each device has an active area with a surface area of 0.168 cm^2.
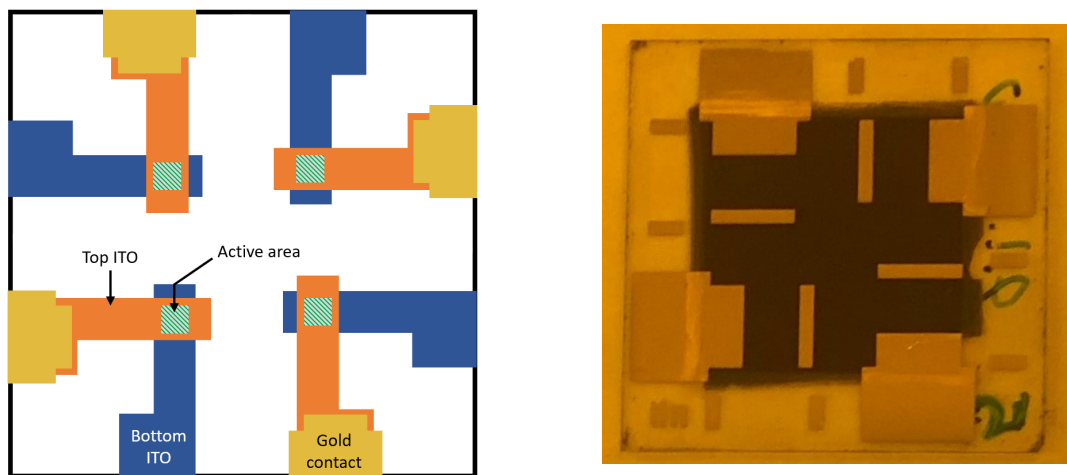
Figure 3.1: Sample layout
(a) Schematic layout of the ITO layers and the overlapping active area, (b) photograph of the fabricated sample with four devices.

3.3 Device characterization

Current-voltage (J-V) characteristics

Measurements were done in a setup (MiniSunSim) of Solliance's design, containing a Keithley 2400 Source Meter wired to a sample holder in a nitrogen-filled glove-box. A halogen lamp is used as light source, which is calibrated to AM1.5 solar conditions with an intensity of 100 mW/cm^2 using a silicon reference cell. The samples are masked during the measurements with an aperture of 0.09 cm^2, resulting in an aperture-to-cell area ratio X of approximately 0.536. Throughout the rest of the thesis, a measurement from the HTL side will be referred to as the "glass side" and a measurement from the ETL side will be referred to as the "ITO side". A scan rate of 165 mV/s with a step size of 20 mV is used over the range of -0.2 V to 1.2 V. Both a forward and reverse scan is done to analyze the hysteresis. Each sample is measured at 1 sun equivalent intensity followed by MPP tracking for 120 seconds to check the stabilization. After that, a second measurement is done which is used in the actual data analysis. Lastly, a light intensity measurement is done, which can only measure the device in the reverse scan direction. Neutral density filters are used to adjust the illumination intensity to obtain 1, 0.84, 0.54, 0,33, 0,1 0,01, 1E-3 and 1E-4 sun.

External quantum efficiency

The external quantum efficiency (EQE) is measured using a setup by Rera Solutions. A range from 300 to 850 nm is measured with a step size of 10 nm. No external bias is applied during the measurements to allow for the calculation of the J_{SC}. The bandgap and Urbach energy are calculated using a Matlab script developed by Dong Zhang based on the paper by Krückemeier et al.[163]. The Urbach energy is determined from the slope of the absorption onset and gives an indication of the quality of the absorber material. A small Urbach energy is associated with low structural disorder and hence desired[164].

UV-vis

The optical transmittance and reflectance of devices are measured using a Agilent Cary 5000. The measurement range spans from 300 to 850 nm and the step size is 1 nm. A Certified Reflectance Standard is used for the calibration for the 100% reflectance and black paper is used for the calibration of the 0% transmittance. The small spot kit is used to hold the samples, but due to their small size it is easy to damage the sample. Hence, only one of each type of composition is measured to prevent the loss of devices.

X-ray diffraction

X-ray diffraction (XRD) analysis is done to learn more about the crystallographic structure of the perovskite layer. The structure characterization was performed with a X-ray diffractometer

by PanAlytical Empyrean. The measurements were done in ambient conditions and a range
of 5 to 90 degrees with a step size of 0.013 degrees.

3.4   Aging

An in-house made aging set-up shown in Figure 3.2 is used to test the stability of the devices.
The set-up is located in a nitrogen filled glove-box to prevent oxygen and moisture from
reacting and possibly damaging the samples, which is necessary since the samples are not
encapsulated. The samples are positioned in pairs under halogen lamps and simultaneously
cooled using a cold plate which has a continuous flow of water through it of around 20°C. This
way, it is ensured that the temperature in the samples remains constant and significant heating
is prevented. The devices are aged at open-circuit conditions, meaning that all generated
charge carriers recombine in the solar cell. In the end, only light soaking can possibly induce
aging effect in the sample, which is precisely the aim of the stability test.
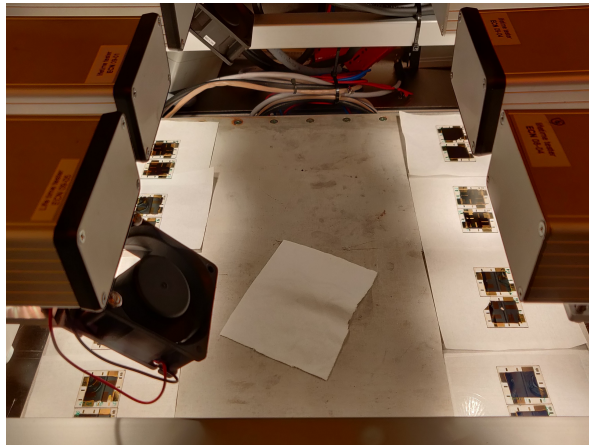
Figure 3.2: Photograph of the samples in the aging set-up

4. Simulations

In this chapter the ins and outs of the simulations are discussed. The inputs, limitations and assumptions are addressed and the influence of the many different parameters is explained.

To validate the experimental observations that are found, simulations are done on both one sun JV-curves as well as light intensity data. The simulation consists of two parts: an optical simulation which calculates the charge carrier generation profile in the perovskite cell and an electrical part that simulates the transport of the charge carriers through the device as well as the charge carrier collection.

4.1 Optical simulation

A transfer matrix model is used to calculate the generation rate of charge carriers in the perovskite solar cell. A free-to-use Matlab script that has been made available by McGehee Group of Stanford University[165, 166] is used which forms the basis of the optical simulation. Small adaptations are made to suit the layer stack of the samples and a piece of code is added to automate the creation of the generation file. These adaptations and additions can be found in Appendix A. The generation file contains the amount of charge carriers generated per m^3 s as function of position in the device. These units are chosen specifically such that the file can directly be used as an input in the electrical simulation.

4.1.1 Inputs

The optical simulation is centered around the different layers of the device and their corresponding thicknesses that have to be defined by the user. Each layer is accompanied by wavelength-dependent complex refractive index data that is used to calculate the propagation of the electromagnetic waves through the device. This data is placed in the Excel file that is provided along with the script. Other general parameters that have to be set are the wavelength range for which field patterns are calculated and the step size defined as the distance between lattice points in the device cross-section. The wavelength range is set from 300 to 850 nm equal to the range of the EQE measurements and the step size is set to 1 nm. The thickness as well as the source of the complex refractive index data of each layer in the device can be found in Table 4.1 and 4.2 depending on the illumination side. The thickness has been determined in the past from similar samples made in Solliance. Similarly, some layers have been measured before to determine their complex refractive index, while the data for other layers are obtained from literature. Neither source has a data set with the exact step size of 1 nm used in the simulation, so the data is expanded using cubic spline interpolation.

The layers in Table 4.1 and 4.2 are listed in order of the incident of the light. The model always assumes that the light is incident on the first defined layer. There are two possible illumination sides due to the semi-transparent nature of the device, hence the need for two different sets of layers. Furthermore, due to the definitions and assumptions in the model the two sets of layers are not symmetrical, which makes it impossible to simply reverse the order of the layers when switching from glass side illumination to ITO side illumination. More on this in the next section. Even though the glass and air layer have no thickness, they set the conditions as if the light was coming from this material.

Table 4.1: Overview of the order of the layers when illuminating from glass side
The layers are listed in order of the incident of the light. Thicknesses and the source of the complex refractive index data are given for each layer. If no reference is given, the data was obtained in house.

Layer	Glass	ITO	PTAA	Perovskite	PCBM	SnO$_2$	ITO
Thickness (nm)	0	170	10	600	40	40	180
Source complex refractive index	[167]	-	-	[168]	-	-	-

Table 4.2: Overview of the order of the layers when illuminating from ITO side.
The layers are listed in order of the incident of the light. Thicknesses and the source of the complex refractive index data are given for each layer. If no reference is given, the data was obtained in house.

Layer	Air	MgF$_2$	ITO	SnO$_2$	PCBM	Perovskite	PTAA	ITO
Thickness (nm)	0	100	180	40	40	600	10	170
Source complex refractive index	[166]	-	-	-	-	[168]	-	-

4.1.2 Assumptions

Obviously the model is not a perfect representation of the real sample and various assumptions have to be made. For illumination from the glass side, it is assumed that the sample is in a n=1 environment (air) and the first layer is a thick substrate so that incoherent reflection from the air/1st layer interface is taken into account before the coherent interference is calculated in the remaining layers. The thickness of the first layer is irrelevant, hence it is set to zero. This description is analogous to light hitting the device from glass side where the glass layer accounts for this process as can be seen in Table 4.1. In section 1.2 it was shown that both sides of the sample are covered with an anti-reflection layer to improve current density. Due to the above assumption however, it is not possible to have the anti-reflection layer in front of the glass substrate in the model, thus it has to be accounted for in a different way. Since the anti-reflection layer increases the light coupling and only affects the current density it is practicable to simply multiply the charge carrier generation. The value used in this multiplication is based on the performance increase gained by adding the anti-reflection layer. Fortunately, a sample

was measured both with and without such layer and an increase of 2.5% was found, hence a value of 1.025 was used. Similar values are found in literature[169, 170]. When illuminating from the ITO side there is no thick substrate to account for the incoherent reflection, but this can be circumvented by choosing air as the first layer, as shown in Table 4.2. The absence of a substrate on this side of the device makes it possible to add the MgF_2 layer to the model by simply inserting it in between the air and the top ITO layer.

Another important part of the optical simulation are the complex refractive index values as function of wavelength of each layer. The data of most layers have been measured in-house in the past, but some, including the perovskite layer, are obtained from literature. The wide variety of possible perovskite compositions makes it difficult to find a paper that has the exact same composition and also provides the complex refractive index data. There are papers that contain the complex refractive indices of $Cs_xFA_{1-x}Pb(I_{1-y}Br_y)_3$ type perovskites, but unfortunately the ratios are not the same. In the end, the values of a $MAPbI_3$ perovskite measured by Manzoor et al.[168] are used. Even though both the cation and halide parts are different, the cut off wavelength of this composition is the closest to the measured UV-vis data, which is crucial for simulating the correct amount of absorption in the device.

Besides optimizing the amount of absorption as best as possible, it is also important to correctly determine where the charge carriers are generated in the device. In this model, it is assumed that the generation of charge carriers only occurs in the perovskite layer. In reality, other layers will also absorb part of the light, especially those who are closer to the illuminated surface compared to the perovskite. Charge carriers that are generated in non-perovskite layers will almost immediately recombine due to the overwhelmingly amount of majority carriers resulting in less collection of carriers.

Finally, there are a number of general assumptions needed to limit the complexity of the simulation. It is assumed that the light hits the sample normal to its interface. This assumption is in agreement with the measurements since the lamp in the solar simulator is positioned directly above the sample and is directed straight down. It would not hold for real-world tests where the angle of incidence changes over time, but those types of experiments were not performed during this project. Other assumptions are that each layer has a uniform thickness, the different layers are all parallel to each other and each interface is perfectly flat, i.e., no roughness or texture. In reality, there are variations in the thicknesses due to imperfect layer formation, which automatically also means that the interfaces are not flat. Accounting for this in the simulation would add unreasonable amount of calculation time. Furthermore, the location of thickness variations are unknown and assuming an uniform thickness with an average based on the variations is the best approximation. The simulation has the possibility of calculating the J_{SC}. To do this, it assumes an internal quantum efficiency (IQE) of 100%. Finally, the model makes use of the AM1.5G solar spectrum but the measurements are done in a solar simulator with a halogen lamp, which does not have the same spectrum. Also, as mentioned before, the wavelength range used in the simulation is 300 to 850 nm while the spectrum of the lamp extends beyond these boundaries.

4.1.3 Outputs

After running the simulation it outputs a series of figures as well as the important variables such as the absorptance and reflectance. One of the figures depicts the optical electric field intensity as function of the position in the device for different wavelengths that can be defined by the user. Besides confirming that light with a higher wavelength reaches further into the perovskite layer as is expected, it is not used further for analysis or its data. A second figure that is created by the simulation shows the generation rate as function of the position in the device. Since the model assumes charge carrier generation only occurs in the perovskite, it is the only area that shows a curve. In Figure 4.1 the generation profile in the perovskite layer is plotted for illumination from glass and ITO side. The location of the PTAA and PCBM layers are indicated to help with the orientation of the device.
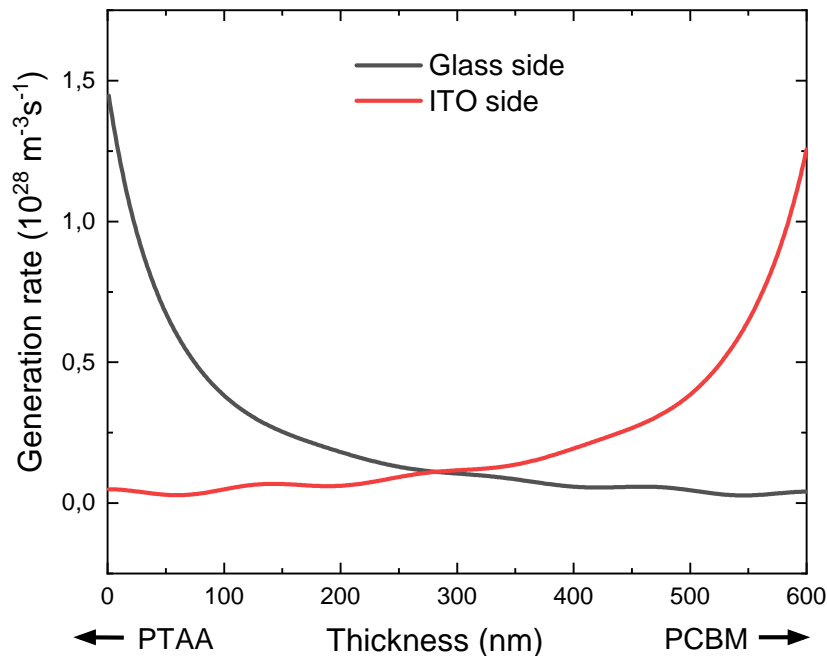
Figure 4.1: Generation rate as function of position in the perovskite layer
Illumination from glass side (black) and ITO side (red). The location of the PTAA and PCBM layers is indicated with arrows to help with orientation.

It shows that most of the charge carriers are generated near the side of the device where the light is incident. The maximum of the curve at the boundaries of the perovskite is in part determined by the bandgap of the material, which is expected to be the same throughout the entire perovskite layer. This means that the part of the solar spectrum that has an energy high enough to generate an electron-hole pair is independent of the layer thickness. However, the depth that light can penetrate a material *is* dependent on its energy. The simulation shows that the generation rate decreases exponentially with the thickness of the perovskite layer, albeit with some oscillations in the second part of the layer. In general, high energy light has a higher chance of being absorbed by the perovskite compared to low energy light. The effect

of this is that the spectrum changes as the ratio of high to low energy decreases when moving deeper into the perovskite. This is confirmed by the electric field intensity graph mentioned before. In other words, the part of the spectrum that is able to generate an electron-hole pair decreases as function of perovskite thickness and thus the generation rate also decreases.

This description can also be used to explain the difference in absolute maximum between glass and ITO side illumination. When illumination from ITO side the light has to travel through a thicker part of the device to reach the perovskite absorber. Hence a larger part of the high energy spectrum has already been absorbed by the ITO and PCBM layers resulting in less generation in the perovskite.
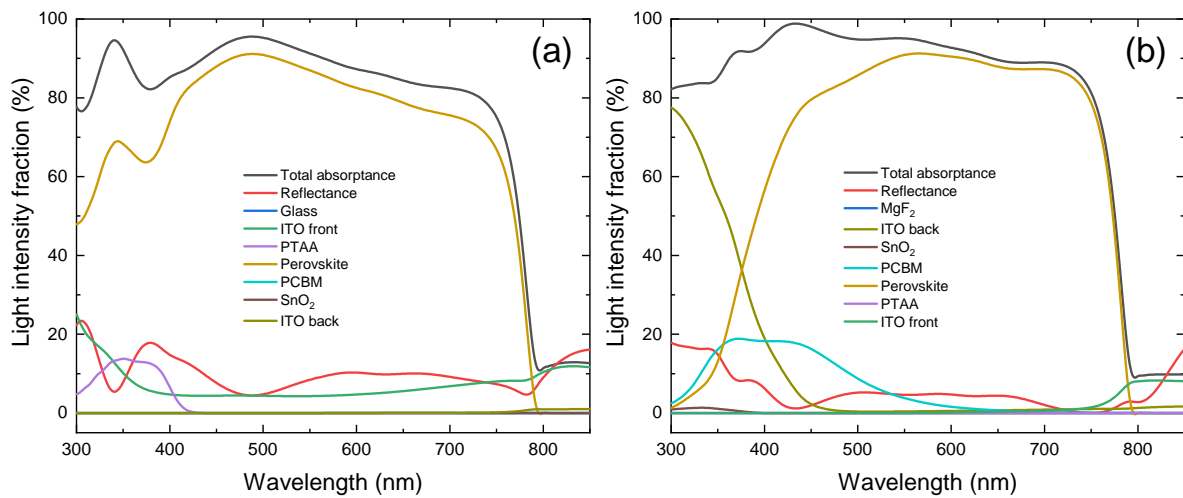
Figure 4.2: The fraction of absorbed light by each layer including the total absorptance and reflectance
(a) Illumination from glass side (b) Illumination from ITO side.

The final figure that is generated by the simulation contains the total absorptance and reflectance of the device as function of wavelength as well as the contribution of each layer to absorptance. The results for the device used in this project are shown in Figure 4.2a and b for illumination from glass side and ITO side, respectively. Even though these results are not used in the electrical part of the simulation, it is still very useful to see where the device is limited in its performance and which layers contribute most to the losses. When illuminating from glass side it appears that both the front ITO and PTAA are the largest contributors to the parasitic absorption, especially in the low wavelength regime. The effect of this parasitic absorption results in decreased perovskite absorption in this part of the spectrum. At the other side of the spectrum it shows the tail of the perovskite absorption which is determined by the bandgap of the material. Illuminating from the other side shows clearly that the back ITO is the main contributor to the parasitic absorption in the low wavelength range, severely limiting the perovskite absorption. Around 400 nm the PCBM also adds to the losses by absorbing roughly 20% of the light. The reduced reflectance and ITO absorption from 550 to 750 nm results in a higher perovskite absorption in this part of the spectrum compared to

illumination from glass side.

Finally, since the model assumes 100% IQE it is possible to calculate the J_{SC} by multiplying the charge carrier generation rate with the step size and elementary charge. This result can be compared to the J_{SC} calculated from the JV-curve as well as the value obtained from the EQE measurements. Furthermore, the absorptance data can be compared to the data obtained from the UV-vis measurement. This is all discussed in section 5.1.2 and section 5.2.1, respectively.

4.2 Electrical simulation

With the generation profile in the perovskite layer calculated, the next step is to determine the transport and collection behavior of the charge carriers. To do this, the one dimensional Solar Cell Capacitance Simulator program SCAPS-1D developed at the Department of Electronics and Information Systems (ELIS) of the University of Gent, Belgium is used (Version 3.3.07)[171,172]. SCAPS is a solar cell simulation program developed for thin-film solar cells, such as CdTe and $Cu(In,Ga)Se_2$ type solar cells. It was later updated for crystalline and amorphous type solar cells. Even though it is not explicitly mentioned by the developer, it has been shown by Minemoto et al. that it is possible to simulate organic-inorganic perovskite solar cells using SCAPS[173].

4.2.1 Solar cell definition

Similar to the optical model, SCAPS is centered around the definitions and properties of each layer of the device. Figure 4.3 shows the 'solar cell definition'-panel in SCAPS. Here, each layer is defined with its corresponding set of properties. After defining two or more layers, the properties of the interfaces can be added to the boxes that are automatically generated by the software. The boundaries of the device are defined in the boxes labeled 'left contact' and 'right contact'.

The stack as defined by the user is automatically depicted on the right side of the panel. Using the sliders above the schematic, the user can define the illumination side, to which contact the voltage is applied and whether the device is a consumer or generator, i.e., light source or solar cell. In this case, the illumination side is not relevant for the simulations since the carrier generation profile is not calculated by SCAPS, but provided by the optical model. This brings up an important distinction between the optical and electric model that has to be clarified. As mentioned in section 4.1.1, the optical model is set up such that it simulates with illumination incident on the first defined layer, meaning that the calculated generation profile has its maximum carrier generation at the beginning of the file for both glass and ITO side illumination. Using these files directly in SCAPS would effectively result in simulating from the same illumination side for both cases, assuming the same solar cell structure is used in SCAPS. In reality, the location of the maximum carrier generation depends on the illumination side as can be seen in Figure 4.1. There are two solutions for matching the generation file with SCAPS so that each illumination side is correctly simulated. The generation files can
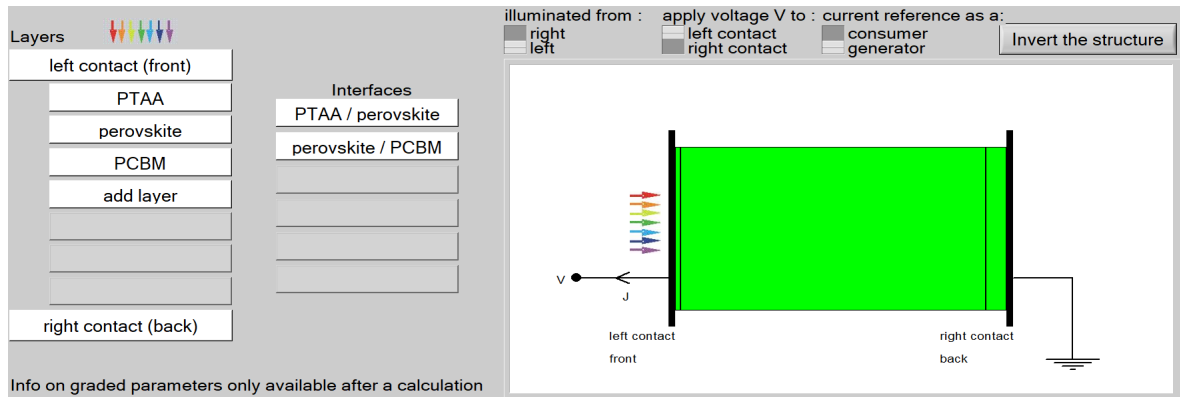
Figure 4.3: SCAPS solar cell definition panel
On the left side, the layers, interfaces and contacts are defined with their corresponding properties. On the right, a schematic is shown with a summary of the device and the illumination and electronic settings can be adjusted.

be set up to work with a single solar cell structure in SCAPS. The Matlab code for filling the generation file is unique for each illumination side as shown in Appendix A. This way, the generation from the ITO side is effectively flipped, making both files compatible with a single solar cells structure in SCAPS. Alternatively, the generation files remain unchanged, but the structure in SCAPS is changed. Luckily, SCAPS is provided with a button to invert the entire structure, automatically accounting for all interfaces and contacts as can be seen in Figure 4.3. When switching from a glass side to ITO side measurement simply inverting the structure is sufficient. Both solutions were tested and should in theory yield identical results. Interestingly, minor differences were found in the short-circuit current and FF most likely due to the effect of rounding somewhere in the calculations in SCAPS. During the simulations only the second method was used to maintain consistency in the results.

Up to seven layers can be added in SCAPS which is enough for the device stack used in this project. However, only the perovskite and both carrier transport layers are chosen to be simulated. As mentioned before, it is assumed that charge carriers are only generated in the perovskite layer. The consequence of this assumption is that the minority carriers are only present in the perovskite meaning that trap-assisted recombination is only possible in this layer. Once the majority carriers have reached the transport layers, trap-assisted recombination becomes irrelevant and perfect extraction is assumed from the contact onwards. In reality, this is of course not the case and charge carriers are generated throughout the entire stack as evident from the absorptance in Figure 4.2 resulting in losses.

A important mechanism in perovskite solar cells is the migration of mobile ions, which, among other things, leads to hysteresis as discussed in section 2.3. SCAPS is unfortunately unable to account for this process in its simulations, hence the hysteresis that is also present in the device shown in this thesis cannot be described correctly. There are alternative simulation programs, such as gpvdm[174], which do account for this process, but are not used during this project.

4.2.2 Parameters

Figure 4.3 shows the layers as used in the simulations. Each layer, interface and contact has a significant amount of variables and in this section they will be looked at in more detail. Table 4.3 shows the final parameter values that are used for the simulation of the fresh IBr devices. Many of these parameters have been optimized during the simulations and to give a better idea of the possible range of these variables, each will be briefly discussed. For some parameters a more elaborate view of the background physics is given to motivate the range of values found.

Table 4.3: Overview of the simulation parameters of each layer
The top part shows the general properties of the layer and the bottom part shows the parameters related to recombination and defects. These parameters are used for the simulation of the fresh IBr devices. If no reference is given, the parameter is either measured or optimized with simulations.

	PTAA		Perovskite		PCBM	
Parameter	Value	Ref	Value	Ref	Value	Ref
Thickness (nm)	10		600		40	
Bandgap, E_g (eV)	3.4		1.569		2.0	
Electron affinity χ (eV)	1.9		3.88		4.0	
Relative dielectric permittivity ϵ_r	2.67	[175]	24.1	[176]	3.75	[175]
Effective density of states N_c, N_v (cm^{-3})	2.5 x 10^{19}	[175]	8.1 x 10^{18}	[177]	2.5 x 10^{19}	[175]
Thermal velocity v_{th} (cm/s)	1 x 10^7		1 x 10^7		1 x 10^7	
Mobility μ_n, μ_p (cm^2/V s)	6 x 10^{-3}	[175]	1		2 x 10^{-3}	[175]
Doping concentration N_D, N_A (cm^{-3})	0		1 x 10^{14}		0	
Radiative recombination coefficient B (cm^3/s)	0		1 x 10^{-9}	[103]	0	
Auger capture coefficient C (cm^6/s)	0		1.55 x 10^{-28}	[178]	0	
Defect type	neutral		neutral		neutral	
Capture cross-section σ_n, σ_p (cm^2)	1 x 10^{-15}		1 x 10^{-15}		1 x 10^{-15}	
Energy distribution	single		single		single	
Defect energy level above perovskite E_v (eV)	0.60		0.79		0.60	
Bulk defect density $N_{t,bulk}$ (cm^{-3})	1 x 10^{14}		2.5 x 10^{14}		1 x 10^{17}	
Interface defect density $N_{t,interface}$ (cm^{-2})		1 x 10^9		2 x 10^9		

Bandgap and electron affinity

The bandgap and electron affinity (EA) together determine the height of the energy levels of the CBM and the VBM in the energy band diagram. The EA is defined as the energy gained from moving an electron from the vacuum energy level to the bottom of the conduction band. Another parameter often associated with the band diagram, but not directly used in SCAPS, is the ionization energy (IE) which is defined as the energy needed to transfer an electron from the top of the valence band to the vacuum level. The three parameters adhere to the

following relation:

$$E_g = E_{IE} - \chi \tag{4.1}$$

where E_g is the bandgap, E_{IE} is the IE and χ is the EA. When designing a device stack, it is critical to choose layers with aligning energy levels to assure proper charge carrier extraction. Misalignment can lead to either an extraction barrier resulting in charge accumulation at the interface followed by a major increase in non-radiative recombination or an injection barrier limiting the quasi-Fermi level splitting (QFLS) resulting in significant loss in V_{OC}[179, 180].

Starting with the PTAA layer, the value for the bandgap itself is not important for the simulation since it is assumed that no light is absorbed in the transport layers, but it does, together with the EA, determine the height of the IE in SCAPS. The EA of the hole transport material determines how effective the layer is at blocking the electrons. It should have a small enough value for the layer to maintain its charge selectivity. The values obtained from literature for these parameters have quite a significant spread. A range from 2.8 to 3.5 eV is found for the bandgap and for the EA the values range approximately from 1.7 to 2.7 eV[181–185]. The boundary values found for the EA are checked with SCAPS, while maintaining a constant IE, to see if the figures of merit are affected. No changes are observed meaning the energy difference to the perovskite CBM remains large enough to preserve excellent charge selection at the interface.

It often occurs that papers only give the value for the IE as this is the most critical parameter for the hole transport layer with respect to the energy level alignment. It determines the effectiveness of the charge extraction of the holes and should correctly align with the VBM of the perovskite. For the IE, a slightly smaller spread of values between 5.1 and 5.5 eV is found based on the literature mentioned above and using Equation 4.1. Even though the spread is smaller, it is still large enough to span both the charge carrier extraction and charge blocking regimes, depending on the perovskite layer. Overall, the uncertainty in both the bandgap and EA of the PTAA is significant and this could have multiple reasons. It is a common practice to dope the organic hole transport layer to improve conductivity and mobility and reduce the series resistance[186], but this does have an influence on the energy levels of the material[187, 188]. Not every paper mentions to what extend the hole transport layer is doped which could explain why the range of values is so large, although PTAA is rarely doped. Other possible reasons could be because of variations in thickness, preparation and deposition method or measurement technique.

Next is the perovskite absorber that is responsible for the carrier generation. The bandgap is an important parameter in this regard since it determines the absorption onset. However, since the generation is predetermined by the optical model, it will only be relevant for the band characteristics. The bandgap is one of the values that has been extracted from the measurements and is found to be 1.569 eV for the IBr samples. Comparing this value to literature is not trivial as the bandgap is very much depended on the composition of the perovskite. It is well established that the halides can be interchanged or mixed to tune the bandgap of the absorber layer[24, 189, 190]. Furthermore, also the use of different cations in

different ratios is found to have an effect on the bandgap[191–193], albeit significantly less than for the halides. Then there is, like for the PTAA layer, still the deviations in the value found in literature. Even for the most common studied composition, $MAPbI_3$, deviations of up to 0.2 eV in the reported bandgap can be found[194–196]. The perovskite used in this project has a more complex composition with a mixture of cations ($Cs_{0.15}FA_{0.85}$) as well as a mixture of halides in the case of the bromide containing samples ($I_{2.94}Br_{0.06}$). No band diagram related information can be found of this exact composition in literature. The closest composition found is $Cs_{0.15}FA_{0.85}PbI_3$ which gives a bandgap between 1.54 and 1.56 eV[191,197,198]. Accounting for the 2% bromide giving a slight increase, this is in excellent agreement with the measured bandgap.

The height of the EA and IE of the perovskite are key values that influence how efficient the extraction of electrons and holes is, respectively. The best comparable composition in literature that is also provided with data on the energy levels is in this case $Cs_{0.17}FA_{0.83}PbI_3$ which gives an EA ranging from 3.77 to 4.43 eV and values between 5.33 and 5.97 eV for IE[192,199,200]. It is difficult to validate the correctness of these values due to the limited amount of data. An alternative option is to look at $MAPbI_3$, which has a similar bandgap, to get an idea of the diversity of the values. Olthof investigated the distribution of measured ionization energies and found a large spread of values ranging from 5.1 to 6.65 eV with a mean of 5.6 eV[201]. Interestingly, when evaluating review-like papers that only show an overview of the energy levels without any direct measurements or references, the values almost always appear to be 3.9 eV for the EA and 5.4 eV for the IE[184,202–206]. It seems that there is a consensus on these particular values even though the spread in the measured values is found to be significant. The two popular values fall within the range found for the CsFA-type perovskite which is a good sign, but since the compositions are different this is by no means conclusive evidence. Especially for perovskite, the preparation and deposition method as well as the the stoichiometry have a large influence on the IE of the perovskite[207,208]. Furthermore, the method of analysis of the measurement data can yield vastly different results[201].

Finally, there is the PCBM layer, responsible for the collection of electrons while simultaneously blocking the holes. The purpose of the layer is thus the exact opposite to that of the PTAA layer with regard to the charge carriers and this is reflected in the characteristic energy levels. The alignment of the EA to the CBM of the perovskite determines the effectiveness of the electron extraction while the IE should be more positive than the VBM of the perovskite to ensure the blocking of holes. The bandgap is again only relevant for the determination of the height of the IE. According to literature, the range of values vary between 1.6 and 2.2 eV for the bandgap and 3.8 to 4.3 eV for the EA[128,205,209–212]. This translates to a range of 5.8 to 6.3 eV for the IE. Again, the boundary values of the IE are tested in SCAPS to examine the effectiveness of the hole blocking and no changes are observed. In literature, it is not always explicitly clear which type of PCBM is used. By far the most common variant used in perovskite solar cells is $PC_{61}BM$, however, $PC_{71}BM$ is also suitable as the electron acceptor material[213–215]. Differences in the carbon part of PCBM does seem to have an effect on the height of the energy levels, but the differences are within the uncertainty range[216,217]. Other

explanations for the spread in the data could be the thickness, different processing steps, such as annealing,[218] and deposition methods.

All in all, the values chosen for the bandgap and EA shown in table 4.3 are based on the ranges discussed in the paragraphs above, but also their collective band structure. It is crucial to have correctly aligning bands such that the simulation truly represents the working solar cell device. The values are once more summarized in Figure 4.4 to give a visual interpretation.
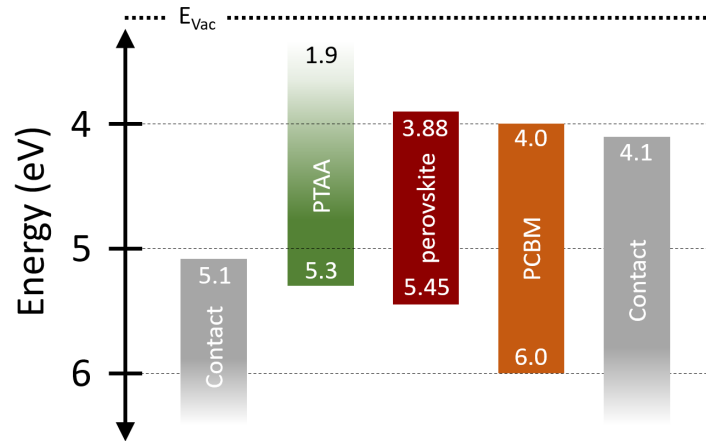
Figure 4.4: Band diagram of the values used in the simulation
The top value indicates the EA and the bottom values indicates the IE.

Relative dielectric permittivity

The relative dielectric permittivity ϵ_r is defined as the ratio of the dielectric permittivity of a material ϵ to the vacuum permittivity ϵ_0. It describes how strongly a material becomes polarized when placed in an external electric field. Due to the polarization, the electric field present in the material is reduced, i.e., screened, which affects the Coulomb forces between the photo-generated carriers[219, 220]. In solar cells, an absorber material with a high dielectric permittivity is desired since this leads to a larger distance between the two generated charge carriers and thus a lower binding energy making it easier to separate them. Another name for the parameter is the dielectric constant, but this is misleading since it is actually dependent on both the temperature of the material as well as the frequency of the applied field[221]. Materials with a complex structure, such as perovskites, have multiple polarization mechanisms originating from different physical processes that occur simultaneously at various frequencies. The static dielectric constant, $\epsilon_r(0)$, and optical dielectric constant, $\epsilon_r(\infty)$, are commonly used to indicate the low and high frequency regime, respectively. Assuming these processes are independent, their contribution to the permittivity can be summed[219, 222]. An interesting phenomenon is observed in perovskites under illumination in the very low frequency regime where the dielectric permittivity increases by orders of magnitude. This is referred to as *Giant dielectric constant* and originates from the redistribution of ions over macroscopic distances[223, 224]. Altogether, this makes the calculation of the relative dielectric permittivity

not trivial, which is confirmed by the range of values found in literature.

For the perovskite, values as low as 6.5 and as high as 100+ are reported[225]. A similar range of values is found in papers on device simulations[226–230]. The value of 24.1 used in the simulations is an intermediate value measured by Brivio et al.[176]. The relative dielectric permittivity of PTAA is more consistent in literature and found to be around 3 [86, 175, 181, 231–233]. Finally, the PCBM layer shows no significant frequency dependence and has a value of around 3.9 [139, 175, 185, 234–236].

Effective density of states

The effective density of states (DOS) in the conduction band, N_c, and the valence band, N_v, are defined as the amount of available states per unit volume which depends on temperature and the effective mass of the electrons and holes, respectively[237]. It has been found that the effective DOS of perovskites is generally lower than that of silicon which is believed to be part of the reason why perovskite solar cells have such high performance[195, 238]. The effective DOS determines how close the Fermi level approaches the conduction or valence band for a certain charge carrier density. Hence, a high carrier density combined with a low effective DOS results in a quasi Fermi level close to the band edge and thus a high V_{OC}[238, 239]. The effective DOS can be calculated from the effective mass of the charge carriers according to the following equation:

$$N_{c,v} = 2 \left(\frac{2\pi m^* k_B T}{h^2} \right)^{3/2},$$ (4.2)

where m^* the effective mass and h Planck's constant. Hence, to obtain a small effective DOS, the effective mass of the charge carriers should also be small. Theoretical values found using these methods for perovskites are in the order of 10^{17} - 10^{19} cm^{-3} [238, 240–242]. Values used in device simulations show a similar range as should be expected[173, 177, 232, 243]. The values for N_c and N_v often differ due to the asymmetry in the valence and conduction band[244]. Interestingly, in theoretical calculations the values for N_c are generally reported to be higher than the N_v, while in device simulations the exact opposite is found. For simplicity, the perovskite values used in this project are assumed to be of equal magnitude. As for the values of the transport layers, it seems that the literature on these is scarce. This is evident from other simulations as no references to measurements or calculations are given. The values found are sometimes assumed to be equal to perovskite, but overall show a broad range of values from 10^{18} to 10^{21} cm^{-3} [175, 181, 185, 245, 246].

Thermal velocity

In the absence of an electric field or concentration gradient, the electrons and holes move randomly through the material due to thermal energy. The average velocity with which this happens is called the thermal velocity and can be calculated in the following way[247]:

$$v_{th} = \left(\frac{3k_B T}{m^*} \right)^{1/2}.$$ (4.3)

The thermal velocity is important for the recombination processes in the device, since the carrier lifetime is inversely proportional to v_{th} meaning that low values are desired. No in-depth investigation can be found in literature, but using the above equation together with commonly reported effective masses in perovskites a value in the order of 10^7 cm/s can be found. Regarding values reported in SCAPS simulations, the literature seems to unanimously agree on a value of $1 \cdot 10^7$ cm/s[228, 232, 248–250]. The thermal velocity of the transport layers is chosen the same as the perovskite as is done in literature[86, 185, 245, 246].

Mobility

When an electric field is applied over a material, the charge carriers will be pulled a certain direction and gain a drift velocity. How easy it is for the carriers to move through the material is governed by the mobility. This property is strongly affected by the various scattering processes as well as the effective mass of the charge carrier which can be expressed in the following relation:

$$\mu(T) = \frac{q\tau_{m}(T)}{m^*}, \tag{4.4}$$

where $\tau_{m}(T)$ is the temperature-dependent mean scattering time[251]. Perovskites are often praised for their long carrier diffusion length and carrier lifetime, but their mobility is not on the same level, especially when compared to traditional inorganic photovoltaic materials such as Si and GaAs[252]. It has been shown that the effective masses in perovskites are small[240, 253], so this means that the mobility is ultimately limited by scattering processes. The underlying physics of charge transport is a heavily debated part of perovskite research with a variety of scattering mechanisms[254, 255]. Possible theoretical explanations involve impurities[256], charge carrier interactions with lattice vibrations, i.e., phonons,[257, 258] and polarons[259, 260] as the limiting factor of charge transport in perovskites. In a classical sense, one would consider the impurities and defects to be excellent candidates for the scattering of charge carriers. However, the observed long lifetime of carriers in perovskites contradict this idea. Furthermore, investigations on the temperature dependence of mobility have shown it is approximately proportional to $T^{-3/2}$ [261–263], while scattering from ionized impurities is known to have a $T^{3/2}$ dependence[251].

The interactions of the charge carriers with phonons are believed to play an important role in perovskites, especially due to the "soft" nature of the material[252, 264]. Regarding these interactions, two types of mechanisms are commonly used to explain the observations in charge transport[255, 265, 266]. The first is non-polar deformation potential scattering originating from acoustic phonons, which has the same theoretical characteristic as the observed $T^{-3/2}$ dependence of the mobility[251], but transport solely based on this mechanism results in a increased mobility of one to two orders of magnitude compared to experimental measurements[267]. The second is longitudinal optical phonon-electron coupling via polar Fröhlich type interactions which are expected to be significant due to the large difference in static and optical dielectric constants[219, 266]. One way of determining which interaction is dominating is by looking at the polarity of perovskite, but apparently this is a hotly debated topic in itself and appears

to very much depend on the composition and processing technique[268,269]. Both mechanisms have been deemed to be the dominating limitation of the mobility in perovskites[270,271], but so far no general consensus has been achieved.

If the electron-phonon coupling is strong enough, a polaron can be formed, which is a quasiparticle consisting of a charge carrier with its self-induced polarization in a polar material[272]. In the last few years, the description of charge transport in terms of polaronic phenomena has gained traction[255,259,260,273]. Depending on the strength of the electron-phonon coupling, described by the Fröhlich coupling constant, the polaron can be classified as either small or large meaning it is localized in a region in the order of a unit cell or spans over multiple lattice sides, respectively[255]. From calculations on the Fröhlich coupling constant, polarons in perovskites are expected to be of the intermediate to large variant[259,260,274,275], which is the leading candidate to satisfy the experimental observations. Most importantly, the mobility at room temperature can be correctly calculated using polarons. Also, an essential property of large polarons is their coherent transport that effectively screens the charge carriers and reduces scattering significantly, explaining the long lifetimes observed. The higher effective mass for polarons adds to this effect and can explain other phenomena such as the slow cooling of hot carriers[255,276]. However, the reported values vary from tens of percent to orders of magnitude higher compared to the bare carrier mass[259,273], which conflicts with measurements. Furthermore, not the $T^{-3/2}$ dependence but a $T^{-1/2}$ is found when measuring over a large temperature range[258,273,277].

All in all, there are multiple mechanisms put forward as possible explanation for the modest mobilities observed in perovskites, but so far none has checked all the boxes regarding measurement outcomes. Maybe a combination of different mechanisms could describe the observations correctly or perhaps a completely new model has to be derived[258,278].

Now finally, what are these modest mobilities values alluded to in the paragraphs above? A great overview is given by Herz showing the mobilities of various perovskites compositions including the fabrication route and measurement type[279]. It clearly shows the orders of magnitude difference reported in literature with values as low as 0.2 cm^2/V s and high as 2320 cm^2/V s. It has been shown that the mobility can differ due to the method of processing, influencing the extrinsic factors such as grain boundaries and doping[280], even for identical compositions[279]. However, even for single crystal perovskites, the difference can be two orders of magnitude, while it is expected that crystals of the same stoichiometry and structure should give the same mobility. It is thus most probable that the uncertainties originate from the measurement techniques[279]. Regarding device simulations, the absolute range of values found is 0.05 to 50 cm^2/V s, but most authors use a value between 1 and 10 cm^2/V s[86,177,181,281–283]. No values for the exact composition used in this project could be found in literature. The final values used in the simulations are obtained via optimizations and are similar to the values used by Głowienka et al., which has the same bromide concentration and almost same ratio of cesium and formamidinium[175]. For the carrier transport layers it is more difficult to find measurement values of the mobility. The PTAA is reported to have a mobility between 10^{-3} - 10^{-2} cm^2/V s[284–286] and for PCBM it is expected to be close to 10^{-3} cm^2/V s[104,287,288]. In

simulations, the values are nicely distributed around these values[177, 232, 233, 245, 289, 290].

Doping concentration

It is a common practice to intentionally dope a semiconductor with impurities to add extra charge carriers and improve the conductivity of the material. This is no different for perovskites, however, other aspects such as photophysical properties and stability play a factor as well[291, 292]. Doping can be applied to the A-site and B-site cations using alkali metals[38, 71], alkali earth metals[293, 294] and group IV transition metals[295]. Also possible, but less common is the doping of the X-site anions using divalent or organic anions[296, 297].

Perovskites can either be n-type or p-type doped caused by unintentional self-doping and this depends on the ratio of the precursors and processing conditions[298–300]. The material is n-doped when the precursor solution is PbI_2-rich/MAI-deficient and p-doped when it is PbI_2-deficient/MAI-rich in case of a $MAPbI_3$ composition. The mismatch in compounds results in interstitial and vacancy defects causing the doping of the material[301, 302]. This effect has been exploited by groups to create a p-n homojunction type perovskite[303, 304].

Concrete values on the donor/acceptor concentrations from theoretical calculations or experimental measurement are difficult to find in literature. Cui et al.[304] found values between $\sim 10^{10}$ and 10^{13} cm^{-3} for their p and n-type layers when varying the PbI_2/MAI precursor ratio. However, most papers use molar or percent to indicate the doping concentration instead of cm^{-3} [34, 305]. In SCAPS, the range of values shows a large discrepancy of many orders of magnitude difference with concentrations as low as 10^9 cm^{-3} and as high as 10^{20} cm^{-3} [250, 306–310]. Furthermore, donor type, acceptor type and a simultaneous combination of both have been used to characterize the doping concentration in the perovskite layer[229, 249, 311]. The values used in this project has been obtained via optimizations.

As mentioned before, it is quite common to dope the carrier transport layers as well to improve conductivity and reduce the series resistance. This is also evident by the fact that most simulations have a certain donor and acceptor concentration for the electron and hole transport layer, respectively. In general, the transport layers are higher doped than the perovskite and from simulations in literature it appears that the range of concentrations is approximately from 10^{17} to 10^{20} [185, 233, 246, 290]. The PTAA and PCBM in this project are undoped and so the doping values are set to zero for both.

Recombination rate

In SCAPS, the SRH recombination is described in terms of defect density, so the monomolecular recombination coefficient does not have a defined value in this case. The recombination coefficients are commonly determined by fitting the rate equation (2.3) to experimental data obtained from, for example, photoluminescence or transient spectroscopy, but due to the unknown charge carrier density and simultaneous fitting of all three coefficients large uncertainties can be introduced[42, 312]. Furthermore, processes such as photo reabsorption can mask

the real intrinsic bimolecular recombination coefficient resulting in an underestimation of the value[313].

Starting with the bimolecular recombination coefficient, the values reported in literature are found in the range of 10^{-12} to 10^{-9} cm^{3}s^{-1} with values most commonly found in the higher limit of the range.[42, 45, 178, 262, 312, 314–320]. The values themselves are, together with the typical mobility of perovskites, orders of magnitude lower than predicted by the Langevin theory, which states that the bimolecular coefficient relates to the mobility and relative dielectric permittivity according to $B/\mu = q(\epsilon_0\epsilon_\mathrm{r})^{-1}$, with the simple assumption that an electron and hole will recombine when their capture radii overlap at any given point[45, 321]. It is found that these non-Langevin ratios B/μ, lower than the limit predicted by the Langevin theory, also appear for other compositions and deposition methods suggesting that there is a fundamental property of perovskites that determines these particular values. It has been proposed that the polaronic nature of charge carriers in perovskites could explain this large observed difference between measurements and Langevin theory[259].

The values for the third-order Auger recombination coefficient appear to generally fall in the range of 10^{-31} to 10^{-27} cm^{6}s^{-1} with a mean value around 10^{-28} cm^{6}s^{-1} [45, 178, 312, 316–319, 321–323]. Compared to other conventional semiconductors with similar bandgaps, the Auger coefficient for perovskites is around 2 orders of magnitude stronger[42], suggesting it strongly contributes to recombination, especially at high carrier densities where its n^3-dependence becomes important. However, Milot et al. showed that for operation at room temperature and 1 sun equivalent illumination, the contribution of Auger recombination in photovoltaic applications is limited[178], while the use in laser applications requires optimizations of the perovskite material to minimize the effect of higher order recombination mechanisms. This can be done by tuning the composition of the perovskite as has been shown by Rehman et al., which can change the values of both the radiative and Auger coefficients by up to an order of magnitude and is believed to be caused by changes to the intrinsic band structure[324, 325]. Furthermore, Staub et al.[322] have shown that the Auger coefficient can vary orders of magnitude depending on the depth of the defects in the bandgap, which is also determined by the composition and processing method of the perovskite.

The values for the bimolecular recombination coefficient used in SCAPS simulations fall nicely within the range of values given above[103, 233, 239, 243, 245, 306]. Auger recombination is either ignored or not mentioned in almost all papers on SCAPS simulations, but in this project it is included for completeness. Since no minority carrier are present in the carrier transport layers due to the assumption that all charge is generated in the perovskite, it is not possible to have radiative nor Auger recombination there, hence the values are set to zero.

Capture cross-section

The capture cross-section is a property of the defects which describes the effective area where an electron or hole would be captured by the defect if one would move within it. It is an important factor that influences the charge carrier lifetime $\tau_\mathrm{n,p}$ of the electrons and holes

according to the following equation:

$$\tau_{\mathrm{n,p}} = \frac{1}{v_{\mathrm{th}}\sigma_{\mathrm{n,p}}N_{\mathrm{T}}}, \tag{4.5}$$

where $\sigma_{\mathrm{n,p}}$ is the capture cross-section and N_{T} the defect density[79]. There are various methods for obtaining information from defects including the capture cross-section. Most commonly used are Deep Level Transient Spectroscopy (DLTS)[326,327] and Thermally Stimulated Current (TSC)[328,329], which are both temperature-dependent measurement techniques. Different defect levels are dominant at different temperatures and these techniques allow for their detection. Landi et al.[330] thoroughly investigated the behavior of the defects in a MAPbI$_3$ solar cell over a broad temperature range and found that the capture of electrons is an interplay between shallow and deep defects with the assistance of phonons.

The values reported in literature span over many orders of magnitude all the way from $\sim 10^{-22}$ to 10^{-12} cm^2 [326–329,331–334]. The composition of the perovskite as well as the fabrication method have a large influence on the final properties of the defects. An interesting relation between the electron capture cross-section and the defect energy level is observed in a paper by Zhang et al.[335], where it seems that the capture cross-section decreases for increased depth of the defect in the bandgap. Additionally, this is not limited to perovskites, but can also be found for silicon solar cells[336]. The relation is not mentioned by the authors and is presumably not an universal fact. Of course, more properties of the material should be accounted for, but nevertheless it is interesting to mention.

The range of the values found in simulations varies orders of magnitude as well, roughly from 10^{-20} to 10^{-13} cm^2 with most values around 10^{-14} cm^2 [86,233,248,281,309–311]. Interestingly, in two papers[281,309] the authors use different capture cross-sections depending on the energy level of the defect and both cases follow the relation introduced above. Unfortunately, no underlying reasons for their choice were given in the papers. The capture cross-sections in the simulations in this project were set to a value of 10^{-15} cm^2 and chosen equal for electrons and holes, which is however not necessarily true[329]. Furthermore, the values for the defects at the interfaces and in the transport layers were also assumed to be equal to the perovskite layer.

Defect characteristics

Defects have a strong impact on the performance of solar cells and thus it is crucial to understand their properties and chemical nature to reduce their effect, evidenced by the vast amount of papers on this subject. In this section, the defect density in the bulk and at the interface will be elucidated together with other settings, such as the type of defects and their energy level and distribution. The defect parameters of the two transport layers are set to reasonable values that can be expected, but have no effect on the figures of merit due to the generation only occurring in the perovskite layer. However, very high defect densities show an effect in the quasi-Fermi levels most likely due to the filling of the traps and can result in a convergence failure.

Perovskite thin films are most often processed from solution and at low temperature, which are favorable conditions for the formation of defects and hence a high defect density is expected. The defect density is heavily influenced by the composition as well as the processing method leading to a large variety of reported values in literature ranging from $\sim 10^{10}$ to 10^{20} cm^{-3} [43, 45, 293, 314, 322, 337–339]. However, a distinction has to be made between single crystal and polycrystalline perovskites. Due to additional extrinsic effects, such as grain boundaries, the defect density in thin films is generally higher, typically around 10^{15}–10^{17} cm^{-3}, whereas it is only $\sim 10^{10}$–10^{11} cm^{-3} in single crystal perovskites[339, 340]. Indeed, this is higher than observed in conventional materials such as polycrystalline silicon ($\sim 10^{13}$ cm^{-3})[341] and CIGS (10^{13}–10^{14} cm^{-3})[342]. While these values all appear to refer to bulk defect density, values for the total defect density at the interface are not often mentioned even though the interface can be a severely limiting factor of a perovskite device[103, 343, 344]. Ni et al.[233] show that the defect density at the interface is significantly higher compared to the bulk, independent of the degree of crystallinity or composition. Xing et al.[345] modelled the photoluminescence intensity as a function of photon-generated exciton density and also found the defect density at the interface to be higher than in the bulk. It is believed that the migration of ionic defects to the interface plays an important role in this observation[346, 347].

Similar to the measurements, the reported values in SCAPS simulations vary quite significantly. For the bulk defect density, values range from 10^{11} to 10^{17} cm^{-3} [229, 310, 348–351] and for the interface defect density it spans from 10^7 to 10^{11} cm^{-2} [103, 177, 227, 348, 352–354]. Both the bulk and interface defect density in the simulations have been optimized by fitting the measurement data and a value in the order of 10^{14} cm^{-3} for bulk and 10^9 cm^{-2} for the interfaces were found to fit nicely. Notice that the units of the interface defect density is in cm^{-2} while the bulk is in cm^{-3}. This may seem obvious, but it appears that in literature both cm^{-2} [177, 227] and cm^{-3} [233, 243, 355] are used as units for interface defect density. In reality, the interface between two layers is not perfect and due to roughness and mixing of the materials, it will have a certain "depth". Researchers have tried to mimic this region in SCAPS by adding thin interlayers with slightly altered properties and giving these layers a bulk defect density representative of the expected interface defect density[226, 229, 308]. It was decided not to include this in this project due to the additional complexity, parameters and computation time.

Besides the density of defects, each defect is of a certain type which also has to be specified in SCAPS. A defect can for example act as a single donor or acceptor. A donor defect has an excess electron that is loosely bound to the defect, which corresponds to its neutral (0) state. The electron can be donated to the conduction band of the material where it becomes a free carrier, which corresponds to its charged (+1) state. This ionization can be represented via the reaction $D^0 = D^+ + 1e^-$. Similarly, an acceptor defect has an excess hole corresponding to its neutral (0) state. The hole can be donated to the valence band where it becomes a free carrier and this corresponds to its charged (-1) state, following the reaction $A^0 = A^- + 1h^+$ [338, 356, 357]. In terms of recombination, a donor (acceptor) defect in the +1 (-1) state can capture an electron (hole), converting the defect to the 0 state. Subsequently, the trapped electron (hole) can recombine with a hole (electron) in the valence (conduction) band and the

defect is converted back to the charge +1 (-1) state[338]. Hence, both single donor and acceptor defects have two possible charge states. The same analogy is used in SCAPS to refer to the charge state of the defects[358]. It is possible for a defect to have more charge states, i.e., it can capture multiple electron or holes, making it a multivalent defect. Then there are also amphoteric defects able to capture either type of charge. In SCAPS, there is an extra option for the defects, namely the neutral type (not to be confused with its charge state), which is an idealization of a defect that contributes to the non-radiative recombination by giving the charge carriers a certain lifetime, but does not contribute to the space charge. It does not exist in reality, but it is a useful solution when the origin and nature of the defects is unknown without introducing to many other effects. This is the preferred defect type used in the simulations in this project.

Another important characteristic is the depth of the energy level of the defects. The wide variety of compositions and processing methods result in many different possible defects, each with its own specific energy level. Defects with a shallow energy level lie in or just above (below) the valence (conduction) band while deep defects have their energy level close to the middle of the bandgap and are the main contributors to non-radiative recombination[359]. The experimental techniques mentioned in the section on the capture cross-section are able to determine these energy levels as well and both shallow and deep defects have been observed[326, 329, 337, 340]. Theoretical calculations are needed to identify the molecular origin of each defect and confirm its corresponding energy level, so that the most detrimental ones can be prevented with an optimized processing route[360] or neutralized using targeted passivation[361]. Density functional theory (DFT) is the preferred computational modeling tool to simulate the electronic band structure of materials at the atomic level. The first calculations using this method predicted shallow defects to be dominant due to their low formation energy and deep defects, while still possible, unlikely to be introduced due to their high formation energy[299, 301]. Over time, the calculations were optimized by correcting for the self-interaction error and including spin-orbit coupling (SOC), leading to a better agreement on the height of the energy bands while also predicting the correct bandgap[337, 356]. Using the improved simulations, it was found that it is possible for deep intrinsic defects to form in perovskite materials[339, 362]. In SCAPS simulations, the most commonly used height for the energy level is the standard setting, which is 0.6 eV above the valence band, or in the middle of the bandgap resulting both in deep defects[229, 290, 311, 354]. For the simulations done here, the energy level is also put in the middle of the bandgap of the perovskite for both the bulk and interface defects.

The last settings are the spatial distribution of defects and the energetic distribution of their energy level. It is assumed that the defects are uniformly distributed throughout the layer, i.e., no grading is applied. SCAPS has multiple options for the defect energy level, such as a single level, a uniform or Gaussian distribution with a characteristic energy determining the width or a tail at either the conduction or valence band. By far the most common setting used in literature is the Gaussian distribution with an occasional use of the single distribution[243, 248, 250, 281, 353, 363]. The settings used in this project are a uniform distribution of defects with a single energy level. The difference between both distributions is tested and

gave a negligible difference in J_{SC} with the other figures of merit remaining the same.

Other parameters

Finally, there are a few parameters that are not related to a specific internal layer, but to the device as a whole, such as the temperature, resistance and the work functions of the metal contacts. The temperature is set to 300 K, which is slightly higher than room temperature. During the JV-measurements the sample is heated by the light justifying the higher value.

The resistance in the device can be divided into two parts, namely the series resistance R_s and the shunt resistance R_{sh}. R_s originates from the resistance of the transport layers, the metal contacts and their connections and should be as low as possible. The main impact of R_s is on the FF, but at very high values it will also affect the J_{SC}. At high light intensities it will be the dominant resistance. The range of values typically found in perovskite solar cells is 2 to 15 $\Omega\,cm^2$ [307,355,364–367] where an excellent solar cell has a value in the low single digits. The R_{sh} is related to manufacturing quality of the layers where shunts, i.e., alternative pathways for the current, reduce the power output of the device, hence R_{sh} should be as high as possible. These shunts can be caused by incomplete coverage of the surface area by any of the layers or material of the metal contacts penetrates the transport layers or even the perovskite [368]. A low R_{sh} mainly affects the FF as well as the V_{OC} while leaving the J_{SC} unaffected. Its limitation on performance is dominant at low light intensities. The values for the R_{sh} range from $\sim 10^2$ to 10^5 $\Omega\,cm^2$ [19,185,369–373]. Both the R_s and R_{sh} are optimized during the simulations and good fits are found for a R_s of 12 $\Omega\,cm^2$ and a R_{sh} of $4.5 \cdot 10^6$ $\Omega\,cm^2$. R_s falls nicely in the range found in literature, but the R_{sh} is over an order of magnitude larger. Lower values would significantly decrease the FF at low light intensities and contradict the measurements. Similar values for the R_{sh} are used by other authors in simulations [349,374].

As mentioned before, not the entire device is simulated, therefore the left (right) contact in SCAPS should represent the layer adjacent to hole (electron) transport layer of the real device. For the left contact the situation is identical to the real device as it is adjacent to the ITO. However, this is not true for the right contact, which should represent the ALD SnO_2 layer instead of the gold electrode. The height of the work function of the ITO layer is found to lie in the range of 4.4 to 5 eV [181,204,205,209,375]. In the end, a value of 5.1 eV is used in the simulations giving a injection barrier of 0.2 eV as seen in Figure 4.4. Any lower values would result in a significant blockage of injected carriers leading to low FF values and a flattening of the JV-curve at high voltages, which does not correspond to the measurement data. The value for the right contact should correspond to the EA of the SnO_2 layer, which can vary depending on the deposition technique [376]. A value of 4.1 eV is used that gives a injection barrier of 0.1 eV, while higher values would again result in an undesired injection barrier.

As a final notice, it is not claimed that these individual parameters are in perfect agreement with the real device, but in the context of the existing literature they are considered plausible. Most parameters are optimized in SCAPS based on the measurement results, instead of measured directly.

5. Results and discussion

In this chapter the most important results of the project are shown and elaborated on. Both the measurements and the simulations are discussed and compared and a hypothesis is put forward as explanation for the observations.

The chapter is divided into four main sections. The first two discuss the measurement and simulation results prior to aging, respectively, and follow more or less the natural order of how the data is obtained. The two subsequent chapters discuss the effect of the aging process on the photovoltaic parameters and the simulations to evaluate and understand the underlying processes that happen.

5.1 Measurements of fresh devices

5.1.1 J-V measurements

Figure 5.1a and b show the averaged J-V curves of each composition when measured from the glass and ITO side, respectively. The devices are measured with a forward (reverse) sweep as indicated by the dashed (solid) lines. It is clear from their mismatch that all compositions suffer from hysteresis, independent of the measurement side, albeit considerably less for the devices with RbCl-doped perovskite.
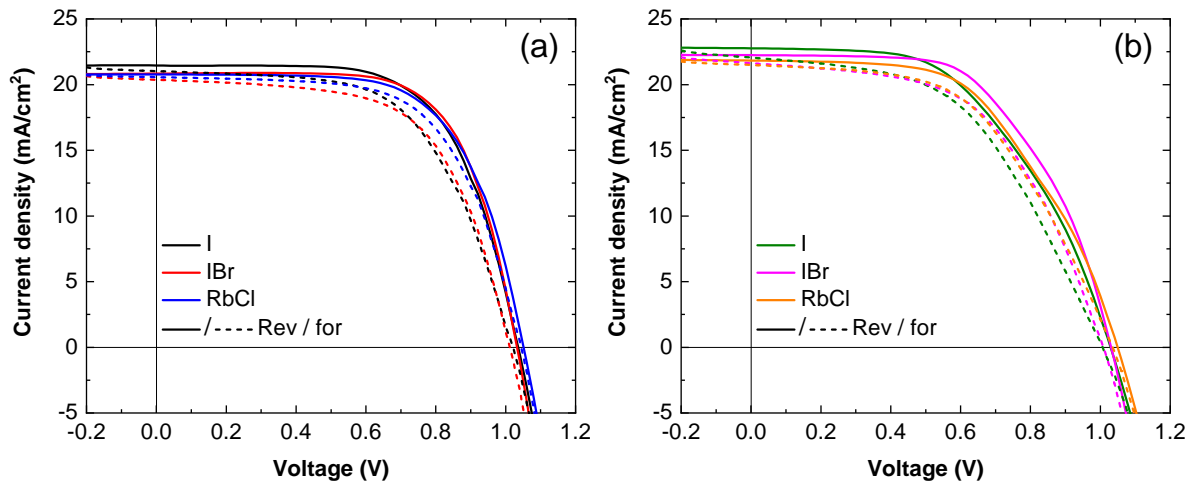
Figure 5.1: J-V measurements of the fresh devices
The averages of the J-V measurements of the different perovskite compositions with the solid (dashed) lines indicating the reverse (forward) measurement. (a) Illumination from glass side, (b) illumination from ITO side.

Looking at the curves in more detail, a small "shift" can be observed around 0.9 V in all compositions, which is best visible in Figure 5.1a. One could argue that this is perhaps due to the process of averaging the measurements, introducing artifacts in the curve. However, this effect is even more clearly present in the original measurements. Hence, it appears that the averaging only leads to a smoothing of J-V curve in this regard. The shift has also been observed by Li et al.[377] and is typically found in a fast forward scan. According to Li et al., it is at this exact point during the sweep when flat-band conditions are achieved, making diffusion the dominant transport mechanism. If the device is influenced by ion migration, it means that also the ions will diffuse. This will rearrange the built-in potential, which in turn shifts the V_{OC} resulting in a jump in the J-V curve.

Another interesting peculiarity can be observed in the reverse bias curves when illuminating from the ITO side. It appears that the curve has a subtle kink in between the MPP and V_{OC}. Again, this is not a feature due to the averaging of the measurements, but can also be observed in the original measurements. This kink is an undesirable effect, since it appears to limit the FF of the devices. No relevant literature could be found on this, so it is difficult to speculate on the origin of this effect. Interestingly, the kink can only be observed in the measurements from ITO side, suggesting it is related to the electron transport layer(s).

To get a better understanding of the differences between the two measurement sides as well as the different compositions, the extracted figures of merit are plotted in Figure 5.2 for comparison. Each solid (open) data point represents a single reverse (forward) J-V sweep accompanied by the statistical spread in the form of bars. The colors are consistent with the colors used in Figure 5.1. Starting with the PCE, it is clear that illumination from glass side yields a higher efficiency, independent of the composition. It is a common practice to determine the ratio of the PCE of both illumination sides, which gives the bifaciality factor, to assess the performance of a semi-transparent solar cell. Calculating the factor for the three compositions gives a value of 85%, 88% and 90% for the I pure, IBr and RbCl devices, respectively. These are excellent values, however, an asterisk has to be added, which will be clarified after the other photovoltaic parameters are discussed. Regarding the compositions, it appears that the IBr devices are performing slightly better than both the I pure and RbCl devices, independent of the illumination side. This, however, is only true when looking at the reverse sweep. The difference between the reverse and forward data gives a more concrete impression of the amount of hysteresis than by comparing the J-V curves. If it is assumed that the "correct" value for the same device without hysteresis would be in between both sweeps, the two device types containing 2% bromide would more or less have the same PCE, while the I-pure devices perform less efficient. This appears to be true for both illuminations sides. Continuing with the hysteresis, the RbCl-doped devices indeed show less hysteresis and the effect is most noticeable when illuminating from glass side. The improved V_{OC} and FF in the forward sweep are the most significant contributors to this reduction.

Moving on to the J_{SC}, the first thing that stands out are the significant higher values for the measurements from ITO side. This is a surprising result, because the illumination of the rear side of semi-transparent perovskite solar cells normally leads to a substantially lower
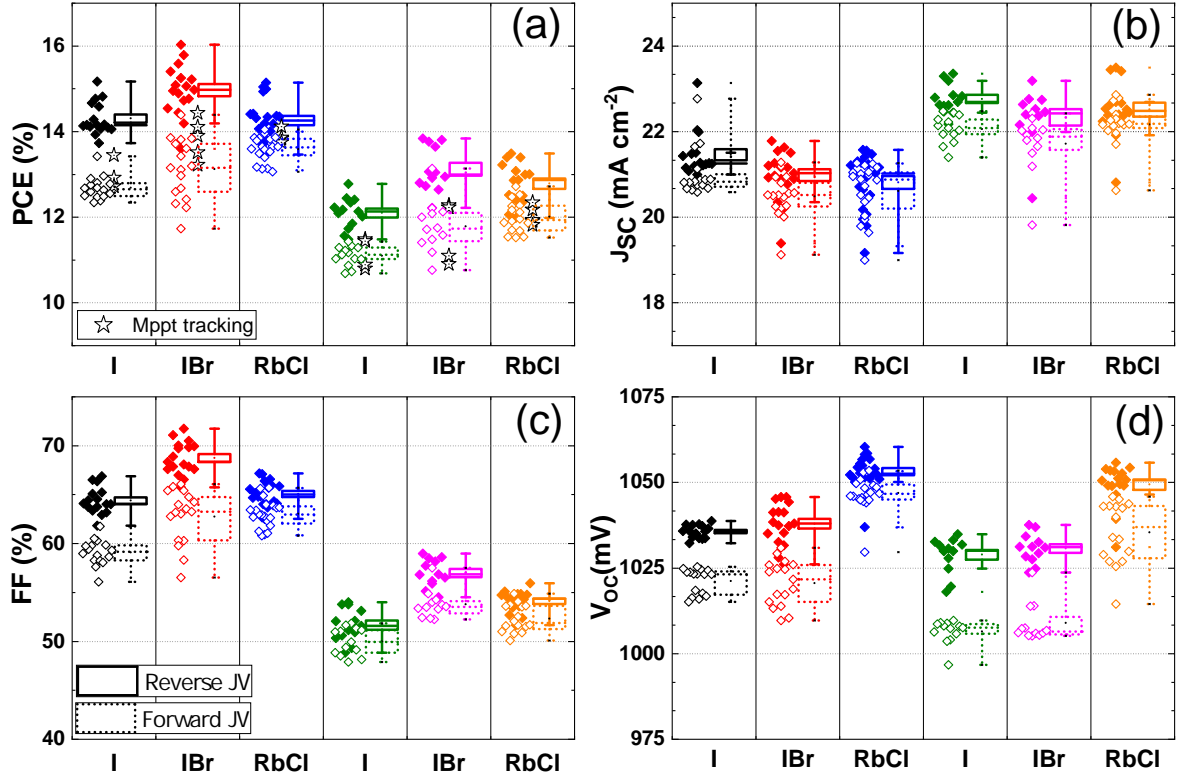
Figure 5.2: Figures of merit of the fresh devices

Photovoltaic parameters of the different perovskite compositions with statistical deviation obtained from the J-V measurements. The solid (open) data points and solid (dotted) bars indicate the reverse (forward) measurement. The three data sets on the left (right) in each graph are the measurements from glass (ITO) side. (a) PCE, (b) J_{SC}, (c) FF and (d) V_{OC}.

current density[378–380]. Hence, it is unclear whether these results are genuine or there is a flaw in the measurement. A comparison to the J_{SC} obtained from the EQE measurements should help understand these results better, which is done in section 5.1.2. Another observation is the slightly higher J_{SC} for the I pure devices compared to the 2% bromide devices. The addition of 2% bromide results in a small increase in bandgap and thus a shift in the absorption onset to smaller wavelengths. Hence, a part of the spectrum is lost and that leads to a decrease in the J_{SC}.

The FF follows a similar pattern to the PCE indicating its importance for the final efficiency. The IBr devices have the best FF for both illumination sides and again the amount of hysteresis differs depending on the composition. The illumination side has a large influence on the value and there is a substantial loss of approximately 10% when switching to ITO side illumination. The unusual shape of the J-V curve as seen in Figure 5.1b certainly attributes to the decreased FF. The values typically found in literature for semi-transparent cells are approximately the same for both sides or sometimes even better for illumination from the rear side[378,379,381,382]. More fundamental information about the device is difficult to extract for

this parameter due to the complex relations and dependencies on its properties.

Lastly, the V_{OC} shows similar behavior between the different devices types for both illumination sides. The addition of 2% bromide slightly increases the bandgap and thus also the V_{OC}. The devices with RbCl-doped perovskite show a measurable increase of around 20 mV. Combined with the fact that the hysteresis of these devices is also lower, it could be that the doping decreases the amount of defects. Interestingly, this is the only parameter that shows more hysteresis when measured from ITO side, which was not the case for the other figures of merit.

Coming back to the bifaciality factor, the unusually high values for the J_{SC} measured from the ITO side (partly) compensate for the significant decrease in FF. Hence, the final PCEs for the ITO side measurements are still decent and this leads to excellent bifaciality factors. However, due to the questionable validity of the J_{SC} ITO side values, it possibly also calls into question the bifaciality factors. Whether this is the case all depends on the relations between the J_{SC}, FF and PCE. The PCE ultimately depends on the maximum power point, which is linked to the FF and J_{SC}. If the J_{SC} is indeed incorrectly measured it should be significantly lower, even lower than the values for the glass side measurement. Such a large change would also lower the maximum power point, followed by the PCE and thus the bifaciality factor. Interestingly, as a result the FF would increase, aligning the parameter more with the expectation as seen in literature.

5.1.2   EQE measurements

The EQE is measured as function of wavelength in order to learn more about the conversion efficiency of light to charge carriers that also contribute to the current. The averaged result for each composition and illumination side is plotted in Figure 5.3. An inset is added with a close-up of the bandgap and the color of each curve is again consistent with the J-V curves.

The general shape of the curves of each illumination side is identical for all three compositions with only slight variations in height at certain wavelengths, indicating that there are no major differences to the optical and electrical properties between the different compositions when no voltage is applied. The addition of 2% bromide slightly improves the EQE values over the entire spectrum. There is a small difference for the RbCl devices, which appears to initially follow the I pure curve and switch to the IBr curve near 450 nm. The possible origin for this behavior remains unknown. Ideally, 100% of the light is converted to collected charge carriers, but this is not attainable due optical losses, such as parasitic absorption by non-perovskite layers, reflectance and transmittance as well as electrical losses, such as charge carrier recombination during the transport to the electrodes. Additional information is needed to know the origin of certain losses in the EQE curves, which will be discussed in detail in section 5.1.3 and 5.2.1. There are a few useful parameters that can be extracted from the EQE curve, namely the J_{SC}, the bandgap of the perovskite and the Urbach energy. The calculated J_{SC} values for the three compositions for both illumination sides are given in Table 5.1 together with the extracted values of the J-V curves for comparison.
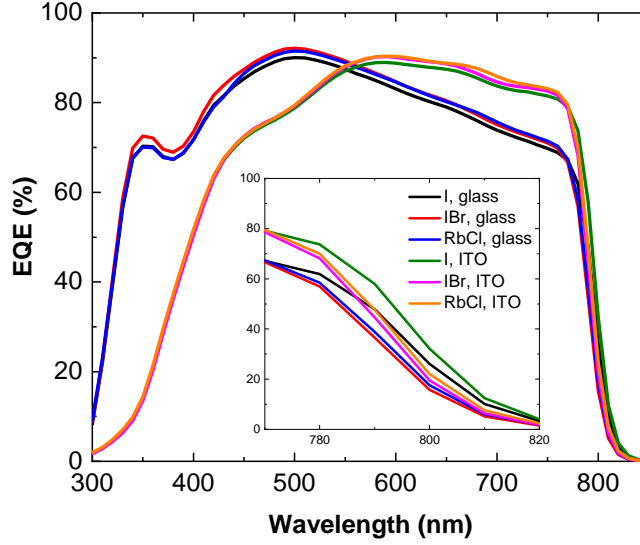
Figure 5.3: EQE measurements of the fresh devices
The averaged EQE measurement of the different perovskite compositions for both illumination sides.
Inset: a close-up near the bandgap.

Table 5.1: Comparison of the J_{SC} extracted from EQE and J-V measurements
The data represents averaged values with uncertainties calculated using standard deviation. The J-V
values are based on the average of the forward and reverse sweep. The units are in mA cm^{-2}.

	Glass side		ITO side	
	$J_{SC,\ EQE}$	$J_{SC,\ JV}$	$J_{SC,\ EQE}$	$J_{SC,\ JV}$
I	21.4 ± 0.1	21.2 ± 0.5	21.5 ± 0.1	22.4 ± 0.3
IBr	21.5 ± 0.2	20.7 ± 0.5	21.3 ± 0.3	22.0 ± 0.6
RbCl	21.6 ± 0.1	20.7 ± 0.6	21.6 ± 0.1	22.3 ± 0.6

The difference between glass and ITO side illumination for the J-V measurement is again clearly visible after the data is compressed into single values. The values obtained from the EQE measurements, however, give a completely different picture, being more or less equal from both illumination sides. Furthermore, the differences between the compositions is negligible, which is not necessarily the case for the J-V measurements. Another interesting thing to note is the difference in the uncertainties between both types of measurement, indicating that the EQE measurement is a more accurate method for determining the J_{SC}. The most striking observation is the mismatch between the J-V and EQE extracted J_{SC} values, which in theory should be equal. Saliba et al.[383] reported on this discrepancy and found that $J_{SC,\ EQE}$ is generally lower than $J_{SC,\ JV}$. The exact reason for this difference is still unknown, but could potentially be related to the duration of the measurements. A typical EQE measurement takes considerably longer than a J-V sweep. Effects such as ion migration and sample degradation play an important role on these timescales and could affects the final results[383]. From Table 5.1

it is clear that Saliba's observation only holds for the ITO side measurements, while the glass side measurements show the opposite behavior. Coincidentally, the results listed in the paper are only from devices with a n-i-p structure, which is equivalent to the ITO side illumination. This could be merely a coincidence, but is nevertheless interesting to note. Another reason could be the light source of the solar simulator set-up. Ideally, the light source perfectly simulates the solar spectrum, but in practice this is almost impossible to do. A halogen lamp is used, which has a lower (higher) emission in the blue (red) part of the spectrum compared to the solar spectrum. From the EQE measurement it is evident that the glass side outperforms the ITO side at lower wavelengths, while it is the other way around at higher wavelengths. Hence, combining these two observations would explain why the J-V measurement from glass (ITO) side has a lower (higher) J_{SC} compared to the EQE measurement. This could be further investigated by using various LEDs of specific wavelengths in order to measure the response at different wavelength for each illumination side.

The bandgap of the perovskite and the Urbach energy are listed in Table 5.2 below. Both values are calculated from the EQE data using a Matlab script developed by Dong Zhang as explained in section 3.3. Starting with the bandgap, there is a minuscule difference between the two illumination sides for each composition, but the values are within the error range that in itself is small. The addition of 2% bromide leads to an increase in the bandgap of approximately 10 meV. This change compared to the pure iodide devices is more clearly visible in the inset in Figure 5.3. The RbCl doping appears to slightly decrease the bandgap, albeit marginally. This is a peculiar change, since both rubidium and chloride typically cause the bandgap to increase[384–387]. However, the 0.1% doping used in the RbCl devices is significantly less than usually reported in literature. Even though Saidaminov et al.[387] found a blue shifting for higher concentrations of chloride, they also report the data for concentrations similar to this project, which arguably show a small red shift. Similarly, Li et al.[388] found a slight decrease in bandgap for a small addition of rubidium. Hence, it appears plausible that the RbCl doping results in a modest decrease of the perovskite bandgap.

Table 5.2: Perovskite bandgaps and Urbach energies
The data represents averaged data calculated from EQE measurements.

	Glass side		ITO side	
	bandgap (eV)	E_{Urbach} (meV)	bandgap (eV)	E_{Urbach} (meV)
I	1.558 ± 0.001	16.1 ± 0.1	1.556 ± 0.001	15.5 ± 0.5
IBr	1.569 ± 0.001	15.5 ± 0.1	1.568 ± 0.000	15.4 ± 0.1
RbCl	1.567 ± 0.002	16.0 ± 0.2	1.566 ± 0.001	15.9 ± 0.2

The Urbach energy is found to be around 15 to 16 meV for all compositions, which is in excellent agreement with values reported in literature[21,389]. It is important that these values are below the thermal energy of $\sim$26 meV. This way, charge carriers that are trapped in the tail states within the bandgap can still be thermally excited back to the valence or conduction

band. Values higher than the thermal energy make this process impossible and hence the charge carriers will eventually be lost via (non-radiative) recombination. The values for the IBr devices are slightly better, but pinpointing the exact reason for this is impossible without additional information due to the many parameters that can affect the tail states.

5.1.3 UV-vis measurements

The transmittance $T(\lambda)$ and reflectance $R(\lambda)$ are measured to learn more about the optical losses in the devices as function of wavelength λ. The measurement data is converted to absorptance $A(\lambda)$ using the following equation:

$$A(\lambda) = 1 - T(\lambda) - R(\lambda) \tag{5.1}$$

and plotted as solid lines in Figure 5.4 together with the EQE data as dashed lines. The original transmittance and reflectance data can be found in Figure B.1 of the appendix. The total absorptance not only gives information about which part of the spectrum is not (fully) absorbed by the device, but by comparing it to the EQE data, it also provides insight into the losses that occur in between light absorption and charge carrier collection i.e. the internal quantum efficiency (IQE) loss. These losses are caused by parasitic absorption by layers other than the perovskite as well as the recombination of the carriers before their collection.
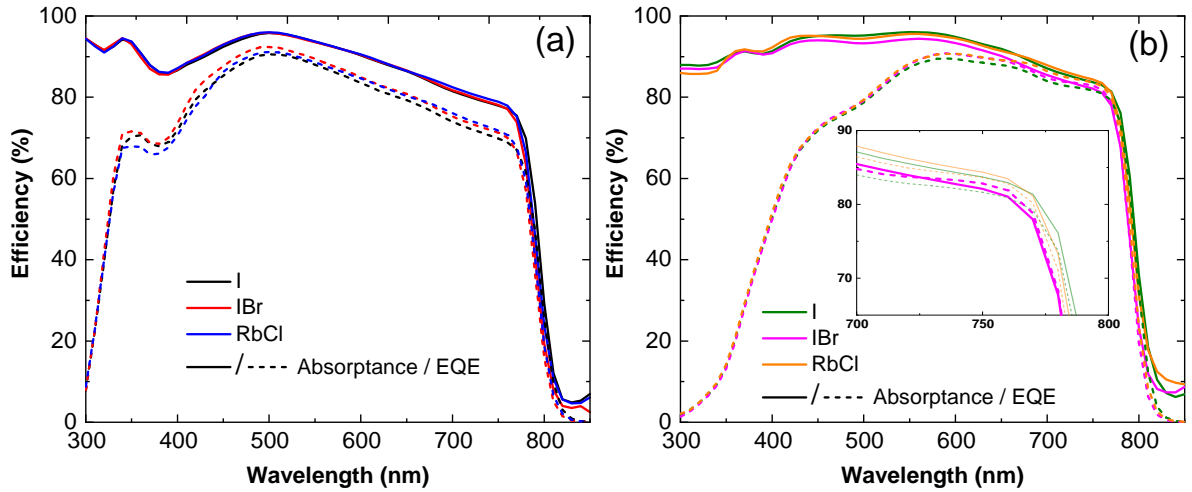
Figure 5.4: Absorptance vs EQE of the fresh samples
Values calculated from the transmittance and reflectance and accompanied by the EQE for comparison for all three compositions. (a) Illumination from glass side, (b) Illumination from ITO side. Inset: close-up of intersecting curves.

For both illumination sides it is the case that optical losses are dominated by reflectance till around 650 nm after which the transmittance becomes the dominant loss factor, as can be seen in Figure B.1. The absorptance drops off after the bandgap and the device becomes mostly transparent. The results for illumination from the glass side are shown in Figure 5.4a.

No major differences are observed between the three compositions, once more confirming the optical similarities between the devices. Comparing the absorptance and EQE gives a clear picture of the amount of internal losses occurring at the different wavelengths. The biggest losses occur at short wavelengths with a more or less constant loss of around 5 to 10% after 450 nm. The absorptance from ITO side illumination is shown in Figure 5.4b. There is slightly more deviation between the compositions, but the overall behavior is still the same. The internal losses after absorption are significantly larger at short wavelengths compared to the glass side and extend further to longer wavelengths as well. However, this is partly compensated around 700 to 800 nm where the absorptance almost overlaps with the EQE and thus reaching an IQE close to 100%. In fact, the absorptance of the IBr intersects with the EQE measurement near 750 nm as can be seen in the inset, suggesting that there are more charge carriers generated than photons absorbed, which is impossible. As said in section 3.3, the small size of the samples made it difficult to measure UV-vis, so it is most likely that this is due to an error in the measurement. The actual origins of the losses in IQE will be discussed with the help of the optical simulations in section 5.2.1.

5.1.4 XRD measurements

XRD measurements are done to compare the crystal structure of the three different perovskite layers and the results are shown in Figure 5.5 below. Overall, the three compositions show peaks at the same angles as well as have similar relative heights between the peaks within each measurement, suggesting that the crystal structure of the layers are comparable. Most peaks are labeled corresponding to the most likely crystal composition contributing to the measurement signal as determined from XRD reference cards, previous experience and analysis in Solliance and several papers with similar perovskite compositions[19, 175, 192, 390, 391].

The main peaks can be attributed to the expected α-perovskite phase. There are however a series of smaller peaks and based on literature and analysis they are attributed to a $CsPbI_3$ phase. It thus appears that there are different phases present in the perovskite layer, rather than a single uniform perovskite phase. Using the software Vesta, which can calculate the powder diffraction pattern of a crystal structure, the XRD signal for the similar $Cs_{0.1}FA_{0.9}PbI_3$ composition investigated by Charles et al.[392] is calculated based on their provided crystal structure model and compared to the I pure measurement in appendix B.2. The calculation represents the desired single perovskite crystal phase and while the peaks of the calculation are slightly shifted compared to the measurement, they are in excellent agreement with the location of the α-perovskite phase. Additionally, precisely the peaks corresponding to the $CsPbI_3$ are not found in the calculation, which further supports the hypothesis that there are multiple crystal phases present in the perovskite.

There are a few peaks for which the origin remains unsure and the most prominent one is around 8.2°, which is not observed in similar compositions reported in literature. The measurement is done under ambient conditions, hence it could be related to surface contamination from particles in the air. However, the sharpness of the peak rather suggests a genuine source
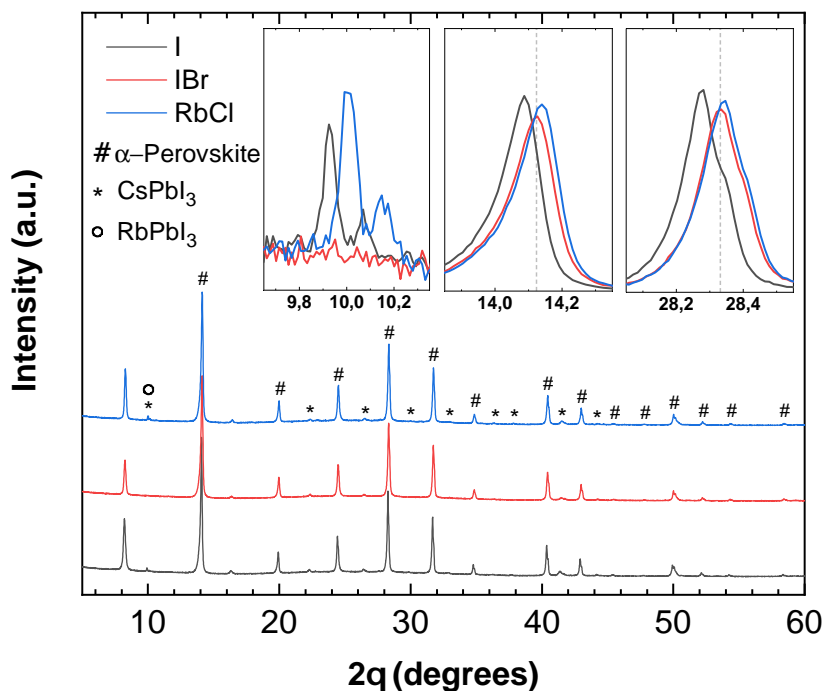
Figure 5.5: XRD measurement of the fresh perovskite films
Most peaks are labeled to indicate their expected crystalline origin. The insets show a close-up of three different angles to emphasize the differences between the compositions.

in the perovskite crystal structure. Based on the experience in Solliance the peak could originate from a NMP-PbI$_2$ complex that is present in the perovskite layer after spin coating[393]. This is further supported by the small unknown peak at approximately 16.4°, which is double the reflection angle of the main peak. Important peaks to look out for in perovskite layers are located at ~11.7° and ~12.6° corresponding to the δ-FAPbI$_3$ and PbI$_2$, respectively[108,390]. These peaks are not observed in any of the compositions meaning that the layers have excellent crystallinity.

Different close-ups of the three measurements stacked on top of each other are shown as insets to give a better view of the mutual differences. The addition of 2% bromide leads to a shift of the peaks to higher angles, which is observed for all peaks and is made visible for the two larges peaks shown in the middle and right inset. Generally, such shifts are attributed to a decrease in lattice parameter, caused by the incorporation of smaller ions[394,395]. The substitution of the iodide partly by smaller bromide ions fits this explanation. Furthermore, doping the perovskite with RbCl introduces even smaller ions, again shifting the peaks to higher angles. This effect in not as large compared to the bromide substitution because the amount of dopant is very small and the difference is close to the step size of the measurement, hence it remains uncertain whether the RbCl is incorporated into the lattice.

The only significant difference regarding peak size that can be observed is the small peak around 10°, and more specifically, the lack thereof in the IBr sample as can be seen in the left

inset. According to Lee et al.[19] and the analysis, the peak originates from $CsPbI_3$, but since all samples contain the same amount of cesium, it is expected to then also see the peak for the IBr sample. The possibility that the addition of bromide could prevent the formation of $CsPbI_3$ seems highly unlikely due to the substantial amount of cesium. Furthermore, the other peaks associated with $CsPbI_3$ *are* present for the IBr sample. Looking at the measurement of the RbCl-doped sample, which has the same amount of bromide, the peak reappears and shows the same characteristics as the iodide pure sample. The small addititional peak on the right side is present for both samples, which suggests the signal originates from the same crystal structure. This makes it unlikely that the 2% bromide affects the crystal formation of $CsPbI_3$. Similar to the $CsPbI_3$, a peak appears at 10° for $RbPbI_3$ as shown by Turren-Cruz et al.[391]. However, since the amount of doping is very small, it is highly improbable that the entire peak solely originates from the $RbPbI_3$. Interestingly, this is the only peak where the RbCl sample has a higher intensity compared to the iodide pure sample suggesting instead that the combined intensity of $CsPbI_3$ and $RbPbI_3$ could be the reason.

All in all, the crystal structures for all three compositions are very similar and based on the analysis it is found that there are three different crystal phases present, namely an α-perovskite-, $CsPbI_3$- and NMP-PbI_2 complex phase. The general shifts observed confirm that the addition of bromide and possibly the RbCl doping are incorporated into the perovskite layer. The origin of the missing peak at 10° for the IBr sample remains a mystery and a detailed analysis with additional measurements is needed to find the explanation.

5.1.5 Light intensity measurements

Besides the different characterization techniques at one sun illumination, also J-V measurements at different light intensities are done to get a better understanding of the dominant charge carrier recombination mechanisms. Figure 5.6 shows the averaged light intensity measurement of the IBr devices ranging from one to 10^{-4} sun illumination intensity as an example of a result. Obviously, the most affected parameter is the J_{SC} due to the decreased amount of photons that generate charge carriers. Furthermore, the V_{OC} also decreases with decreased light intensity due to the quasi Fermi level splitting reducing for the same reason[396]. Analyzing such graphs and comparing them directly between different measurements is impractical because the FF cannot be compared properly and the curves at low light intensity start to overlap. Furthermore, the values become so small that the linear scale no longer suffices.

Hence, to better understand the light intensity dependence of the figures of merit, each curve's values are extracted and the averages including their standard deviation are plotted in Figure 5.7 and 5.8 for glass and ITO side illumination, respectively. Starting with illumination from glass side, the PCE follows a similar trend for all compositions with a slight difference in slope between the iodide pure and 2% bromide-containing devices at lower light intensity. The curves show that a higher light intensity not necessarily results in a higher efficiency since the maximum for all compositions can be found around 0.1 sun. The J_{SC} is plotted in panel b and follows the expected decrease as function of decreasing light intensity. The curves
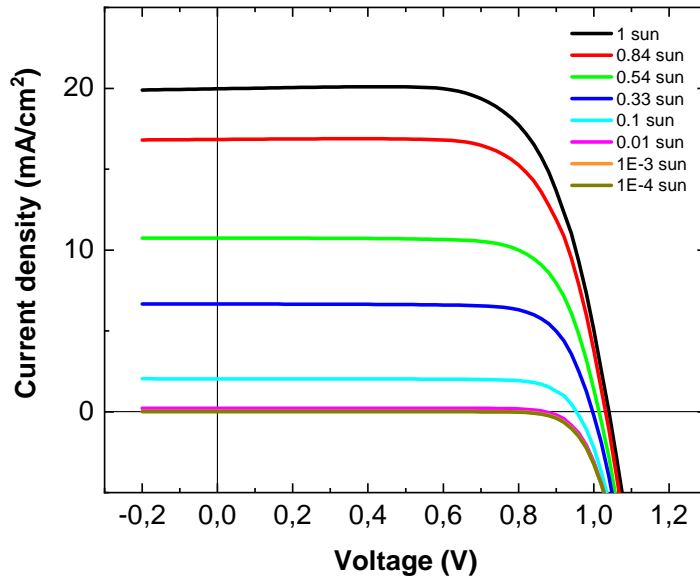
Figure 5.6: J-V curves at different light intensity
Illumination from glass side. Each curve is averaged over all IBr samples.

are almost perfectly overlapping with only the iodide pure device deviating slightly at higher intensities. The inset shows the same data but plotted on a log-log scale from which the power law dependence parameter α is determined as explained in section 2.4.2.

The FF is plotted in panel c and shows a more complex dependence on light intensity. The 2% bromide-containing compositions have a similar shape with a maximum just below 0.1 sun intensity, while the iodide pure devices appear to remain mostly constant at low light intensity. Contrary to the J_{SC} and V_{OC}, there are only a handful of papers reporting on the light intensity characteristics of the FF. In this study, the FF shows a variety of different dependencies for decreasing light intensity, which is also observed by other researchers[397,398]. While these are certainly not the only possibilities with regard to the shape of the curve[107,399], it also very much depends over which intensity range the measurement is performed. The exact shape depends on many device parameters and not all are equally dominant at all intensity ranges. Various authors have observed changes to the curve by changing certain parameters, such as the composition[99,107], thickness[399] and precursor ratios[400] of the perovskite as well as the transport layer configuration[397]. However, simulations are needed to properly analyze and fit the curve to determine which parameters contribute the most at which light intensities.

The last panel contains the data of the V_{OC}. The 2% bromide substitution appears to improve the V_{OC} at lower light intensities while remaining unchanged at higher intensities compared to the iodide pure devices. Adding the RbCl doping measurably improves the V_{OC} at higher light intensities, but this comes at a cost at lower intensities where it decreases below the values of the IBr devices. The ideality factor n_{id}, obtained from the slope of the curve, gives additional information about the recombination dynamics as explained in section 2.4.1.
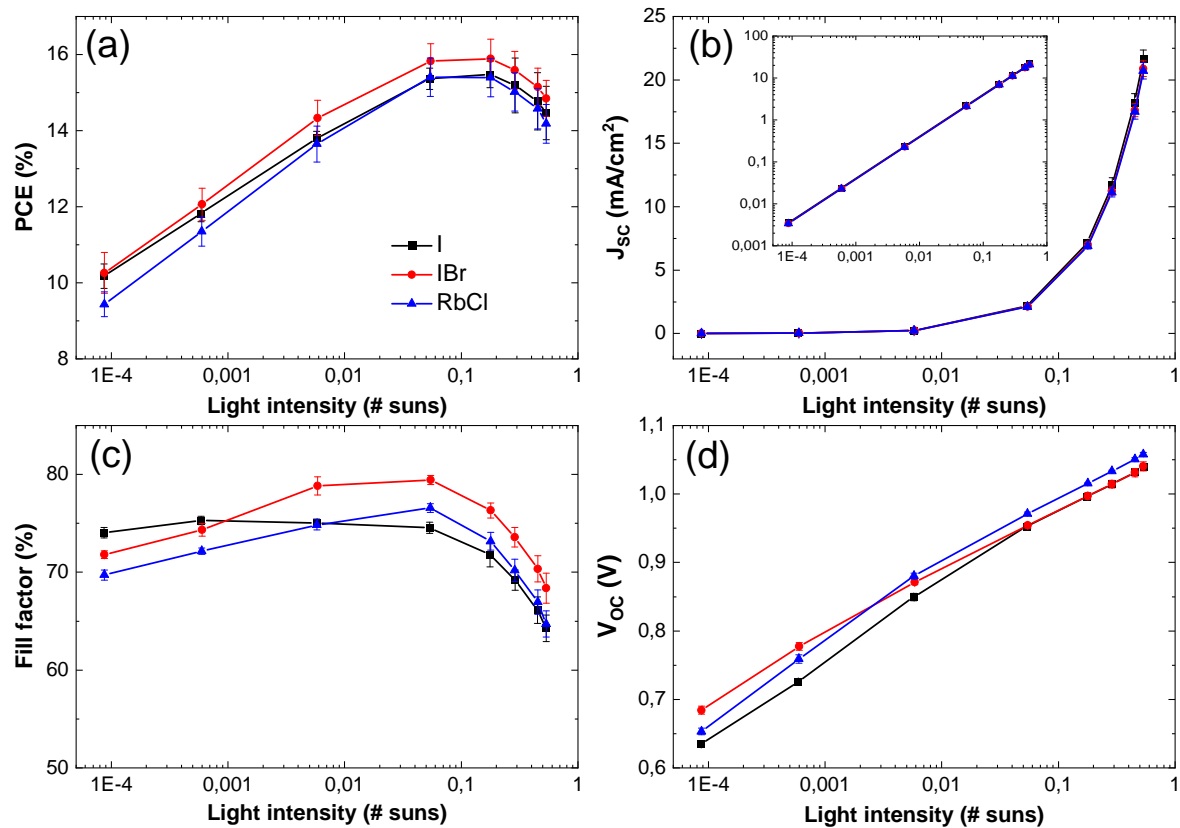
Figure 5.7: Photovoltaic parameters from light intensity measurements from glass side
Data is obtained from the fresh devices. (a) PCE, (b) J_{SC} with the data plotted on a log-log scale as inset, (c) FF and (d) V_{OC}.

The figures of merit for illumination from ITO side are plotted in Figure 5.8 and do show differences compared to glass side illumination. The location of the maximum in the PCE has shifted slightly to lower intensities. This is mostly the result of a similar change in the FF, caused by a considerable decrease of the values in the high light intensity regime and holds for all compositions. This becomes especially clear when looking at the ratio of the FF, similar to the bifaciality factor for the PCE, at each light intensity data point. Near 1 sun intensity the ratio ITO to glass is around 80-85% depending on the composition, but this value increases to approximately 100% at 10^{-4} sun intensity. As mentioned before, the FF is usually observed to be similar from both illumination sides at 1 sun in semi-transparent devices, hence this means that there is a mechanism at play causing losses in FF when measuring from ITO side. Since these losses increase with increased light intensity it is likely due to a problem at the interface, specifically the perovskite/PCBM interface. Głowienka et al.[374] investigated the same device stack and found that the deposition process of the ALD SnO_2 layer is the cause of loss in FF at high light intensities. The ALD process influences the perovskite/PCBM interface resulting in high interface defect density as well as band bending due to changes to the energy levels.
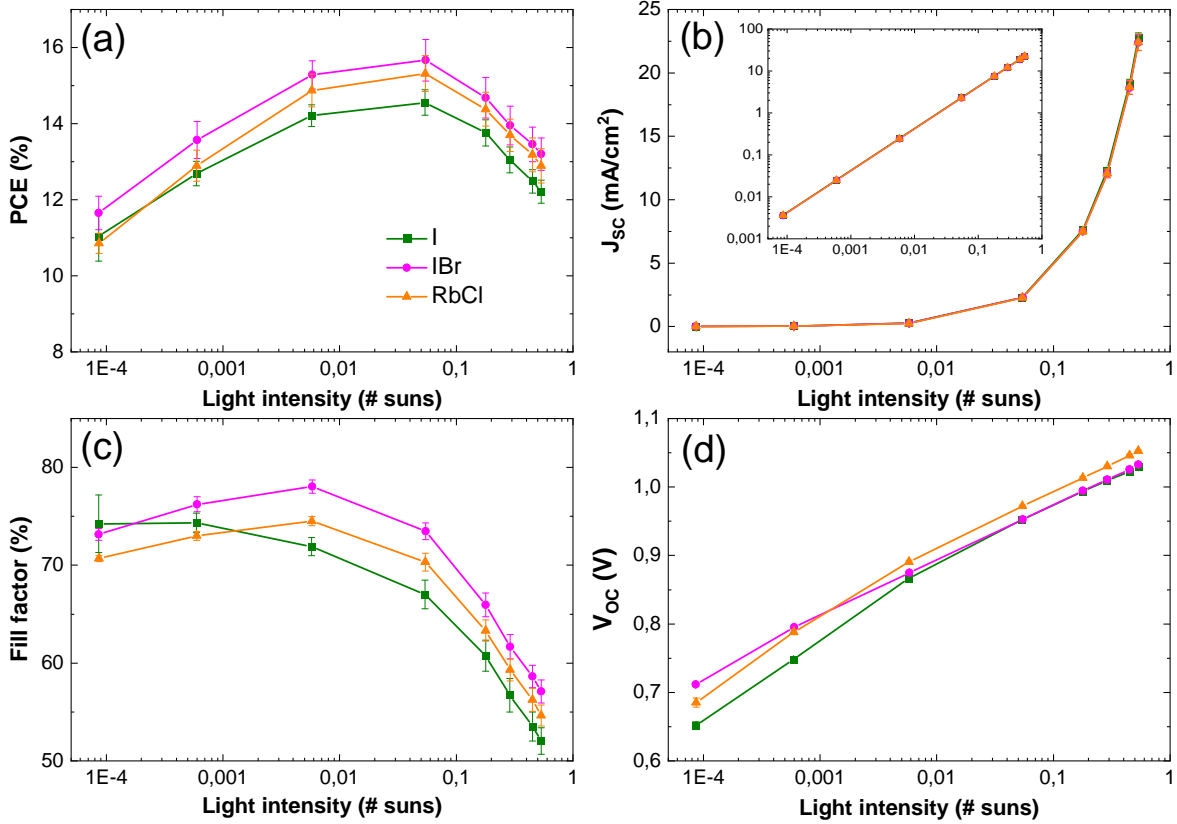
Figure 5.8: Photovoltaic parameters from light intensity measurements from ITO side
Data is obtained from the fresh devices. (a) PCE, (b) J_{SC} with the data plotted on a log-log scale as inset, (c) FF and (d) V_{OC}.

Extending the ratio analogy to the other figures of merit, the J_{SC} has a constant ratio of 105-108% over the entire intensity range, showing that the unexpected higher values from ITO side that are observed in the 1 sun J-V measurement are in fact independent of the illumination intensity. The shape of the curves themselves appears to be the same as for the glass side. The V_{OC} ratio shows a minor dependence on light intensity with a value of 99% at 1 sun, which slowly increases to 105% at 10^{-4} sun. The mutual differences between the compositions is almost identical to the glass side, indicating that both the bromide substitution and RbCl doping do not introduce any orientational dependence on light intensity with regards to the V_{OC}. In the end, the bifaciality factor of the PCE is found to be 85-90% around 1 sun intensity and increasing towards 109-115% at 1E-4 sun intensity. This means that the side that is most efficient actually changes depending on the light intensity, which could be a useful property for semi-transparent solar cells in applications such as windows.

FF on a linear scale

Interesting characteristics can be observed for the FF by converting the light intensity axis to a linear scale as is shown in Figure 5.9 below. This way, the emphasis is essentially placed on the

five data points in the high intensity regime, which is difficult to compare as seen in the previous two figures. The linear scale of the x-axis reveals that there is a vastly different dependence on light intensity for both illumination sides. For the glass side, a linear relation is found down to around 5% of the solar intensity and the slope is independent of the composition of the perovskite. For the ITO side on the other hand, the relation is clearly non-linear. Once again the relation is identical for the three compositions, suggesting that the type of dependence is determined by the charge transport layers and/or metal contacts. While research on the light intensity dependence of the FF in itself is already rare, measurement data plotted on a linear scale is even more scarce. Nevertheless, the papers that can be found almost exclusively show the linear dependence[400–402]. The non-linear dependence is thus an unusual behavior, but due to the complexity of the FF its exact origin remains unknown and can only be determined using simulations.
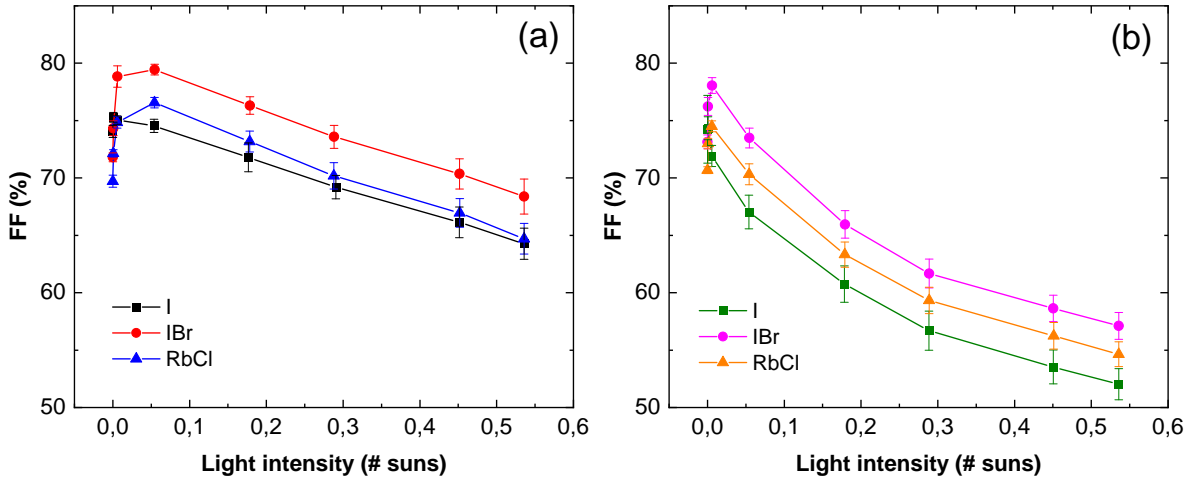
Figure 5.9: FF as function of a linear light intensity scale
Data is obtained from the fresh devices. (a) Illumination from glass side, (b) Illumination from ITO side.

The ideality factor n_{id} and power law factor α are given in Table 5.3 below for the three compositions and both illumination sides. It is important to remember that these parameters provide information on the recombination and extraction properties at specifically the V_{OC} and J_{SC}, respectively.

Table 5.3: Ideality factor and the power law factor of the fresh devices
Values for both illumination sides as well as the three composition.

	Glass side		ITO side	
	n_{id} ($k_B T/q$)	α (-)	n_{id} ($k_B T/q$)	α (-)
I	1.831 ± 0.027	0.964 ± 0.005	1.683 ± 0.025	0.964 ± 0.002
IBr	1.565 ± 0.023	0.963 ± 0.003	1.415 ± 0.022	0.964 ± 0.002
RbCl	1.795 ± 0.027	0.963 ± 0.004	1.607 ± 0.028	0.964 ± 0.002

Starting with the ideality factor, there is a similar trend between the compositions for both illumination sides. The iodide pure and RbCl-doped devices both have similar high values, while the values for the IBr devices are clearly lower. Based on the definition of the ideality factor together with the increased PCE over the entire intensity range it could thus be argued that the substitution of 2% bromide reduces the trap-assisted recombination in the bulk. Furthermore, it will be shown later using simulations that the defects in the bulk are more effective at lower light intensities. From the light intensity data it is clear that this is where the V_{OC} of the IBr devices is the highest compared to the other compositions. Based on the same analogy, the overall decrease of the PCE and lower V_{OC} at lower light intensities of the RbCl devices compared to the IBr devices thus suggests that the doping has led to more defects in the bulk, which is in agreement with the increase in the ideality factor.

Another interesting observation is that the curve of the iodide pure and RbCl devices can be divided into a high and low intensity part, each with its own distinct slope, while the IBr devices have a more or less uniform slope over the entire light intensity range. This is an indication that there is a competition between multiple recombination mechanisms where different mechanisms are dominant at different light intensities. At high illumination intensities the slope is the same for all compositions meaning that the difference in ideality factor is determined by the low light intensity part, which is where lower (higher) bulk recombination in the IBr (RbCl) devices translates to a lower (higher) ideality factor.

Comparing the glass to ITO side measurement there is an overall decrease in ideality factor, which on its own seems to suggest less bulk recombination. However, while the V_{OC} remains reasonably similar compared to glass side, the FF decreases significantly at high light intensity as is also clear from its ratio to glass side. This suggests instead that the interfacial recombination is more dominant from this illumination side[86]. This is in agreement with the research of Głowienka et al.[374] where they state that the perovskite/PCBM interface contains an increased amount of defects.

Interestingly, the exponential factor α is independent of the measurement side as well as the composition of the perovskite. This means that the modifications to the perovskite layer do not have an influence on the transport and extraction properties of the device. The value is close to unity meaning that the charge extraction is mostly independent of light intensity at J_{SC}. Thus, it can be concluded that the space-charge effects are minimal and the bimolecular recombination is weak.

5.2 Simulations of fresh devices

In this section, the optical and electrical simulations of the fresh devices are shown and compared to the measurements. Note, all simulations are optimized to the data of the IBr devices due to time constraints and because this composition can be compared directly to the other two variants.

5.2.1 Optical simulations

In the explanation of the outputs of the optical simulation in section 4.1.3, the absorptance and corresponding parasitic losses were already introduced for the IBr device. In addition, the IQE loss has been introduced in section 5.1.3 by comparing UV-vis and EQE measurements, but its origin has not been discussed yet. Here, the UV-vis measurement is directly compared to the optical simulation to see if they match. Furthermore, the IQE loss is elaborated on by comparing it to the parasitic absorption obtained from the optical simulation.

The absorptance and reflectance obtained from the measurements as well as the simulations are plotted in Figure 5.10a and b for illumination from glass and ITO side, respectively. Overall, the shape of the simulations is in good correspondence with the measurements according to the absolute values as well as the locations of the maxima and minima, which reflects that the thicknesses of the layers are in agreement with the real device. The oscillations in the curve appear to be larger for the simulation, most likely due to the assumption of perfectly flat surfaces and interfaces. The imperfections at the surfaces in the actual device will lead to random shifts in the optical electric field reducing the absolute intensities of the interference and thus the oscillations in the transmittance and reflectance.
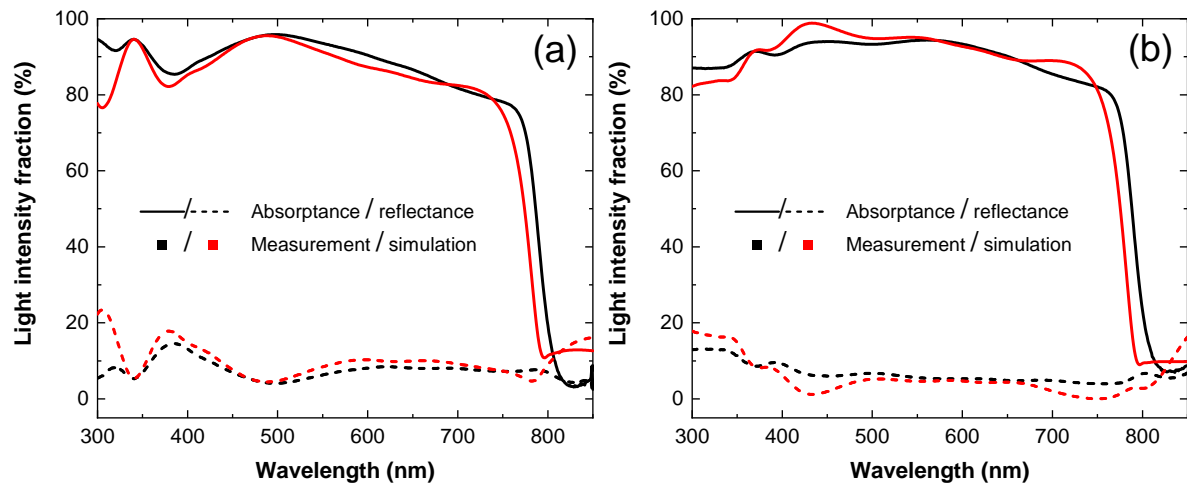
Figure 5.10: Simulation fitting of the absorptance and reflectance
(a) Illumination from glass side, (b) Illumination from ITO side.

One clear difference between the measurements and simulations is the absorption onset, which is determined by the bandgap of the perovskite. The onset of the simulations is shifted towards lower wavelength meaning that the bandgap is presumably larger. The complex refractive index values used for the perovskite are obtained from a $MAPbI_3$ layer by Manzoor et al.[168] with a reported bandgap of 1.57 eV. Comparing that to the bandgap of the IBr device of 1.569 eV, it is clear that the complex refractive index data does not reflect the predicted bandgap. Using the same Matlab script that is used to calculate the bandgap from the EQE data, the bandgap can be estimated from the absorptance data. The bandgap values obtained for the measurements are around 1.57 eV and thus in excellent agreement with the values

obtained for the EQE data. The values of the simulations are approximately 1.59 eV, which confirms that the bandgap of the MAPbI$_3$ layer is indeed larger than reported by the authors of the paper.

By comparing the IQE loss to the parasitic absorption it is possible to see to what extent it contributes to the loss. The IQE loss is defined as the difference between the absorptance and the EQE and the parasitic absorption is defined as the summation of all non-perovskite layer absorption. Both are shown in Figure 5.11a and b for the glass and ITO side illumination, respectively. From the reasonable overlap between both curves is evident that approximately all IQE loss originates from parasitic absorption, independent of the illumination side. However, for the glass side a large difference is seen between 300 to 350 nm. This is due to incorrect complex refractive index data of the glass substrate, underestimating its parasitic absorption in this high energy part of the spectrum. At around 800 nm the parasitic absorption shows a slight deviation, especially for the glass side, which is due to an overestimation of the back ITO.
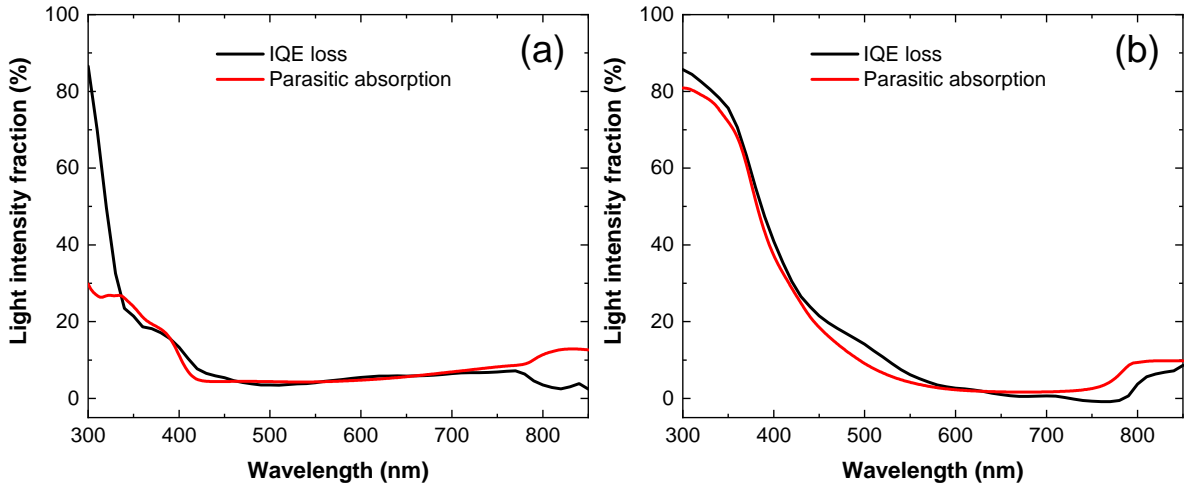
Figure 5.11: The IQE loss compared to the parasitic absorptance of the fresh devices. The IQE loss is calculated from the absorptance and EQE measurements. The parasitic absorption is obtained from the optical simulation. (a) Illumination from glass side, (b) Illumination from ITO side.

5.2.2   Electrical simulations

Before discussing the final optimized simulations and comparing them to the measurements, a few details have to be addressed first. Even though the simulations of the JV-curves will be discussed, the actual simulation parameters are optimized for the light intensity measurements. Due to the large amount of simulation parameters it is possible to have multiple different sets that all more or less fit the experimental JV-curve. However, the goal of the simulation is to find a single set of parameters that accurately describes the fresh devices, such that it can serve as a baseline for the simulation of the aged devices. It is thus important to have the essential parameters, such as the defect density and height of the energy levels, set as

accurately as possible in order to correctly interpret the changes that occur during aging. The optimization of certain parameters based on the JV-curve is troublesome, but due to their more specific dependence on light intensity it is easier to use those measurements. This makes it much more likely to find a single set of parameters that correctly represents the real device. It is for this reason that the simulation is optimized for the light intensity measurement and the JV-curves are merely used to check as conformation.

Another important detail that has to be mentioned is the masking of the devices during measurements. The mask ensures that the correct J_{SC} is measured, but leads to unintended errors in the V_{OC} and FF as described in section 2.6. By using a mask, the solar cell is not actually operating under its intended light intensity, but instead a lower intensity corresponding to factor X. The whole point of the simulation is to correctly estimate the parameters, but by masking the solar cell, it is effectively operating under different transport and recombination dynamics than expected. Hence, if this data would be directly used to optimize the simulation, the final parameters will be estimated wrong. To solve this, the light intensity data can be multiplied with the ratio X, which will shift the entire curve to lower light intensity corresponding to the correct dynamics. That is why none of the previous and subsequent light intensity graphs have a data point at exactly 1 sun intensity.

The most important figures of merit to use in the optimization of the simulation are the V_{OC} and FF. The J_{SC} is almost linear in light intensity and the absolute values are almost completely determined by the optical model. Furthermore, it has become clear from the vast amount of electrical simulations that parameter values within their expected range, which was extensively explained in chapter 4, lead to hardly any transport or extraction losses to the current density at short-circuit current. The PCE is calculated from these three figures of merit, hence if the simulation is correctly optimized for those values, it will also be correct for the PCE and thus it will not be shown.

The optimization of the electrical simulation took a considerable amount of time due to the large amount of parameters in SCAPS. The values for the optimized fresh device simulation are listed in the previous chapter of which most in Table 4.3. In total, there are around 50(!) parameters that require a value as input and of those, around 20 are actually optimized by systematically investigating their behavior on the figures of merit. A few of the critical parameters are discussed below to get a better understanding of their dependence on the light intensity. The sweeps are done for illumination from glass side and all other parameters are set according to the optimized fresh device simulation except for the doping, which is set to zero to represent the typical p-i-n device structure.

The effect of resistance

It is commonly known that the FF is affected by the series and shunt resistance of the solar cell and since the FF is one of the more complex figures of merit with regards to light intensity it is useful to investigate their behavior. The simulation results of the series resistance are plotted in Figure 5.12. As expected, the absence of current flowing in the device means that the V_{OC} is not affected by the series resistance and remains constant for all light intensities. The FF decreases for increased series resistance because the moving charge carriers are more affected by the higher internal resistance. The loss in FF decreases as the light intensity is lowered due to a reduction in the amount of charges flowing through the device. The most interesting result appears when the FF is plotted on a linear scale as is shown in the inset. The FF is clearly linear dependent on the light intensity down to the about 5% of one sun and its slope is in fact determined by the series resistance. This observation could potentially be used to estimate the series resistance by plotting the measurement data on a linear scale and using a simulation to fit the slope. Of course, the series resistance is not the only parameter that affects this slope, but in the investigation of the many critical parameters no other showed such a clear change of slope. Hence, this method could perhaps be useful for obtaining a ballpark estimation of the series resistance. Although this method does not work when the slope is non-linear, as is the case for the ITO side measurement, at least it is clear from the simulation sweep that a typical series resistance cannot create such behavior.
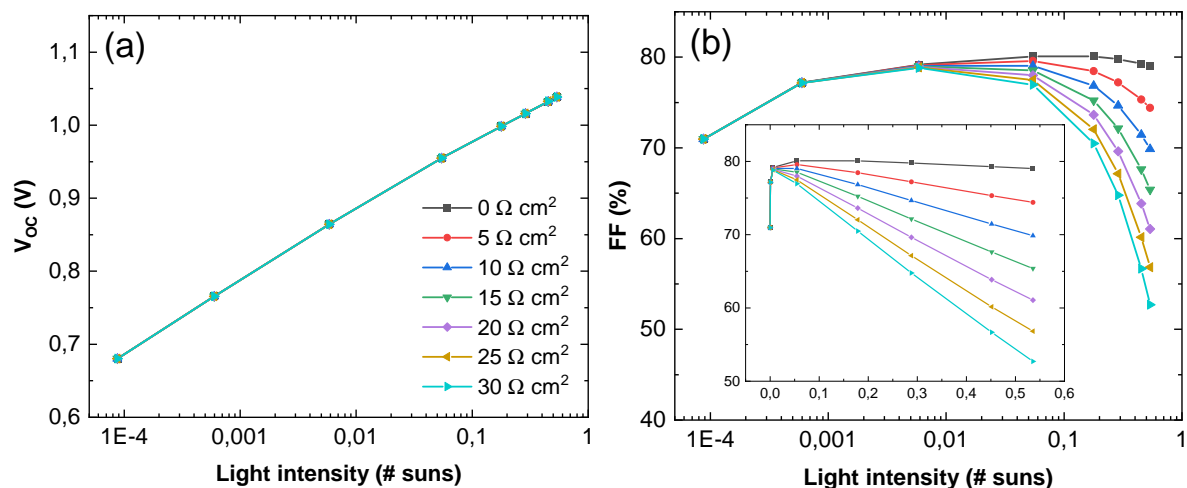
Figure 5.12: Simulation sweep of the series resistance
Illumination from glass side. The other parameters are set according to the optimized fresh device with doping set to zero. (a) V_{OC}, (b) FF. Inset: the FF plotted on a linear scale.

The investigation of the shunt resistance is shown in Figure 5.13 and the its effect on the figures of merit are most noticeable for low light intensities. Contrary to the series resistance, the shunt resistance can influence the V_{OC}. If the shunt resistance is too low the shunts can function as a recombination mechanism, which will decrease the V_{OC} at low illumination intensities. The FF also decreases for lower shunt resistance and the effect becomes stronger for lower intensities.
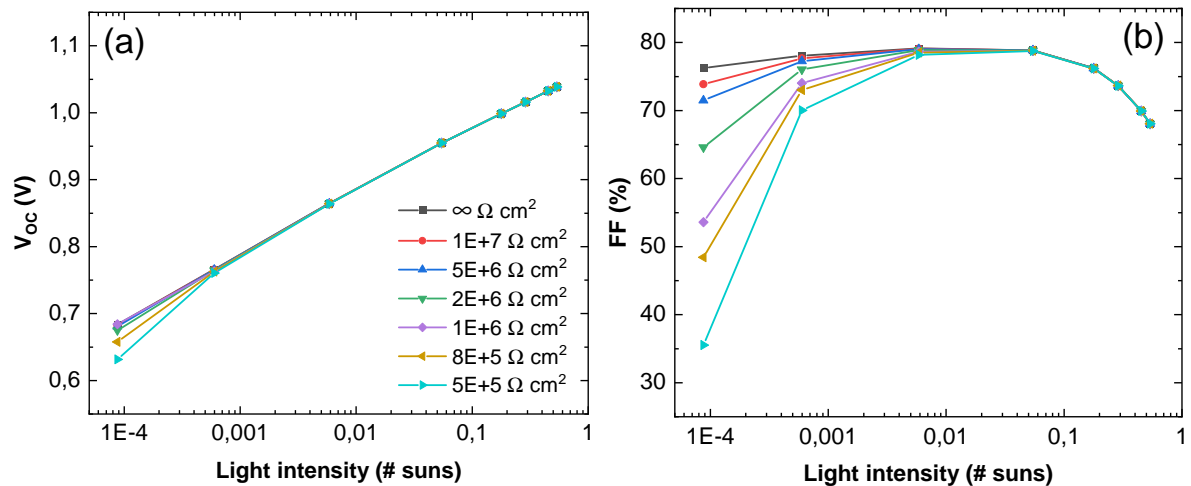
Figure 5.13: Simulation sweep of the shunt resistance
Illumination from glass side. The other parameters are set according to the optimized fresh device with doping set to zero. (a) V_{OC}, (b) FF.

The effect of defect density

Figure 5.14 shows the effect of the defect density in the bulk of the perovskite on the V_{OC} and FF. The increase of the defect density decreases the V_{OC} as more charge carriers are trapped, increasing the non-radiative recombination resulting in a decrease of the QFLS. Interestingly, the decrease is most prominent at lower light intensities. Due to the lower amount of generated charge carriers a higher percentage is used in trap filling, meaning that there is a reduced quantity of free carriers. This is also evident from the collection efficiency, which decreases more quickly at low light intensity. Increasing the defect density to high enough values will also start to affect the V_{OC} near 1 sun intensity. Another interesting parameter to investigate is the ideality factor, which clearly increases for increased amount of traps. This is expected according to the classical understanding as explained in section 2.4.1. The bulk defect density is independent of light intensity with regards to the FF, which means that an increase in the defect density results in a more or less uniform decrease of the values.
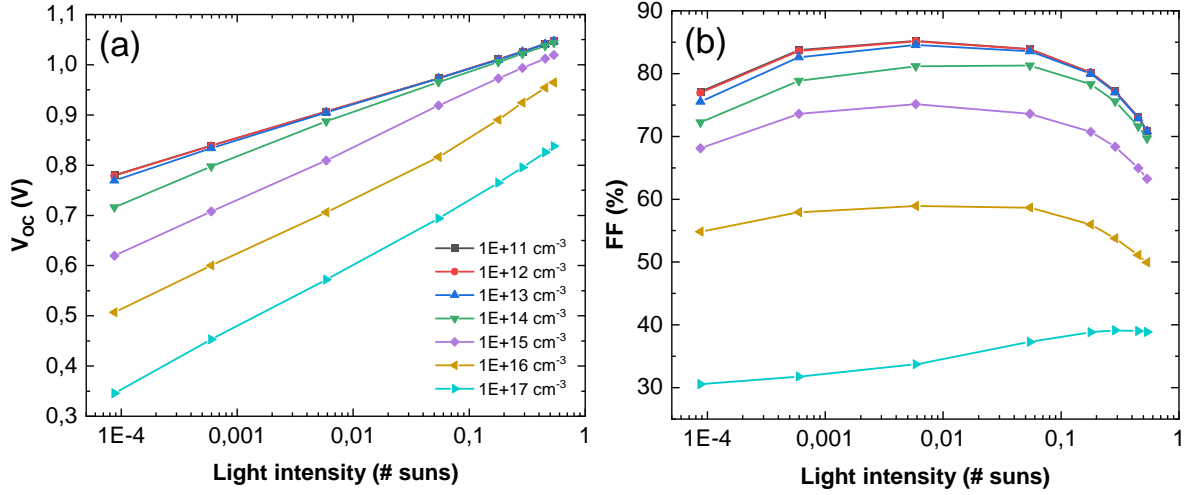
Figure 5.14: Simulation sweep of the perovskite bulk defect density
Illumination from glass side. The other parameters are set according to the optimized fresh device with doping set to zero. (a) V_{OC}, (b) FF.

The effect of different defect densities at the PTAA/perovskite interface is shown in Figure 5.15. Similar to the bulk defect density, a decrease in V_{OC} is observed for increasing defects density. However, in this case the decrease is larger at higher light intensities. Charge carrier accumulation at the interface becomes progressively more significant due to the increased generation, especially since the illumination is from glass side. This means that charges will have a higher chance of being trapped and subsequently recombine, leading to a faster decrease of the V_{OC}. Comparing again the slope of the curves it is clear that this time the ideality factor decreases for increased defect density.
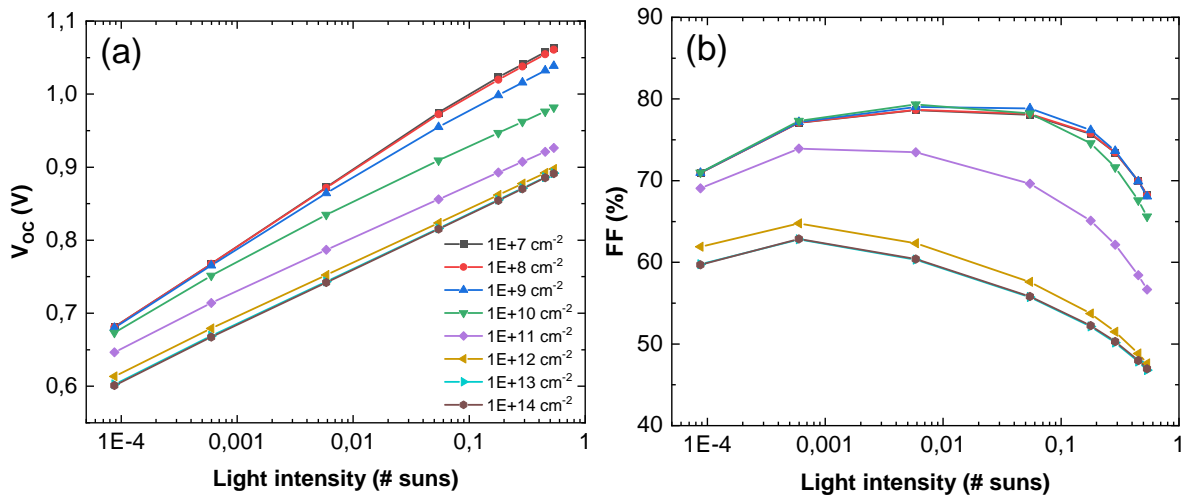
Figure 5.15: Simulation sweep of the PTAA/perovskite interface defect density
Illumination from glass side. The other parameters are set according to the optimized fresh device with doping set to zero. (a) V_{OC}, (b) FF.

This is in agreement with Caprioglio et al.[86] and confirms that more defects not necessary always increases the ideality factors as explained in section 2.4.1. It is thus always important to compare to ideality factor to the absolute values of the V_{OC} to determine the dominant recombination mechanism. The effect of the charge accumulation extends to the FF, where the value decreases more quickly at higher light intensities. Playing with the interface defect densities is thus one of the methods for shifting the maximum in the FF. For both the V_{OC} and FF a high enough defect density will decrease even the values at low light intensity. Lastly, contrary to the bulk defect density, there appears to be a deceleration of the decreasing figures of merit towards a certain saturation point, which is approximately reached between 10^{13} and 10^{14} cm^{-2}. This effect is independent of the light intensity as well as the applied voltage over the device. This could perhaps mean that the defects are filled via current injection from the contacts, but the exact reason for this remains unclear.

Figure 5.16 shows the figures of merit for different defect densities at the perovskite/P-CBM interface. Overall, the conclusions from the PTAA/perovskite interface hold here as well, but there are also differences that need explaining. Again there is a saturation point and it is reached for the same defect densities. Nevertheless, the total decrease in absolute terms between the lowest and highest defect density is significantly less compared to the PTAA/perovskite interface, i.e., the rate at which the figures of merit decrease is different depending on the interface. This suggests either that the defects at this interface are less 'effective' at trapping carriers or that there is less recombination, possibly due to longer recombination lifetimes or lack of opposite charge carriers.
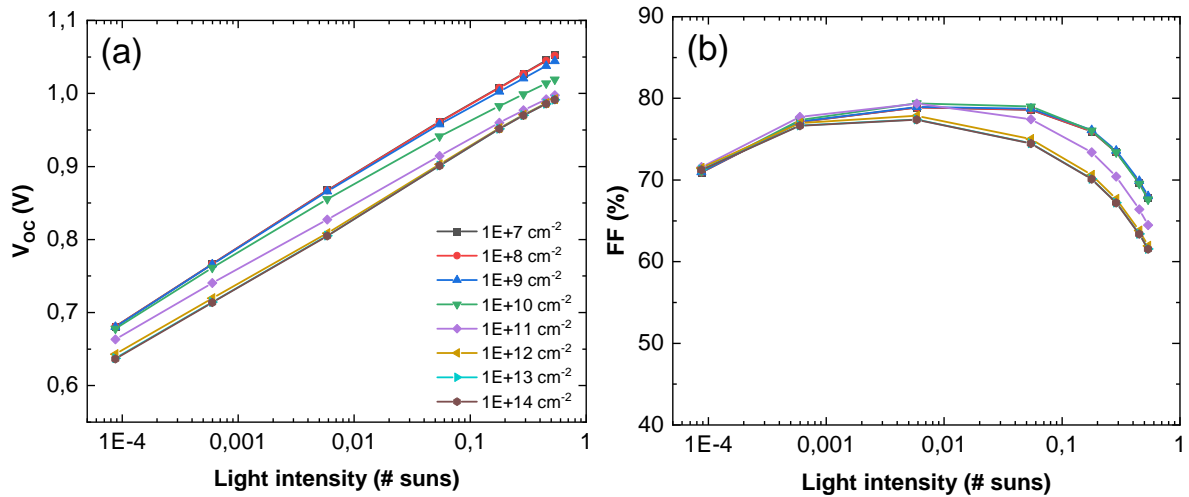
Figure 5.16: Simulation sweep of the perovskite/PCBM interface defect density
Illumination from glass side. The other parameters are set according to the optimized fresh device with doping set to zero. (a) V_{OC}, (b) FF.

A cause for less effective defects could be shallower energy levels in relation to the conduction and valence band of the transport layer. However, the energy level of the defects is set to the middle of the perovskite bandgap and the energy difference to the PTAA's VBM and

PCBM's CBM is similar meaning that the depth of the defects is similar at both interfaces. The results of the interface defect density sweep with regard to the J_{SC} is plotted in Figure B.3 in the appendix for both interfaces. The graphs show that the J_{SC} remains unchanged for increased defect density at the perovskite/PCBM interface, while the values clearly decrease uniformly for the PTAA/perovskite interface, meaning that more carriers recombine. Since the device is illuminated from glass side, both carrier types will be abundantly present at the PTAA/perovskite interface, but only a single carrier type will be present near the perovskite/PCBM interface depending on the voltage. Hence, recombination is much more likely to occur near the PTAA/perovskite interface than at the other side, which leads to the observed larger decrease of the figures of merit. To confirm this explanation the illumination is switched to the ITO side and the results are shown in Figure B.4 in the appendix. With the majority of the charge carriers generated near the perovskite/PCBM interface it is indeed the case that the behavior has switched, proving that the location of the generation is key to amount of (non-radiative) recombination and thus the losses to the figures of merit.

The effect of defect energy level

As mentioned before, the defects in the perovskite absorber can have both a shallow or deep energy level, hence it is interesting to investigate the effect of changes to their depth on the figures of merit. Figure 5.17 shows the results for a sweep of the energy level of the bulk perovskite defects from the VBM to the CBM, i.e., from a shallow depth to a deep level in the middle of the bandgap and back to shallow again.

Figure 5.17: Simulation sweep of the energy level of the bulk defects
Illumination from glass side. The other parameters are set according to the optimized fresh device with doping set to zero. (a) V_{OC}, (b) FF.

To get a better understanding of the different energy levels of the defects in relation to the important energy levels of the absorber and transport layers, a schematic representation of the band diagram is shown in Figure 5.18a. The different energy levels investigated in the

sweep are depicted as colored bars corresponding to the colors used in the legend of Figure 5.17a. In general, defects that have their energy level within a band (0.0 eV and 1.6 eV) are considered harmless since the charges can easily detrap back to the conduction/valence band[339]. A simulation without any bulk defects present in the perovskite gives identical figures of merit confirming that this is indeed true. Hence, it is no surprise that both the V_{OC} and FF have the highest values, independent of the light intensity.
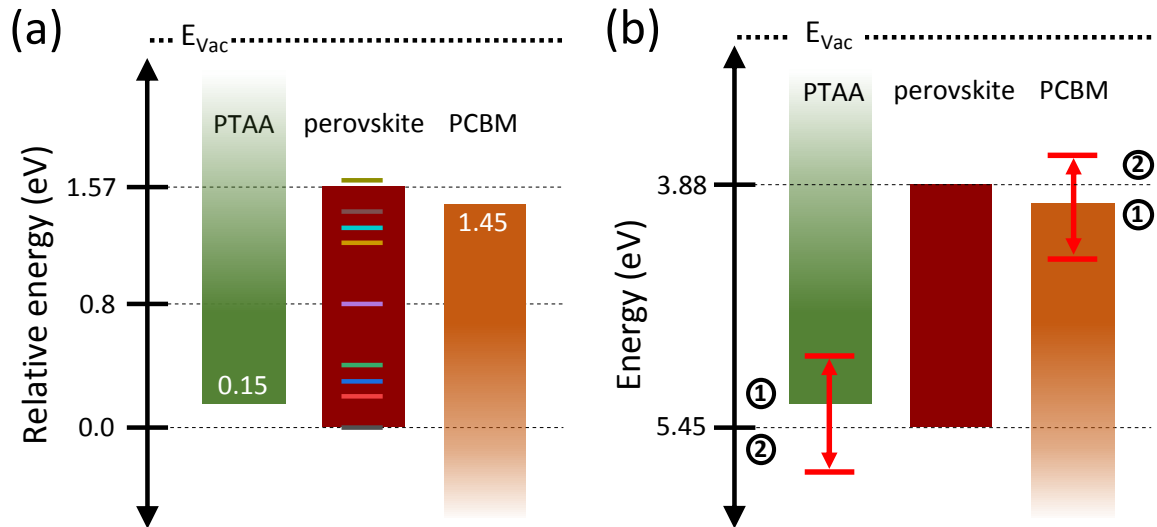
Figure 5.18: Band diagrams of the investigated energy levels
The other parameters are set according to the optimized fresh device with doping set to zero. (a) Bulk defect energy level sweep. (b) Transport layer energy level sweep. (1): injection barrier, (2): extraction barrier. The height of the minority carrier blocking is kept constant and the metal contact is simultaneously adjusted such that the metal/transport layer offset remains constant.

Moving the energy level just inside the bandgap (0.2 and 1.4 eV), there is only a minimal decrease in the V_{OC} and FF meaning that the defects hardly contribute to the non-radiative recombination. Looking at the band diagram in Figure 5.18a it can be seen that the energy level of the defects is just above (below) the IE (EA) of the PTAA (PCBM), hence it is energetically more favorable for the holes (electrons) to occupy the trap state. However, the energy difference between the defect and the transport layer is only twice the thermal energy at room temperature, which can statistically still be overcome and that explains why the reduction in the figures of merit is limited. The defects start to contribute more to the losses when the energy level is placed deeper (0.3 and 1.3 eV) within the bandgap. This trend continues for deeper energy levels as the defect states become more and more favorable for the charge carriers. The maximum losses for both the V_{OC} and FF ultimately occur when the energy level is placed in the middle of the bandgap ($\sim$0.8 eV). In other words, the energy level can be viewed as a representation of the effectiveness of the defect. Similar to the sweep of the bulk defect density, the V_{OC} decreases more at lower light intensities leading to a higher

ideality factor. Interestingly, the FF does not decrease uniformly, as is the case for the bulk defect density sweep, but the deepening of the defect energy level instead corresponds to a transition of the largest losses to lower light intensities. That is, shallow defects mostly introduce losses at high light intensity, while deep defects result in larger losses at low light intensity.

For completeness, the energy level of the interface defects is also investigated and shown in Figure B.5 in the appendix for both interfaces. Similar as for increased interface defect density, the ideality factor decreases when the defects are positioned deeper within the bandgap. Also, the perovskite/PCBM interface once again shows a reduced response to changes to the defects compared to the PTAA/perovskite interface as is the case for the defect density sweep, which is similarly explained based on the location of charge generation. At first sight there does appear to be a difference in the FF between both the defect density and energy level sweep. Interestingly, the FF increases for deeper defects, which is not what one would expect, given that the defects become more effective at capturing charge carriers. However, a closer investigation of the lower defect densities (10^7 to 10^9-10^{10}) in Figure 5.15 and 5.16 shows that the FF actually also slightly increases for this range. It is thus evident from all the above mentioned similarities that a change of the defect density has the same characteristic effect on the figures of merit as a change to the energy level of the defects. Intuitively, this also makes sense, since a change in the recombination dynamics can either be achieved by playing with the amount of defects or by changing the effectiveness of the defects itself.

The effect of transport layer energy level

The last type of sweep that is discussed is related to the process of injection and extraction of charge carriers. By adjusting the energy level of the transport layer it is possible to create an injection or extraction barrier as is schematically shown in Figure 5.18b. The IE of the PTAA layer is changed over a certain range such that both barrier types are evaluated and the effect on the figures of merit is shown in Figure 5.19. The V_{OC} significantly increases for increased IE up to 5.5 eV, which is when optimal alignment to the VBM of the perovskite (5.45 eV) is reached. All values below this point have a majority carrier band offset ΔE_{maj} that causes a reduction of the quasi-Fermi level in the PTAA relative to the perovskite, which leads to a limitation on the overall external V_{OC}, even though the QFLS in the perovskite bulk itself is still higher[181]. For values of 5.5 eV and higher the V_{OC} remains approximately constant, since the QFLS in the perovskite bulk will now be the limiting factor and is not changed.

An interesting observation is the sudden increase in ideality factor when increasing the IE from 5.2 to 5.3 eV as a result of improved V_{OC} at higher light intensities. At first side, it is peculiar that there is such a difference since both energy levels still result in a injection barrier. Caprioglio et al. have shown that the dominant recombination channel will set the upper limit for the V_{OC} and thus defines the ideality factor[86,403]. From the simulation it is noted that at V_{OC} over 70% of the charge carriers recombine at the PTAA/perovskite interface when the IE is equal to 5.2 eV, while this value reduces to 43% for an IE of 5.3

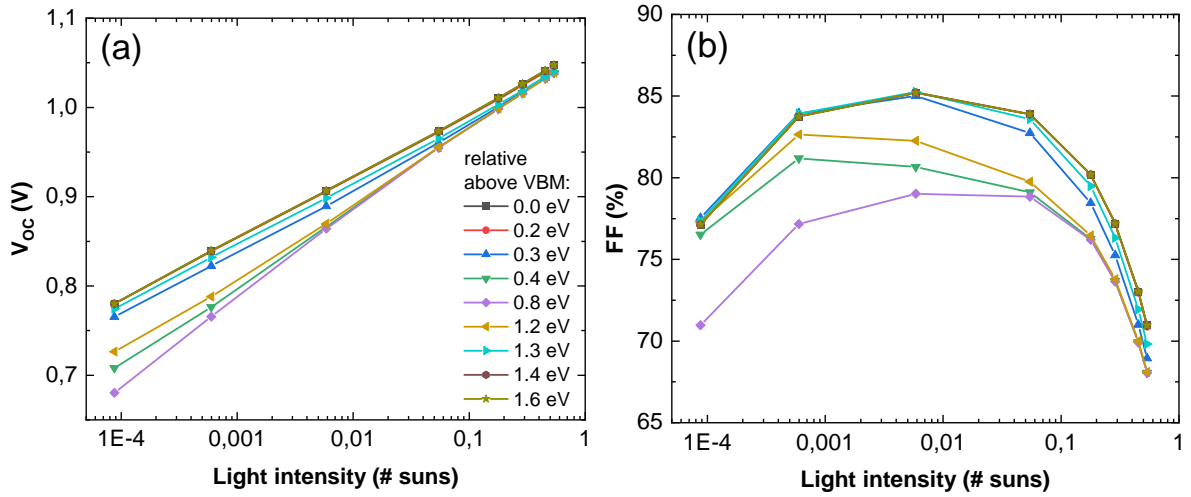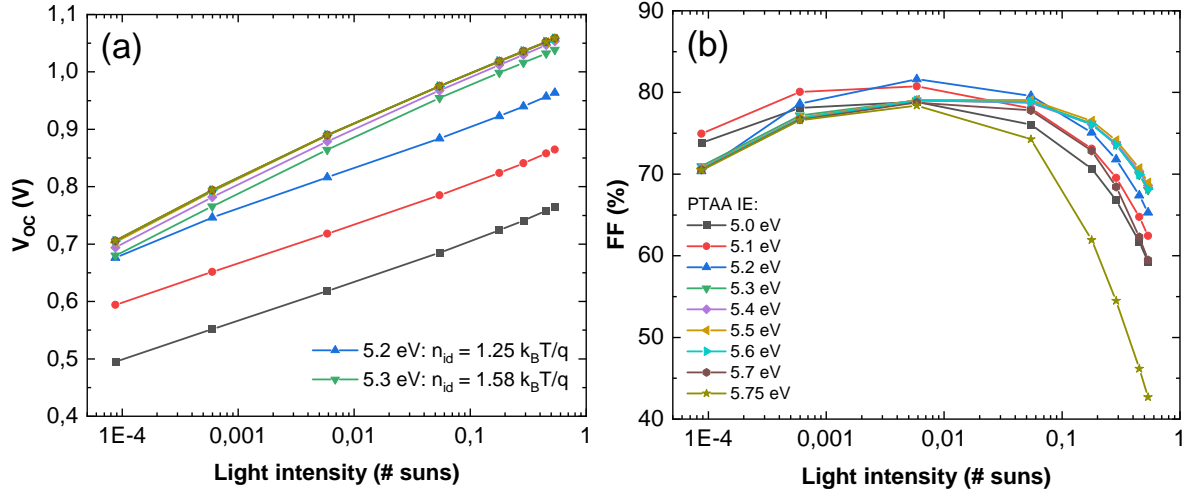**Figure 5.19: Simulation sweep of the IE of the PTAA**
Illumination from glass side. Most other parameters are set according to the optimized fresh device with doping set to zero. The EA of the PTAA is kept constant to prevent changes to the electron blocking. The front contact is changed as well to keep a constant metal/PTAA injection barrier (a) V_{OC}, (b) FF.

eV. Placing the energy level at equal height of the VBM of the perovskite almost completely removes the interface recombination as expected. Clearly, the PTAA/perovskite interface is the dominant recombination location when there is a high enough energy offset. It is thus important to investigate the recombination dynamics at this interface by analyzing the charge carrier density and QFLS in order to find the origin of the difference in ideality factor.

A closer look at the simulated band diagram in Figure 5.20a reveals that an energy level of 5.2 eV leads to band bending of the majority (hole) quasi-Fermi level near the PTAA/perovskite interface, while 5.3 eV results in the desirable perfectly flat quasi-Fermi levels. The combination of dominant interface recombination and majority carrier band offset will lead to a depletion of the majority carriers at the perovskite side of the interface as is evident from Figure 5.20b. The hole carrier density at the PTAA side remains high due to carrier injection from the metal contacts. The injection barrier created by the energy offset prevents the holes at the PTAA side from recovering the induced deficit at the perovskite side. The result is a large gradient in hole carrier density, which will cause the observed band bending of the corresponding quasi-Fermi level[86].

An additional effect is that the carrier density of the holes will be significantly less dependent on light intensity, while the minority carriers (electrons) will still increase linearly with intensity as can be seen in Figure 5.20b, since they are supplied by the bulk. The result is a charge carrier imbalance that grows with increased illumination intensity. It is well known that the QFLS will increase for higher light intensity and is generally symmetric for both quasi-Fermi levels relative to the intrinsic dark Fermi level. In this case, however, the quasi-Fermi levels will split asymmetrically instead because of the carrier imbalance as shown
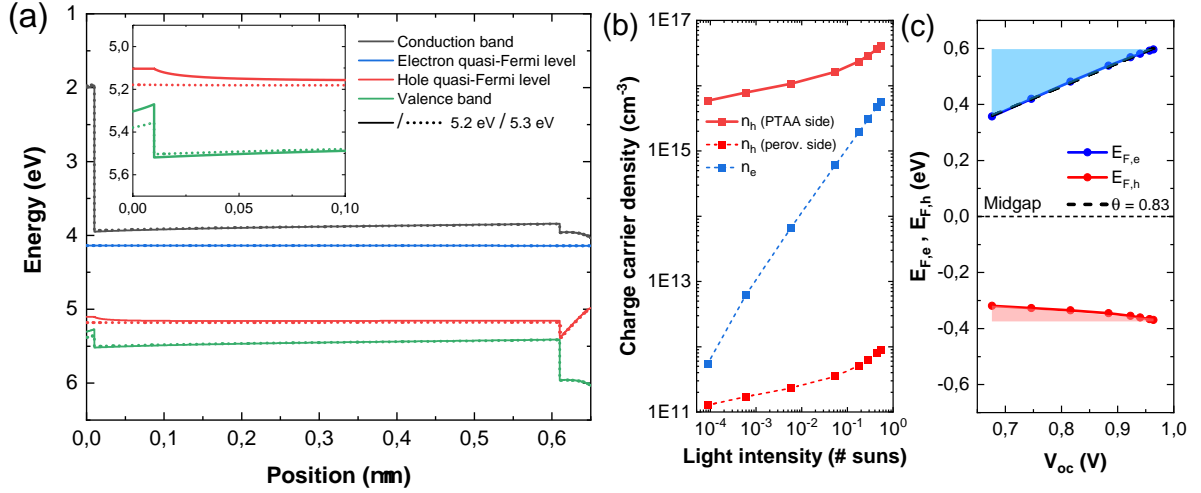
Figure 5.20: Effect of a majority carrier band offset on the PTAA/perovskite interface
(a) The band diagram at V_{OC} for an IE of 5.2 and 5.3 eV. A significant majority carrier band offset will result in band bending at that specific interface. Inset: close-up of the PTAA/perovskite interface. (b) Charge carrier density at the interface as function of light intensity for the 5.2 eV energy level. (c) The electron and hole quasi-Fermi levels as function of V_{OC} for energy level of 5.2 eV. The dominant contribution of the electrons to the QFLS is fitted and translates to $n_{\mathrm{id}} = 1/\theta = 1.20\ \mathrm{k_B T/q}$, matching the ideality factor obtained from the Suns-V_{OC} method.

in Figure 5.20c. The consequence of this effect is that the minority carrier density almost completely determines the total amount of QFLS.

Furthermore, this means that the SRH recombination rate R_{SRH}, which is explained in section 2.2, can be simplified by assuming equal capture cross sections and negligible detrapping for both carrier types and is thus predominantly determined by the minority carrier density n_{min}. By using $n = N_{\mathrm{c}} \exp\left(\frac{E_{\mathrm{F,n}} - E_{\mathrm{F}}^0}{k_{\mathrm{B}} T}\right)$, the recombination rate can be linked to the QFLS and hence to the ideality factor as shown in equation 5.2 below and is discussed in more detail in the following reference[86].

$$R_{\mathrm{SRH}}(I) \propto n_{\mathrm{min}}(I) \propto \exp\left(\frac{E_{\mathrm{F,min}} - E_{\mathrm{F}}^0}{k_{\mathrm{B}} T}\right) \propto \exp\left(\frac{\Delta E_{\mathrm{F,min}}(I)}{k_{\mathrm{B}} T}\right) \propto \exp\left(\frac{\theta \times \mathrm{QFLS}(I)}{k_{\mathrm{B}} T}\right) \propto \exp\left(\frac{\mathrm{QFLS}(I)}{n_{\mathrm{id}} k_{\mathrm{B}} T}\right) \quad (5.2)$$

Here, the $E_{\mathrm{F,min}}$ is the quasi-Fermi level of the minority carriers and E_{F}^0 the intrinsic Fermi level in the dark and their difference is equal to the QFLS of the minority carriers $\Delta E_{\mathrm{F,min}}$. This can also be expressed as $\theta \times \mathrm{QFLS}$ where θ is the share of the minority carriers contribution to the total QFLS. Based on the Shockley diode equation the factor can be rewritten[87,403] such that the relation $n_{\mathrm{id}} = 1/\theta$ is found. θ can be determined from the slope of the intensity-dependent minority carrier QFLS as function of the V_{OC}. In the case of symmetric QFLS θ is equal to 0.5 and thus the ideality factor equals two, which corresponds to dominant SRH recombination typically occurring in the bulk where the charge carrier densities are approximately balanced. For the 5.2 eV energy level a larger slope of 0.83 is found because of the dominant contribution of the minority carriers to the total QFLS, resulting in an ideality factor of 1.20 $\mathrm{k_B T/q}$. This value is very close to the ideality factor obtained from the Suns-

V_{OC} method, which confirms that the V_{OC} of the solar cell is indeed ultimately limited by this interface. It is important to note that this method only works at the location where the recombination rate is most dominant. The determination of the ideality factor using θ does not work for the 5.3 eV simulation, which means that this interface is not the single dominant recombination channel for such an energy offset. Stolterfoht et al.[181] found that a ΔE_{maj} of at least 0.2 eV is necessary to create a mismatch between the bulk QFLS and external V_{OC}, which is in excellent agreement with the observation here.

The dependence of the FF on the IE of the PTAA is shown in Figure 5.19b. Similar to the V_{OC}, the FF increases for values up to 5.5 eV due to the decreasing injection barrier. The highest value is reached when the IE equals the VBM of the perovskite (5.45 eV) and the charge carriers can be extracted without any major losses. If the energy level is increased further an extraction barrier is created, which blocks the charge carriers at the interface leading to a significant increase in recombination that tremendously decreases the FF. All this is true for the higher light intensities, however, the values at lower intensity behave slightly different. Interestingly, the FF shows a few higher values for large injection barriers of which the origin remains unclear, but overall the values are less affected and only marginally decrease for IEs after 5.3 eV. This behavior regarding light intensity is seen before for the defect density sweeps and shows that interface effects are most noticeable at higher light intensities.

To complete the picture, also an energy level sweep of the EA of the PCBM is carried out and the results are shown in Figure B.6 in the appendix. Overall, the figures of merit exhibit the same behavior as for the PTAA and the sudden change in ideality factor once more appears between the 4.0 and 4.1 eV energy levels. The same analogy based on the band bending and QFLS can be used to explain the phenomenon as is done for the other interface. One noteworthy difference is the slow increase of the FF at low light intensities, which is opposite to the behavior of the PTAA layer. The most likely explanation is that the ratio of electron and hole carrier density is different owing to the illumination side, leading to different recombination dynamics at each interface. The carrier densities can be influenced by switching to ITO side illumination and those results are shown in Figure B.7 in the appendix. Indeed, the behavior of the FF at low light intensity appears to change and is more similar to what is observed for the PTAA layer illuminated from glass side. However, the exact mechanism remains unknown, partly because of the small influence of interfaces at low light intensity, but also due to other possible changes that simultaneously affect the values.

In reality, there is to some degree always a certain energy mismatch between one or both transport layers and the perovskite. This investigation on the energy levels shows the importance of selecting suitable materials to have correct alignment to the energy bands of the perovskite absorber and that failure in doing so will lead to significant performance losses.

The final parameter set

Having evaluated the most important parameters (and many more that are not discussed here), a final optimized parameter set is found that best agrees with the experimental measurements.

The fitting of the experimental data using the optimized simulation is presented in Figure 5.21 below for illumination from glass side and shows an excellent agreement for both figures of merit.
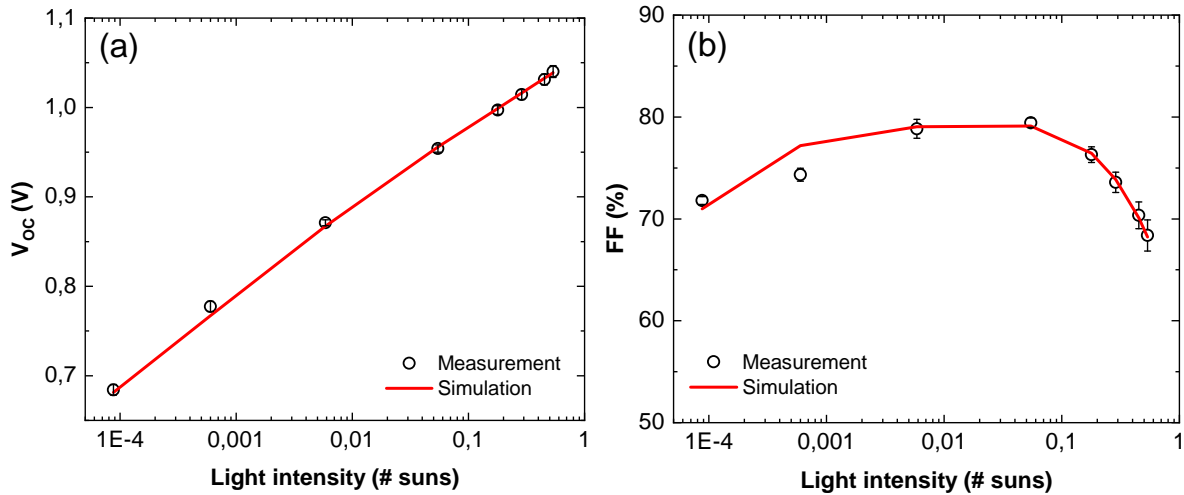
Figure 5.21: Light intensity simulations from glass side of the IBr device
The open circles indicate the experimental measurement data and the solid red line the optimized simulation. (a) V_{OC}, (b) FF.

The ultimate goal is to find a single set of parameters that would describe the measurement results from both illumination sides. Figure 5.22 shows the results for illumination from ITO side and it is clear that the optimized parameter set does not fully simulate both curves correctly.
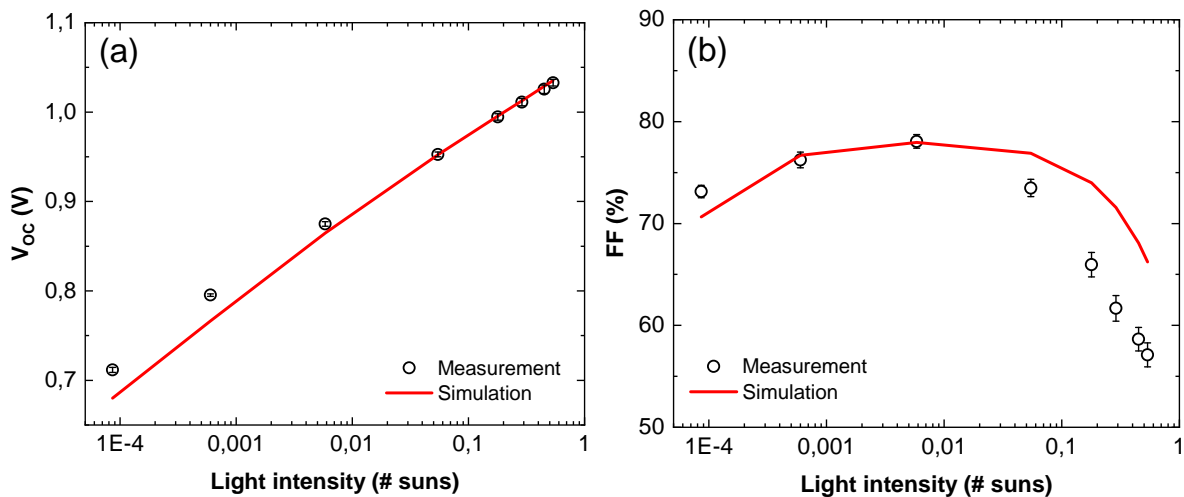
Figure 5.22: Light intensity simulations from ITO side of the IBr device
The open circles indicate the experimental measurement data and the solid red line the optimized simulation. (a) V_{OC}, (b) FF.

Many different adaptations have been tried to improve the ITO side simulation, but that would almost always lead to a disagreement between simulation and measurement of the glass side. In the end there are two main regions where the simulation differs from the measurement. One of which is an underestimation of the V_{OC} at low light intensity, however, this is mainly because the measurement values themselves are quite peculiar. Comparing both illumination sides shows that the ITO side actually has higher values at low light intensity, while the simulation ones are marginally lower as is generally observed for semi-transparent perovskite solar cells[379, 404], although no papers could be found that investigated the bifaciality at light intensities other than 1 sun. Of all the simulations done, not once was such a large difference realized. It could be possible that there is a specific set of parameter values that is able to create this difference, but it was not found during the optimization as well as the origin of it.

The other discrepancy is in the values of the FF at high light intensity, where the simulation significantly overestimates the measurement. By plotting the data on a linear scale it has been shown that the FF has completely different characteristics for both illumination sides, which should be correctly incorporated in the simulation. The IBr data of the FF is plotted again together with the optimized simulation in Figure B.8 in the appendix and it clearly shows that the non-linear behavior is not simulated correctly. Throughout the investigation of the different parameters it became clear that it *is* possible to simulate such non-linear behavior under certain conditions, for example, by assuming a very high donor doping, extremely low mobility or high interface defect density. However, this usually comes at a cost of the accuracy of the glass side simulation. The most likely candidate is a high interface defect density at the perovskite/PCBM interface, since the simulation from glass side can still be optimized quite decently and it is this side of the solar cell that shows the non-linear behavior. Furthermore, Głowienka et al.[374] also found a significant difference in FF between both illumination sides for the same device configuration and attributed the observation to a large interface defect density at that exact interface.

To complete the trilogy of the base figures of merit, the simulation of the J_{SC} is shown in Figure B.9 in the appendix. Again, it has to be noted that the simulation accounts for masking by adjusting the light intensity to correctly simulate the V_{OC} and FF. This does however mean that the J_{SC} outputted by the simulation is incomparable to the original measurements. This is solved by converting the measurements to the expected values at that specific intensity, which is done by multiplying the values with the factor X. The simulation from glass side almost perfectly overlaps with the measurement data. For the ITO side there is a slight general underestimation of the J_{SC}, which is more pronounced at higher light intensities. The unusual high J_{SC} from ITO side has been extensively discussed previously and it appears that neither the optical nor electrical simulation cannot predict the higher values, enforcing the believe that it is related to an error in the measurement as a result of the spectral mismatch between halogen lamp and solar spectrum.

As said before, the simulation is optimized for the light intensity measurements, but the J-V curves can still be used to confirm if the simulation is correct. The averaged J-V curves of the IBr devices at 1 sun intensity are plotted and fitted with the simulation in Figure 5.23a

and b for illumination from glass and ITO side, respectively. Once more, the measurements are compensated for masking by multiplying the data with the ratio X. However, caution is required when doing so for the entire J-V curve as seen in Figure B.10. The approximately linear relation of the J_{SC} with the solar intensity makes it possible to scale these values, but for higher voltages the curve will deviate from the actual measurement at lower light intensity. Hence, this method should not be used for illumination intensities far below one sun. The glass side is in overall good agreement with the simulation, which strengthens the believe that the parameters are close to the actual values of the device. The inset shows the dark J-V curve and the first thing that stands out is the offset of the minimum of the measurement data, which is due to ion accumulation at the interface resulting in a modified internal electric field[49,405]. The size of the offset depends on the scan rate as well as the scan direction. The fast scan used here does not allow the ions to reach equilibrium, leading to an internal voltage and hence the offset. The simulation does not account for ion migration and thus has its minimum at 0 V.
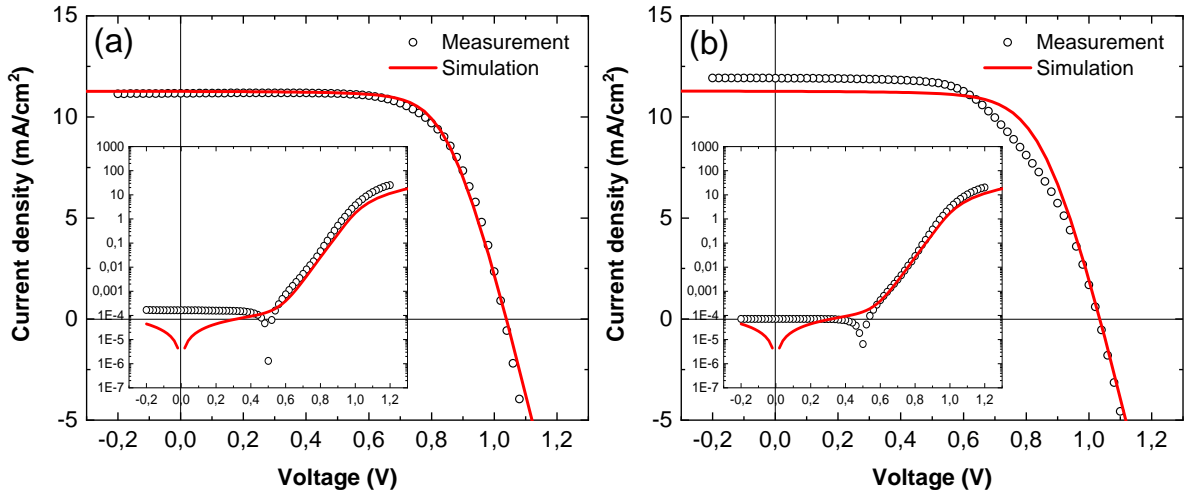
Figure 5.23: Simulated J-V curves of the IBr device
The measurement data is from the reverse direction sweep. (a) Illumination from glass side, (b) Illumination from ITO side. Inset: the averaged dark measurements fitted with the simulation.

Even though the region after the minimum is slightly off it still follows the general shape quite well, suggesting that the fundamental underlying mechanisms are captured by the model. A similar case is true for the dark J-V curve of the ITO side. The light J-V curve, however, does not have a decent overall fit, especially near the MPP and J_{SC}. The J_{SC} is once again underestimated due to the believed spectral mismatch in the illumination source as mentioned before. Assuming that the J_{SC} would be in line with the simulation, there still is an overestimation of the FF at the MPP. Interestingly, the kink that was also mentioned in section 5.1.1 is clearly visible in the measurement as well as the fact the simulation does not have this feature incorporated in its curve. An attempt is made to simulate this effect, while simultaneously maintaining the correctly fitted glass side, of which the best optimization is shown

in Figure B.11 in the appendix. Fascinatingly, it appears that the kink can be successfully simulated by only slightly changing the parameters. However, the changes have to be made to the PTAA/perovskite interface, which is rather counterintuitive. Similar changes to the other interface did not result in an observable kink and the range of flexibility for the parameters itself is very small. Furthermore, extending this parameter set to the light intensity simulations shows a large discrepancy between the measurements and simulations. In the end, it is chosen to not include these changes in the final optimized parameter set for the fresh devices.

5.3 Measurements of aged devices

In this section the results of the aging are presented and discussed. The exact details of the aging process itself is discussed in section 3.4. All device types are investigated and have both a series of samples light soaked from the HTL side, which is referred to as "superstrate-aged", as well as a series light soaked from the ETL side, which is referred to as "substrate-aged". Each series is measured from both illumination sides, named the glass and ITO side as consistently referred to throughout the thesis. The reason for naming each side of the device twice is to have a clear distinction when talking about the aging itself or the measurement.

For the representation of the measurements there are actually two options that each give a different view on the data. The different compositions can either be directly compared to one another for each step in the aging process, similar to the representation of the data in section 5.1, which allows for a clear view of the differences (and similarities) between the compositions. Another way is to plot each composition individually with all of its aging data. The advantage of this representation is the direct link of the figures of merit to the development of the device throughout the aging process as well as a clear indication of the consequence of each particular aging step. The latter possibility is used first for the iodide pure to study the effect of the different aging steps in more detail. After that, the former representation method is used to discuss the effects of bromide substitution and RbCl doping.

The axis in the light intensity plots for both the V_{OC} and FF are fixed between all aging related graphs in this section to allow for direct comparison between graphs and better visualize the absolute differences between the compositions.

Having mentioned the administrative matters it is finally time to discuss the actual measurements. The aging results for the iodide pure devices when measured from glass side are shown in Figure 5.24. Light soaking the device for 1250 hours leads to a slight decrease of both the V_{OC} and FF compared to the fresh devices and is more or less independent of the measured light intensity. The orientation of the device during light soaking appears to have a small effect, although there is an overlap of the uncertainties. The reason for the higher FF for the substrate-aged devices is mainly because the J_{SC} is actually lower compared to the superstrate-aged devices, while the V_{OC} and MPP are similar as can be seen in Figure 5.25a, effectively improving the squareness of the J-V curve. The stability of the cells is quite decent for both aging orientations, only reducing to around 80% of the original PCE after the entire

Figure 5.24: Light intensity measurements from glass side of the aged I devices
The colors indicate the period in time during the aging process. Fresh means before aging, light soaking means after 1250 hours of aging and storage means after 2 months stored. The solid (dashed) line refers to the superstrate-aged (substrate-aged) devices. (a) V_{OC}, (b) FF.

light soaking duration. Troughton et al. investigated the exact same perovskite composition, albeit in the n-i-p configuration with a different hole transport material, and found a similar reduction in efficiency[99]. Although not good enough for commercial use, it is a positive sign that the cells are still alive, and more importantly, produce a reasonable amount of power.
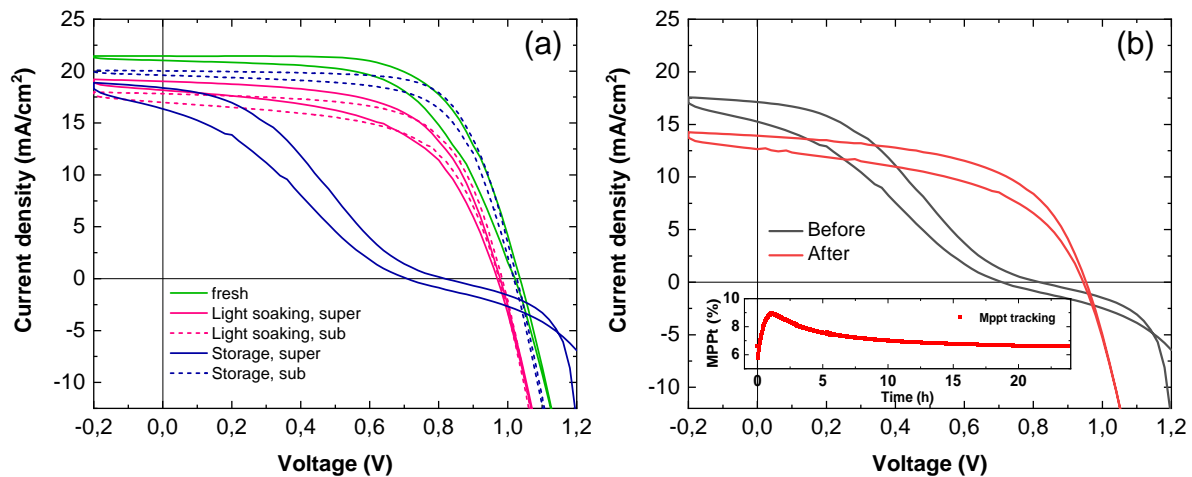
Figure 5.25: The effect of aging on the J-V curves for glass side measurements
Both the forward (inner) and reverse (outer) scan J-V curves are plotted. (a) The J-V curves of the I pure devices measured at each aging step showing the effect of the aging side. (b) The I pure superstrate-aged device before and after 24 hours of light soaking showing that the S-shape is reversible. Inset: MPP tracking during the 24 hours.

After the 1250 hours of light soaking the devices are left in a dark inert environment for two months. Surprisingly, this storage period leads to drastic changes to the figures of merit as well as a clear distinction between the two aging sides. The superstrate-aged devices show a tremendous decrease in both V_{OC} and FF. Strangely, there is an initial increase in the V_{OC} for decreasing light intensity leading to bending of the curve, which means that there is in fact a local negative ideality factor, as seen in Figure 5.24a. The established theory on the ideality factor is limited to values within the range of $n_{id} = 1$ to $n_{id} = 2$ and no perovskite papers could be found that mention or discuss negative values. Even for other types of solar cells it appears the concept is absent in literature. However, there is a paper by Gunawan et al.[406] which also observes the bending effect at the higher light intensity regime in kesterite solar cells. Two possible explanations are given related to heating and a non-ohmic contact. Heating can lead to a decrease in V_{OC} and more heat is generated at higher light intensities. However, the amount of heat generated at 1 sun intensity for the duration of the measurement has a negligible effect. Even if all light is converted into heat it would be highly unlikely that the V_{OC} decreases by such a significant amount. The other explanation involves a non-ohmic contact, which could arise at one of the interfaces. A diode model is suggested with a primary diode representing the main photovoltaic junction and a secondary parasitic contact junction in the opposing direction. If the parasitic junction has the right conditions a sizeable photovoltage can develop that generates an opposing voltage to the main diode, subsequently reducing the external V_{OC}. Considering the aging orientation it would be most probable that either the ITO/PTAA or PTAA/perovskite interface is responsible for the opposing voltage, if the explanation indeed also applies to the perovskite devices. The exact mechanism that would have to occur during storage in the dark to create such a non-ohmic contact at one of those interfaces remains unknown.

The devices shown in the paper that have the characteristic bending additionally suffer from a low FF, as is also the case here, which the authors ascribe to a high series resistance. However, a quick comparison between the J-V curves of the paper and the perovskite devices shows that they have a vastly different shape. The origin of the low FF of the superstrate-aged devices is a severe S-shape as is evident from Figure 5.25a. S-shaped J-V curves are a well-known occurrence in solar cells and especially often discussed in organic solar cells[179, 407–411]. By far the most common explanation is the existence of an energetic barrier between the absorber and one of the transport layers or at the contacts, that limits the charge carrier transport and increases non-radiative recombination[407, 412–414]. The precise origin and location of the energetic barrier requires additional measurements, such as capacitance-voltage- and impedance measurements[415] or transient photocurrent[411], in combination with simulations. The J-V curves also show that the hysteresis has become more severe after superstrate aging.

As explained in section 2.5, the effects of aging on perovskite solar cells can either be reversible or irreversible. Besides reducing the figures of merit, light soaking can also help to improve a device, hence a superstrate-aged sample is illuminated for 24 hours while keeping the device at MPP to investigate whether the sample can recover. Figure 5.25b shows the J-V curves before and after the treatment and confirms that the S-shape can be removed. Hence

the effect appears to be reversible, although there are some remaining losses for all figures of merit, especially the J_{SC}, compared to the device just after 1250 hours light soaking. The MPP is tracked during the 24 hours as seen in the inset and has an initial increase to a certain maximum after which the curve slowly decreases towards a stabilized value, a behavior that is typically observed for inverted perovskite solar cells[416].

While the superstrate-aged devices experience a severely negative effect as a result of the storage, the substrate-aged devices exhibit in fact the opposite effect by showing significant performance improvements as seen in Figure 5.24. Both figures of merit increase over the entire light intensity range and in case of the FF even improve beyond the values of the fresh devices. Also, the amount of hysteresis has decreased. From Figure 5.25a it is clear that while the V_{OC} and FF can recover, the J_{SC} does have a partial irreversible loss.

The striking contrast between both aging sides after a long storage period raises questions on what the possible mechanisms could be that cause such a difference. Also, it is not necessarily straightforward to conclude that the differences are only established *after* the light soaking period. In other words, since it is clear that illuminating the device for several hours can (partly) recover the performance, it could be the case that the deterioration of the superstrate-aged devices has already started during the light soaking period, but is essentially masked by temporary recovery. A control sample which is not light soaked at all could give more information on the baseline degradation in the dark and thus better clarify the exact changes occurring because of light soaking. Devices were kept aside for this reason, but were unfortunately not measured again. However, one sample of each composition was measured just before they were light soaked, which is around one and a half months after the first measurement, and the results are compared to the fresh devices in Figure B.12 for both the measurement sides. It shows that the performance of the devices is not significantly altered solely by storage in dark. Hence, it is clear is that the difference between the two orientations has to be triggered by the light soaking, since this is the only time during the aging experiment that a distinction between the orientations is made.

The devices are also measured from ITO side to verify whether the measurement side potentially influences the results, which are shown in Figure 5.26. Contrary to the glass side measurements, there already appears to be a distinctly different behavior between the aging sides for the devices just after 1250 hours light soaking. The superstrate-aged devices have degraded drastically, especially at higher light intensities, as is evident from the slight bending of the V_{OC} curve and large drop in FF. The V_{OC} of the substrate-aged devices is closer to that of the fresh devices and the FF even surpasses those values. The reason for this difference compared to the glass side has actually nothing to do with the measurement orientation itself, but rather the timing. After the 1250 hours all devices were measured first from glass side, but due to time constraints the ITO side was measured only after a few days during which they were stored in the glove-box. Thus, the devices already underwent some time in the dark, which explains why the results have similar characteristics as those after a few months of storage. It also confirms that the process of degradation and recovery of the superstrate- and substrate-aged devices, respectively, happens over a time period of days rather than minutes
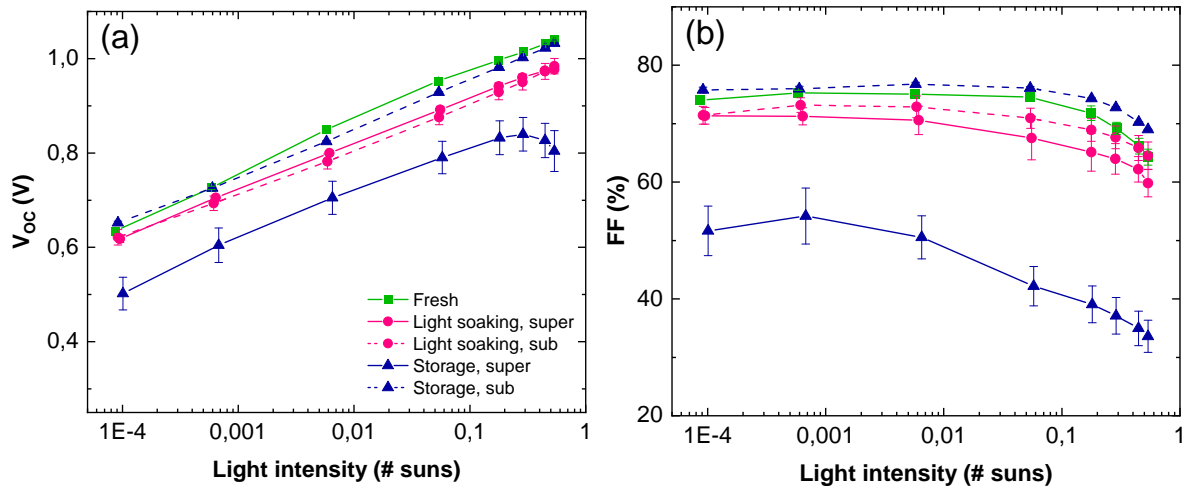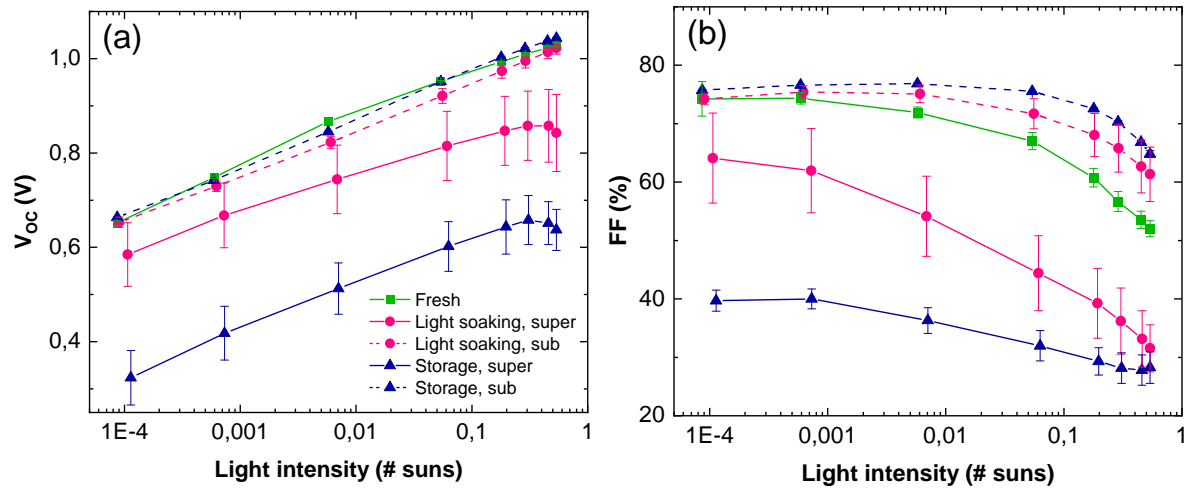
Figure 5.26: Light intensity measurements from ITO side of the aged I devices
The color indicate the period in time during the aging process. Fresh means before aging, light soaking means after 1250 hours of aging and storage means after 3 months stored. The solid (dashed) line refers to the superstrate-aged (substrate-aged) devices. (a) V_{OC}, (b) FF.

and that the figures of merit continue to change over time. After three months of storage the figures of merit have developed further according to their aging side. Furthermore, it appears that the changes are initially more effective at higher light intensities and over time also start to affect the performance at low light intensity.

The J-V curves of the ITO side measurement in Figure 5.27 confirm the development of the devices over time and also show that the measurement side has no apparent effect on the results, since the curves have a clear resemblance to the glass side. Another reason for showing
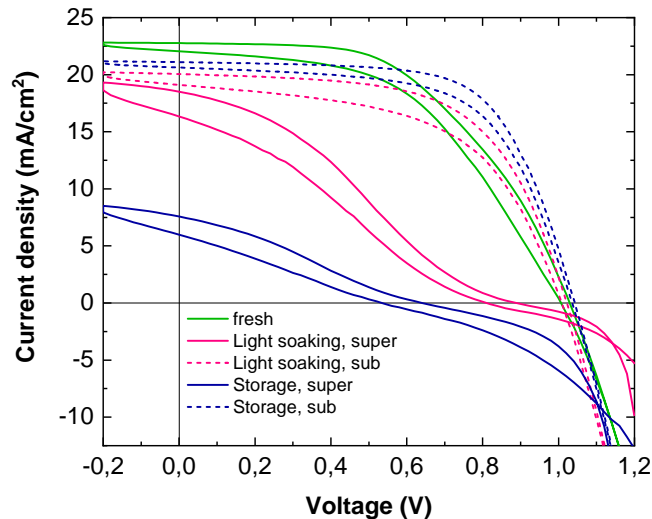
Figure 5.27: The effect of aging on the J-V curves for ITO side measurements
The J-V curves of the I pure devices at each aging step showing the effect of the aging side. Both the forward (inner) and reverse (outer) scan J-V curves are plotted.

the J-V curves is the fact that the kink mentioned in section 5.1.1 has actually disappeared after light soaking and apparently also does not return upon storage, which is clearly visible for the substrate-aged devices. Its removal increases the FF and is part of the reason why the improvements relative to the fresh devices is larger compared to the glass side measurement. Since the kink is only present for measurements from the ITO side it was reasoned that it could be related to one of the electron transport layers. The fact that precisely the substrate-aged devices no longer have the kink suggests that the light soaking has cured the unknown problem of one of the electron transport layers. Whether the kink is also gone for the superstrate-aged devices remains unclear due to the particular shape of their J-V curves, so other possibilities cannot be excluded. Based on the results just before light soaking in Figure B.12 it can be concluded that only storage in dark does not remove the kink, which further strengthens the hypothesis that the light soaking somehow has a curing effect on the substrate-aged devices.

Now that it is clear what the general effects are of both light soaking and storage on the devices as well as the dependence on their orientation, it is time to compare the three different compositions and observe whether the substitution of bromide or RbCl doping influences the aging. Figure 5.28 shows a comparison of the compositions after 1250 hours light soaking for both the glass side measurement in subfigure (a) and (c), and ITO side measurement in subfigure (b) and (d). Starting with the glass side, there are no significant variations to observe for the V_{OC}, suggesting that the composition does not substantially change the effect of light soaking on the QFLS. The orientation appears to be marginally in favor of the superstrate-aged devices, but is not completely independent of light intensity.

The FF, on the other hand, has a few interesting characteristics. Firstly, the small but noticeable difference between the aging sides observed before for the iodide pure perovskite seems to be a general trend for all compositions. The J_{SC} as function of light intensity for the glass side measurement is plotted in Figure B.13a in the appendix and confirms that the higher FF for the substrate-aged devices is indeed caused by a lower J_{SC}. With both a lower V_{OC} and J_{SC} it thus appears that the substrate side is more affected by light soaking. Secondly, the overall shape of the bromide-containing devices is clearly different to the iodide pure devices, indicating that the substitution of bromide alters the light soaking response. However, due to the complexity of the FF it is difficult to pinpoint a possible origin for this difference.

Lastly, the IBr devices and specifically its superstrate-aged side has significantly lower values compared to the other two compositions. Before aging, it was observed that it is the most efficient composition over the entire light intensity range. The substitution of bromide is also expected to help stabilize the device during aging based on literature. However, specifically for light soaking it is found that it actually has the lowest efficiency due to the combination of lower values for all figures of merit. A quick look at the J-V curves in Figure B.14 in the appendix reveals that the IBr devices have a much lower shunt resistance already for 1 sun intensity. Since the shunt resistance is most dominate at lower light intensities, it could explain why the differences become larger when the intensity is decreased. Furthermore, a subtle larger decrease in V_{OC} near 1E-4 sun supports this explanation. A low shunt resistance

is typically caused by a lower quality of the perovskite film. The fact that the J_{SC} is clearly lower compared to the other compositions as seen in Figure B.13a adds to the suggestion that the charge carriers are lost more easily in the bulk due to shunts. However, it has to be mentioned that the J_{SC} is then expected to decrease relatively more quickly at lower light intensity compared to the other compositions, which is not observed. The actual origin of the lower values is thus more nuanced and requires additional measurements to locate. Doping the perovskite with RbCl appears to alleviate the losses. The V_{OC} is still improved as was the case for the fresh devices. The values of the FF have improved, while still maintaining the same characteristics. An explanation could be that the RbCl somehow strengthens the crystallization of the perovskite layer against the light soaking. Indeed, an improved crystallinity and/or decreased amount of grain boundaries reduces the number of defects and hence improves the performance[290].

Figure 5.28: Composition comparison after 1250 hours of light soaking
The glass side measurement is shown on the left with (a) V_{OC} and (c) FF. The ITO side measurement is show on the right with (b) V_{OC} and (d) FF.

The comparison for the ITO side measurement is shown on the right side in Figure 5.28. Keeping in mind that the devices have already been stored for a couple of days, there are still some interesting differences between the compositions to observe. While the substrate-aged

devices all have similar results, the superstrate-aged devices with substituted bromide perform drastically better compared to the iodide pure devices with both the V_{OC} and FF improving over all light intensities. Thus, it appears that the addition of bromide in the perovskite helps to reduce the losses shortly after light soaking. The results of the long storage period have to show whether this is a lasting effect.

The comparison of the compositions after two to three months of storage in dark is shown in Figure 5.29 with again the glass (ITO) side measurement on the left (right). There are no obvious differences between the two measurement sides, showing that the effects of aging are not selective to the location of charge generation in the device. For the superstrate-aged devices, both the V_{OC} and FF show a clear contrast between the iodide pure and bromide-containing devices. While the iodide pure solar cells have substantially decreased values as previously observed, the bromide-containing cells are clearly less affected in regards to performance. Their V_{OC} is still on par with the substrate-aged devices and the FF has much higher values over the entire light intensity range. Also, since there is a difference of approx-
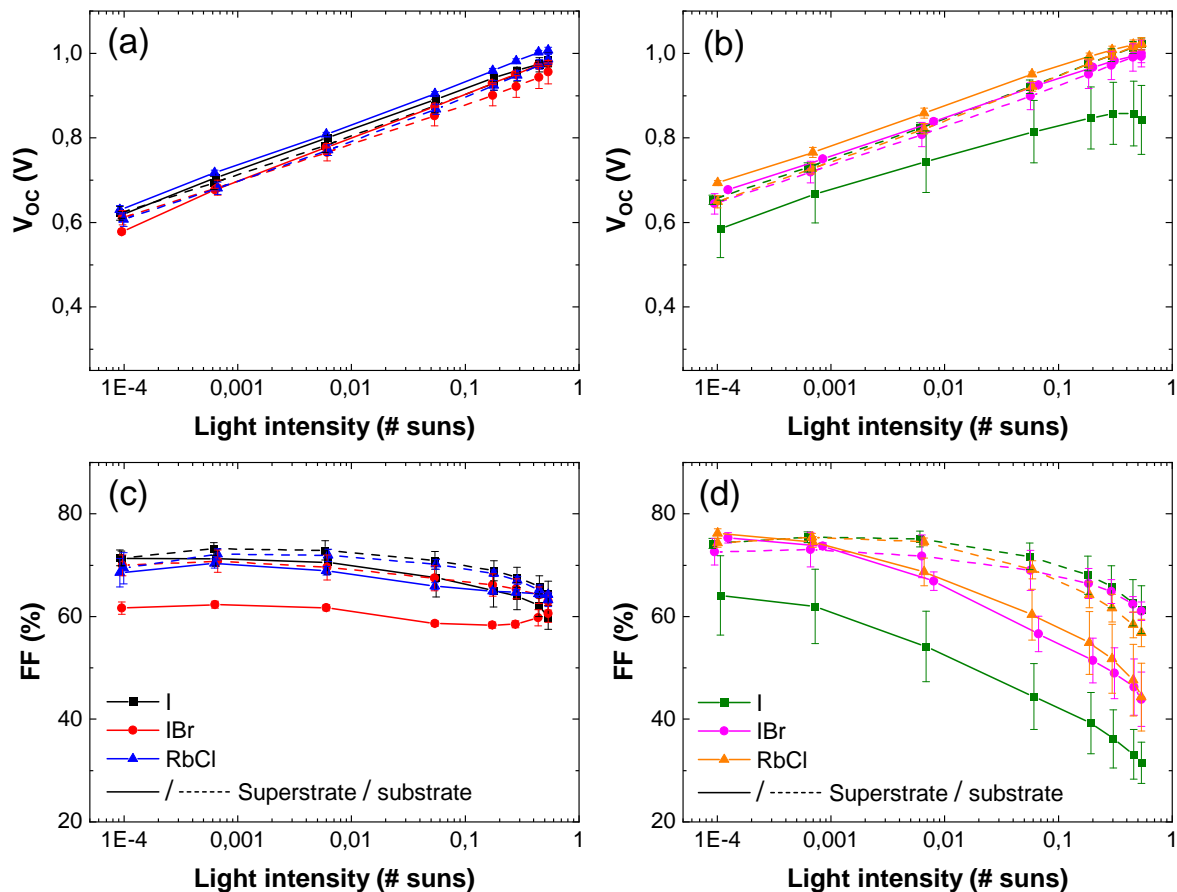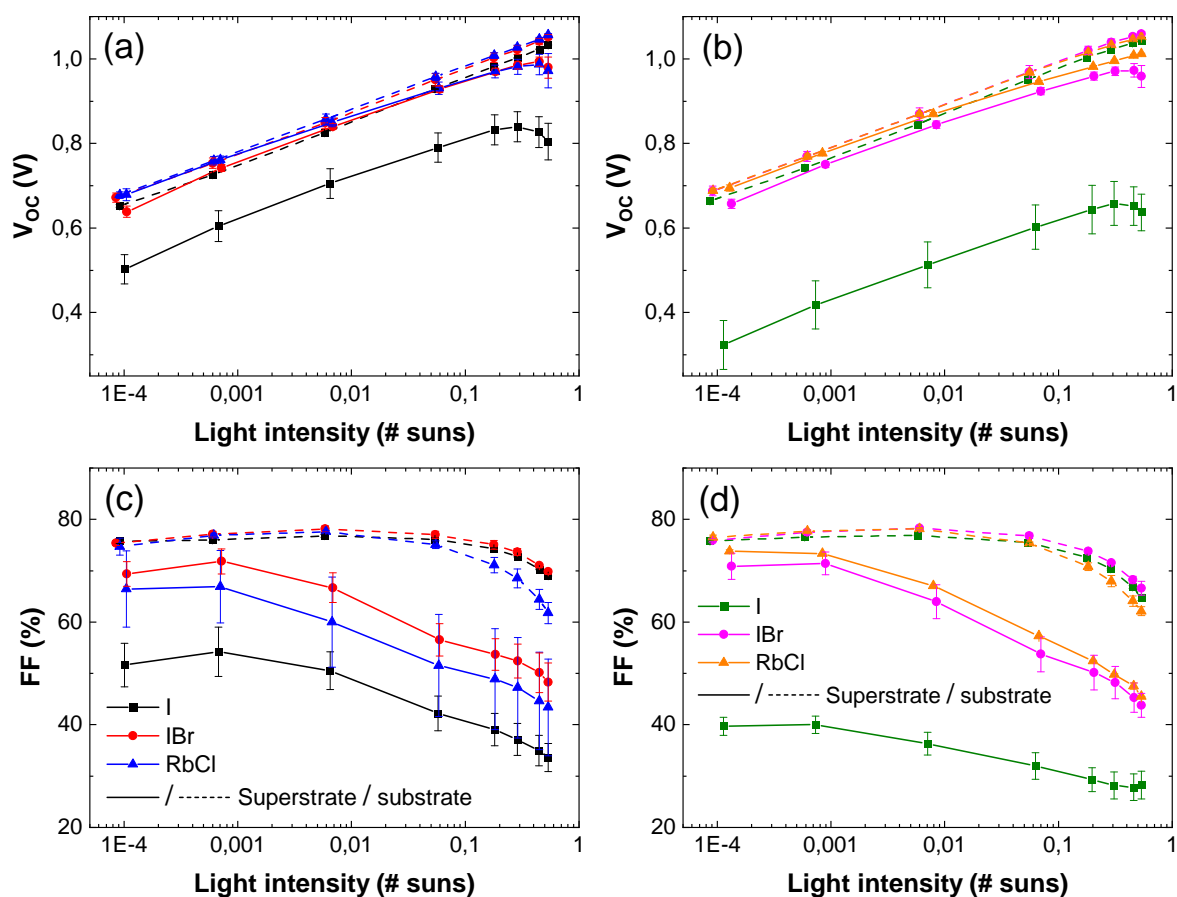

Figure 5.29: Composition comparison after months of storage in dark
The glass side measurement is shown on the left with (a) V_{OC} and (c) FF. The ITO side measurement is show on the right with (b) V_{OC} and (d) FF.

imately one month between the glass and ITO side measurement, the data essentially gives an idea of the degradation over time. While the I devices continue to decrease in performance, the devices with substituted bromide remain similar in values indicating that the degradation has stabilized.

The J_{SC} after storage for the glass side measurement is depicted in Figure B.13b. The extracted current at low light intensity is approximately the same for all compositions and independent of the aging side. At high light intensity, however, there is a clear difference between the aging side. The substrate-aged solar cells have mostly recovered to around 20 mA/cm^2, while the superstrate-aged cells have values that are comparatively 2 to 3 mA/cm^2 lower. Since the difference grows with increased light intensity it is most likely related to an interface problem. This is in agreement with the expectation that the S-shape is caused by an extraction barrier. The charge carriers are thus lost due to increased recombination at the interface, which lowers the current density.

The last difference to mention is the fact that the RbCl doped devices aged from the substrate side have a lower FF at high light intensities compared to the other compositions. The graph is plotted again but on a linear scale in Figure B.15 in the appendix and clearly shows that the slope of the curve is higher for both measurements sides. In section 5.2.2 it was found that the slope depends on the series resistance. Hence, it could be the case that the RbCl devices suffer from a higher resistance, assuming that other parameters do not significantly influence the slope of the curve. A possible explanation could be that the Rb- or Cl ions diffuse towards the perovskite/PCBM interface and negatively affect the contact resistance. To confirm this, first the actual series resistance would have to be measured. For the second part the surface could be probed with, for example, X-ray photoelectron spectroscopy (XPS) or Secondary-ion mass spectrometry (SIMS) to confirm an increase in the doping ions. However, since these are surface techniques it would require specific samples without the ETLs that are aged exactly the same. Such samples are also fabricated and used to measure the XRD, but are unfortunately not put through aging.

Regarding similarities, it is observed that all compositions do show the S-shape as well as the local negative ideality factor. However, from analysis of the individual J-V curves it is found that all I cells have an S-shape, around three out of four of the IBr cells and about half of the RbCl cells. Although not enough cells are tested for it to be statistically evident, it does suggest that the perovskite modifications reduce the change of an S-shape developing after storage. A fascinating observation is that the general shape of the FF as function of light intensity has the exact same characteristics for all compositions, which is especially clear for the glass side measurement. This particular shape is unusual and has not been found in any literature. Again, the complexity of the FF and the many parameters that influence its behavior makes it difficult to comment on the origin. However, it is clear that both this, the S-shape and the negative ideality factor are linked to the aging from the superstrate side.

Coming back to Figure B.15, the I and IBr devices have a similar slope for both aging sides, which suggests that their series resistance is more or less the same. In other words, the aging side does not appear to affect the series resistance of these devices. Also interesting is that the

non-linear behavior seen in the ITO side measurements of the fresh devices has disappeared for both aging sides. If the speculation of high defect density at the perovskite/PCBM interface as its origin is indeed correct, it appears that long term light soaking from either side or storage can alleviate the problem. Unfortunately, the ITO side measurement after light soaking already has the storage characteristics, so it is not possible to determine whether the light soaking or storage is the cause.

The ideality factor n_{id} and power law dependence α are extracted from the light intensity data of both the light soaking and storage measurements. The results for the glass side measurement are shown in Table 5.4 together with the results of the fresh devices for ease of comparison. The top section of the table shows the values for the ideality factor and the bottom section the values for the factor α. The results of the ITO side measurement are not shown because the general conclusions are the same, once more supporting the argument that the measurement side does not influence the aging results.

Table 5.4: Ideality factor and the power law factor of the aged devices
The top part shows the values of the ideality factor n_{id} and the bottom part the values of the power law dependence α. Measurement from glass side for all three compositions.

	Fresh	Light soaking		Storage	
	-	superstrate	substrate	superstrate	substrate
I	1.831 ± 0.027	1.645 ± 0.042	1.653 ± 0.083	1.480 ± 0.084	1.740 ± 0.006
IBr	1.565 ± 0.023	1.802 ± 0.043	1.560 ± 0.031	1.611 ± 0.036	1.711 ± 0.024
RbCl	1.795 ± 0.027	1.712 ± 0.038	1.728 ± 0.060	1.414 ± 0.099	1.715 ± 0.014
I	0.964 ± 0.005	0.953 ± 0.008	0.956 ± 0.004	0.945 ± 0.006	0.960 ± 0.002
IBr	0.963 ± 0.003	0.950 ± 0.006	0.943 ± 0.013	0.939 ± 0.006	0.965 ± 0.003
RbCl	0.963 ± 0.004	0.955 ± 0.005	0.947 ± 0.005	0.940 ± 0.006	0.958 ± 0.005

For the results of the devices after light soaking it is difficult to uncover any clear connections. This is not surprising since all V_{OC} curves are close together with similar characteristics as seen in Figure 5.28a. Also, the ITO side measurement cannot be used for comparison because of the slight delay in the time of measurement. The iodide pure and RbCl devices show a slight decrease compared to the fresh results, but not enough such that it can be pinpointed to a certain recombination mechanism. The standout value is the one of the IBr aged from superstrate side, which is the only value showing a clear increase. Coincidentally, it is these devices that showed the large drop in FF seen in Figure 5.28c that was hypothesized to be caused by a decrease in film quality resulting in a lower shunt resistance. Such film would likely also have an increased bulk defect density, subsequently enhancing the contribution of trap-assisted recombination and hence increase the ideality factor. The α shows a small overall decrease in value compared to the fresh devices indicating more loss of charge carriers. An increase in radiative recombination is possible, but unlikely to cause significant changes due to its small contribution in perovskite solar cells. More likely is a change in the charge

distribution, possibly due to ion migration, resulting in a space-charge that limits the charge carrier extraction. Any details on the specific origin remains difficult to identify solely on these measurement.

Moving on to the values after a few months of storage. The clear differences observed between the two aging sides in the J-V and light intensity graphs are reflected in the values of n_{id} and α. Both values for the devices aged from superstrate side have decreased relative to the light soaking results. The combination of the severe S-shape with the larger losses of the J_{SC} and local bending of the V_{OC} at high light intensity means it is almost certain that the presence of an extraction barrier at the PTAA/perovskite interface is at the core of the problem. The charge carriers are blocked at the interface which reduces the carrier extraction, leading to a decrease of α. Consequently, the non-radiative interface recombination increases, which explains the decrease in ideality factor. The opposite effect is observed for the substrate-aged devices. The recovery of the figures of merit means overall less recombination and more charge collection. The large initial difference between the FF of both measurement sides of the fresh devices has disappeared. It is expected that a problem with the perovskite/PCBM interface due to the ALD process of the SnO_2 lead to a higher interface defect density. Light soaking appears to help cure the problem and reduces the defect density, which is in agreement with the observed increase in ideality factor and power law factor.

All in all, a lot of aging results have been shown and various explanations are put forward. While most information of the J-V and light intensity data is self-consistent such that hypotheses can be composed, due to the lack of variation in measurements it is difficult to prove them. Instead, simulations are used to find the physical origin of changes made by the aging process, which will be elaborated on in the next section.

5.4   Simulations of aged devices

The final simulation of the fresh IBr devices is used as a starting point for the optimization of the parameters to accurately fit the aging data. However, even for only one type of composition there are already so many results that it is not possible to optimize every single one due to time constraints. Hence, the decision is made to focus on the most interesting result that could provide the most useful information. The results of the light soaking period are not strikingly different compared to the fresh results and are also seemingly more random, which makes it difficult to optimize the many different parameters. Instead, the focus is placed on the results after storage, since their general changes are clear and distinct. Furthermore, since these changes are identical for all compositions, a single simulation essentially provides information for all three types of devices. Of the two aging sides the superstrate orientation has the most potential, because the characteristic S-shape serves as a great focus point due to the finite number of parameters that could create such a shape. Also, in the pursuit for more stable perovskite solar cells it is more interesting to simulate the superstrate-aged devices and try to unravel the physical origin for why these samples in particular degrade so significantly.

This information can then be used for a more targeted approach in solving the bottleneck.

To get straight to the point, the final optimized J-V curve simulation of the IBr superstrate-aged devices is shown in Figure 5.30. At first sight, the measurement data and simulation appear to be in excellent agreement in both size and shape. However, there are a few details that have to be addressed before talking about the physics behind the model.
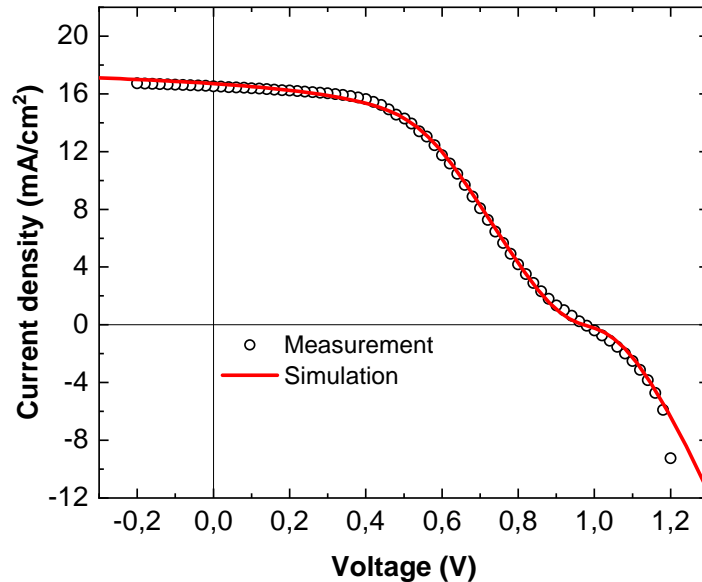
Figure 5.30: S-shape simulation of the superstrate-aged device after storage
The open circles indicate the experimental data of the IBr devices measured from glass side and the solid red line the optimized simulation.

Firstly, the strategy of optimization is chosen opposite to that of the fresh devices. The complex characteristics of the aged light intensity results combined with the fact that light intensity measurements in general are an order of magnitude more difficult to fit means it is better to start with the J-V curves. Secondly, the measurement data in the graph are the average values of all S-shaped J-V curves. There are also samples which did not have an S-shape as mentioned before, but they are not included in the averaging. The focus of the simulation is specifically on the S-shaped curves and including the non-S-shaped ones would result in an unnatural curve with no connection to the physics of the real devices.

Thirdly, observant readers might have noticed that the J_{SC} in this figure is higher than for the fresh results in Figure 5.23a, even though a clear decrease in charge collection is observed after aging. The reason for this is that the J-V curve of the aged measurement is not compensated for masking. To be clear, the effect of masking is such that the V_{OC} and FF values correspond to a lower light intensity than is actually used during the measurement and for this the simulation is correctly optimized. However, the J_{SC} should be adjusted to this lower light intensity to have all the figures of merit correct, which can be done by multiplying the value by the ratio X assuming linear dependence. Unfortunately, multiplying the entire J-V curve leads to a flawed rescaling and thus to incorrect values for the FF as seen in Figure B.10.

Hence, the choice is made to use the original J-V data to preserve the correct characteristics of the shape as well as the value of the V_{OC}, despite the fact that the J_{SC} is overestimated. This does mean that the V_{OC} and FF values obtained from the simulation will be slightly off regarding light intensity, but the most important aspect is that the particular shape of the curve is correctly accounted for by the model.

That brings up the final point, namely that even with the effect of masking in mind the simulation would always overestimate the J_{SC}. Trying to lower the J_{SC} by adjusted the parameters accordingly would result in early bending of the curve and not remain flat near short-circuit current. This suggests that there is a different origin for the reduced current density. It is possible that a decrease in the perovskite film quality reduces the total amount of light absorption. This can be checked by remeasuring the EQE and UV-vis to see whether the optical properties have changed and XRD for possible changes to the crystallinity. The generation file from the optical simulation is still the same as the one calculated for the fresh devices, but might need to be recalculated to account for the aging. In the ideal case the complex refractive index data of the different layers is measured after aging to calculate a new generation profile, but that is not possible. Instead, the charge carrier generation is simply reduced to 85% to artificially account for the reduced absorption of the perovskite layer. From Figure B.10 it is clear that this slight reduction in intensity has no detrimental effects on the FF and V_{OC}.

Table 5.5: Adjusted simulation parameters for the aging simulation
All other parameters are identical to the values reported in section 4.2.2.

Parameter	Location	Value
Work function	Left contact	5.5 eV
Bandgap	PTAA	3.74 eV
Defect density	PTAA/perovskite interface	4.7×10^{11} cm^{-2}
Defect type	PTAA/perovskite interface	Donor
Defect density	Perovskite/PCBM interface	2×10^{10} cm^{-2}

With these considerations and limitations in mind the optimized parameters are discussed next, which are listed in Table 5.5. The fact that only a few parameters have to be adjusted is a good sign that the baseline simulation is representing the actual fresh solar cells reasonably accurately. The first step in creating an S-shape is constructing an energetic barrier for the charge carriers. Either a large enough injection or extraction barrier can generate a S-shape, but the final outcome for the J-V curve will be different. To fit the particular S-shape of the aging data, a combination of both barriers is needed. Based on the aging orientation of the device it is expected that modifications to the HTL side of the device are the cause for the S-shape. Both the work function of the left contact, i.e., the glass side ITO layer as well as the bandgap of the PTAA are increased, resulting in an injection barrier of 0.14 eV and an extraction barrier of 0.19 eV. It is decided to change the bandgap of the PTAA rather than

its EA to maintain the same size barrier for electron blocking to limit any additional changes.

Next, the defect density has to be increased to tune the V_{OC} and FF. It is found that solely increasing the defect density at the PTAA/perovskite interface is not sufficient for correctly fitting the measurement data. Additionally, the bulk defect density could be increased, which would be in line with the expected decrease of the perovskite film quality. However, this does not lead to improved fitting of the curve. Perhaps surprisingly, since it is at the other side of where the light soaking happened, but increasing the defect density of the perovskite/PCBM interface does allow for a good fit of the data. The reason for this could be that these higher values are already present in the fresh devices, as alluded to in section 5.2.2. In other words, based on the research by Głowienka et al.[374] it is very well possible that the perovskite/PCBM interface has a higher defect density than is ultimately accounted for in the final simulation of the fresh devices. Furthermore, this approach has been applied to try to find the optimum parameter set for both measurement sides. While promising results were found, in the end the glass side optimized simulation is used.

The final required ingredient is based on the properties of the defects. Up to this point all defects where set as neutral type which potentially only gives an S-shape with its location of maximum bending, or inflection point, below V_{OC}. This is similar to what Shi et al.[414] found by employing an injection barrier with a high interface defect density. However, the S-shape observed for the superstrate-aged devices has its inflection point exactly at V_{OC}. This might seem like a small difference, but with the already discussed parameters it has proven to be impossible to accurately fit the entire J-V curve using neutral-type defects. It turns out that the solution is to assume donor-type defects at the PTAA/perovskite interface. Thus, it appears that the charge state of the defects plays a vital role in the creation of this type of S-shape and that there are different mechanisms at play for both types.

The model is applied to the light intensity measurements and the results are shown in Figure 5.31. Overall, it is clear that the simulation does not capture the particular characteristics of neither the V_{OC} nor FF. The general slope of the V_{OC} is slightly lower for the simulation, suggesting simultaneously too high (low) interface (bulk) defect density in the model. Furthermore, the local negative ideality factor near 1 sun intensity is not accounted for at all, which could mean that its origin is not related to the S-shape although further investigation is required to prove this. The values of the FF are reasonably close in absolute terms and the maximum is correctly predicted, but the detailed features are not accounted for. Thus, although the S-shaped J-V curve can be fully described by the simulation, there are still elements of the physics missing.

Finally, alternative possibilities for the location of the S-shape are also considered. It is found that the J-V curve can likewise be fitted by assuming an injection and extraction barrier together with a high acceptor type interface defect density at the perovskite/PCBM interface and even a combination of both interfaces is possible. However, when comparing the simulation to the light intensity measurement there is significantly more deviation than is observed for the PTAA/perovskite optimized model. While these possibilities cannot be excluded solely based on the J-V measurements, the fact that the S-shape only occurs for the

superstrate-aged devices and no S-shape is observed after one and a half months storage prior to light soaking, it is improbable that they are representative of the real devices.
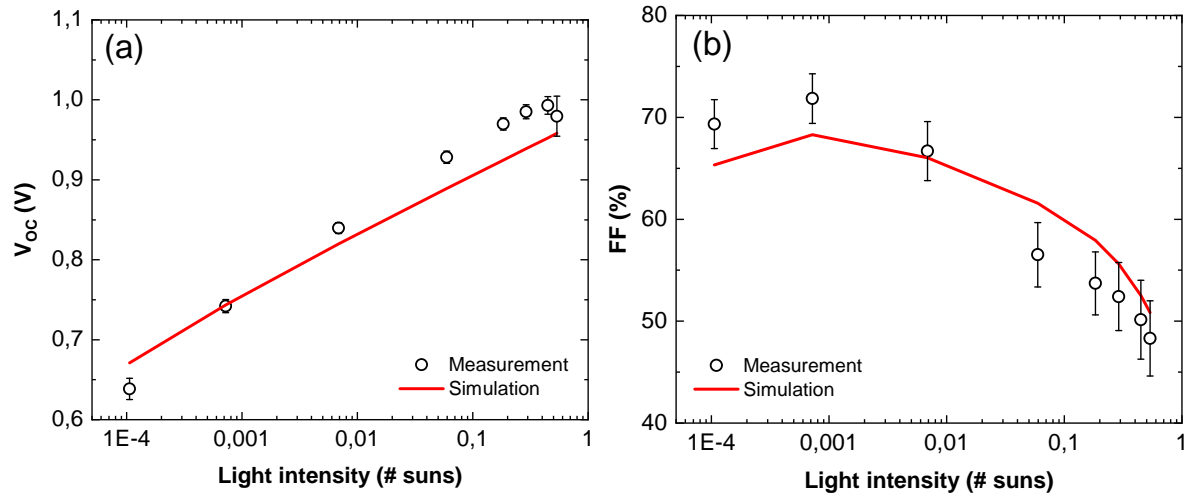
Figure 5.31: Light intensity simulation of the superstrate-aged device after storage
Measurement from glass side of the IBr device. (a) V_{OC}, (b) FF.

Hypothesis on the origin of the S-shape

From the simulation it is learned that the superstrate S-shape can only be constructed by assuming that the defects at the PTAA/perovskite interface are donors. This is confirmed in Figure B.16 where the J-V curve of the aging optimized simulation is compared for different defect types. Both neutral and acceptor defects yield identical results and a similar shaped curve as the fresh simulation. The data in the graphs shown in this section are all obtained for illumination from glass side.

To get a better understanding of the effect of donor defects with regards to different recombination mechanisms, the simulated recombination currents as function of voltage are shown in Figure 5.32 for the fresh devices and the aged devices with either neutral or donor defects. The total generation is independent of the voltage and hence plotted as a horizontal line. The total recombination can be divided into recombination in the bulk and at the interfaces. Subsequently, the bulk is divided into SRH-, radiative- and Auger recombination. The last one is not shown since it is orders of magnitude lower and thus negligible. The curves are normalized against the generation to account for the different illumination intensities. The voltage at which the total recombination crosses the generation is equal to the V_{OC}. In Figure 5.32a the fresh simulation is compared to the aging simulation with neutral defects to investigate the effect of the barriers in combination with the high interface defect density. For the fresh simulation there is a transition from bulk-dominant- to interface-dominant recombination around 0.8 V. It is near this point that the applied voltage equals the built-in voltage and the electric field switches its direction, which means the carriers will drift to the wrong interface and recombine. For the aged simulation with neutral defects there is a clear increase

in recombination leading to reduced performance as well as dominant interface recombination over the entire voltage range. The combination of charge carrier blocking with a high defect density is therefore an effective way of increasing the interface recombination.

The simulation also gives information on the positional origin of the charge carriers that recombine. For example, for the fresh simulation the recombination at the PTAA/perovskite interface is driven by holes from the PTAA layer and electrons from the perovskite, as expected. However, due to the extraction barrier, the holes are prevented from extracting and hence the recombination is driven by both the electrons and holes in the perovskite layer. This is found to be true for both neutral and donor defects.
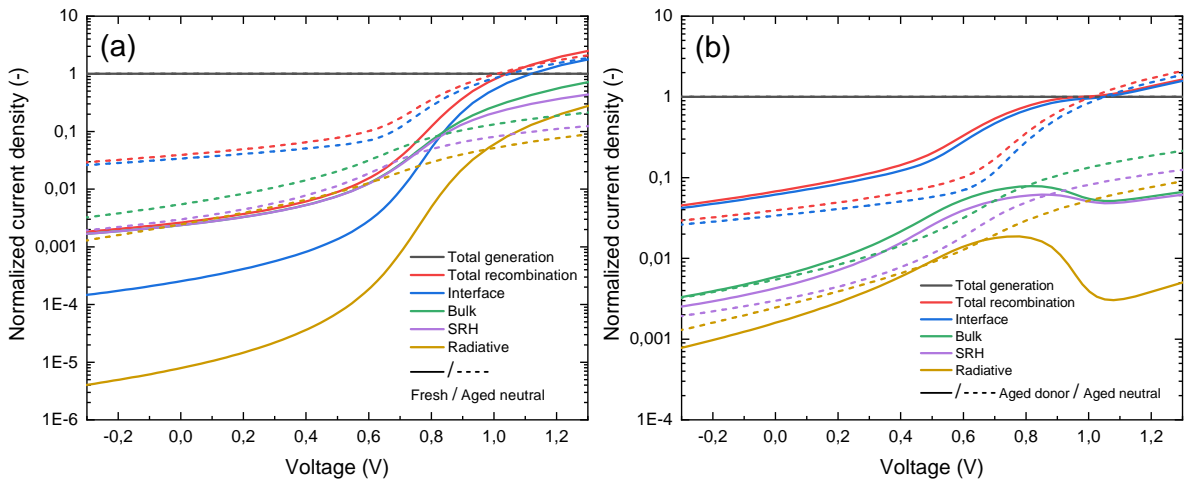
Figure 5.32: Comparison of the fresh vs. aged simulated recombination currents
(a) Fresh vs. aged with neutral defects, (b) aged with donor defects vs. aged with neutral defects.

The comparison between the aged simulation with either neutral or donor defects is shown in Figure 5.32b. It appears that donors defects further increase the interface recombination and account for close to 100% of the overall recombination as well. The most distinct and interesting difference is the local decrease in bulk recombination around 0.9 V. The effect increases for higher order recombination mechanisms suggesting it is related to the charge carrier density in the bulk. It is surprising that a property change of the interface defects can create such as a difference for the bulk recombination. In addition, the local decrease approximately overlaps with the concave part of the measured J-V as can be seen in Figure B.17 in the appendix. Furthermore, it seems that the position of largest decrease of the bulk recombination, i.e., the part with the largest negative slope, corresponds to the inflection point of the S-shape in the J-V curve. Hence, it is useful to look further into this part of the voltage range.

Next, the free charge carrier density throughout the device is investigated for the case of neutral and donor defects using the aging simulation. Figure 5.33 shows the carrier density of the electrons as function of position in the device. Position zero indicates the start of the PTAA layer as schematically added to the top of the figure. In case of neutral defects

there is a continuous increase in charge carrier density over the entire bulk perovskite for increased voltage. The maximum of the curves slowly moves towards the PTAA side of the device, possibly due to the lowering of the built-in voltage and hence reducing drift towards the perovskite/PCBM interface.
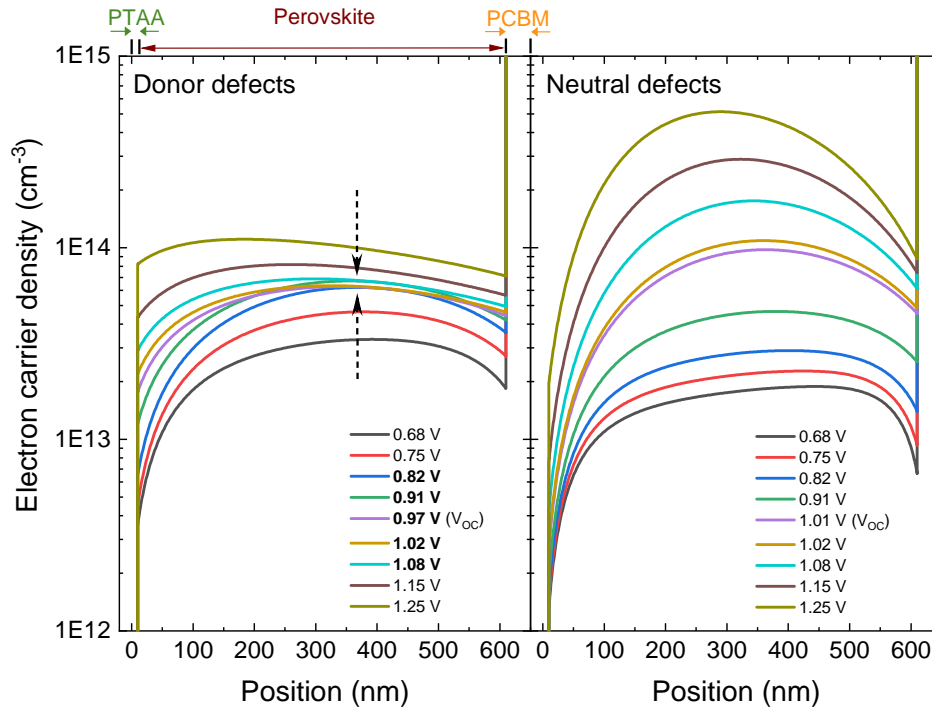
Figure 5.33: Simulated electron carrier density in the device
The electron carrier density as function of position in the device is plotted for various voltages.

Moving on to the donor defects, the voltage range of interest corresponding to the local decrease in bulk recombination spans roughly from 0.80 to 1.06 V as seen in Figure B.17 and the voltage values near this range are labeled in bold in the legend. Initially, there is the same overall increase of the carrier density similar to the neutral defects. However, precisely for the specified voltage range indicated in bold there appears to be saturation of the carrier density indicated by the two arrows, and more interestingly, even a small decrease for 0.97 and 1.02 V. This decrease occurs precisely at the maximum in the perovskite bulk and will thus put the upper limit on the total amount of recombination possible. After 1.08 V the carrier density continues to increase again, which shows the saturation period only occurs for this specific voltage range. An additional difference to the neutral defects is the larger increase of the carrier density near the PTAA/perovskite interface, which is more clearly visible in the close-up of the interface in Figure B.18a in the appendix. In short, due to the donor defects the electron carrier density increases near its interface, which could potentially be the cause of the observed decrease of the density deeper in the perovskite bulk.

The carrier density of the holes is shown in Figure 5.34. For the neutral defect a decrease

(increase) in carrier density is observed near the PTAA/perovskite (perovskite/PCBM) interface. The fact that the figure is plotted on a logarithmic scale makes it appear that the carrier density near the HTL is almost constant while significantly increasing near the ETL. However, the carrier density at the PTAA/perovskite interface is over an order of magnitude larger compared to the other interface, which is caused by poor collection of the holes due to the extraction barrier. Hence, this interface will be the dominant factor for the characteristics of the charge transport. Switching to donor defects still gives the same overall behavior, but with different carrier density ratios. The main difference is the enormous decrease in hole carrier density near the PTAA/perovskite interface. A close-up of the interface is shown in Figure B.18b, which highlights the differences for both defect types. Consequently, this results in an unusual fluctuation of the carrier density in the middle of the perovskite for increased voltage. Interestingly, exactly for the particular voltage range mentioned above there is a decrease in the carrier density, while it increases as expected outside of this range.
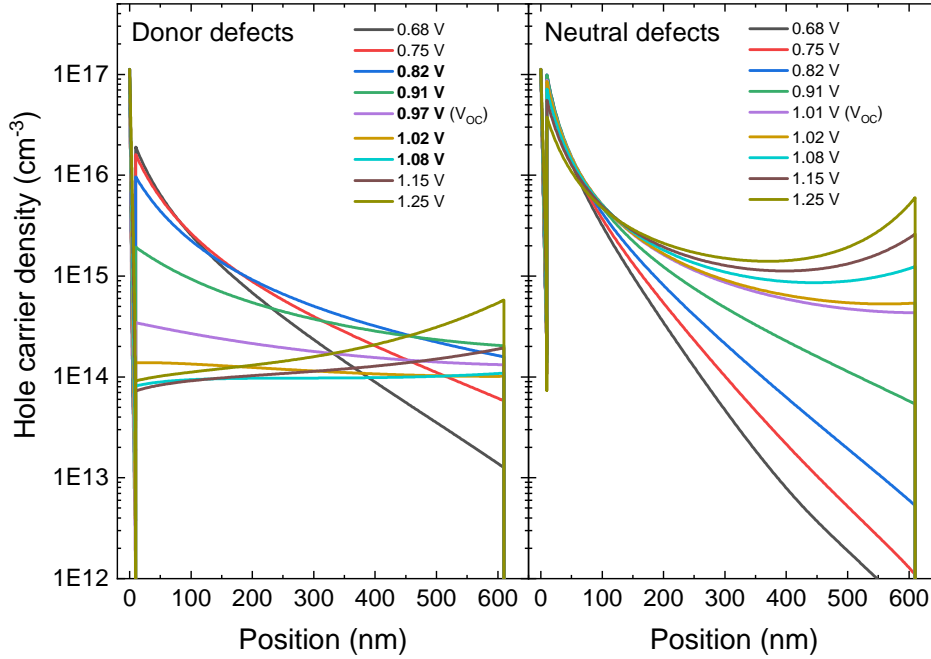
Figure 5.34: Simulated free hole carrier density in the device
The hole carrier density as function of position in the device is plotted for various voltages.

To link the local decrease in bulk recombination to the carrier density, the information of both charge carriers has to be combined, especially since the effect is more pronounced for higher order recombination mechanisms. The charge carrier with the lowest density will put the upper limit on the total amount of recombination that is possible. For the neutral defects there are only increasing values for the lowest carrier densities, which means the bulk recombination will continuously increase for increased voltage. This is in agreement with the observed curve in Figure 5.32b. In case of donor defects the electrons are the limiting factor for the voltage range of interest. The small decrease in carrier density observed at 0.97 and

1.02 V correspond precisely with the voltage for which the decreasing bulk recombination is observed. In addition, the temporary decrease of the hole carrier density between 0.8 and 1.08 V does overlap accurately with the reduced bulk recombination and will lead to a larger effect on higher orders of recombination.

The question that still remains is how exactly the donor defects are responsible for the observed changes in charge carrier density. In essence, the only difference between neutral and donor defects in the simulation is the fact that the charge state of the defect is taking into account for donor defects, while it is ignored for neutral defects. As explained in section 4.2.2, the single donor defect can either be in the neutral (0) state or the positively charged (+1) state. SCAPS has the option to check the occupation probability of the defects, i.e., the ratio of the 0 and +1 charge states of the defects. It turns out that the vast majority of donor defects at the PTAA/perovskite interface are in the +1 charge state over the entire voltage sweep. Thus, for the donor defects this will lead to a significant local charge density that will influence the free carriers around it, while this strong local charge will not be present in the case of neutral defects. A possible explanation could thus be that electrostatic repulsion of the positively charged donors combined with the baseline decrease of the built-in voltage causes an accelerated decrease of the hole carrier density near the interface compared to the neutral defects, as is indeed observed in the close-up in Figure B.18b. Simultaneously, electrons are pulled towards the interface more strongly leading to a higher increase of the electron carrier density as verified in Figure B.18a.

It is clear that an increase of the defect density at the PTAA/perovskite interface is needed for an accurate fit of the S-shape. However, the origin of this increase has not been elaborated on up to this point. The hypothesis for this is as follows. Based on the fundamental properties of perovskite and the observation of increased hysteresis for the superstrate-aged cells, it is expected that ion migration plays an important role in the device. Under the influence of light soaking the activation energy of the ionic donor species will be overcome, hence the positively charged ions can migrate to the PTAA/perovskite interface due to the built-in field. This leads to an accumulation of the ions at the interface, which explains the increase in defect density. Additionally, ion migration is believed to screen the internal electric field[68,74,347,348]. Figure 5.35 shows the simulated electric field in the device for the case of neutral and donor defects. Indeed, the reduction in free hole carriers at the interface as a result of the presence of positively charged defects leads to effective screening of the electric field as seen for the donor defects. Without the charged defects the hole carrier density remains high at the interface resulting in continuous band bending, which is the case for the neutral defects.

Xu et al.[417] observed the same type of S-shape as found in this project and derived a similar hypothesis based on ion accumulation and electric field screening. In their explanation they used a equivalent circuit model to fit the J-V curve, which is based on the work of García-Sánchez et al.[418]. Interestingly, the circuit contains two additional diodes that represent the charge accumulating at the ions and trap states of which one is connected in reverse polarity. This particular part of the equivalent circuit has been observed before in the paper by Gunawan et al.[406] describing the negative ideality factor, although the total circuit is different. Since

both phenomena are observed in the devices of this project, it could perhaps be the case that a combination of the two equivalent circuits could explain both the effects simultaneously.
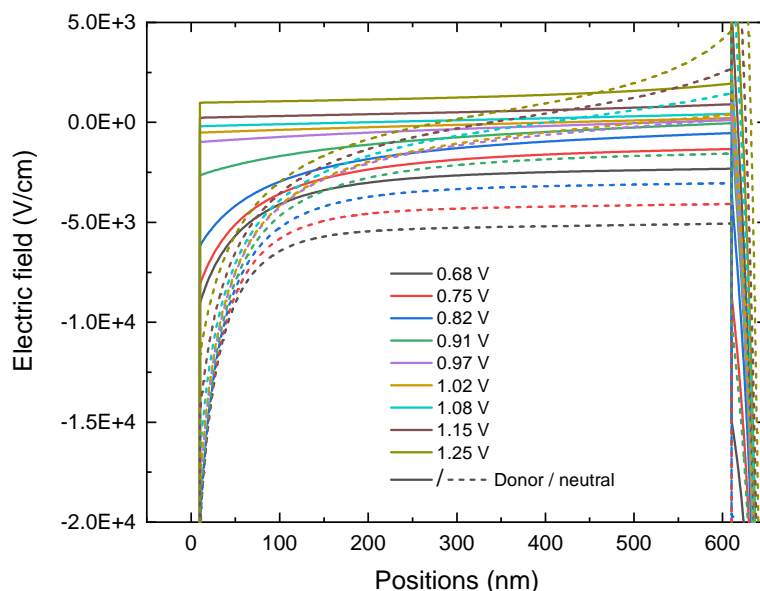
Figure 5.35: Simulated electric field in the device
The internal electric field as function of position in the device is plotted for various voltages for both donor defects and neutral defects. A negative electric field is defined as the arrow pointing from right to left, i.e., from the PCBM to the PTAA.

From the measurement results it is observed that the S-shape is reversible by light soaking at MPP. This is an additional indication that an explanation based on ion migration is more likely to be true than chemical degradation for example, which is generally irreversible. Upon illumination while keeping the device at MPP, the ions could be reactivated and will redistribute in the bulk due to the modified internal field at MPP compared to light soaking at open-circuit voltage.

The chemical origin of the donor defects is another question that needs to be answered in order to know how to solve the degradation problem. There is an active group in perovskite research working on the determination of the different activation energies of the defects using measurements and DFT calculations. Generally, the anion vacancy, mono- and divalent cation interstitial and certain antisites and are classified as donor defects[301,419–421]. Their activation energy depends on the composition of the perovskite, but even the values themselves contain quite some spread due to different processing conditions and calculation methods[339,347,356]. Furthermore, Figure B.19 in the appendix shows a simulation sweep of the energy level of the interface defects which confirms that an S-shape is created anywhere from 0.3 eV above the VBM to inside the CBM. Hence, there are many possible candidates for the donor defect. In general, the vacancies will have the lowest activation energy followed by the interstitials and then the antisites[339,422]. In the context of ion migration, the vacancies and interstitials are thus most often suggested as candidates.

Also important is the timescale on which the migration occurs. It is not clear from the experiment how quickly the devices become S-shaped, but from the MPP recovery in Figure 5.25 it appears it can take hours to fully stabilize. Domanski et al.[148] show that the migration of cations occurs on a much longer timescale compared to the anions, which could thus be a possible candidate in the devices of this project, especially since all device types contain the same cations. A clear difference in terms of stability is observed between the iodide pure and bromide-containing devices, which suggests that the small amount of bromide stabilizes the perovskite. It has been found that the substitution of bromide increases the activation energy for the anions and thus reduces the ion migration[423,424].

Finally, the question remains why only the devices aged from the superstrate side become S-shaped. Perhaps the activation energy of the diffusing ions is low enough to be activated from the glass side, but too high when illuminating from ITO side. From the optical simulation in Figure 4.2 it is observed that a large part of the high energy light is absorbed by the back ITO layer when illuminating from ITO side, while the perovskite already absorbs quite well at 300 nm for glass side illumination. However, even light of 400 nm ($\sim$ 3.1 eV) has an energy which exceeds all energy values found in literature, making this an unlikely explanation. To fully exclude this possibility, an aging study could be conducted in which devices are aged using a range of LEDs, each with a different specific wavelength, to see if there are wavelengths that create a difference between the two illumination sides. Alternatively, the answer might be hidden in the effect of the location of the charge carrier generation. It could be that the location of generation has a different influence on the internal electric field depending on the illumination side. Illumination from ITO side could adjust the electric field such that the ions cannot migrate to the PTAA/perovskite interface. Or they could even migrate to the perovskite/PCBM interface and subsequently enhancing the internal field, which would correspond with the observed improved figures of merit for that illumination side.

With an eye on the future, it is difficult to pinpoint the solution that would lead to the prevention of the S-shape. If the hypothesis is true, ideally the ion migration could be prevented, which would put a stop to the accumulation of the ions at the interface. However, ion migration is such a widespread phenomenon that it appears to be an intrinsic property of perovskites, making it challenging to achieve, if possible at all. Alternatively, the HTL or contacts could be altered or changed. Although it does not prevent ion migration[74], it could perhaps reduce the effectiveness of the interface defects or prevent the appearance of the carrier blocking layer.

6. Conclusions and recommendations

A research study is carried out to investigate the light soaking stability of semi-transparent perovskite solar cells with three different perovskite compositions based on their orientation to the incoming light. The devices are both aged as well as measured for their two different orientations. The measurements were done after fabrication, after light soaking and after a long storage period in dark to investigate the changes that occurred during each step. Both optical and electrical simulations are used to dissect the measurement results and provide the connection to the physical origin of the observed effects. Additionally in chapter 4, an extensive overview of the range of values of the different parameters is given as well as the value range typically used in SCAPS, which could be useful for someone interested in doing electrical simulations of perovskite solar cells.

In general, the measurements of the fresh devices show that the three different perovskite compositions are very similar regarding both the optical and electrical characteristics. The IBr devices have the highest efficiency after fabrication due to a higher FF, possibly because of a reduced bulk defect density. Besides improving the V_{OC} at solar intensities and reducing hysteresis, the RbCl doping did not significantly alter the performance of the devices. One of the more distinct differences is observed between the two measurement sides. The ITO side has a significantly lower FF at higher light intensities, which suggests a problem with the perovskite/PCBM interface. Based on research on the same device stack, it is expected that the ALD SnO_2 fabrication process has altered the perovskite/PCBM interface leading to increased interface defect density as well as local band bending.

The most important parameters for the electrical simulation are investigated in-depth to help interpret the light intensity measurement results. This knowledge is used to optimize a fit of the light intensity results and excellent agreement is found for the glass side measurement. Unfortunately, it was not possible to optimize the model such that it would accurately fit both measurement sides simultaneously. The missing link is most likely the higher interface defect combined with the band bending at the perovskite/PCBM interface.

After the devices have light soaked for 1250 hours, a general decrease in performance is observed for all three compositions measured from glass side. The orientation of the device does not appear to be of influence for the light soaking. The IBr device, which was initially the best performing composition, now shows the worst figures of merit possibly due to a decrease of the shunt resistance. Again, the RbCl-doped device did not show any significant differences compared to the IBr devices. The measurement from ITO side shows a difference between the two aging sides, but this is because the devices were measured a few days after the glass side meaning they already spent a few days in the dark.

Extending the storage period in dark to two months shows a clear different between both

aging sides. The performance for the superstrate-aged devices has decreased significantly and a S-shape has formed in the J-V curve. By light soaking the device at MPP it is possible to remove it, which shows that the degradation is partly recoverable. On the contrary, the substrate-aged devices have improved compared to their original fresh measurement, which is attributed to a curing effect of the light on the the perovskite/PCBM interface. This time there is a clear difference for the devices with and without bromide, but the origin for this occurrence remains unknown.

In an effort to better understand the origin of the S-shape, the curve is fitted with a modified model of the fresh devices. A combination of an injection and extraction barrier together with high donor-type interface defect density at the PTAA/perovskite interface can accurately fit the S-shape. Based on the investigation of the recombination currents and charge carrier densities is expected that the increase in donor defect density is caused by ions accumulating at the interface. The ions act as donor-type defects and modify the internal electric field that subsequently will lead to a large increase in non-radiative interface recombination, but for specific voltages to a decrease of the bulk recombination.

6.1 Outlook

Many different questions were possible to answer with reasonable certainty, but there are still (smaller) questions of which the answer remains mostly unknown. Throughout the thesis different experimental measurements are mentioned that could explain certain smaller questions or provide useful additional information. However, care has to be taken to make sure it does not raise more questions than it provide answers. Unfortunately, due to unforeseen circumstances it was not possible to do the EQE and UV-vis measurements on the devices after the aging process. The optical information could have provided useful information on whether the optical properties of the different layers have changed and if the assumption of reduced absorption in the perovskite is valid. XRD would also be a very useful measurement to do after aging to see if the perovskite crystal structure has actually been affected. Also, it provides the most detailed information with respect to the composition, hence is could possibly help explain why the bromide-containing devices remain relatively more stable.

For a future stability test it would always be better to do more intermediate measurements if it does not disturb the devices too much. One of the remaining questions is the timescale corresponding to the ion migration and with more measurements a trend could become visible that could perhaps be used to estimate this timescale. Additionally, a research study could be conducted to investigate the day/night cycle performance of the devices for both its orientations. Since the S-shape is reversible, it could be the case that it is not as detrimental in more realistic operational conditions. The performance loss that would occur during the night could be compensated by the operation under illumination during the day. This gives the ability to investigate whether the devices can maintain long-term stability or will have an overall performance decrease. Furthermore, the duration of the multiple aging and recovery

processes could provide a better understanding of the timescale of the ion migration.

The biggest unanswered question is why the devices have such a distinct different behavior between the two aging sides. A variety of different devices with different transport layers could shed light on the contribution of the interface, although if they were to be simulated it would take a significantly long time. Alternatively, different simulation software could be used that can account for ion migration, such as gpvdm. An advantage of this would be that most parameter values can simply be copied.

Bibliography

[1] Our World in Data - Global energy consumption by source. https://ourworldindata.org/grapher/global-energy-consumption-source. 1

[2] J. Olivier and J. Peters. Trends in Global CO2 and Total Greenhouse Gas Emissions: Report 2019. *PBL Netherlands Environmental Assessment Agency*, 2020(February):70, 2020. 1

[3] Paris Agreement - Status of Ratification. https://unfccc.int/process/the-paris-agreement/status-of-ratification. 1

[4] P. Breeze. Chapter 13 - Solar Power. In P. Breeze, editor, *Power Generation Technologies (Third Edition)*, chapter 13, pages 293–321. Newnes, third edit edition, 2019. 1

[5] A. Louwen, W. van Sark, R. Schropp, and A. Faaij. A cost roadmap for silicon heterojunction solar cells. *Solar Energy Materials and Solar Cells*, 147:295–314, apr 2016. 1

[6] R. B. Jackson, C. Le Quéré, R. M. Andrew, J. G. Canadell, J. I. Korsbakken, Z. Liu, G. P. Peters, and B. Zheng. Global energy growth is outpacing decarbonization. *Environmental Research Letters*, 13(12):120401, dec 2018. 1

[7] A. R. Chakhmouradian and P. M. Woodward. Celebrating 175 years of perovskite research: a tribute to Roger H. Mitchell. *Physics and Chemistry of Minerals*, 41(6):387–391, jun 2014. 1

[8] H. Cho, S.-H. Jeong, M.-H. Park, Y.-H. Kim, C. Wolf, C.-L. Lee, J. H. Heo, A. Sadhanala, N. Myoung, S. Yoo, S. H. Im, R. H. Friend, and T.-W. Lee. Overcoming the electroluminescence efficiency limitations of perovskite light-emitting diodes. *Science*, 350(6265):1222–1225, dec 2015. 1

[9] C. Qin, A. S. D. Sandanayaka, C. Zhao, T. Matsushima, D. Zhang, T. Fujihara, and C. Adachi. Stable room-temperature continuous-wave lasing in quasi-2D perovskite films. *Nature*, 585(7823):53–57, sep 2020. 1

[10] J. Miao and F. Zhang. Recent progress on highly sensitive perovskite photodetectors. *Journal of Materials Chemistry C*, 7(7):1741–1791, 2019. 1

[11] W. Yu, F. Li, L. Yu, M. R. Niazi, Y. Zou, D. Corzo, A. Basu, C. Ma, S. Dey, M. L. Tietze, U. Buttner, X. Wang, Z. Wang, M. N. Hedhili, C. Guo, T. Wu, and A. Amassian. Single crystal hybrid perovskite field-effect transistors. *Nature Communications*, 9(1):5354, dec 2018. 1

[12] J. W. Fergus. Perovskite oxides for semiconductor-based gas sensors. *Sensors and Actuators B: Chemical*, 123(2):1169–1179, may 2007. 1

[13] E. J. Yoo, M. Lyu, J.-H. Yun, C. J. Kang, Y. J. Choi, and L. Wang. Resistive Switching Behavior in Organic-Inorganic Hybrid CH3NH3PbI3-x Clx Perovskite for Resistive Random Access Memory Devices. *Advanced Materials*, 27(40):6170–6175, oct 2015. 1

[14] A. Kojima, K. Teshima, Y. Shirai, and T. Miyasaka. Organometal Halide Perovskites as Visible-Light Sensitizers for Photovoltaic Cells. *Journal of the American Chemical Society*, 131(17):6050–6051, may 2009. 1

[15] J. Jeong, M. Kim, J. Seo, H. Lu, P. Ahlawat, A. Mishra, Y. Yang, M. A. Hope, F. T. Eickemeyer, M. Kim, Y. J. Yoon, I. W. Choi, B. P. Darwich, S. J. Choi, Y. Jo, J. H. Lee, B. Walker, S. M. Zakeeruddin, L. Emsley, U. Rothlisberger, A. Hagfeldt, D. S. Kim, M. Grätzel, and J. Y. Kim. Pseudo-halide anion engineering for α-FAPbI3 perovskite solar cells. *Nature*, 592(7854):381–385, apr 2021. 1

[16] National Renewable Energy Laboratory - Best Research-Cell Efficiency Chart. https://www.nrel.gov/pv/cell-efficiency.html, 2021. 1

[17] A. Szemjonov, K. Galkowski, M. Anaya, Z. Andaji-Garmaroudi, T. K. Baikie, S. Mackowski, I. D. Baikie, S. D. Stranks, and M. S. Islam. Impact of Oxygen on the Electronic Structure of Triple-Cation Halide Perovskites. *ACS Materials Letters*, 1(5):506–510, 2019. 2

[18] M. Grätzel. The Rise of Highly Efficient and Stable Perovskite Solar Cells. *Accounts of Chemical Research*, 50(3):487–491, mar 2017. 2

[19] J.-W. Lee, D.-H. Kim, H.-S. Kim, S.-W. Seo, S. M. Cho, and N.-G. Park. Formamidinium and Cesium Hybridization for Photo- and Moisture-Stable Perovskite Solar Cell. *Advanced Energy Materials*, 5(20):1501310, oct 2015. 2, 38, 46, 48

[20] Z. Li, M. Yang, J.-S. Park, S.-H. Wei, J. J. Berry, and K. Zhu. Stabilizing Perovskite Structures by Tuning Tolerance Factor: Formation of Formamidinium and Cesium Lead Iodide Solid-State Alloys. *Chemistry of Materials*, 28(1):284–292, jan 2016. 2

[21] S. De Wolf, J. Holovsky, S.-J. Moon, P. Löper, B. Niesen, M. Ledinsky, F.-J. Haug, J.-H. Yum, and C. Ballif. Organometallic Halide Perovskites: Sharp Optical Absorption Edge and Its Relation to Photovoltaic Performance. *The Journal of Physical Chemistry Letters*, 5(6):1035–1039, mar 2014. 2, 44

[22] S. Liu, L. Wang, W.-C. Lin, S. Sucharitakul, C. Burda, and X. P. A. Gao. Imaging the Long Transport Lengths of Photo-generated Carriers in Oriented Perovskite Films. *Nano Letters*, 16(12):7925–7929, dec 2016. 2

[23] A. Miyata, A. Mitioglu, P. Plochocka, O. Portugall, J. T.-W. Wang, S. D. Stranks, H. J. Snaith, and R. J. Nicholas. Direct measurement of the exciton binding energy and effective masses for charge carriers in organic–inorganic tri-halide perovskites. *Nature Physics*, 11(7):582–587, jul 2015. 2

[24] E. L. Unger, L. Kegelmann, K. Suchan, D. Sörell, L. Korte, and S. Albrecht. Roadmap and roadblocks for the band gap tunability of metal halide perovskites. *Journal of Materials Chemistry A*, 5(23):11401–11409, 2017. 2, 27

[25] N. K. Kumawat, A. Dey, A. Kumar, S. P. Gopinathan, K. L. Narasimhan, and D. Kabra. Band Gap Tuning of CH3NH3Pb(Br1xClx)3 Hybrid Perovskite for Blue Electroluminescence. *ACS Applied Materials & Interfaces*, 7(24):13119–13124, jun 2015. 2

[26] F. Di Giacomo, A. Fakharuddin, R. Jose, and T. M. Brown. Progress, challenges and perspectives in flexible perovskite solar cells. *Energy & Environmental Science*, 9(10):3007–3035, 2016. 2

[27] K. Hwang, Y.-S. Jung, Y.-J. Heo, F. H. Scholes, S. E. Watkins, J. Subbiah, D. J. Jones, D.-Y. Kim, and D. Vak. Toward Large Scale Roll-to-Roll Production of Fully Printed Perovskite Solar Cells. *Advanced Materials*, 27(7):1241–1247, feb 2015. 2

[28] L. Meng, J. You, and Y. Yang. Addressing the stability issue of perovskite solar cells for commercial applications. *Nature Communications*, 9(1):5265, dec 2018. 3

[29] Z. Wang, Z. Shi, T. Li, Y. Chen, and W. Huang. Stability of Perovskite Solar Cells: A Prospective on the Substitution of the A Cation and X Anion. *Angewandte Chemie International Edition*, 56(5):1190–1212, jan 2017. 3, 12

[30] S. Pont, D. Bryant, C.-T. Lin, N. Aristidou, S. Wheeler, X. Ma, R. Godin, S. A. Haque, and J. R. Durrant. Tuning CH3NH3Pb(I1-xBrx)3 perovskite oxygen stability in thin films and solar cells. *Journal of Materials Chemistry A*, 5(20):9553–9560, 2017. 3

[31] J. H. Noh, S. H. Im, J. H. Heo, T. N. Mandal, and S. I. Seok. Chemical Management for Colorful, Efficient, and Stable Inorganic–Organic Hybrid Nanostructured Solar Cells. *Nano Letters*, 13(4):1764–1769, apr 2013. 3

[32] A. Aziz, N. Aristidou, X. Bu, R. J. E. Westbrook, S. A. Haque, and M. S. Islam. Understanding the Enhanced Stability of Bromide Substitution in Lead Iodide Perovskites. *Chemistry of Materials*, 32(1):400–409, jan 2020. 3

[33] L. Atourki, E. Vega, M. Mollar, B. Marí, H. Kirou, K. Bouabid, and A. Ihlal. Impact of iodide substitution on the physical properties and stability of cesium lead halide perovskite thin films CsPbBr3-xIx (0 < x < 1). *Journal of Alloys and Compounds*, 702:404–409, apr 2017. 3

[34] D.-Y. Son, S.-G. Kim, J.-Y. Seo, S.-H. Lee, H. Shin, D. Lee, and N.-G. Park. Universal Approach toward Hysteresis-Free Perovskite Solar Cell via Defect Engineering. *Journal of the American Chemical Society*, 140(4):1358–1364, jan 2018. 3, 33

[35] D. B. Khadka, Y. Shirai, M. Yanagida, and K. Miyano. Attenuating the defect activities with a rubidium additive for efficient and stable Sn-based halide perovskite solar cells. *Journal of Materials Chemistry C*, 8(7):2307–2313, 2020. 3

[36] A. Albadri, P. Yadav, M. Alotaibi, N. Arora, A. Alyamani, H. Albrithen, M. I. Dar, S. M. Zakeeruddin, and M. Grätzel. Unraveling the Impact of Rubidium Incorporation on the Transport-Recombination Mechanisms in Highly Efficient Perovskite Solar Cells by Small-Perturbation Techniques. *The Journal of Physical Chemistry C*, 121(45):24903–24908, nov 2017. 3

[37] C. Li, A. Wang, L. Xie, X. Deng, K. Liao, J.-a. Yang, T. Li, and F. Hao. Emerging alkali metal ion (Li + , Na + , K + and Rb +) doped perovskite films for efficient solar cells: recent advances and prospects. *Journal of Materials Chemistry A*, 7(42):24150–24163, 2019. 3

[38] C. Liu, J. Sun, W. L. Tan, J. Lu, T. R. Gengenbach, C. R. McNeill, Z. Ge, Y.-B. Cheng, and U. Bach. Alkali Cation Doping for Improving the Structural Stability of 2D Perovskite in 3D/2D PSCs. *Nano Letters*, 20(2):1240–1251, feb 2020. 3, 33

[39] Q. Xue, R. Xia, C. J. Brabec, and H.-L. Yip. Recent advances in semi-transparent polymer and perovskite solar cells for power generating window applications. *Energy & Environmental Science*, 11(7):1688–1709, 2018. 4

[40] D. Kiermasch. *Charge Carrier Recombination Dynamics in Hybrid Metal Halide Perovskite Solar Cells*. PhD thesis, Julius-Maximilians-Universität Würzburg, 2020. 6, 9

[41] K. McIntosh. *Lumps, humps and bumps : three detrimental effects in the current-voltage curve of silicon solar cells*. PhD thesis, University of New South Wales, New South Wales, 2001. 6

[42] X. Zhang, J. Shen, and C. G. Van de Walle. First-Principles Simulation of Carrier Recombination Mechanisms in Halide Perovskites. *Advanced Energy Materials*, 10(13):1902830, apr 2020. 7, 33, 34

[43] J. M. Ball and A. Petrozza. Defects in perovskite-halides and their effects in solar cells. *Nature Energy*, 1(11):16149, nov 2016. 7, 36

[44] L. M. Pazos-Outon, M. Szumilo, R. Lamboll, J. M. Richter, M. Crespo-Quesada, M. Abdi-Jalebi, H. J. Beeson, M. Vru ini, M. Alsari, H. J. Snaith, B. Ehrler, R. H. Friend, and F. Deschler. Photon recycling in lead iodide perovskite solar cells. *Science*, 351(6280):1430–1433, mar 2016. 7

[45] L. M. Herz. Charge-Carrier Dynamics in Organic-Inorganic Metal Halide Perovskites. *Annual Review of Physical Chemistry*, 67(1):65–89, may 2016. 7, 34, 36

[46] H. J. Snaith, A. Abate, J. M. Ball, G. E. Eperon, T. Leijtens, N. K. Noel, S. D. Stranks, J. T.-W. Wang, K. Wojciechowski, and W. Zhang. Anomalous Hysteresis in Perovskite Solar Cells. *The Journal of Physical Chemistry Letters*, 5(9):1511–1515, may 2014. 8

[47] B. Chen, M. Yang, S. Priya, and K. Zhu. Origin of J-V Hysteresis in Perovskite Solar Cells. *The Journal of Physical Chemistry Letters*, 7(5):905–917, mar 2016. 8

[48] P. Liu, W. Wang, S. Liu, H. Yang, and Z. Shao. Fundamental Understanding of Photocurrent Hysteresis in Perovskite Solar Cells. *Advanced Energy Materials*, 9(13):1803017, apr 2019. 8

[49] W. Tress, N. Marinova, T. Moehl, S. M. Zakeeruddin, M. K. Nazeeruddin, and M. Grätzel. Understanding the rate-dependent J–V hysteresis, slow time component, and aging in CH3NH3PbI3 perovskite solar cells: the role of a compensated electric field. *Energy & Environmental Science*, 8(3):995–1004, 2015. 8, 69

[50] G. Nemnes, C. Besleaga, A. Tomulescu, I. Pintilie, L. Pintilie, K. Torfason, and A. Manolescu. Dynamic electrical behavior of halide perovskite based solar cells. *Solar Energy Materials and Solar Cells*, 159:197–203, jan 2017. 8

[51] I. Levine, P. K. Nayak, J. T.-W. Wang, N. Sakai, S. Van Reenen, T. M. Brenner, S. Mukhopadhyay, H. J. Snaith, G. Hodes, and D. Cahen. Interface-Dependent Ion Migration/Accumulation Controls Hysteresis in MAPbI3 Solar Cells. *The Journal of Physical Chemistry C*, 120(30):16399–16411, aug 2016. 8

[52] E. L. Unger, E. T. Hoke, C. D. Bailie, W. H. Nguyen, A. R. Bowring, T. Heumüller, M. G. Christoforo, and M. D. McGehee. Hysteresis and transient behavior in current–voltage measurements of hybrid-perovskite absorber solar cells. *Energy Environ. Sci.*, 7(11):3690–3698, 2014. 8

[53] L. K. Ono, S. R. Raga, S. Wang, Y. Kato, and Y. Qi. Temperature-dependent hysteresis effects in perovskite-based solar cells. *Journal of Materials Chemistry A*, 3(17):9074–9080, 2015. 8

[54] N. J. Jeon, J. H. Noh, Y. C. Kim, W. S. Yang, S. Ryu, and S. I. Seok. Solvent engineering for high-performance inorganic–organic hybrid perovskite solar cells. *Nature Materials*, 13(9):897–903, sep 2014. 8

[55] K. Wojciechowski, S. D. Stranks, A. Abate, G. Sadoughi, A. Sadhanala, N. Kopidakis, G. Rumbles, C.-z. Li, R. H. Friend, A. K. Jen, and H. J. Snaith. Heterojunction Modification for Highly Solar Cells. *ACS nano*, 8(12):12701–12709, 2014. 8

[56] T. Bu, X. Liu, Y. Zhou, J. Yi, X. Huang, L. Luo, J. Xiao, Z. Ku, Y. Peng, F. Huang, Y. B. Cheng, and J. Zhong. A novel quadruple-cation absorber for universal hysteresis elimination for high efficiency and stable perovskite solar cells. *Energy and Environmental Science*, 10(12):2509–2515, 2017. 8

[57] O. Almora, I. Zarazua, E. Mas-Marza, I. Mora-Sero, J. Bisquert, and G. Garcia-Belmonte. Capacitive Dark Currents, Hysteresis, and Electrode Polarization in Lead Halide Perovskite Solar Cells. *The Journal of Physical Chemistry Letters*, 6(9):1645–1652, may 2015. 8

[58] R. S. Sanchez, V. Gonzalez-Pedro, J.-W. Lee, N.-G. Park, Y. S. Kang, I. Mora-Sero, and J. Bisquert. Slow Dynamic Processes in Lead Halide Perovskite Solar Cells. Characteristic Times and Hysteresis. *The Journal of Physical Chemistry Letters*, 5(13):2357–2363, jul 2014. 8

[59] H.-W. Chen, N. Sakai, M. Ikegami, and T. Miyasaka. Emergence of Hysteresis and Transient Ferroelectric Response in Organo-Lead Halide Perovskite Solar Cells. *The Journal of Physical Chemistry Letters*, 6(1):164–169, jan 2015. 8

[60] J. M. Frost, K. T. Butler, and A. Walsh. Molecular ferroelectric contributions to anomalous hysteresis in hybrid perovskite solar cells. *APL Materials*, 2(8):081506, aug 2014. 8

[61] Y. Shao, Z. Xiao, C. Bi, Y. Yuan, and J. Huang. Origin and elimination of photocurrent hysteresis by fullerene passivation in CH3NH3PbI3 planar heterojunction solar cells. *Nature Communications*, 5(1):5784, dec 2014. 8

[62] H. Zhang, C. Liang, Y. Zhao, M. Sun, H. Liu, J. Liang, D. Li, F. Zhang, and Z. He. Dynamic interface charge governing the current–voltage hysteresis in perovskite solar cells. *Physical Chemistry Chemical Physics*, 17(15):9613–9618, 2015. 8, 12

[63] C. Eames, J. M. Frost, P. R. F. Barnes, B. C. O'Regan, A. Walsh, and M. S. Islam. Ionic transport in hybrid lead iodide perovskite solar cells. *Nature Communications*, 6(1):7497, nov 2015. 8

[64] M. De Bastiani, G. Dell'Erba, M. Gandini, V. D'Innocenzo, S. Neutzner, A. R. S. Kandada, G. Grancini, M. Binda, M. Prato, J. M. Ball, M. Caironi, and A. Petrozza. Ion Migration and the Role of Preconditioning Cycles in the Stabilization of the J - V Characteristics of Inverted Hybrid Perovskite Solar Cells. *Advanced Energy Materials*, 6(2):1501453, jan 2016. 8, 13

[65] S. Meloni, T. Moehl, W. Tress, M. Franckevičius, M. Saliba, Y. H. Lee, P. Gao, M. K. Nazeeruddin, S. M. Zakeeruddin, U. Rothlisberger, and M. Graetzel. Ionic polarization-induced current–voltage hysteresis in CH3NH3PbX3 perovskite solar cells. *Nature Communications*, 7(1):10334, apr 2016. 8

[66] J. MIZUSAKI, K. ARAI, and K. FUEKI. Ionic conduction of the perovskite-type halides. *Solid State Ionics*, 11(3):203–211, nov 1983. 8

[67] Y.-C. Zhao, W.-K. Zhou, X. Zhou, K.-H. Liu, D.-P. Yu, and Q. Zhao. Quantification of light-enhanced ionic transport in lead iodide perovskite thin films and its solar cell applications. *Light: Science & Applications*, 6(5):e16243–e16243, may 2017. 8

[68] R. A. Belisle, W. H. Nguyen, A. R. Bowring, P. Calado, X. Li, S. J. C. Irvine, M. D. McGehee, P. R. F. Barnes, and B. C. O'Regan. Interpretation of inverted photocurrent transients in organic lead halide perovskite solar cells: proof of the field screening by mobile ions and determination of the space charge layer widths. *Energy & Environmental Science*, 10(1):192–204, 2017. 9, 88

[69] S. N. Habisreutinger, N. K. Noel, and H. J. Snaith. Hysteresis Index: A Figure without Merit for Quantifying Hysteresis in Perovskite Solar Cells. *ACS Energy Letters*, 3(10):2472–2476, oct 2018. 9

[70] N. K. Elumalai and A. Uddin. Hysteresis in organic-inorganic hybrid perovskite solar cells. *Solar Energy Materials and Solar Cells*, 157:476–509, dec 2016. 9

[71] Z. Tang, T. Bessho, F. Awai, T. Kinoshita, M. M. Maitani, R. Jono, T. N. Murakami, H. Wang, T. Kubo, S. Uchida, and H. Segawa. Hysteresis-free perovskite solar cells made of potassium-doped organometal halide perovskite. *Scientific Reports*, 7(1):12183, dec 2017. 9, 33

[72] J. Cao, S. X. Tao, P. A. Bobbert, C.-P. Wong, and N. Zhao. Interstitial Occupancy by Extrinsic Alkali Cations in Perovskites and Its Impact on Ion Migration. *Advanced Materials*, 30(26):1707350, jun 2018. 9

[73] M. T. Neukom, S. Züfle, E. Knapp, M. Makha, R. Hany, and B. Ruhstaller. Why perovskite solar cells with high efficiency show small IV-curve hysteresis. *Solar Energy Materials and Solar Cells*, 169(May):159–166, sep 2017. 9

[74] P. Calado, A. M. Telford, D. Bryant, X. Li, J. Nelson, B. C. O'Regan, and P. R. Barnes. Evidence for ion migration in hybrid perovskite solar cells with minimal hysteresis. *Nature Communications*, 7(1):13831, dec 2016. 9, 88, 90

[75] W. Tress. Metal Halide Perovskites as Mixed Electronic-Ionic Conductors: Challenges and Opportunities-From Hysteresis to Memristivity. *The Journal of Physical Chemistry Letters*, 8(13):3106–3114, jul 2017. 9, 13

[76] L. J. Koster, V. D. Mihailetchi, R. Ramaker, and P. W. Blom. Light intensity dependence of open-circuit voltage of polymer:fullerene solar cells. *Applied Physics Letters*, 86(12):1–3, 2005. 9

[77] N. K. Elumalai and A. Uddin. Open circuit voltage of organic solar cells: an in-depth review. *Energy & Environmental Science*, 9(2):391–410, 2016. 9

[78] P. Hartnagel and T. Kirchartz. Understanding the Light-Intensity Dependence of the Short-Circuit Current of Organic Solar Cells. *Advanced Theory and Simulations*, 3(10):2000116, oct 2020. 9, 11, 12

[79] J. Nelson. *The Physics of Solar Cells*. Imperial College Press, may 2003. 10, 35

[80] O. Almora, K. T. Cho, S. Aghazada, I. Zimmermann, G. J. Matt, C. J. Brabec, M. K. Nazeeruddin, and G. Garcia-Belmonte. Discerning recombination mechanisms and ideality factors through impedance analysis of high-efficiency perovskite solar cells. *Nano Energy*, 48(February):63–72, jun 2018. 10, 11

[81] H. D. Kim, H. Ohkita, H. Benten, and S. Ito. Photovoltaic Performance of Perovskite Solar Cells with Different Grain Sizes. *Advanced Materials*, 28(5):917–922, feb 2016. 10

[82] T. Singh and T. Miyasaka. Stabilizing the Efficiency Beyond 20% with a Mixed Cation Perovskite Solar Cell Fabricated in Ambient Air under Controlled Humidity. *Advanced Energy Materials*, 8(3):1700677, jan 2018. 10, 12

[83] D. Yang, X. Zhou, R. Yang, Z. Yang, W. Yu, X. Wang, C. Li, S. F. Liu, and R. P. H. Chang. Surface optimization to eliminate hysteresis for record efficiency planar perovskite solar cells. *Energy & Environmental Science*, 9(10):3071–3078, 2016. 10, 11

[84] Y. Yang, H. Peng, C. Liu, Z. Arain, Y. Ding, S. Ma, X. Liu, T. Hayat, A. Alsaedi, and S. Dai. Bi-functional additive engineering for high-performance perovskite solar cells with reduced trap density. *Journal of Materials Chemistry A*, 7(11):6450–6458, 2019. 10

[85] V. Srivastava, S. H. Reddy, M. Mohan, B. Anitha, B. Adara, and M. A. G. Namboothiry. Study on the defect density of states in light soaking effect enhanced performance of perovskite solar cells. *Journal of Physics D: Applied Physics*, 52(26):265302, jun 2019. 10, 13

[86] P. Caprioglio, C. M. Wolff, O. J. Sandberg, A. Armin, B. Rech, S. Albrecht, D. Neher, and M. Stolterfoht. On the Origin of the Ideality Factor in Perovskite Solar Cells. *Advanced Energy Materials*, 10(27):2000502, jul 2020. 10, 30, 31, 32, 35, 53, 60, 63, 64, 65

[87] P. Calado, D. Burkitt, J. Yao, J. Troughton, T. M. Watson, M. J. Carnie, A. M. Telford, B. C. O'Regan, J. Nelson, and P. R. Barnes. Identifying Dominant Recombination Mechanisms in Perovskite Solar Cells by Measuring the Transient Ideality Factor. *Physical Review Applied*, 11(4):044005, apr 2019. 10, 11, 65

[88] M. Bashahu and P. Nkundabakura. Review and tests of methods for the determination of the solar cell junction ideality factors. *Solar Energy*, 81(7):856–863, 2007. 10

[89] W. Tress, M. Yavari, K. Domanski, P. Yadav, B. Niesen, J. P. Correa Baena, A. Hagfeldt, and M. Graetzel. Interpretation and evolution of open-circuit voltage, recombination, ideality factor and subgap defect states during reversible light-soaking and irreversible degradation of perovskite solar cells. *Energy & Environmental Science*, 11(1):151–165, 2018. 10, 11, 13

[90] K. Tvingstedt, L. Gil-Escrig, C. Momblona, P. Rieder, D. Kiermasch, M. Sessolo, A. Baumann, H. J. Bolink, and V. Dyakonov. Removing Leakage and Surface Recombination in Planar Perovskite Solar Cells. *ACS Energy Letters*, 2(2):424–430, feb 2017. 10, 11

[91] N. Courtier. Interpreting Ideality Factors for Planar Perovskite Solar Cells: Ectypal Diode Theory for Steady-State Operation. *Physical Review Applied*, 14(2):024031, aug 2020. 10

[92] G.-J. A. H. Wetzelaer, M. Scheepers, A. M. Sempere, C. Momblona, J. Ávila, and H. J. Bolink. Trap-Assisted Non-Radiative Recombination in Organic-Inorganic Perovskite Solar Cells. *Advanced Materials*, 27(11):1837–1841, mar 2015. 11

[93] D. Kiermasch, L. Gil-Escrig, A. Baumann, H. J. Bolink, V. Dyakonov, and K. Tvingstedt. Unravelling steady-state bulk recombination dynamics in thick efficient vacuum-deposited perovskite solar cells by transient methods. *Journal of Materials Chemistry A*, 7(24):14712–14722, 2019. 11

[94] V. M. Le Corre, T. S. Sherkar, M. Koopmans, and L. J. A. Koster. Identification of the dominant recombination process for perovskite solar cells based on machine learning. *Cell Reports Physical Science*, 2(2):100346, feb 2021. 11

[95] P. Schilinsky, C. Waldauf, and C. J. Brabec. Recombination and loss analysis in polythiophene based bulk heterojunction photodetectors. *Applied Physics Letters*, 81(20):3885–3887, nov 2002. 11

[96] J. K. J. van Duren, X. Yang, J. Loos, C. W. T. Bulle-Lieuwma, A. B. Sieval, J. C. Hummelen, and R. A. J. Janssen. Relating the Morphology of Poly(p-phenylene vinylene)/Methanofullerene Blends to Solar-Cell Performance. *Advanced Functional Materials*, 14(5):425–434, may 2004. 11

[97] I. Riedel, J. Parisi, V. Dyakonov, L. Lutsen, D. Vanderzande, and J. C. Hummelen. Effect of Temperature and Illumination on the Electrical Characteristics of Polymer–Fullerene Bulk-Heterojunction Solar Cells. *Advanced Functional Materials*, 14(1):38–44, jan 2004. 11

[98] D. Lee, J. Kim, G. Park, H. W. Bae, M. An, and J. Y. Kim. Enhanced Operating Temperature Stability of Organic Solar Cells with Metal Oxide Hole Extraction Layer. *Polymers*, 12(4):992, apr 2020. 11

[99] J. Troughton, N. Gasparini, and D. Baran. Cs0.15FA0.85PbI3 perovskite solar cells for concentrator photovoltaic applications. *Journal of Materials Chemistry A*, 6(44):21913–21917, 2018. 11, 13, 49, 71

[100] Y. Cheng, H.-W. Li, J. Qing, Q.-D. Yang, Z. Guan, C. Liu, S. H. Cheung, S. K. So, C.-S. Lee, and S.-W. Tsang. The detrimental effect of excess mobile ions in planar CH3NH3PbI3 perovskite solar cells. *Journal of Materials Chemistry A*, 4(33):12748–12755, 2016. 11

[101] C. Deibel and A. Wagenpfahl. Comment on "Interface state recombination in organic solar cells". *Physical Review B*, 82(20):207301, nov 2010. 11

[102] J. Chen and N. Park. Causes and Solutions of Recombination in Perovskite Solar Cells. *Advanced Materials*, 31(47):1803019, nov 2019. 11

[103] T. S. Sherkar, C. Momblona, L. Gil-Escrig, J. Ávila, M. Sessolo, H. J. Bolink, and L. J. A. Koster. Recombination in Perovskite Solar Cells: Significance of Grain Boundaries, Interface Traps, and Defect Ions. *ACS Energy Letters*, 2(5):1214–1222, may 2017. 11, 26, 34, 36

[104] V. D. Mihailetchi. *Device physics of organic bulk heterojunction solar cells*. PhD thesis, 2005. 12, 32

[105] T. Tong, X. Li, S. Guo, J. Han, and B. Wei. Sequential solvent processing with hole transport materials for improving efficiency of traditionally-structured perovskite solar cells. *Nano Energy*, 41(October):591–599, nov 2017. 12

[106] T. Liu, Z. Wang, L. Lou, S. Xiao, S. Zheng, and S. Yang. Interfacial Post-Treatment for Enhancing the Performance of Printable Carbon-Based Perovskite Solar Cells. *Solar RRL*, 4(2):1900278, feb 2020. 12

[107] Y. Wang, T. Mahmoudi, and Y. Hahn. Highly stable and Efficient Perovskite Solar Cells Based on FAMA-Perovskite-Cu:NiO Composites with 20.7% Efficiency and 80.5% Fill Factor. *Advanced Energy Materials*, 10(27):2000967, jul 2020. 12, 49

[108] Y. Yu, C. Wang, C. R. Grice, N. Shrestha, J. Chen, D. Zhao, W. Liao, A. J. Cimaroli, P. J. Roland, R. J. Ellingson, and Y. Yan. Improving the Performance of Formamidinium and Cesium Lead Triiodide Perovskite Solar Cells using Lead Thiocyanate Additives. *ChemSusChem*, 9(23):3288–3297, dec 2016. 12, 47

[109] D. Zhao, M. Sexton, H.-Y. Park, G. Baure, J. C. Nino, and F. So. High-Efficiency Solution-Processed Planar Perovskite Solar Cells with a Polymer Hole Transport Layer. *Advanced Energy Materials*, 5(6):1401855, mar 2015. 12

[110] X. Zheng, B. Chen, M. Yang, C. Wu, B. Orler, R. B. Moore, K. Zhu, and S. Priya. The Controlling Mechanism for Potential Loss in CH3NH3PbBr3 Hybrid Solar Cells. *ACS Energy Letters*, 1(2):424–430, aug 2016. 12

[111] L. J. A. Koster, V. D. Mihailetchi, H. Xie, and P. W. M. Blom. Origin of the light intensity dependence of the short-circuit current of polymer/fullerene solar cells. *Applied Physics Letters*, 87(20):203502, nov 2005. 12

[112] B. Maynard, Q. Long, E. A. Schiff, M. Yang, K. Zhu, R. Kottokkaran, H. Abbas, and V. L. Dalal. Electron and hole drift mobility measurements on methylammonium lead iodide perovskite solar cells. *Applied Physics Letters*, 108(17):173505, apr 2016. 12

[113] Y. Chen, J. Peng, D. Su, X. Chen, and Z. Liang. Efficient and Balanced Charge Transport Revealed in Planar Perovskite Solar Cells. *ACS Applied Materials & Interfaces*, 7(8):4471–4475, mar 2015. 12

[114] G. Y. Kim, A. Senocrate, D. Moia, and J. Maier. Ionically Generated Built-In Equilibrium Space Charge Zones-a Paradigm Change for Lead Halide Perovskite Interfaces. *Advanced Functional Materials*, 30(31):2002426, aug 2020. 12

[115] V. W. Bergmann, Y. Guo, H. Tanaka, I. M. Hermes, D. Li, A. Klasen, S. A. Bretschneider, E. Nakamura, R. Berger, and S. A. L. Weber. Local Time-Dependent Charging in a Perovskite Solar Cell. *ACS Applied Materials & Interfaces*, 8(30):19402–19409, aug 2016. 12

[116] A. K. K. Kyaw, D. H. Wang, V. Gupta, W. L. Leong, L. Ke, G. C. Bazan, and A. J. Heeger. Intensity Dependence of Current–Voltage Characteristics and Recombination in High-Efficiency Solution-Processed Small-Molecule Solar Cells. *ACS Nano*, 7(5):4569–4577, may 2013. 12

[117] W. Yan, Y. Li, Y. Li, S. Ye, Z. Liu, S. Wang, Z. Bian, and C. Huang. Stable high-performance hybrid perovskite solar cells with ultrathin polythiophene as hole-transporting layer. *Nano Research*, 8(8):2474–2480, 2015. 12

[118] A. R. B. Mohd Yusoff, M. A. Mat Teridi, and J. Jang. Null current hysteresis for acetylacetonate electron extraction layer in perovskite solar cells. *Nanoscale*, 8(12):6328–6334, 2016. 12

[119] M. Asghar, J. Zhang, H. Wang, and P. Lund. Device stability of perovskite solar cells - A review. *Renewable and Sustainable Energy Reviews*, 77(February):131–146, sep 2017. 12

[120] C. C. Boyd, R. Cheacharoen, T. Leijtens, and M. D. McGehee. Understanding Degradation Mechanisms and Improving Stability of Perovskite Photovoltaics. *Chemical Reviews*, 119(5):3418–3451, mar 2019. 12

[121] S. Kundu and T. L. Kelly. In situ studies of the degradation mechanisms of perovskite solar cells. *EcoMat*, 2(2):1–22, jun 2020. 12

[122] T. Leijtens, K. Bush, R. Cheacharoen, R. Beal, A. Bowring, and M. D. McGehee. Towards enabling stable lead halide perovskite solar cells; interplay between structural, environmental, and thermal stability. *Journal of Materials Chemistry A*, 5(23):11483–11500, 2017. 12

[123] L. K. Ono, Y. Qi, and S. F. Liu. Progress toward Stable Lead Halide Perovskite Solar Cells. *Joule*, 2(10):1961–1990, oct 2018. 12

[124] P. Roy, N. Kumar Sinha, S. Tiwari, and A. Khare. A review on perovskite solar cells: Evolution of architecture, fabrication techniques, commercialization issues and status. *Solar Energy*, 198(December 2019):665–688, mar 2020. 12

[125] B. Salhi, Y. Wudil, M. Hossain, A. Al-Ahmed, and F. Al-Sulaiman. Review of recent developments and persistent challenges in stability of perovskite solar cells. *Renewable and Sustainable Energy Reviews*, 90(February 2017):210–222, jul 2018. 12

[126] F. Matteocci, L. Cinà, E. Lamanna, S. Cacovich, G. Divitini, P. A. Midgley, C. Ducati, and A. Di Carlo. Encapsulation for long-term stability enhancement of perovskite solar cells. *Nano Energy*, 30(September):162–172, dec 2016. 12

[127] R. Cheacharoen, C. C. Boyd, G. F. Burkhard, T. Leijtens, J. A. Raiford, K. A. Bush, S. F. Bent, and M. D. McGehee. Encapsulating perovskite solar cells to withstand damp heat and thermal cycling. *Sustainable Energy & Fuels*, 2(11):2398–2406, 2018. 12

[128] K. Wang, C. Liu, P. Du, J. Zheng, and X. Gong. Bulk heterojunction perovskite hybrid solar cells with large fill factor. *Energy & Environmental Science*, 8(4):1245–1255, 2015. 12, 28

[129] D. Yang, Z. Yang, W. Qin, Y. Zhang, S. F. Liu, and C. Li. Alternating precursor layer deposition for highly stable perovskite films towards efficient solar cells using vacuum deposition. *Journal of Materials Chemistry A*, 3(18):9401–9405, 2015. 12

[130] S. Seo, S. Jeong, H. Park, H. Shin, and N.-G. Park. Atomic layer deposition for efficient and stable perovskite solar cells. *Chemical Communications*, 55(17):2403–2416, 2019. 12

[131] S. Guarnera, A. Abate, W. Zhang, J. M. Foster, G. Richardson, A. Petrozza, and H. J. Snaith. Improving the Long-Term Stability of Perovskite Solar Cells with a Porous Al 2 O 3 Buffer Layer. *The Journal of Physical Chemistry Letters*, 6(3):432–437, feb 2015. 12

[132] J. Kim, A. Ho-Baillie, and S. Huang. Review of Novel Passivation Techniques for Efficient and Stable Perovskite Solar Cells. *Solar RRL*, 3(4):1800302, apr 2019. 12

[133] H. Tan, A. Jain, O. Voznyy, X. Lan, F. P. García de Arquer, J. Z. Fan, R. Quintero-Bermudez, M. Yuan, B. Zhang, Y. Zhao, F. Fan, P. Li, L. N. Quan, Y. Zhao, Z.-H. Lu, Z. Yang, S. Hoogland, and E. H. Sargent. Efficient and stable solution-processed planar perovskite solar cells via contact passivation. *Science*, 355(6326):722–726, feb 2017. 12

[134] C. L. Watts, L. Aspitarte, Y.-H. Lin, W. Li, R. Elzein, R. Addou, M. J. Hong, G. S. Herman, H. J. Snaith, and J. G. Labram. Light soaking in metal halide perovskites studied via steady-state microwave conductivity. *Communications Physics*, 3(1):73, dec 2020. 13

[135] D. W. DeQuilettes, W. Zhang, V. M. Burlakov, D. J. Graham, T. Leijtens, A. Osherov, V. Bulović, H. J. Snaith, D. S. Ginger, and S. D. Stranks. Photo-induced halide redistribution in organic–inorganic perovskite films. *Nature Communications*, 7(1):11683, sep 2016. 13

[136] E. Mosconi, D. Meggiolaro, H. J. Snaith, S. D. Stranks, and F. De Angelis. Light-induced annihilation of Frenkel defects in organo-lead halide perovskites. *Energy & Environmental Science*, 9(10):3180–3187, 2016. 13

[137] G. Liu, B. Yang, B. Liu, C. Zhang, S. Xiao, Y. Yuan, H. Xie, D. Niu, J. Yang, Y. Gao, and C. Zhou. Irreversible light-soaking effect of perovskite solar cells caused by light-induced oxygen vacancies in titanium oxide. *Applied Physics Letters*, 111(15):153501, oct 2017. 13

[138] S. Shao, M. Abdu-Aguye, T. S. Sherkar, H.-H. Fang, S. Adjokatse, G. ten Brink, B. J. Kooi, L. J. A. Koster, and M. A. Loi. The Effect of the Microstructure on Trap-Assisted Recombination and Light Soaking Phenomenon in Hybrid Perovskite Solar Cells. *Advanced Functional Materials*, 26(44):8094–8102, nov 2016. 13

[139] S. Shao, M. Abdu-Aguye, L. Qiu, L.-H. Lai, J. Liu, S. Adjokatse, F. Jahani, M. E. Kamminga, G. H. ten Brink, T. T. M. Palstra, B. J. Kooi, J. C. Hummelen, and M. Antonietta Loi. Elimination of the light soaking effect and performance enhancement in perovskite solar cells using a fullerene derivative. *Energy & Environmental Science*, 9(7):2444–2452, 2016. 13, 30

[140] H. Tsai, R. Asadpour, J.-C. Blancon, C. C. Stoumpos, O. Durand, J. W. Strzalka, B. Chen, R. Verduzco, P. M. Ajayan, S. Tretiak, J. Even, M. A. Alam, M. G. Kanatzidis, W. Nie, and A. D. Mohite. Light-induced lattice expansion leads to high-efficiency perovskite solar cells. *Science*, 360(6384):67–70, apr 2018. 13

[141] T. Zhang, S. H. Cheung, X. Meng, L. Zhu, Y. Bai, C. H. Y. Ho, S. Xiao, Q. Xue, S. K. So, and S. Yang. Pinning Down the Anomalous Light Soaking Effect toward High-Performance and Fast-Response Perovskite Solar Cells: The Ion-Migration-Induced Charge Accumulation. *The Journal of Physical Chemistry Letters*, 8(20):5069–5076, oct 2017. 13

[142] C. Zhao, B. Chen, X. Qiao, L. Luan, K. Lu, and B. Hu. Revealing Underlying Processes Involved in Light Soaking Effects and Hysteresis Phenomena in Perovskite Solar Cells. *Advanced Energy Materials*, 5(14):1500279, jul 2015. 13

[143] A. F. Akbulatov, M. I. Ustinova, L. Gutsev, S. A. Tsarev, N. N. Dremova, I. Zhidkov, S. Y. Luchkin, B. R. Ramachandran, L. Frolova, E. Z. Kurmaev, K. J. Stevenson, S. M. Aldoshin, and P. A. Troshin. When iodide meets bromide: Halide mixing facilitates the light-induced decomposition of perovskite absorber films. *Nano Energy*, 86:106082, aug 2021. 13

[144] C. Awino, G. Barasa, and V. Odari. Light induced degradation of the transport length of CH3NH3PbI3 studied by modulated surface photovoltage spectroscopy after Goodman. *Organic Electronics*, 77:105503, feb 2020. 13

[145] S. Draguta, O. Sharia, S. J. Yoon, M. C. Brennan, Y. V. Morozov, J. S. Manser, P. V. Kamat, W. F. Schneider, and M. Kuno. Rationalizing the light-induced phase separation of mixed halide organic–inorganic perovskites. *Nature Communications*, 8(1):200, dec 2017. 13

[146] Y. Liu, C. Xie, W. Tan, X. Liu, Y. Yuan, Q. Xie, Y. Li, and Y. Gao. Analysis of light-induced degradation in inverted perovskite solar cells under short-circuited conditions. *Organic Electronics*, 71(February):123–130, aug 2019. 13

[147] S. G. Motti, M. Gandini, A. J. Barker, J. M. Ball, A. R. Srimath Kandada, and A. Petrozza. Photoinduced Emissive Trap States in Lead Halide Perovskite Semiconductors. *ACS Energy Letters*, 1(4):726–730, oct 2016. 13

[148] K. Domanski, B. Roose, T. Matsui, M. Saliba, S.-H. Turren-Cruz, J.-P. Correa-Baena, C. R. Carmona, G. Richardson, J. M. Foster, F. De Angelis, J. M. Ball, A. Petrozza, N. Mine, M. K. Nazeeruddin, W. Tress, M. Grätzel, U. Steiner, A. Hagfeldt, and A. Abate. Migration of cations induces reversible performance losses over day/night cycling in perovskite solar cells. *Energy & Environmental Science*, 10(2):604–613, 2017. 13, 90

[149] K. Domanski, E. A. Alharbi, A. Hagfeldt, M. Grätzel, and W. Tress. Systematic investigation of the impact of operation conditions on the degradation behaviour of perovskite solar cells. *Nature Energy*, 3(1):61–67, jan 2018. 13

[150] W. Nie, J.-C. Blancon, A. J. Neukirch, K. Appavoo, H. Tsai, M. Chhowalla, M. A. Alam, M. Y. Sfeir, C. Katan, J. Even, S. Tretiak, J. J. Crochet, G. Gupta, and A. D. Mohite. Light-activated photocurrent degradation and self-healing in perovskite solar cells. *Nature Communications*, 7(1):11574, sep 2016. 13

[151] T.-H.-Y. Vu, W. Chen, X. Deng, C. F. J. Lau, S. Huang, A. Ho-Baillie, B. Jia, and X. Wen. Visualizing the Impact of Light Soaking on Morphological Domains in an Oper-

ational Cesium Lead Halide Perovskite Solar Cell. *The Journal of Physical Chemistry Letters*, 11(1):136–143, jan 2020. 13

[152] E. T. Hoke, D. J. Slotcavage, E. R. Dohner, A. R. Bowring, H. I. Karunadasa, and M. D. McGehee. Reversible photo-induced trap formation in mixed-halide hybrid perovskites for photovoltaics. *Chemical Science*, 6(1):613–617, 2015. 13

[153] A. G. Boldyreva, I. S. Zhidkov, S. Tsarev, A. F. Akbulatov, M. M. Tepliakova, Y. S. Fedotov, S. I. Bredikhin, E. Y. Postnova, S. Y. Luchkin, E. Z. Kurmaev, K. J. Stevenson, and P. A. Troshin. Unraveling the Impact of Hole Transport Materials on Photostability of Perovskite Films and p-i-n Solar Cells. *ACS Applied Materials & Interfaces*, 12(16):19161–19173, apr 2020. 13

[154] N. Li, Y. Luo, Z. Chen, X. Niu, X. Zhang, J. Lu, R. Kumar, J. Jiang, H. Liu, X. Guo, B. Lai, G. Brocks, Q. Chen, S. Tao, D. P. Fenning, and H. Zhou. Microscopic Degradation in Formamidinium-Cesium Lead Iodide Perovskite Solar Cells under Operational Stressors. *Joule*, 4(8):1743–1758, aug 2020. 13

[155] X. Deng, X. Wen, J. Zheng, T. Young, C. F. J. Lau, J. Kim, M. Green, S. Huang, and A. Ho-Baillie. Dynamic study of the light soaking effect on perovskite solar cells by in-situ photoluminescence microscopy. *Nano Energy*, 46(October 2017):356–364, apr 2018. 13

[156] J. Hong, H. Kim, and I. Hwang. Aging-induced light-soaking effects and open-circuit voltage hysteretic behavior of inverted perovskite solar cells incorporating a hole transport metal halide layer via morphology-dependent inflow of iodide ions. *Journal of Materials Chemistry C*, 7(5):1173–1181, 2019. 13

[157] H. J. Snaith. The perils of solar cell efficiency measurements. *Nature Photonics*, 6(6):337–340, jun 2012. 13

[158] J. A. Christians, J. S. Manser, and P. V. Kamat. Best Practices in Perovskite Solar Cell Efficiency Measurements. Avoiding the Error of Making Bad Cells Look Good. *The Journal of Physical Chemistry Letters*, 6(5):852–857, mar 2015. 13

[159] H. J. Snaith. How should you measure your excitonic solar cells? *Energy & Environmental Science*, 5(4):6513, 2012. 13

[160] D. Kiermasch, L. Gil-Escrig, H. J. Bolink, and K. Tvingstedt. Effects of Masking on Open-Circuit Voltage and Fill Factor in Solar Cells. *Joule*, 3(1):16–26, jan 2019. 13, 14

[161] A. Babayigit, J. D'Haen, H.-G. Boyen, and B. Conings. Gas Quenching for Perovskite Thin Film Deposition. *Joule*, 2(7):1205–1209, jul 2018. 16

[162] A. E. A. Bracesco, C. H. Burgess, A. Todinova, V. Zardetto, D. Koushik, W. M. M. E. Kessels, I. Dogan, C. H. L. Weijtens, S. Veenstra, R. Andriessen, and M. Creatore. The chemistry and energetics of the interface between metal halide perovskite and atomic

layer deposited metal oxides. *Journal of Vacuum Science & Technology A*, 38(6):063206, dec 2020. 16

[163] L. Krückemeier, U. Rau, M. Stolterfoht, and T. Kirchartz. How to Report Record Open-Circuit Voltages in Lead-Halide Perovskite Solar Cells. *Advanced Energy Materials*, 10(1), 2020. 17

[164] M. Ledinsky, T. Schönfeldová, J. Holovský, E. Aydin, Z. Hájková, L. Landová, N. Neyková, A. Fejfar, and S. De Wolf. Temperature Dependence of the Urbach Energy in Lead Iodide Perovskites. *The Journal of Physical Chemistry Letters*, 10(6):1368–1373, mar 2019. 17

[165] G. F. Burkhard, E. T. Hoke, and M. D. McGehee. Accounting for Interference, Scattering, and Electrode Absorption to Make Accurate Internal Quantum Efficiency Measurements in Organic and Other Thin Solar Cells. *Advanced Materials*, 22(30):3293–3297, aug 2010. 19

[166] M. D. McGehee. Transfer Matrix Optical Modeling. http://web.stanford.edu/group/mcgehee/transfermatrix/index.html. 19, 20

[167] L. Gao, F. Lemarchand, and M. Lequime. Refractive index determination of SiO2 layer in the UV/Vis/NIR range: spectrophotometric reverse engineering on single and bi-layer designs. *Journal of the European Optical Society: Rapid Publications*, 8:13010, jan 2013. 20

[168] S. Manzoor, J. Häusele, K. A. Bush, A. F. Palmstrom, J. Carpenter, Z. J. Yu, S. F. Bent, M. D. Mcgehee, and Z. C. Holman. Optical modeling of wide-bandgap perovskite and perovskite/silicon tandem solar cells using complex refractive indices for arbitrary-bandgap perovskite absorbers. *Optics Express*, 26(21):27441, oct 2018. 20, 21, 54

[169] M. Zhang, J. S. Yun, Q. Ma, J. Zheng, C. F. J. Lau, X. Deng, J. Kim, D. Kim, J. Seidel, M. A. Green, S. Huang, and A. W. Y. Ho-Baillie. High-Efficiency Rubidium-Incorporated Perovskite Solar Cells by Gas Quenching. *ACS Energy Letters*, 2(2):438–444, feb 2017. 21

[170] M. Filipič, P. Löper, B. Niesen, S. De Wolf, J. Krč, C. Ballif, and M. Topič. CH3NH3PbI3 perovskite/silicon tandem solar cells: characterization based optical simulations. *Optics Express*, 23(7):A263, apr 2015. 21

[171] M. Burgelman, P. Nollet, and S. Degrave. Modelling polycrystalline semiconductor solar cells. *Thin Solid Films*, 361-362:527–532, feb 2000. 24

[172] M. Burgelman. Simulation programme SCAPS-1D for thin film solar cells. http://scaps.elis.ugent.be/. 24

[173] T. Minemoto and M. Murata. Device modeling of perovskite solar cells based on structural similarity with thin film inorganic semiconductor solar cells. *Journal of Applied Physics*, 116(5):054505, aug 2014. 24, 30

[174] R. Mackenzie. gpvdm - A free drift diffusion model for Generic solar cells. 25

[175] D. Głowienka, F. Di Giacomo, M. Najafi, I. Dogan, A. Mameli, F. J. M. Colberts, J. Szmytkowski, and Y. Galagan. Effect of Different Bromine Sources on the Dual Cation Mixed Halide Perovskite Solar Cells. *ACS Applied Energy Materials*, 3(9):8285–8294, sep 2020. 26, 30, 32, 46

[176] F. Brivio, K. T. Butler, A. Walsh, and M. van Schilfgaarde. Relativistic quasiparticle self-consistent electronic structure of hybrid halide perovskite photovoltaic absorbers. *Physical Review B*, 89(15):155204, apr 2014. 26, 30

[177] T. S. Sherkar, C. Momblona, L. Gil-Escrig, H. J. Bolink, and L. J. A. Koster. Improving Perovskite Solar Cells: Insights From a Validated Device Model. *Advanced Energy Materials*, 7(13):1602432, jul 2017. 26, 30, 32, 33, 36

[178] R. L. Milot, G. E. Eperon, H. J. Snaith, M. B. Johnston, and L. M. Herz. Temperature-Dependent Charge-Carrier Dynamics in CH3NH3PbI3 Perovskite Thin Films. *Advanced Functional Materials*, 25(39):6218–6227, oct 2015. 26, 34

[179] W. Tress, K. Leo, and M. Riede. Influence of Hole-Transport Layers and Donor Materials on Open-Circuit Voltage and Shape of I-V Curves of Organic Solar Cells. *Advanced Functional Materials*, 21(11):2140–2149, jun 2011. 27, 72

[180] J. P. Correa Baena, L. Steier, W. Tress, M. Saliba, S. Neutzner, T. Matsui, F. Giordano, T. J. Jacobsson, A. R. Srimath Kandada, S. M. Zakeeruddin, A. Petrozza, A. Abate, M. K. Nazeeruddin, M. Grätzel, and A. Hagfeldt. Highly efficient planar perovskite solar cells through band alignment engineering. *Energy & Environmental Science*, 8(10):2928–2934, 2015. 27

[181] M. Stolterfoht, P. Caprioglio, C. M. Wolff, J. A. Márquez, J. Nordmann, S. Zhang, D. Rothhardt, U. Hörmann, Y. Amir, A. Redinger, L. Kegelmann, F. Zu, S. Albrecht, N. Koch, T. Kirchartz, M. Saliba, T. Unold, and D. Neher. The impact of energy alignment and interfacial recombination on the internal and external open-circuit voltage of perovskite solar cells. *Energy & Environmental Science*, 12(9):2778–2788, 2019. 27, 30, 32, 38, 63, 66

[182] J. Endres, M. Kulbak, L. Zhao, B. P. Rand, D. Cahen, G. Hodes, and A. Kahn. Electronic structure of the CsPbBr3/polytriarylamine (PTAA) system. *Journal of Applied Physics*, 121(3):035304, jan 2017. 27

[183] A. Intaniwet, C. A. Mills, P. J. Sellin, M. Shkunov, and J. L. Keddie. Achieving a Stable Time Response in Polymeric Radiation Sensors under Charge Injection by X-rays. *ACS Applied Materials & Interfaces*, 2(6):1692–1699, jun 2010. 27

[184] I. Hussain, H. P. Tran, J. Jaksik, J. Moore, N. Islam, and M. J. Uddin. Functional materials, device architecture, and flexibility of perovskite solar cell. *Emergent Materials*, 1(3-4):133–154, dec 2018. 27, 28

[185] D. B. Khadka, Y. Shirai, M. Yanagida, J. W. Ryan, and K. Miyano. Exploring the effects of interfacial carrier transport layers on device performance and optoelectronic properties of planar perovskite solar cells. *Journal of Materials Chemistry C*, 5(34):8819–8827, 2017. 27, 30, 31, 33, 38

[186] X. Huang, K. Wang, C. Yi, T. Meng, and X. Gong. Efficient Perovskite Hybrid Solar Cells by Highly Electrical Conductive PEDOT:PSS Hole Transport Layer. *Advanced Energy Materials*, 6(3):1501773, feb 2016. 27

[187] T. H. Schloemer, J. A. Christians, J. M. Luther, and A. Sellinger. Doping strategies for small molecule organic hole-transport materials: impacts on perovskite solar cell performance and stability. *Chemical Science*, 10(7):1904–1935, 2019. 27

[188] J. Luo, J. Xia, H. Yang, L. Chen, Z. Wan, F. Han, H. A. Malik, X. Zhu, and C. Jia. Toward high-efficiency, hysteresis-less, stable perovskite solar cells: unusual doping of a hole-transporting material using a fluorine-containing hydrophobic Lewis acid. *Energy & Environmental Science*, 11(8):2035–2045, 2018. 27

[189] S. A. Kulkarni, T. Baikie, P. P. Boix, N. Yantara, N. Mathews, and S. Mhaisalkar. Band-gap tuning of lead halide perovskites using a sequential deposition process. *J. Mater. Chem. A*, 2(24):9221–9225, 2014. 27

[190] R. J. Sutton, G. E. Eperon, L. Miranda, E. S. Parrott, B. A. Kamino, J. B. Patel, M. T. Hörantner, M. B. Johnston, A. A. Haghighirad, D. T. Moore, and H. J. Snaith. Bandgap-Tunable Cesium Lead Halide Perovskites with High Thermal Stability for Efficient Solar Cells. *Advanced Energy Materials*, 6(8):1502458, apr 2016. 27

[191] P. Luo, S. Zhou, Y. Zhou, W. Xia, L. Sun, J. Cheng, C. Xu, and Y. Lu. Fabrication of CsxFA1-xPbI3 Mixed-Cation Perovskites via Gas-Phase-Assisted Compositional Modulation for Efficient and Stable Photovoltaic Devices. *ACS Applied Materials & Interfaces*, 9(49):42708–42716, dec 2017. 28

[192] Y. Jiang, M. R. Leyden, L. Qiu, S. Wang, L. K. Ono, Z. Wu, E. J. Juarez-Perez, and Y. Qi. Combination of Hybrid CVD and Cation Exchange for Upscaling Cs-Substituted Mixed Cation Perovskite Solar Cells with High Efficiency and Stability. *Advanced Functional Materials*, 28(1):1703835, jan 2018. 28, 46

[193] A. Amat, E. Mosconi, E. Ronca, C. Quarti, P. Umari, M. K. Nazeeruddin, M. Grätzel, and F. De Angelis. Cation-Induced Band-Gap Tuning in Organohalide Perovskites: Interplay of Spin–Orbit Coupling and Octahedra Tilting. *Nano Letters*, 14(6):3608–3616, jun 2014. 28

[194] Z.-K. Yu, W.-F. Fu, W.-Q. Liu, Z.-Q. Zhang, Y.-J. Liu, J.-L. Yan, T. Ye, W.-T. Yang, H.-Y. Li, and H.-Z. Chen. Solution-processed CuOx as an efficient hole-extraction layer for inverted planar heterojunction perovskite solar cells. *Chinese Chemical Letters*, 28(1):13–18, jan 2017. 28

[195] J. Endres, D. A. Egger, M. Kulbak, R. A. Kerner, L. Zhao, S. H. Silver, G. Hodes, B. P. Rand, D. Cahen, L. Kronik, and A. Kahn. Valence and Conduction Band Densities of States of Metal Halide Perovskites: A Combined Experimental–Theoretical Study. *The Journal of Physical Chemistry Letters*, 7(14):2722–2729, jul 2016. 28, 30

[196] P. Schulz, E. Edri, S. Kirmayer, G. Hodes, D. Cahen, and A. Kahn. Interface energetics in organo-metal halide perovskite-based photovoltaic cells. *Energy & Environmental Science*, 7(4):1377, 2014. 28

[197] Z. Peng, Q. Wei, H. Chen, Y. Liu, F. Wang, X. Jiang, W. Liu, W. Zhou, S. Ling, and Z. Ning. Cs0.15FA0.85PbI3/CsxFA1-xPbI3 Core/Shell Heterostructure for Highly Stable and Efficient Perovskite Solar Cells. *Cell Reports Physical Science*, 1(10):100224, oct 2020. 28

[198] M. Jaysankar, B. A. L. Raul, J. Bastos, C. Burgess, C. Weijtens, M. Creatore, T. Aernouts, Y. Kuang, R. Gehlhaar, A. Hadipour, and J. Poortmans. Minimizing Voltage Loss in Wide-Bandgap Perovskites for Tandem Solar Cells. *ACS Energy Letters*, 4(1):259–264, jan 2019. 28

[199] S. Prathapani, P. Bhargava, and S. Mallick. Electronic band structure and carrier concentration of formamidinium–cesium mixed cation lead mixed halide hybrid perovskites. *Applied Physics Letters*, 112(9):092104, feb 2018. 28

[200] N. D. Pham, C. Zhang, V. T. Tiong, S. Zhang, G. Will, A. Bou, J. Bisquert, P. E. Shaw, A. Du, G. J. Wilson, and H. Wang. Tailoring Crystal Structure of FA0.83Cs0.17PbI3 Perovskite Through Guanidinium Doping for Enhanced Performance and Tunable Hysteresis of Planar Perovskite Solar Cells. *Advanced Functional Materials*, 29(1):1806479, jan 2019. 28

[201] S. Olthof. Research Update: The electronic structure of hybrid perovskite layers and their energetic alignment in devices. *APL Materials*, 4(9):091502, sep 2016. 28

[202] L. Etgar, P. Gao, Z. Xue, Q. Peng, A. K. Chandiran, B. Liu, M. K. Nazeeruddin, and M. Grätzel. Mesoscopic CH3NH3PbI3/TiO 2 Heterojunction Solar Cells. *Journal of the American Chemical Society*, 134(42):17396–17399, oct 2012. 28

[203] P. Gao, M. Grätzel, and M. K. Nazeeruddin. Organohalide lead perovskites for photo-voltaic applications. *Energy Environ. Sci.*, 7(8):2448–2463, 2014. 28

[204] M. S. Hamed and G. T. Mola. Mixed Halide Perovskite Solar Cells: Progress and Challenges. *Critical Reviews in Solid State and Materials Sciences*, 45(2):85–112, 2020. 28, 38

[205] C.-C. Chueh, C.-Z. Li, and A. K. Jen. Recent progress and perspective in solution-processed Interfacial materials for efficient and stable polymer and organometal perovskite solar cells. *Energy & Environmental Science*, 8(4):1160–1189, 2015. 28, 38

[206] P. P. Boix, K. Nonomura, N. Mathews, and S. G. Mhaisalkar. Current progress and future perspectives for organic/inorganic perovskite solar cells. *Materials Today*, 17(1):16–23, jan 2014. 28

[207] J. Emara, T. Schnier, N. Pourdavoud, T. Riedl, K. Meerholz, and S. Olthof. Impact of Film Stoichiometry on the Ionization Energy and Electronic Structure of CH3NH3PbI3 Perovskites. *Advanced Materials*, 28(3):553–559, jan 2016. 28

[208] T. G. Kim, S. W. Seo, H. Kwon, J. Hahn, and J. W. Kim. Influence of halide precursor type and its composition on the electronic properties of vacuum deposited perovskite films. *Physical Chemistry Chemical Physics*, 17(37):24342–24348, 2015. 28

[209] P. Da and G. Zheng. Tailoring interface of lead-halide perovskite solar cells. *Nano Research*, 10(5):1471–1497, may 2017. 28, 38

[210] H. Yoshida. Low-Energy Inverse Photoemission Study on the Electron Affinities of Fullerene Derivatives for Organic Photovoltaic Cells. *The Journal of Physical Chemistry C*, 118(42):24377–24382, oct 2014. 28

[211] D. Luo, W. Yang, Z. Wang, A. Sadhanala, Q. Hu, R. Su, R. Shivanna, G. F. Trindade, J. F. Watts, Z. Xu, T. Liu, K. Chen, F. Ye, P. Wu, L. Zhao, J. Wu, Y. Tu, Y. Zhang, X. Yang, W. Zhang, R. H. Friend, Q. Gong, H. J. Snaith, and R. Zhu. Enhanced photovoltage for inverted planar heterojunction perovskite solar cells. *Science*, 360(6396):1442–1446, jun 2018. 28

[212] J. F. Butscher, Q. Sun, Y. Wu, F. Stuck, M. Hoffmann, A. Dreuw, F. Paulus, A. S. K. Hashmi, N. Tessler, and Y. Vaynzof. Dipolar hole-blocking layers for inverted perovskite solar cells: effects of aggregation and electron transport levels. *Journal of Physics: Materials*, 3(2):025002, feb 2020. 28

[213] S.-M. Dai, X. Zhang, W.-Y. Chen, X. Li, Z. Tan, C. Li, L.-L. Deng, X.-X. Zhan, M.-S. Lin, Z. Xing, T. Wen, R.-M. Ho, S.-Y. Xie, R.-B. Huang, and L.-S. Zheng. Formulation engineering for optimizing ternary electron acceptors exemplified by isomeric PC71BM in planar perovskite solar cells. *Journal of Materials Chemistry A*, 4(48):18776–18782, 2016. 28

[214] C.-H. Chiang, Z.-L. Tseng, and C.-G. Wu. Planar heterojunction perovskite/PC71BM solar cells with enhanced open-circuit voltage via a (2/1)-step spin-coating process. *J. Mater. Chem. A*, 2(38):15897–15903, 2014. 28

[215] L. Xu, H. Liu, W. Qiu, K. Xue, X. Liu, J. Wang, H. Zhang, and W. Huang. High-Performance and Hysteresis-Free Planar Solar Cells with PC71BM and C60 Composed Structure Prepared Irrespective of Humidity. *ACS Sustainable Chemistry & Engineering*, 5(11):9718–9724, nov 2017. 28

[216] S. Park, J. Jeong, G. Hyun, M. Kim, H. Lee, and Y. Yi. The origin of high PCE in PTB7 based photovoltaics: proper charge neutrality level and free energy of charge separation at PTB7/PC71BM interface. *Scientific Reports*, 6(1):35262, dec 2016. 28

[217] S. Paek, N. Cho, H. Choi, H. Jeong, J. S. Lim, J.-Y. Hwang, J. K. Lee, and J. Ko. Improved External Quantum Efficiency from Solution-Processed (CH3NH3)PbI3 Perovskite/PC71BM Planar Heterojunction for High Efficiency Hybrid Solar Cells. *The Journal of Physical Chemistry C*, 118(45):25899–25905, nov 2014. 28

[218] Y. Zhong, S. Izawa, K. Hashimoto, K. Tajima, T. Koganezawa, and H. Yoshida. Crystallization-Induced Energy Level Change of [6,6]-Phenyl-C61-Butyric Acid Methyl Ester (PCBM) Film: Impact of Electronic Polarization Energy. *The Journal of Physical Chemistry C*, 119(1):23–28, jan 2015. 29

[219] J. N. Wilson, J. M. Frost, S. K. Wallace, and A. Walsh. Dielectric and ferroic properties of metal halide perovskites. *APL Materials*, 7(1):010901, jan 2019. 29, 31

[220] J. Even, L. Pedesseau, and C. Katan. Analysis of Multivalley and Multibandgap Absorption and Enhancement of Free Carriers Related to Exciton Screening in Hybrid Perovskites. *The Journal of Physical Chemistry C*, 118(22):11566–11572, jun 2014. 29

[221] A. Mattoni and C. Caddeo. Dielectric function of hybrid perovskites at finite temperature investigated by classical molecular dynamics. *The Journal of Chemical Physics*, 152(10):104705, mar 2020. 29

[222] A. K. Bain and P. Chand. Dielectric Properties of Materials. In *Ferroelectrics*, Wiley Online Books, pages 1–18. Wiley-VCH Verlag GmbH & Co. KGaA, Weinheim, Germany, feb 2017. 29

[223] E. J. Juarez-Perez, R. S. Sanchez, L. Badia, G. Garcia-Belmonte, Y. S. Kang, I. Mora-Sero, and J. Bisquert. Photoinduced Giant Dielectric Constant in Lead Halide Perovskite Solar Cells. *The Journal of Physical Chemistry Letters*, 5(13):2390–2394, jul 2014. 29

[224] W. Li, Z. Man, J. Zeng, L. Zheng, G. Li, and A. Kassiba. Relationship of Giant Dielectric Constant and Ion Migration in CH3NH3PbI3 Single Crystal Using Dielectric Spectroscopy. *The Journal of Physical Chemistry C*, 124(24):13348–13355, jun 2020. 29

[225] M. Sajedi Alvar, P. W. M. Blom, and G.-J. A. H. Wetzelaer. Space-charge-limited electron and hole currents in hybrid organic-inorganic perovskites. *Nature Communications*, 11(1):4023, dec 2020. 30

[226] T. Minemoto and M. Murata. Theoretical analysis on effect of band offsets in perovskite solar cells. *Solar Energy Materials and Solar Cells*, 133:8–14, feb 2015. 30, 36

[227] H. Shen, D. A. Jacobs, Y. Wu, T. Duong, J. Peng, X. Wen, X. Fu, S. K. Karuturi, T. P. White, K. Weber, and K. R. Catchpole. Inverted Hysteresis in CH3NH3PbI3 Solar Cells: Role of Stoichiometry and Band Alignment. *The Journal of Physical Chemistry Letters*, 8(12):2672–2680, jun 2017. 30, 36

[228] N. Wu, Y. Wu, D. Walter, H. Shen, T. Duong, D. Grant, C. Barugkin, X. Fu, J. Peng, T. White, K. Catchpole, and K. Weber. Identifying the Cause of Voltage and Fill Factor Losses in Perovskite Solar Cells by Using Luminescence Measurements. *Energy Technology*, 5(10):1827–1835, oct 2017. 30, 31

[229] Y. Raoui, H. Ez-Zahraouy, S. Kazim, and S. Ahmad. Energy level engineering of charge selective contact and halide perovskite by modulating band offset: Mechanistic insights. *Journal of Energy Chemistry*, 54:822–829, mar 2021. 30, 33, 36, 37

[230] D. Głowienka, D. Zhang, F. Di Giacomo, M. Najafi, S. Veenstra, J. Szmytkowski, and Y. Galagan. Role of surface recombination in perovskite solar cells at the interface of HTL/CH3NH3PbI3. *Nano Energy*, 67:104186, jan 2020. 30

[231] K. Masumura, T. Oka, K. Kinashi, W. Sakai, and N. Tsutsumi. Photorefractive dynamics in poly(triarylamine)-based polymer composite: an approach utilizing a second electron trap to reduce the photoconductivity. *Optical Materials Express*, 8(2):401, feb 2018. 30

[232] J. Diekmann, P. Caprioglio, D. Rothhardt, M. Arvind, T. Unold, T. Kirchartz, D. Neher, and M. Stolterfoht. Pathways towards 30% efficient perovskite solar cells. *arXiv*, pages 1–16, 2019. 30, 31, 33

[233] Z. Ni, C. Bao, Y. Liu, Q. Jiang, W.-Q. Wu, S. Chen, X. Dai, B. Chen, B. Hartweg, Z. Yu, Z. Holman, and J. Huang. Resolving spatial and energetic distributions of trap states in metal halide perovskite solar cells. *Science*, 367(6484):1352–1358, mar 2020. 30, 33, 34, 35, 36

[234] F. Jahani, S. Torabi, R. C. Chiechi, L. J. A. Koster, and J. C. Hummelen. Fullerene derivatives with increased dielectric constants. *Chem. Commun.*, 50(73):10645–10647, 2014. 30

[235] S. Torabi, F. Jahani, I. Van Severen, C. Kanimozhi, S. Patil, R. W. A. Havenith, R. C. Chiechi, L. Lutsen, D. J. M. Vanderzande, T. J. Cleij, J. C. Hummelen, and L. J. A. Koster. Strategy for Enhancing the Dielectric Constant of Organic Semiconductors

Without Sacrificing Charge Carrier Mobility and Solubility. *Advanced Functional Materials*, 25(1):150–157, jan 2015. 30

[236] U. Mandadapu, S. V. Vedanayakam, and K. Thyagarajan. Simulation and Analysis of Lead based Perovskite Solar Cell using SCAPS-1D. *Indian Journal of Science and Technology*, 10(11):1–8, mar 2017. 30

[237] T. Kirchartz and U. Rau. Linking structural properties with functionality in solar cell materials - the effective mass and effective density of states. *Sustainable Energy & Fuels*, 2(7):1550–1560, 2018. 30

[238] Y. Zhou and G. Long. Low Density of Conduction and Valence Band States Contribute to the High Open-Circuit Voltage in Perovskite Solar Cells. *The Journal of Physical Chemistry C*, 121(3):1455–1462, jan 2017. 30

[239] N. Tessler and Y. Vaynzof. Insights from Device Modeling of Perovskite Solar Cells. *ACS Energy Letters*, 5(4):1260–1270, apr 2020. 30, 34

[240] Y. H. Chang, C. H. Park, and K. Matsuishi. First-principles study of the structural and the electronic properties of the lead-halide-based inorganic-organic perovskites (CH3NH3)PbX3 and CsPbX3 (X = Cl, Br, I). *Journal of the Korean Physical Society*, 44(4):889–893, 2004. 30, 31

[241] T. Leijtens, G. E. Eperon, A. J. Barker, G. Grancini, W. Zhang, J. M. Ball, A. R. S. Kandada, H. J. Snaith, and A. Petrozza. Carrier trapping and recombination: the role of defect physics in enhancing the open circuit voltage of metal halide perovskite solar cells. *Energy & Environmental Science*, 9(11):3472–3481, 2016. 30

[242] K. Galkowski, A. Mitioglu, A. Miyata, P. Plochocka, O. Portugall, G. E. Eperon, J. T.-W. Wang, T. Stergiopoulos, S. D. Stranks, H. J. Snaith, and R. J. Nicholas. Determination of the exciton binding energy and effective masses for methylammonium and formamidinium lead tri-halide perovskite semiconductors. *Energy & Environmental Science*, 9(3):962–970, 2016. 30

[243] N. Thongprong, T. Supasai, Y. Li, I.-M. Tang, and N. Rujisamphan. Insights into Recombination Processes from Light Intensity–Dependent Open-Circuit Voltages and Ideality Factors in Planar Perovskite Solar Cells. *Energy Technology*, 8(5):1901196, may 2020. 30, 34, 36, 37

[244] P. Umari, E. Mosconi, and F. De Angelis. Relativistic GW calculations on CH3NH3PbI3 and CH3NH3SnI3 Perovskites for Solar Cell Applications. *Scientific Reports*, 4(1):4467, may 2015. 30

[245] S. Ravishankar, T. Unold, and T. Kirchartz. Comment on "Resolving spatial and energetic distributions of trap states in metal halide perovskite solar cells", 2020. 30, 31, 33, 34

[246] A. B. Coulibaly, S. O. Oyedele, N. R. Kre, and B. Aka. Comparative Study of Lead-Free Perovskite Solar Cells Using Different Hole Transporter Materials. *Modeling and Numerical Simulation of Material Science*, 09(04):97–107, 2019. 30, 31, 33

[247] M. Shur. 6 - Semiconductors. In W.-K. CHEN, editor, *The Electrical Engineering Handbook*, pages 153–162. Academic Press, Burlington, 2005. 30

[248] A. Sahu and A. Dixit. Inverted structure perovskite solar cells: A theoretical study. *Current Applied Physics*, 18(12):1583–1591, dec 2018. 31, 35, 37

[249] L. Lin, L. Jiang, Y. Qiu, and Y. Yu. Modeling and analysis of HTM-free perovskite solar cells based on ZnO electron transport layer. *Superlattices and Microstructures*, 104:167–177, apr 2017. 31, 33

[250] A. Husainat, W. Ali, P. Cofie, J. Attia, J. Fuller, and A. Darwish. Simulation and Analysis Method of Different Back Metals Contact of CH3NH3PbI3 Perovskite Solar Cell Along with Electron Transport Layer TiO2 Using MBMT-MAPLE/PLD. *American Journal of Optics and Photonics*, 8(1):6, 2020. 31, 33, 37

[251] S. Sze and K. K. Ng. *Physics and Properties of Semiconductors-A Review*, pages 5–75. John Wiley & Sons, Inc., Hoboken, NJ, USA, apr 2006. 31

[252] T. M. Brenner, D. A. Egger, A. M. Rappe, L. Kronik, G. Hodes, and D. Cahen. Are Mobilities in Hybrid Organic–Inorganic Halide Perovskites Actually "High"? *The Journal of Physical Chemistry Letters*, 6(23):4754–4757, dec 2015. 31

[253] G. Giorgi, J.-I. Fujisawa, H. Segawa, and K. Yamashita. Small Photocarrier Effective Masses Featuring Ambipolar Transport in Methylammonium Lead Iodide Perovskite: A Density Functional Analysis. *The Journal of Physical Chemistry Letters*, 4(24):4213–4216, dec 2013. 31

[254] T. M. Brenner, D. A. Egger, L. Kronik, G. Hodes, and D. Cahen. Hybrid organic—inorganic perovskites: low-cost semiconductors with intriguing charge-transport properties. *Nature Reviews Materials*, 1(1):15007, jan 2016. 31

[255] D. Ghosh, E. Welch, A. J. Neukirch, A. Zakhidov, and S. Tretiak. Polarons in Halide Perovskites: A Perspective. *The Journal of Physical Chemistry Letters*, 11(9):3271–3286, may 2020. 31, 32

[256] T. Zhao, W. Shi, J. Xi, D. Wang, and Z. Shuai. Intrinsic and Extrinsic Charge Transport in CH3NH3PbI3 Perovskites Predicted from First-Principles. *Scientific Reports*, 6(1):19968, feb 2016. 31

[257] D. Zhao, H. Hu, R. Haselsberger, R. A. Marcus, M.-E. Michel-Beyerle, Y. M. Lam, J.-X. Zhu, C. La-o vorakiat, M. C. Beard, and E. E. M. Chia. Monitoring Electron–Phonon

Interactions in Lead Halide Perovskites Using Time-Resolved THz Spectroscopy. *ACS Nano*, 13(8):8826–8835, aug 2019. 31

[258] M. Sendner, P. K. Nayak, D. A. Egger, S. Beck, C. Müller, B. Epding, W. Kowalsky, L. Kronik, H. J. Snaith, A. Pucci, and R. Lovrinčić. Optical phonons in methylammonium lead halide perovskites and implications for charge transport. *Materials Horizons*, 3(6):613–620, jul 2016. 31, 32

[259] X.-Y. Zhu and V. Podzorov. Charge Carriers in Hybrid Organic–Inorganic Lead Halide Perovskites Might Be Protected as Large Polarons. *The Journal of Physical Chemistry Letters*, 6(23):4758–4761, dec 2015. 31, 32, 34

[260] K. Miyata, D. Meggiolaro, M. T. Trinh, P. P. Joshi, E. Mosconi, S. C. Jones, F. De Angelis, and X.-Y. Zhu. Large polarons in lead halide perovskites. *Science Advances*, 3(8):e1701217, aug 2017. 31, 32

[261] H. Oga, A. Saeki, Y. Ogomi, S. Hayase, and S. Seki. Improved Understanding of the Electronic and Energetic Landscapes of Perovskite Solar Cells: High Local Charge Carrier Mobility, Reduced Recombination, and Extremely Shallow Traps. *Journal of the American Chemical Society*, 136(39):13818–13825, oct 2014. 31

[262] T. J. Savenije, C. S. Ponseca, L. Kunneman, M. Abdellah, K. Zheng, Y. Tian, Q. Zhu, S. E. Canton, I. G. Scheblykin, T. Pullerits, A. Yartsev, and V. Sundström. Thermally Activated Exciton Dissociation and Recombination Control the Carrier Dynamics in Organometal Halide Perovskite. *The Journal of Physical Chemistry Letters*, 5(13):2189–2194, jul 2014. 31, 34

[263] M. Karakus, S. A. Jensen, F. D'Angelo, D. Turchinovich, M. Bonn, and E. Cánovas. Phonon–Electron Scattering Limits Free Charge Mobility in Methylammonium Lead Iodide Perovskites. *The Journal of Physical Chemistry Letters*, 6(24):4991–4996, dec 2015. 31

[264] J. Feng. Mechanical properties of hybrid organic-inorganic CH3NH3BX3 (B = Sn, Pb; X = Br, I) perovskites for solar cell absorbers. *APL Materials*, 2(8):081801, aug 2014. 31

[265] A. D. Wright, C. Verdi, R. L. Milot, G. E. Eperon, M. A. Pérez-Osorio, H. J. Snaith, F. Giustino, M. B. Johnston, and L. M. Herz. Electron–phonon coupling in hybrid lead halide perovskites. *Nature Communications*, 7(1):11755, sep 2016. 31

[266] P. Y. Yu and M. Cardona. *Fundamentals of Semiconductors*. Graduate Texts in Physics. Springer Berlin Heidelberg, Berlin, Heidelberg, 4th edition, 2010. 31

[267] Y. He and G. Galli. Perovskites for Solar Thermoelectric Applications: A First Principle Study of CH3NH3AI3 (A = Pb and Sn). *Chemistry of Materials*, 26(18):5394–5400, sep 2014. 31

[268] B. Huang, G. Kong, E. N. Esfahani, S. Chen, Q. Li, J. Yu, N. Xu, Y. Zhang, S. Xie, H. Wen, P. Gao, J. Zhao, and J. Li. Ferroic domains regulate photocurrent in single-crystalline CH3NH3PbI3 films self-grown on FTO/TiO2 substrate. *npj Quantum Materials*, 3(1):30, dec 2018. 32

[269] B. Huang, Z. Liu, C. Wu, Y. Zhang, J. Zhao, X. Wang, and J. Li. Polar or nonpolar? That is not the question for perovskite solar cells. *arXiv*, 3:1–12, apr 2020. 32

[270] P.-A. Mante, C. C. Stoumpos, M. G. Kanatzidis, and A. Yartsev. Electron–acoustic phonon coupling in single crystal CH3NH3PbI3 perovskites revealed by coherent acoustic phonons. *Nature Communications*, 8(1):14398, apr 2017. 32

[271] S. Poncé, M. Schlipf, and F. Giustino. Origin of Low Carrier Mobilities in Halide Perovskites. *ACS Energy Letters*, 4(2):456–463, feb 2019. 32

[272] J. T. Devreese. Polarons. *Encyclopedia of Applied Physics*, 14:383–409, apr 1996. 32

[273] J. M. Frost. Calculating polaron mobility in halide perovskites. *Physical Review B*, 96(19):195202, nov 2017. 32

[274] S. A. Bretschneider, I. Ivanov, H. I. Wang, K. Miyata, X. Zhu, and M. Bonn. Quantifying Polaron Formation and Charge Carrier Cooling in Lead-Iodide Perovskites. *Advanced Materials*, 30(29):1707312, jul 2018. 32

[275] M. Puppin, S. Polishchuk, N. Colonna, A. Crepaldi, D. N. Dirin, O. Nazarenko, R. De Gennaro, G. Gatti, S. Roth, T. Barillot, L. Poletto, R. P. Xian, L. Rettig, M. Wolf, R. Ernstorfer, M. V. Kovalenko, N. Marzari, M. Grioni, and M. Chergui. Evidence of Large Polarons in Photoemission Band Mapping of the Perovskite Semiconductor CsPbBr3. *Physical Review Letters*, 124(20):206402, may 2020. 32

[276] Z. Guo, Y. Wan, M. Yang, J. Snaider, K. Zhu, and L. Huang. Long-range hot-carrier transport in hybrid perovskites visualized by ultrafast microscopy. *Science*, 356(6333):59–62, apr 2017. 32

[277] F. Zheng and L.-w. Wang. Large polaron formation and its effect on electron transport in hybrid perovskites. *Energy & Environmental Science*, 12(4):1219–1230, 2019. 32

[278] D. A. Egger, A. Bera, D. Cahen, G. Hodes, T. Kirchartz, L. Kronik, R. Lovrincic, A. M. Rappe, D. R. Reichman, and O. Yaffe. What Remains Unexplained about the Properties of Halide Perovskites? *Advanced Materials*, 30(20):1800691, may 2018. 32

[279] L. M. Herz. Charge-Carrier Mobilities in Metal Halide Perovskites: Fundamental Mechanisms and Limits. *ACS Energy Letters*, 2(7):1539–1548, jul 2017. 32

[280] J. Lim, M. T. Hörantner, N. Sakai, J. M. Ball, S. Mahesh, N. K. Noel, Y.-H. Lin, J. B. Patel, D. P. McMeekin, M. B. Johnston, B. Wenger, and H. J. Snaith. Elucidating

the long-range charge carrier mobility in metal halide perovskite thin films. *Energy & Environmental Science*, 12(1):169–176, 2019. 32

[281] Y. Deng, Z. Ni, A. F. Palmstrom, J. Zhao, S. Xu, C. H. Van Brackle, X. Xiao, K. Zhu, and J. Huang. Reduced Self-Doping of Perovskites Induced by Short Annealing for Efficient Solar Modules. *Joule*, 4(9):1949–1960, sep 2020. 32, 35, 37

[282] B. Olyaeefar, S. Ahmadi-Kandjani, and A. Asgari. Bulk and interface recombination in planar lead halide perovskite solar cells: A Drift-Diffusion study. *Physica E: Low-dimensional Systems and Nanostructures*, 94(July):118–122, oct 2017. 32

[283] R. Teimouri, Z. Heydari, M. P. Ghaziani, M. Madani, H. Abdy, M. Kolahdouz, and E. Asl-Soleimani. Synthesizing Li doped TiO2 electron transport layers for highly efficient planar perovskite solar cell. *Superlattices and Microstructures*, 145(December 2019):106627, sep 2020. 32

[284] W. Zhang, Y.-C. Wang, X. Li, C. Song, L. Wan, K. Usman, and J. Fang. Recent Advance in Solution-Processed Organic Interlayers for High-Performance Planar Perovskite Solar Cells. *Advanced Science*, 5(7):1800159, jul 2018. 32

[285] J. Veres, S. Ogier, S. Leeming, D. Cupertino, and S. Mohialdin Khaffaf. Low-k Insulators as the Choice of Dielectrics in Organic Field-Effect Transistors. *Advanced Functional Materials*, 13(3):199–204, mar 2003. 32

[286] S. Logan, J. E. Donaghey, W. Zhang, I. McCulloch, and A. J. Campbell. Compatibility of amorphous triarylamine copolymers with solution-processed hole injecting metal oxide bottom contacts. *Journal of Materials Chemistry C*, 3(17):4530–4536, 2015. 32

[287] E. von Hauff, V. Dyakonov, and J. Parisi. Study of field effect mobility in PCBM films and P3HT:PCBM blends. *Solar Energy Materials and Solar Cells*, 87(1-4):149–156, may 2005. 32

[288] Y. Zheng, J. Kong, D. Huang, W. Shi, L. McMillon-Brown, H. E. Katz, J. Yu, and A. D. Taylor. Spray coating of the PCBM electron transport layer significantly improves the efficiency of p-i-n planar perovskite solar cells. *Nanoscale*, 10(24):11342–11348, 2018. 32

[289] K. Tan, P. Lin, G. Wang, Y. Liu, Z. Xu, and Y. Lin. Controllable design of solid-state perovskite solar cells by SCAPS device simulation. *Solid-State Electronics*, 126:75–80, dec 2016. 33

[290] Y. Wang. *Investigation of perovskite-CIGSe tandem solar cells*. PhD thesis, Technische Universität Berlin, 2019. 33, 37, 76

[291] Z.-K. Tang, Z.-F. Xu, D.-Y. Zhang, S.-X. Hu, W.-M. Lau, and L.-M. Liu. Enhanced optical absorption via cation doping hybrid lead iodine perovskites. *Scientific Reports*, 7(1):7843, dec 2017. 33

[292] X. Zhang, X. Ren, B. Liu, R. Munir, X. Zhu, D. Yang, J. Li, Y. Liu, D.-M. Smilgies, R. Li, Z. Yang, T. Niu, X. Wang, A. Amassian, K. Zhao, and S. F. Liu. Stable high efficiency two-dimensional perovskite solar cells via cesium doping. *Energy & Environmental Science*, 10(10):2095–2102, 2017. 33

[293] N. Phung, R. Félix, D. Meggiolaro, A. Al-Ashouri, G. Sousa e Silva, C. Hartmann, J. Hidalgo, H. Köbler, E. Mosconi, B. Lai, R. Gunder, M. Li, K.-L. Wang, Z.-K. Wang, K. Nie, E. Handick, R. G. Wilks, J. A. Marquez, B. Rech, T. Unold, J.-P. Correa-Baena, S. Albrecht, F. De Angelis, M. Bär, and A. Abate. The Doping Mechanism of Halide Perovskite Unveiled by Alkaline Earth Metals. *Journal of the American Chemical Society*, 142(5):2364–2374, feb 2020. 33, 36

[294] S.-H. Chan, M.-C. Wu, K.-M. Lee, W.-C. Chen, T.-H. Lin, and W.-F. Su. Enhancing perovskite solar cell performance and stability by doping barium in methylammonium lead halide. *Journal of Materials Chemistry A*, 5(34):18044–18052, 2017. 33

[295] M. T. Klug, A. Osherov, A. A. Haghighirad, S. D. Stranks, P. R. Brown, S. Bai, J. T. Wang, X. Dang, V. Bulović, H. J. Snaith, and A. M. Belcher. Tailoring metal halide perovskites through metal substitution: influence on photovoltaic and material properties. *Energy & Environmental Science*, 10(1):236–246, 2017. 33

[296] J. Gong, M. Yang, D. Rebollar, J. Rucinski, Z. Liveris, K. Zhu, and T. Xu. Divalent Anionic Doping in Perovskite Solar Cells for Enhanced Chemical Stability. *Advanced Materials*, 30(34):1800973, aug 2018. 33

[297] H. Zhao, Y. Han, Z. Xu, C. Duan, S. Yang, S. Yuan, Z. Yang, Z. Liu, and S. F. Liu. A Novel Anion Doping for Stable CsPbI2Br Perovskite Solar Cells with an Efficiency of 15.56% and an Open Circuit Voltage of 1.30 V. *Advanced Energy Materials*, 9(40):1902279, oct 2019. 33

[298] Q. Wang, Y. Shao, H. Xie, L. Lyu, X. Liu, Y. Gao, and J. Huang. Qualifying composition dependent p and n self-doping in CH3NH3PbI3. *Applied Physics Letters*, 105(16), 2014. 33

[299] J. Kim, S.-H. Lee, J. H. Lee, and K.-H. Hong. The Role of Intrinsic Defects in Methylammonium Lead Iodide Perovskite. *The Journal of Physical Chemistry Letters*, 5(8):1312–1317, apr 2014. 33, 37

[300] D. Song, P. Cui, T. Wang, D. Wei, M. Li, F. Cao, X. Yue, P. Fu, Y. Li, Y. He, B. Jiang, and M. Trevor. Managing Carrier Lifetime and Doping Property of Lead Halide Perovskite by Postannealing Processes for Highly Efficient Perovskite Solar Cells. *The Journal of Physical Chemistry C*, 119(40):22812–22819, oct 2015. 33

[301] W.-J. Yin, T. Shi, and Y. Yan. Unusual defect physics in CH3NH3PbI3 perovskite solar cell absorber. *Applied Physics Letters*, 104(6):063903, feb 2014. 33, 37, 89

[302] L. A. Frolova, N. N. Dremova, and P. A. Troshin. The chemical origin of the p-type and n-type doping effects in the hybrid methylammonium–lead iodide (MAPbI3) perovskite solar cells. *Chemical Communications*, 51(80):14917–14920, 2015. 33

[303] B. Dänekamp, C. Müller, M. Sendner, P. P. Boix, M. Sessolo, R. Lovrincic, and H. J. Bolink. Perovskite-Perovskite Homojunctions via Compositional Doping. *The Journal of Physical Chemistry Letters*, 9(11):2770–2775, jun 2018. 33

[304] P. Cui, D. Wei, J. Ji, H. Huang, E. Jia, S. Dou, T. Wang, W. Wang, and M. Li. Planar p–n homojunction perovskite solar cells with efficiency exceeding 21.3%. *Nature Energy*, 4(2):150–159, feb 2019. 33

[305] C. Lu, J. Zhang, D. Hou, X. Gan, H. Sun, Z. Zeng, R. Chen, H. Tian, Q. Xiong, Y. Zhang, Y. Li, and Y. Zhu. Calcium doped MAPbI3 with better energy state alignment in perovskite solar cells. *Applied Physics Letters*, 112(19):193901, may 2018. 33

[306] M. Chowdhury, S. Shahahmadi, P. Chelvanathan, S. Tiong, N. Amin, K. Techato, N. Nuthammachot, T. Chowdhury, and M. Suklueng. Effect of deep-level defect density of the absorber layer and n/i interface in perovskite solar cells by SCAPS-1D. *Results in Physics*, 16(July 2019):102839, mar 2020. 33, 34

[307] P. Yadav, K. Pandey, P. Bhatt, D. Raval, B. Tripathi, C. Kanth P., M. K. Pandey, and M. Kumar. Exploring the performance limiting parameters of perovskite solar cell through experimental analysis and device simulation. *Solar Energy*, 122:773–782, dec 2015. 33, 38

[308] L. Huang, X. Sun, C. Li, R. Xu, J. Xu, Y. Du, Y. Wu, J. Ni, H. Cai, J. Li, Z. Hu, and J. Zhang. Electron transport layer-free planar perovskite solar cells: Further performance enhancement perspective from device simulation. *Solar Energy Materials and Solar Cells*, 157:1038–1047, dec 2016. 33, 36

[309] F. Liu, J. Zhu, J. Wei, Y. Li, M. Lv, S. Yang, B. Zhang, J. Yao, and S. Dai. Numerical simulation: Toward the design of high-efficiency planar perovskite solar cells. *Applied Physics Letters*, 104(25):253508, jun 2014. 33, 35

[310] F. Anwar, R. Mahbub, S. S. Satter, and S. M. Ullah. Effect of Different HTM Layers and Electrical Parameters on ZnO Nanorod-Based Lead-Free Perovskite Solar Cell for High-Efficiency Performance. *International Journal of Photoenergy*, 2017:1–9, 2017. 33, 35, 36

[311] M. Shasti and A. Mortezaali. Numerical Study of Cu2O, SrCu2O2 , and CuAlO2 as Hole-Transport Materials for Application in Perovskite Solar Cells. *physica status solidi (a)*, 216(18):1900337, sep 2019. 33, 35, 37

[312] M. B. Johnston and L. M. Herz. Hybrid Perovskites for Photovoltaics: Charge-Carrier Recombination, Diffusion, and Radiative Efficiencies. *Accounts of Chemical Research*, 49(1):146–154, jan 2016. 33, 34

[313] T. W. Crothers, R. L. Milot, J. B. Patel, E. S. Parrott, J. Schlipf, P. Müller-Buschbaum, M. B. Johnston, and L. M. Herz. Photon Reabsorption Masks Intrinsic Bimolecular Charge-Carrier Recombination in CH3NH3PbI3 Perovskite. *Nano Letters*, 17(9):5782–5789, sep 2017. 34

[314] A. A. B. Baloch, M. I. Hossain, N. Tabet, and F. H. Alharbi. Practical Efficiency Limit of Methylammonium Lead Iodide Perovskite (CH3NH3PbI3) Solar Cells. *The Journal of Physical Chemistry Letters*, 9(2):426–434, jan 2018. 34, 36

[315] X. Zhang, J.-X. Shen, W. Wang, and C. G. Van de Walle. First-Principles Analysis of Radiative Recombination in Lead-Halide Perovskites. *ACS Energy Letters*, 3(10):2329–2334, oct 2018. 34

[316] X. Fu, K. J. Weber, and T. P. White. Characterization of trap states in perovskite films by simultaneous fitting of steady-state and transient photoluminescence measurements. *Journal of Applied Physics*, 124(7):073102, aug 2018. 34

[317] F. Staub, H. Hempel, J.-C. Hebig, J. Mock, U. W. Paetzold, U. Rau, T. Unold, and T. Kirchartz. Beyond Bulk Lifetimes: Insights into Lead Halide Perovskite Films from Time-Resolved Photoluminescence. *Physical Review Applied*, 6(4):044017, oct 2016. 34

[318] C. Wehrenfennig, G. E. Eperon, M. B. Johnston, H. J. Snaith, and L. M. Herz. High Charge Carrier Mobilities and Lifetimes in Organolead Trihalide Perovskites. *Advanced Materials*, 26(10):1584–1589, mar 2014. 34

[319] M. Saba, M. Cadelano, D. Marongiu, F. Chen, V. Sarritzu, N. Sestu, C. Figus, M. Aresti, R. Piras, A. Geddo Lehmann, C. Cannas, A. Musinu, F. Quochi, A. Mura, and G. Bongiovanni. Correlated electron-hole plasma in organometal perovskites. *Nature Communications*, 5(1):5049, dec 2014. 34

[320] J. S. Manser and P. V. Kamat. Band filling with free charge carriers in organometal halide perovskites. *Nature Photonics*, 8(9):737–743, sep 2014. 34

[321] C. Wehrenfennig, M. Liu, H. J. Snaith, M. B. Johnston, and L. M. Herz. Charge-carrier dynamics in vapour-deposited films of the organolead halide perovskite CH3NH3PbI3-xClx. *Energy Environ. Sci.*, 7(7):2269–2275, 2014. 34

[322] F. Staub, U. Rau, and T. Kirchartz. Statistics of the Auger Recombination of Electrons and Holes via Defect Levels in the Band Gap—Application to Lead-Halide Perovskites. *ACS Omega*, 3(7):8009–8016, jul 2018. 34, 36

[323] M. T. Trinh, X. Wu, D. Niesner, and X.-Y. Zhu. Many-body interactions in photo-excited lead iodide perovskite. *Journal of Materials Chemistry A*, 3(17):9285–9290, 2015. 34

[324] W. Rehman, R. L. Milot, G. E. Eperon, C. Wehrenfennig, J. L. Boland, H. J. Snaith, M. B. Johnston, and L. M. Herz. Charge-Carrier Dynamics and Mobilities in Formamidinium Lead Mixed-Halide Perovskites. *Advanced Materials*, 27(48):7938–7944, dec 2015. 34

[325] W. Rehman, D. P. McMeekin, J. B. Patel, R. L. Milot, M. B. Johnston, H. J. Snaith, and L. M. Herz. Photovoltaic mixed-cation lead mixed-halide perovskites: links between crystallinity, photo-stability and electronic properties. *Energy & Environmental Science*, 10(1):361–369, 2017. 34

[326] W. S. Yang, B.-W. Park, E. H. Jung, N. J. Jeon, Y. C. Kim, D. U. Lee, S. S. Shin, J. Seo, E. K. Kim, J. H. Noh, and S. I. Seok. Iodide management in formamidinium-lead-halide–based perovskite layers for efficient solar cells. *Science*, 356(6345):1376–1379, jun 2017. 35, 37

[327] J. W. Rosenberg, M. J. Legodi, Y. Rakita, D. Cahen, and M. Diale. Laplace current deep level transient spectroscopy measurements of defect states in methylammonium lead bromide single crystals. *Journal of Applied Physics*, 122(14):145701, oct 2017. 35

[328] M. Bruzzi, F. Gabelloni, N. Calisi, S. Caporali, and A. Vinattieri. Defective States in Micro-Crystalline CsPbBr3 and Their Role on Photoconductivity. *Nanomaterials*, 9(2):177, feb 2019. 35

[329] A. Y. Polyakov, N. B. Smirnov, I. V. Shchemerov, D. S. Saranin, T. S. Le, S. I. Didenko, D. V. Kuznetsov, A. Agresti, S. Pescetelli, F. Matteocci, and A. Di Carlo. Trap states in multication mesoscopic perovskite solar cells: A deep levels transient spectroscopy investigation. *Applied Physics Letters*, 113(26):263501, dec 2018. 35, 37

[330] G. Landi, H. C. Neitzert, C. Barone, C. Mauro, F. Lang, S. Albrecht, B. Rech, and S. Pagano. Correlation between Electronic Defect States Distribution and Device Performance of Perovskite Solar Cells. *Advanced Science*, 4(10):1700183, oct 2017. 35

[331] M. Bruzzi, N. Falsini, N. Calisi, and A. Vinattieri. Electrically Active Defects in Polycrystalline and Single Crystal Metal Halide Perovskite. *Energies*, 13(7):1643, apr 2020. 35

[332] S. Heo, G. Seo, Y. Lee, D. Lee, M. Seol, J. Lee, J.-B. Park, K. Kim, D.-J. Yun, Y. S. Kim, J. K. Shin, T. K. Ahn, and M. K. Nazeeruddin. Deep level trapped defect analysis in CH3NH3PbI3 perovskite solar cells by deep level transient spectroscopy. *Energy & Environmental Science*, 10(5):1128–1133, 2017. 35

[333] A. Musiienko, P. Moravec, R. Grill, P. Praus, I. Vasylchenko, J. Pekarek, J. Tisdale, K. Ridzonova, E. Belas, L. Landová, B. Hu, E. Lukosi, and M. Ahmadi. Deep levels, charge transport and mixed conductivity in organometallic halide perovskites. *Energy & Environmental Science*, 12(4):1413–1425, 2019. 35

[334] J. Xue, X. Hu, Y. Guo, G. Weng, J. Jiang, S. Chen, Z. Zhu, and J. Chu. Diagnosis of electrically active defects in CH3NH3PbI3 perovskite solar cells via admittance spectroscopy measurements. *Applied Optics*, 59(2):552, 2020. 35

[335] M. Zhang, Z. Zheng, Q. Fu, P. Guo, S. Zhang, C. Chen, H. Chen, M. Wang, W. Luo, and Y. Tian. Determination of Defect Levels in Melt-Grown All-Inorganic Perovskite CsPbBr3 Crystals by Thermally Stimulated Current Spectra. *The Journal of Physical Chemistry C*, 122(19):10309–10315, may 2018. 35

[336] D. Macdonald and L. J. Geerligs. Recombination activity of interstitial iron and other transition metal point defects in p- and n-type crystalline silicon. *Applied Physics Letters*, 85(18):4061–4063, nov 2004. 35

[337] T. Kirchartz, L. Krückemeier, and E. L. Unger. Research Update: Recombination and open-circuit voltage in lead-halide perovskites. *APL Materials*, 6(10):100702, oct 2018. 36, 37

[338] D. Meggiolaro, S. G. Motti, E. Mosconi, A. J. Barker, J. Ball, C. Andrea Riccardo Perini, F. Deschler, A. Petrozza, and F. De Angelis. Iodine chemistry determines the defect tolerance of lead-halide perovskites. *Energy & Environmental Science*, 11(3):702–713, 2018. 36, 37

[339] H. Jin, E. Debroye, M. Keshavarz, I. G. Scheblykin, M. B. J. Roeffaers, J. Hofkens, and J. A. Steele. It's a trap! On the nature of localised states and charge trapping in lead halide perovskites. *Materials Horizons*, 7(2):397–410, 2020. 36, 37, 62, 89

[340] L. K. Ono, S. F. Liu, and Y. Qi. Reducing Detrimental Defects for High-Performance Metal Halide Perovskite Solar Cells. *Angewandte Chemie International Edition*, 59(17):6676–6698, apr 2020. 36, 37

[341] H. Ikeda. Evaluation of grain boundary trap states in polycrystalline-silicon thin-film transistors by mobility and capacitance measurements. *Journal of Applied Physics*, 91(7):4637–4645, apr 2002. 36

[342] L. Kerr, S. S. Li, S. Johnston, T. Anderson, O. Crisalle, W. Kim, J. Abushama, and R. Noufi. Investigation of defect properties in Cu(In,Ga)Se2 solar cells by deep-level transient spectroscopy. *Solid-State Electronics*, 48(9):1579–1586, sep 2004. 36

[343] S. Shao and M. A. Loi. The Role of the Interfaces in Perovskite Solar Cells. *Advanced Materials Interfaces*, 7(1):1901469, jan 2020. 36

[344] S. Ravishankar, S. Gharibzadeh, C. Roldán-Carmona, G. Grancini, Y. Lee, M. Ralaiar-isoa, A. M. Asiri, N. Koch, J. Bisquert, and M. K. Nazeeruddin. Influence of Charge Transport Layers on Open-Circuit Voltage and Hysteresis in Perovskite Solar Cells. *Joule*, 2(4):788–798, apr 2018. 36

[345] G. Xing, N. Mathews, S. S. Lim, N. Yantara, X. Liu, D. Sabba, M. Grätzel, S. Mhaisalkar, and T. C. Sum. Low-temperature solution-processed wavelength-tunable perovskites for lasing. *Nature Materials*, 13(5):476–480, may 2014. 36

[346] D. Meggiolaro, E. Mosconi, and F. De Angelis. Formation of Surface Defects Dominates Ion Migration in Lead-Halide Perovskites. *ACS Energy Letters*, 4(3):779–785, mar 2019. 36

[347] J.-W. Lee, S.-G. Kim, J.-M. Yang, Y. Yang, and N.-G. Park. Verification and mitigation of ion migration in perovskite solar cells. *APL Materials*, 7(4):041111, apr 2019. 36, 88, 89

[348] D. A. Jacobs, Y. Wu, H. Shen, C. Barugkin, F. J. Beck, T. P. White, K. Weber, and K. R. Catchpole. Hysteresis phenomena in perovskite solar cells: the many and varied effects of ionic accumulation. *Physical Chemistry Chemical Physics*, 19(4):3094–3103, 2017. 36, 88

[349] S. Rai, B. K. Pandey, and D. K. Dwivedi. Modeling of highly efficient and low cost CH3NH3Pb(I1-xClx)3 based perovskite solar cell by numerical simulation. *Optical Materials*, 100(December 2019):109631, 2020. 36, 38

[350] N. Zarabinia, R. Rasuli, and E. Mohajerani. New insight on the open-circuit voltage of perovskite solar cells: The role of defect-density distribution and electric field in the active layer. *International Journal of Energy Research*, 45(4):5190–5200, mar 2021. 36

[351] Y. Raoui, H. Ez-Zahraouy, S. Ahmad, and S. Kazim. Unravelling the theoretical window to fabricate high performance inorganic perovskite solar cells. *Sustainable Energy & Fuels*, 2020. 36

[352] A. S. Chouhan, N. P. Jasti, and S. Avasthi. Effect of interface defect density on performance of perovskite solar cell: Correlation of simulation and experiment. *Materials Letters*, 221:150–153, jun 2018. 36

[353] F. Izadi, A. Ghobadi, A. Gharaati, M. Minbashi, and A. Hajjiah. Effect of interface defects on high efficient perovskite solar cells. *Optik*, 227(August 2020):166061, feb 2021. 36, 37

[354] S. Ahmmed, A. Aktar, M. H. Rahman, J. Hossain, and A. B. M. Ismail. Design and simulation of a high-performance CH3NH3Pb(I1-xClx)3-based perovskite solar cell using a CeO x electron transport layer and NiO hole transport layer. *Semiconductor Science and Technology*, 36(3):035002, mar 2021. 36, 37

[355] D. Prochowicz, P. Yadav, M. Saliba, M. Saski, S. M. Zakeeruddin, J. Lewiński, and M. Grätzel. Reduction in the Interfacial Trap Density of Mechanochemically Synthesized MAPbI3. *ACS Applied Materials & Interfaces*, 9(34):28418–28425, aug 2017. 36, 38

[356] D. Meggiolaro and F. De Angelis. First-Principles Modeling of Defects in Lead Halide Perovskites: Best Practices and Open Issues. *ACS Energy Letters*, 3(9):2206–2222, sep 2018. 36, 37, 89

[357] J. S. Park, S. Kim, Z. Xie, and A. Walsh. Point defect engineering in thin-film solar cells. *Nature Reviews Materials*, 3(7):194–210, jul 2018. 36

[358] M. Burgelman, K. Decock, S. Khelifi, and A. Abass. Advanced electrical simulation of thin film solar cells. *Thin Solid Films*, 535(1):296–301, may 2013. 37

[359] X. Chen, S. Cheng, L. Xiao, and H. Sun. Identifying, understanding and controlling defects and traps in halide perovskites for optoelectronic devices: a review. *Journal of Physics D: Applied Physics*, 53(37), 2020. 37

[360] F. Wang, S. Bai, W. Tress, A. Hagfeldt, and F. Gao. Defects engineering for high-performance perovskite solar cells. *npj Flexible Electronics*, 2(1), 2018. 37

[361] E. Aydin, M. Bastiani, and S. Wolf. Defect and Contact Passivation for Perovskite Solar Cells. *Advanced Materials*, 31(25):1900428, jun 2019. 37

[362] M. H. Du. Density functional calculations of native defects in CH3NH3PbI3: Effects of spin - Orbit coupling and self-interaction error. *Journal of Physical Chemistry Letters*, 6(8):1461–1466, 2015. 37

[363] M. S. Jamal, S. A. Shahahmadi, P. Chelvanathan, N. Asim, H. Misran, M. I. Hossain, N. Amin, K. Sopian, and M. Akhtaruzzaman. Effect of defect density and energy level mismatch on the performance of perovskite solar cells by numerical simulation. *Optik*, 182(December 2018):1204–1210, 2019. 37

[364] W. Ke, G. Fang, J. Wang, P. Qin, H. Tao, H. Lei, Q. Liu, X. Dai, and X. Zhao. Perovskite solar cell with an efficient TiO2 compact film. *ACS Applied Materials and Interfaces*, 6(18):15959–15965, 2014. 38

[365] K. J. Rietwyk, B. Tan, A. Surmiak, J. Lu, D. P. McMeekin, S. R. Raga, N. Duffy, and U. Bach. Light intensity modulated photoluminescence for rapid series resistance mapping of perovskite solar cells. *Nano Energy*, 73(March):104755, jul 2020. 38

[366] N. Mundhaas, Z. J. Yu, K. A. Bush, H. P. Wang, J. Häusele, S. Kavadiya, M. D. McGehee, and Z. C. Holman. Series Resistance Measurements of Perovskite Solar Cells Using Jsc–Voc Measurements. *Solar RRL*, 3(4):5–9, 2019. 38

[367] D. Walter, Y. Wu, T. Duong, J. Peng, L. Jiang, K. C. Fong, and K. Weber. On the Use of Luminescence Intensity Images for Quantified Characterization of Perovskite Solar Cells: Spatial Distribution of Series Resistance. *Advanced Energy Materials*, 8(2):1701522, jan 2018. 38

[368] Y. Li, B. Ding, Q.-Q. Chu, G.-J. Yang, M. Wang, C.-X. Li, and C.-J. Li. Ultra-high open-circuit voltage of perovskite solar cells induced by nucleation thermodynamics on rough substrates. *Scientific Reports*, 7(1):46141, may 2017. 38

[369] D. C. Nguyen, S.-y. Joe, N. Y. Ha, H. J. Park, J.-Y. Park, Y. H. Ahn, and S. Lee. Hole-extraction layer dependence of defect formation and operation of planar CH3NH3PbI3 perovskite solar cells. *physica status solidi (RRL) - Rapid Research Letters*, 11(2):1600395, feb 2017. 38

[370] Y. Wu, X. Yang, H. Chen, K. Zhang, C. Qin, J. Liu, W. Peng, A. Islam, E. Bi, F. Ye, M. Yin, P. Zhang, and L. Han. Highly compact TiO2 layer for efficient hole-blocking in perovskite solar cells. *Applied Physics Express*, 7(5):052301, may 2014. 38

[371] H.-W. Kang, J.-W. Lee, D.-Y. Son, and N.-G. Park. Modulation of photovoltage in mesoscopic perovskite solar cell by controlled interfacial electron injection. *RSC Advances*, 5(59):47334–47340, 2015. 38

[372] A. A. Mamun, T. T. Ava, K. Zhang, H. Baumgart, and G. Namkoong. New PCB-M/carbon based electron transport layer for perovskite solar cells. *Physical Chemistry Chemical Physics*, 19(27):17960–17966, 2017. 38

[373] C.-G. Wu, C.-H. Chiang, Z.-L. Tseng, M. K. Nazeeruddin, A. Hagfeldt, and M. Grätzel. High efficiency stable inverted perovskite solar cells without current hysteresis. *Energy & Environmental Science*, 8(9):2725–2733, 2015. 38

[374] D. Głowienka. Impact of Tin Oxide Buffer Layer Deposition on the Operation of the Perovskite Solar Cell. *To be published*, 2021. 38, 50, 53, 68, 83

[375] J.-Y. Jeng, Y.-F. Chiang, M.-H. Lee, S.-R. Peng, T.-F. Guo, P. Chen, and T.-C. Wen. CH3NH3PbI3 Perovskite/Fullerene Planar-Heterojunction Hybrid Solar Cells. *Advanced Materials*, 25(27):3727–3732, jul 2013. 38

[376] L. Xiong, Y. Guo, J. Wen, H. Liu, G. Yang, P. Qin, and G. Fang. Review on the Application of SnO2 in Perovskite Solar Cells. *Advanced Functional Materials*, 28(35):1802757, aug 2018. 38

[377] C. Li, S. Tscheuschner, F. Paulus, P. E. Hopkinson, J. Kießling, A. Köhler, Y. Vaynzof, and S. Huettner. Iodine Migration and its Effect on Hysteresis in Perovskite Solar Cells. *Advanced Materials*, 28(12):2446–2454, 2016. 40

[378] A. J. Bett, K. M. Winkler, M. Bivour, L. Cojocaru, Ö. S. Kabakli, P. S. C. Schulze, G. Siefer, L. Tutsch, M. Hermle, S. W. Glunz, and J. C. Goldschmidt. Semi-Transparent Perovskite Solar Cells with ITO Directly Sputtered on Spiro-OMeTAD for Tandem Applications. *ACS Applied Materials & Interfaces*, 11(49):45796–45804, dec 2019. 41

[379] D. Chen, S. Pang, L. Zhou, X. Li, A. Su, W. Zhu, J. Chang, J. Zhang, C. Zhang, and Y. Hao. An efficient TeO2/Ag transparent top electrode for 20%efficiency bifacial perovskite solar cells with a bifaciality factor exceeding 80%. *Journal of Materials Chemistry A*, 7(25):15156–15163, 2019. 41, 68

[380] F. Liang, Z. Ying, Y. Lin, B. Tu, Z. Zhang, Y. Zhu, H. Pan, H. Li, L. Luo, O. Ageev, and Z. He. High-Performance Semitransparent and Bifacial Perovskite Solar Cells with MoOx/Ag/WOx as the Rear Transparent Electrode. *Advanced Materials Interfaces*, 7(20):2000591, oct 2020. 41

[381] C. Hanmandlu, C.-Y. Chen, K. M. Boopathi, H.-W. Lin, C.-S. Lai, and C.-W. Chu. Bifacial Perovskite Solar Cells Featuring Semitransparent Electrodes. *ACS Applied Materials & Interfaces*, 9(38):32635–32642, sep 2017. 41

[382] S. Pang, D. Chen, C. Zhang, J. Chang, Z. Lin, H. Yang, X. Sun, J. Mo, H. Xi, G. Han, J. Zhang, and Y. Hao. Efficient bifacial semitransparent perovskite solar cells with silver thin film electrode. *Solar Energy Materials and Solar Cells*, 170(February):278–286, oct 2017. 41

[383] M. Saliba and L. Etgar. Current Density Mismatch in Perovskite Solar Cells. *ACS Energy Letters*, 5(9):2886–2888, sep 2020. 43

[384] D. Amgar, T. Binyamin, V. Uvarov, and L. Etgar. Near ultra-violet to mid-visible band gap tuning of mixed cation RbxCs1-xPbX3(X = Cl or Br) perovskite nanoparticles. *Nanoscale*, 10(13):6060–6068, 2018. 44

[385] Y. Shi, J. Xi, T. Lei, F. Yuan, J. Dai, C. Ran, H. Dong, B. Jiao, X. Hou, and Z. Wu. Rubidium Doping for Enhanced Performance of Highly Efficient Formamidinium-Based Perovskite Light-Emitting Diodes. *ACS Applied Materials & Interfaces*, 10(11):9849–9857, mar 2018. 44

[386] X. Cao, L. Zhi, Y. Jia, Y. Li, K. Zhao, X. Cui, L. Ci, K. Ding, and J. Wei. Enhanced efficiency of perovskite solar cells by introducing controlled chloride incorporation into MAPbI3 perovskite films. *Electrochimica Acta*, 275:1–7, jun 2018. 44

[387] M. I. Saidaminov, J. Kim, A. Jain, R. Quintero-Bermudez, H. Tan, G. Long, F. Tan, A. Johnston, Y. Zhao, O. Voznyy, and E. H. Sargent. Suppression of atomic vacancies via incorporation of isovalent small ions to increase the stability of halide perovskite solar cells in ambient air. *Nature Energy*, 3(8):648–654, aug 2018. 44

[388] J. Li, X. Du, G. Niu, H. Xie, Y. Chen, Y. Yuan, Y. Gao, H. Xiao, J. Tang, A. Pan, and B. Yang. Rubidium Doping to Enhance Carrier Transport in CsPbBr3 Single Crystals for High-Performance X-Ray Detection. *ACS Applied Materials & Interfaces*, 12(1):989–996, jan 2020. 44

[389] M. Samiee, S. Konduri, B. Ganapathy, R. Kottokkaran, H. A. Abbas, A. Kitahara, P. Joshi, L. Zhang, M. Noack, and V. Dalal. Defect density and dielectric constant in perovskite solar cells. *Applied Physics Letters*, 105(15):153502, oct 2014. 44

[390] X. Xu, C. Ma, Y.-M. Xie, Y. Cheng, Y. Tian, M. Li, Y. Ma, C.-S. Lee, and S.-W. Tsang. Air-processed mixed-cation Cs0.15FA0.85PbI3 planar perovskite solar cells derived from a PbI2-CsI-FAI intermediate complex. *Journal of Materials Chemistry A*, 6(17):7731–7740, 2018. 46, 47

[391] S.-H. Turren-Cruz, M. Saliba, M. T. Mayer, H. Juárez-Santiesteban, X. Mathew, L. Nienhaus, W. Tress, M. P. Erodici, M.-J. Sher, M. G. Bawendi, M. Grätzel, A. Abate, A. Hagfeldt, and J.-P. Correa-Baena. Enhanced charge carrier mobility and lifetime suppress hysteresis and improve efficiency in planar perovskite solar cells. *Energy & Environmental Science*, 11(1):78–86, 2018. 46, 48

[392] B. Charles, M. T. Weller, S. Rieger, L. E. Hatcher, P. F. Henry, J. Feldmann, D. Wolverson, and C. C. Wilson. Phase Behavior and Substitution Limit of Mixed Cesium-Formamidinium Lead Triiodide Perovskites. *Chemistry of Materials*, 32(6):2282–2291, mar 2020. 46, 137

[393] C. Wu, X. Zheng, Q. Yang, Y. Yan, M. Sanghadasa, and S. Priya. Crystallization of HC(NH2)2PbI3 Black Polymorph by Solvent Intercalation for Low Temperature Solution Processing of Perovskite Solar Cells. *The Journal of Physical Chemistry C*, 120(47):26710–26719, dec 2016. 47

[394] J. T. Jacobsson, J. P. Correa-Baena, M. Pazoki, M. Saliba, K. Schenk, M. Grätzel, and A. Hagfeldt. Exploration of the compositional space for mixed lead halogen perovskites for high efficiency solar cells. *Energy and Environmental Science*, 9(5):1706–1724, 2016. 47

[395] R. E. Beal, D. J. Slotcavage, T. Leijtens, A. R. Bowring, R. A. Belisle, W. H. Nguyen, G. F. Burkhard, E. T. Hoke, and M. D. McGehee. Cesium Lead Halide Perovskites with Improved Stability for Tandem Solar Cells. *The Journal of Physical Chemistry Letters*, 7(5):746–751, mar 2016. 47

[396] M. Stolterfoht, M. Grischek, P. Caprioglio, C. M. Wolff, E. Gutierrez-Partida, F. Peña-Camargo, D. Rothhardt, S. Zhang, M. Raoufi, J. Wolansky, M. Abdi-Jalebi, S. D. Stranks, S. Albrecht, T. Kirchartz, and D. Neher. How To Quantify the Efficiency Potential of Neat Perovskite Films: Perovskite Semiconductors with an Implied Efficiency Exceeding 28%. *Advanced Materials*, 32(17):2000080, apr 2020. 48

[397] A. Babaei, K. P. S. Zanoni, L. Gil-Escrig, D. Pérez-del Rey, P. P. Boix, M. Sessolo, and H. J. Bolink. Efficient Vacuum Deposited P-I-N Perovskite Solar Cells by Front Contact Optimization. *Frontiers in Chemistry*, 7(January):1–6, jan 2020. 49

[398] S. Ryu, D. C. Nguyen, N. Y. Ha, H. J. Park, Y. H. Ahn, J.-Y. Park, and S. Lee. Light Intensity-dependent Variation in Defect Contributions to Charge Transport and Recombination in a Planar MAPbI3 Perovskite Solar Cell. *Scientific Reports*, 9(1):19846, dec 2019. 49

[399] T. Du, W. Xu, S. Xu, S. R. Ratnasingham, C.-T. Lin, J. Kim, J. Briscoe, M. A. McLachlan, and J. R. Durrant. Light-intensity and thickness dependent efficiency of planar perovskite solar cells: charge recombination versus extraction. *Journal of Materials Chemistry C*, 8(36):12648–12655, 2020. 49

[400] B. Chen, H. Hu, T. Salim, and Y. M. Lam. A facile method to evaluate the influence of trap densities on perovskite solar cell performance. *Journal of Materials Chemistry C*, 7(19):5646–5651, 2019. 49, 52

[401] H. Baig, H. Kanda, A. M. Asiri, M. K. Nazeeruddin, and T. Mallick. Increasing efficiency of perovskite solar cells using low concentrating photovoltaic systems. *Sustainable Energy & Fuels*, 4(2):528–537, 2020. 52

[402] M. Liu, M. Endo, A. Shimazaki, A. Wakamiya, and Y. Tachibana. Light Intensity Dependence of Performance of Lead Halide Perovskite Solar Cells. *Journal of Photopolymer Science and Technology*, 30(5):577–582, 2017. 52

[403] P. Caprioglio, M. Stolterfoht, C. M. Wolff, T. Unold, B. Rech, S. Albrecht, and D. Neher. On the Relation between the Open-Circuit Voltage and Quasi-Fermi Level Splitting in Efficient Perovskite Solar Cells. *Advanced Energy Materials*, 9(33):1901631, sep 2019. 63, 65

[404] B. T. Feleki, C. H. L. Weijtens, M. M. Wienk, and R. A. J. Janssen. Thin Thermally Evaporated Organic Hole Transport Layers for Reduced Optical Losses in Substrate-Configuration Perovskite Solar Cells. *ACS Applied Energy Materials*, 4(4):3033–3043, apr 2021. 68

[405] A. Sadollahkhani, P. Liu, V. Leandri, M. Safdari, W. Zhang, and J. M. Gardner. Energetic Barriers to Interfacial Charge Transfer and Ion Movement in Perovskite Solar Cells. *ChemPhysChem*, 18(21):3047–3055, nov 2017. 69

[406] O. Gunawan, T. Gokmen, and D. B. Mitzi. Suns-Voc characteristics of high performance kesterite solar cells. *Journal of Applied Physics*, 116(8):084504, aug 2014. 72, 88

[407] R. Saive. S-Shaped Current–Voltage Characteristics in Solar Cells: A Review. *IEEE Journal of Photovoltaics*, 9(6):1477–1484, nov 2019. 72

[408] A. Gusain, R. M. Faria, and P. B. Miranda. Polymer Solar Cells—Interfacial Processes Related to Performance Issues. *Frontiers in Chemistry*, 7(February), feb 2019. 72

[409] A. Sundqvist, O. J. Sandberg, M. Nyman, J.-H. Smått, and R. Österbacka. Origin of the S-Shaped JV Curve and the Light-Soaking Issue in Inverted Organic Solar Cells. *Advanced Energy Materials*, 6(6):1502265, mar 2016. 72

[410] W. Tress, A. Petrich, M. Hummert, M. Hein, K. Leo, and M. Riede. Imbalanced mobilities causing S-shaped IV curves in planar heterojunction organic solar cells. *Applied Physics Letters*, 98(6):063301, feb 2011. 72

[411] W. Tress, S. Corvers, K. Leo, and M. Riede. Investigation of Driving Forces for Charge Extraction in Organic Solar Cells: Transient Photocurrent Measurements on Solar Cells Showing S-Shaped Current-Voltage Characteristics. *Advanced Energy Materials*, 3(7):873–880, jul 2013. 72

[412] S.-E. Chiang, J.-R. Wu, H.-M. Cheng, C.-L. Hsu, J.-L. Shen, C.-T. Yuan, and S. H. Chang. Origins of the s-shape characteristic in J – V curve of inverted-type perovskite solar cells. *Nanotechnology*, 31(11):115403, mar 2020. 72

[413] J. Werner, G. Dubuis, A. Walter, P. Löper, S.-J. Moon, S. Nicolay, M. Morales-Masis, S. De Wolf, B. Niesen, and C. Ballif. Sputtered rear electrode with broadband transparency for perovskite solar cells. *Solar Energy Materials and Solar Cells*, 141:407–413, oct 2015. 72

[414] L. X. Shi, Z. S. Wang, Z. Huang, W. E. I. Sha, H. Wang, and Z. Zhou. The effects of interfacial recombination and injection barrier on the electrical characteristics of perovskite solar cells. *AIP Advances*, 8(2):025312, feb 2018. 72, 83

[415] A. Guerrero, J. You, C. Aranda, Y. S. Kang, G. Garcia-Belmonte, H. Zhou, J. Bisquert, and Y. Yang. Interfacial Degradation of Planar Lead Halide Perovskite Solar Cells. *ACS Nano*, 10(1):218–224, jan 2016. 72

[416] M. Saliba, M. Stolterfoht, C. M. Wolff, D. Neher, and A. Abate. Measuring Aging Stability of Perovskite Solar Cells. *Joule*, 2(6):1019–1024, jun 2018. 73

[417] F. Xu, J. Zhu, R. Cao, S. Ge, W. Wang, H. Xu, R. Xu, Y. Wu, M. Gao, Z. Ma, F. Hong, and Z. Jiang. Elucidating the evolution of the current-voltage characteristics of planar organometal halide perovskite solar cells to an S-shape at low temperature. *Solar Energy Materials and Solar Cells*, 157:981–988, dec 2016. 88

[418] F. J. García-Sánchez, D. Lugo-Muñoz, J. Muci, and A. Ortiz-Conde. Lumped Parameter Modeling of Organic Solar Cells' S-Shaped I-V Characteristics. *IEEE Journal of Photovoltaics*, 3(1):330–335, jan 2013. 88

[419] A. Mannodi-Kanakkithodi, J.-S. Park, D. H. Cao, N. Jeon, A. B. Martinson, and M. K. Chan. First-principles Study of Intrinsic and Extrinsic Point Defects in Lead-Based Hybrid Perovskites. In *2018 IEEE 7th World Conference on Photovoltaic Energy Conversion (WCPEC) (A Joint Conference of 45th IEEE PVSC, 28th PVSEC & 34th EU PVSEC)*, pages 0495–0498. IEEE, jun 2018. 89

[420] N. Liu and C. Yam. First-principles study of intrinsic defects in formamidinium lead triiodide perovskite solar cell absorbers. *Physical Chemistry Chemical Physics*, 20(10):6800–6804, 2018. 89

[421] Z. Xiao and Y. Yan. Progress in Theoretical Study of Metal Halide Perovskite Solar Cell Materials. *Advanced Energy Materials*, 7(22):1701136, nov 2017. 89

[422] A. Buin, P. Pietsch, J. Xu, O. Voznyy, A. H. Ip, R. Comin, and E. H. Sargent. Materials Processing Routes to Trap-Free Halide Perovskites. *Nano Letters*, 14(11):6281–6286, nov 2014. 89

[423] C. Lin, S. Li, W. Zhang, C. Shao, and Z. Yang. Effect of Bromine Substitution on the Ion Migration and Optical Absorption in MAPbI 3 Perovskite Solar Cells: The First-Principles Study. *ACS Applied Energy Materials*, 1(3):1374–1380, mar 2018. 90

[424] R. García-Rodríguez, D. Ferdani, S. Pering, P. J. Baker, and P. J. Cameron. Influence of bromide content on iodide migration in inverted MAPb(I1-xBrx)3 perovskite solar cells. *Journal of Materials Chemistry A*, 7(39):22604–22614, 2019. 90

A. Matlab script

```matlab
% set AntiReflection to true if you want to compensate the generation for an MgF2
    anti-reflection layer (glass side only).
% AR_value is the value by which the generation is multiplied to compensate for
    an MgF2 anti-reflection layer (for example 1.025 = 2.5% increase).
AntiReflection = true;
AR_value = 1.025;

% outputs predicted Jsc under AM1.5 illumination assuming 100% internal quantum
    efficiency at all wavelengths
    if AntiReflection == true
        Jsc=sum(Gx)*stepsize*1e-7*q*1e3*AR_value %in mA/cm^2
    else
        Jsc=sum(Gx)*stepsize*1e-7*q*1e3 %in mA/cm^2
    end

%Saves the generation rate as a text file for SCAPS from Glass side
%Save only the HTL (activeLayer-1), perovskite and ETL (activeLayer+1) and
    accounts for their thicknesses.
%Each row is in the file 1 nm, HTL and ETL have a value of 0 for generation.
%Variables activeLayer and thicknesses are defined in the original Matlab code.
generation=[];
count=1;
for i = 1:length(thicknesses)
    if i == activeLayer-1
        for j = 1:thicknesses(1,activeLayer-1)
            generation = [generation; j,0];
        end
    elseif i == activeLayer
        for j = thicknesses(1,activeLayer-1)+1:thicknesses(1,activeLayer-1)+
            thicknesses(1,activeLayer)
            generation = [generation; j,Gx(count)];
            count=count+1;
        end
    elseif i == activeLayer+1
        for j = thicknesses(1,activeLayer-1)+thicknesses(1,activeLayer)+1:
            thicknesses(1,activeLayer-1)+thicknesses(1,activeLayer)+thicknesses(1,
            activeLayer+1)
            generation = [generation; j,0];
        end
    else
    end
end
```

```matlab
%Save the generation rate as a text file for SCAPS for illumination from ITO side
%Save only the HTL (activeLayer+1), perovskite and ETL (activeLayer-1).
%Each row is in the file 1 nm, HTL and ETL have a value of 0 for generation.
%Variables activeLayer and thicknesses are defined in the original Matlab code.
GxFlip=flip(Gx);
generation=[];
count=1;
for i = length(thicknesses):-1:1
    if i == activeLayer+1
        for j = 1:thicknesses(1,activeLayer+1)
            generation = [generation; j,0];
        end
    elseif i == activeLayer
        for j = thicknesses(1,activeLayer+1)+1:thicknesses(1,activeLayer+1)+
            thicknesses(1,activeLayer)
            generation = [generation; j,GxFlip(count)];
            count=count+1;
        end
    elseif i == activeLayer-1
        for j = thicknesses(1,activeLayer+1)+thicknesses(1,activeLayer)+1:
            thicknesses(1,activeLayer+1)+thicknesses(1,activeLayer)+thicknesses(1,
            activeLayer-1)
            generation = [generation; j,0];
        end
    else
    end
end

% convert the values in 'generation' to the correct units (micrometer and (#/m3.s
    )) that are used in SCAPS and save the data to a text file.
for i = 1:length(generation)
    generation(i,1)=generation(i,1)*10^-3;
    if AntiReflection == true
        generation(i,2)=AR_value*generation(i,2)*10^6;
    else
        generation(i,2)=generation(i,2)*10^6;
    end
end

save('generation.txt','generation','-ASCII');
end
```

B. Additional figures

B.1 Transmittance and reflectance data
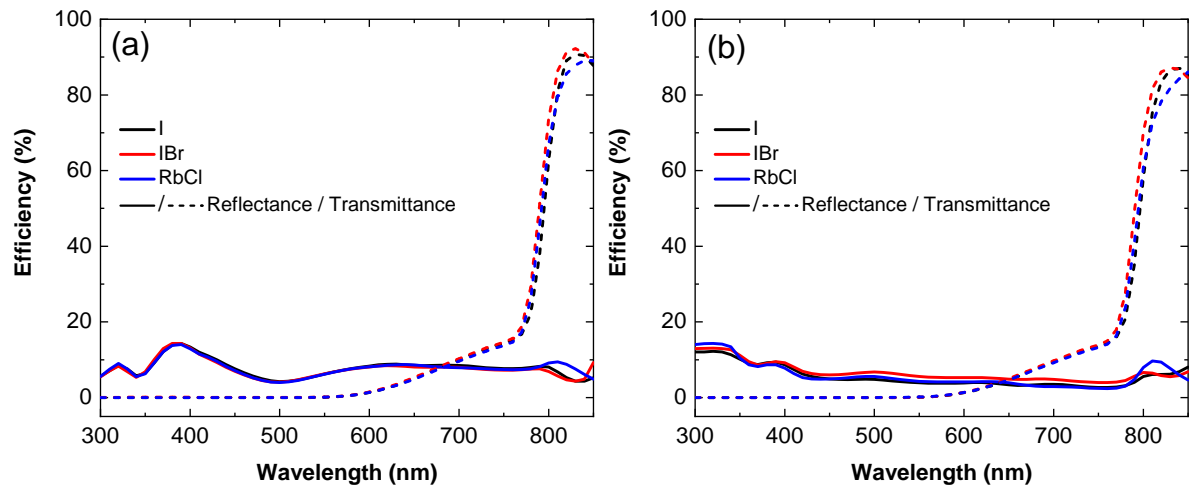
Figure B.1: Transmittance and Reflectance of each composition.
The measurement curve is a single measurement of one sample rather than the average of all samples.
(a) Illumination from glass side (b) Illumination from ITO side.

B.2 XRD Vesta calculation
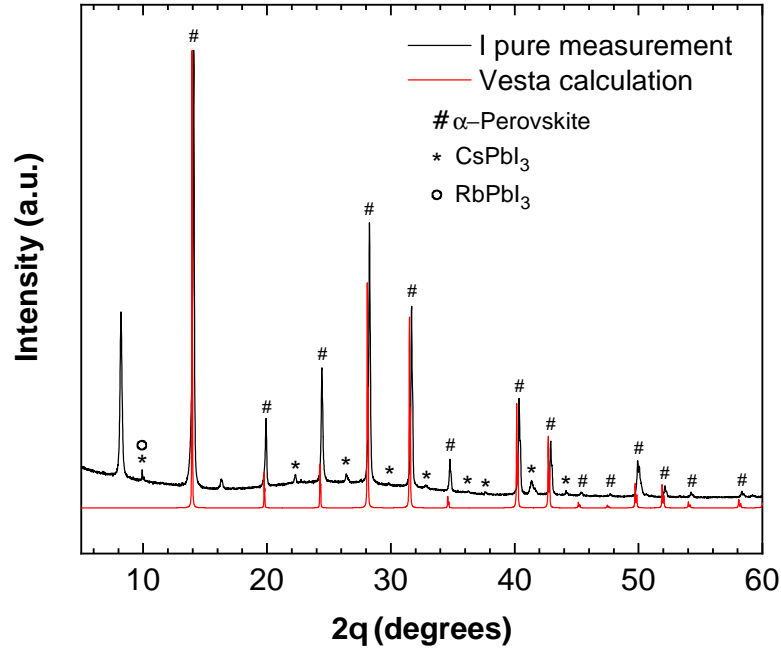
Figure B.2: Comparison XRD measurement and Vesta calculation

The Vesta software has an option to calculate the powder diffraction pattern. This is calculated for a $Cs_{0.1}FA_{0.9}PbI_3$ composition investigated by Charles et al.[392] and shows an agreement with the location of the α-perovskite phase of the I pure perovskite and no correspondence to the $CsPbI_3$ phase.

B.3 Simulation sweeps
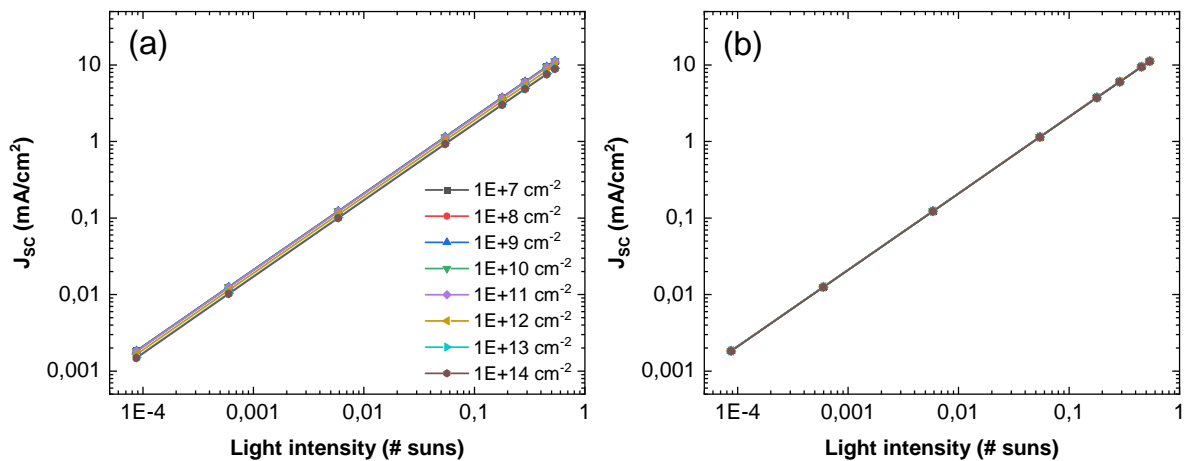
Figure B.3: Simulation sweep of the interface defect densities at J_{SC}

Illumination from glass side. The other parameters are set according to the optimized fresh device with doping set to zero. (a) PTAA/perovskite interface, (b) perovskite/PCBM interface.
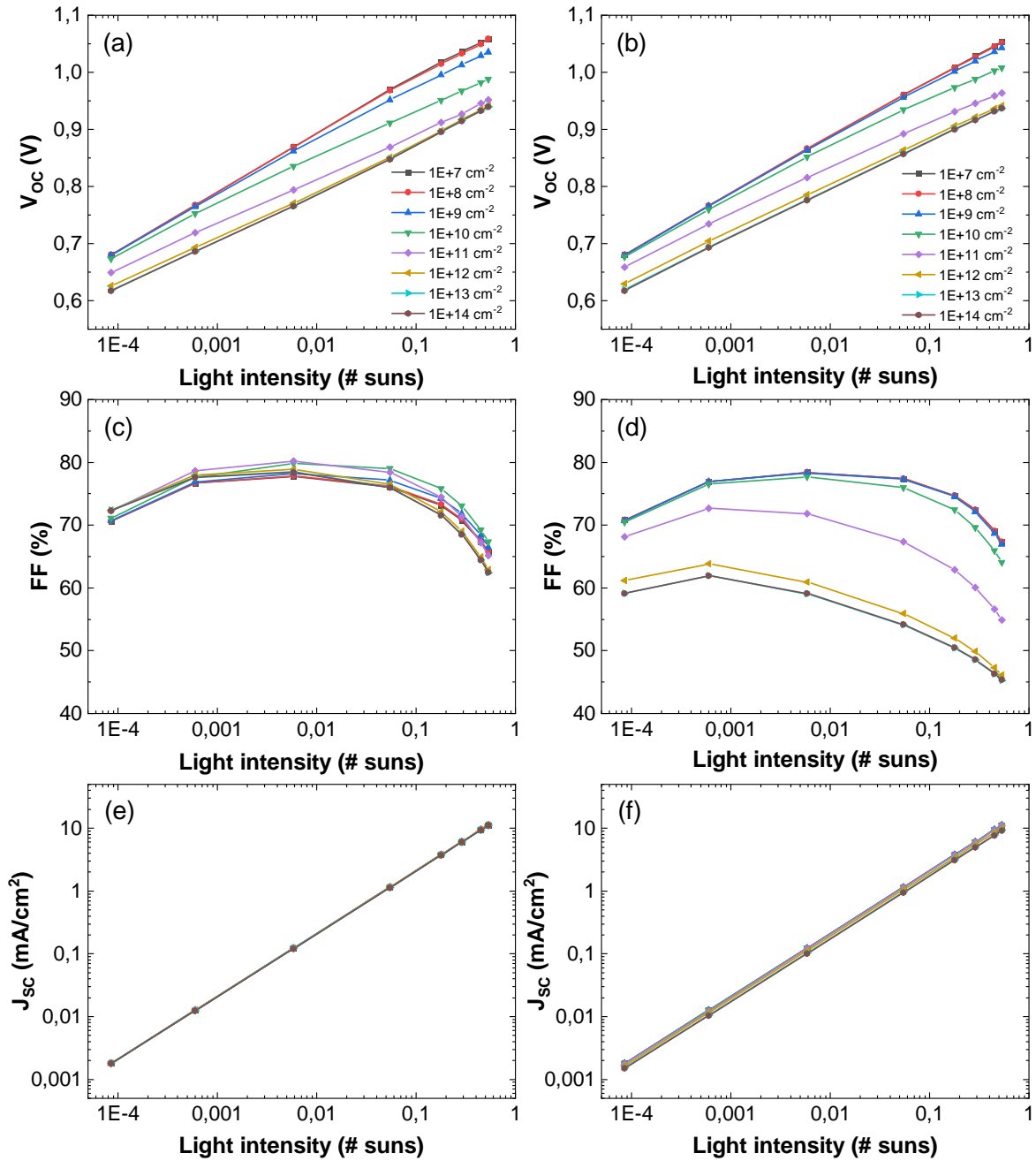
Figure B.4: Simulation sweep of the interface defect densities for ITO side illumination The other parameters are set according to the optimized fresh device with doping set to zero. PTAA/perovskite interface: (a) V_{OC}, (c) FF, (e) J_{SC} and perovskite/PCBM interface: (b) V_{OC}, (d) FF, (f) J_{SC}.
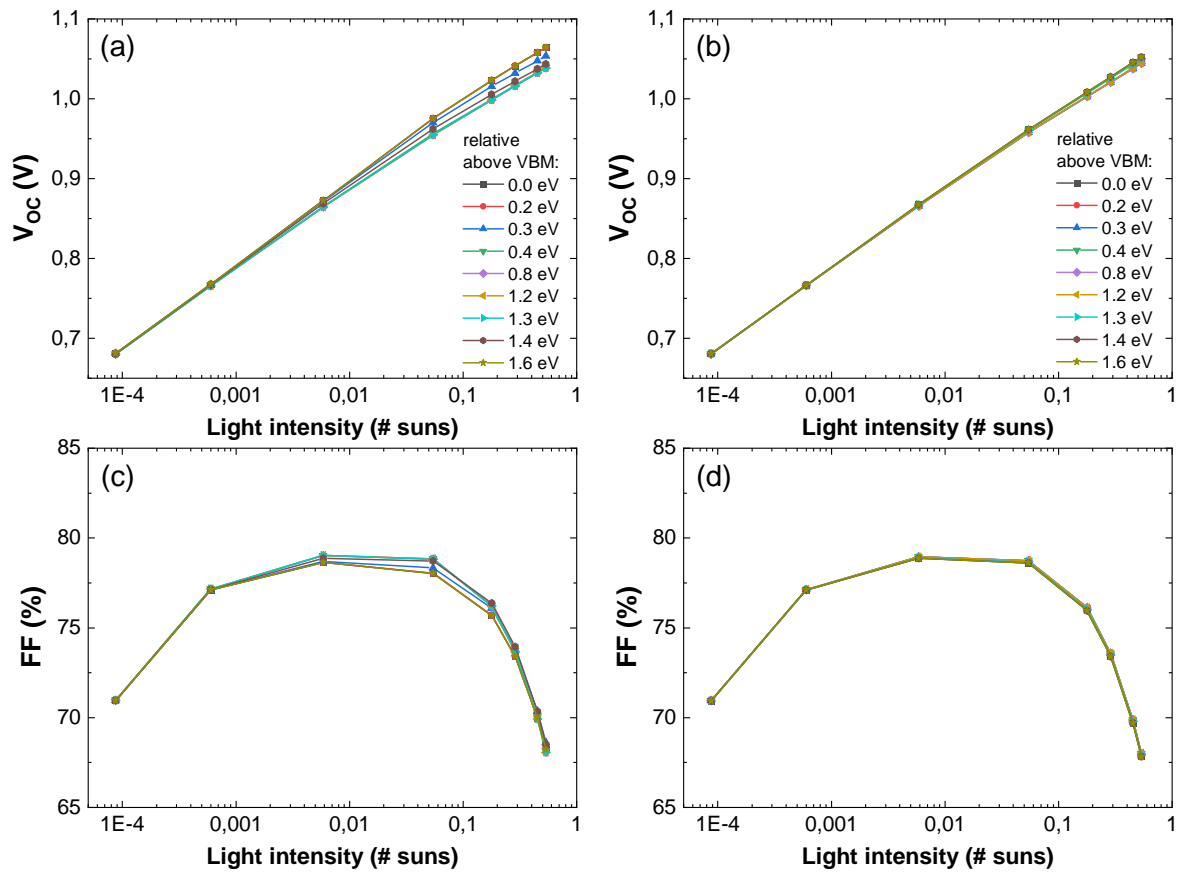
Figure B.5: Simulation sweep of the interface defect energy levels
Illumination from glass side. The other parameters are set according to the optimized fresh device with doping set to zero. PTAA/perovskite interface: (a) V_{OC}, (c) FF and perovskite/PCBM interface: (b) V_{OC}, (d) FF
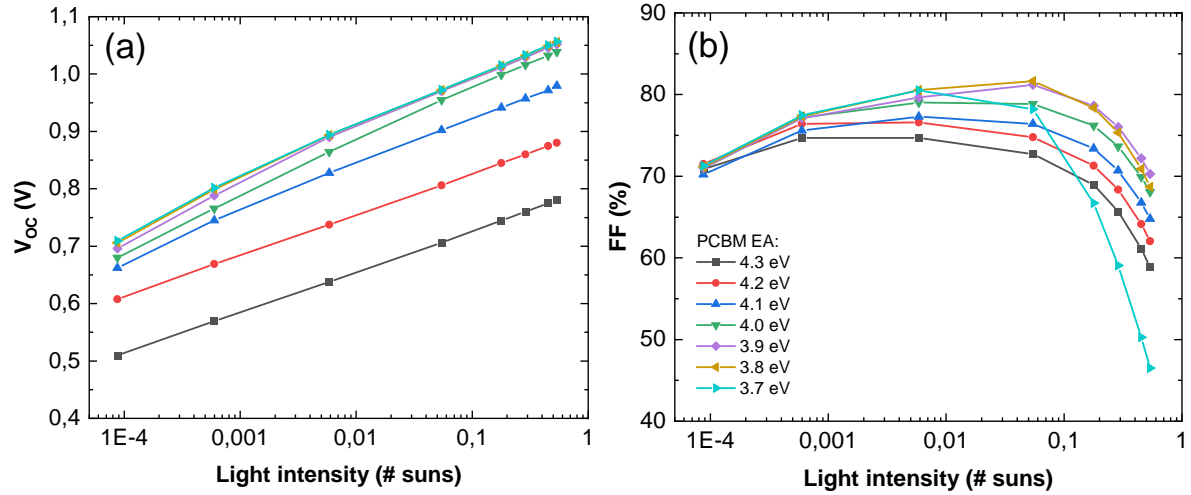
Figure B.6: Simulation sweep of the EA of the PCBM for glass side illumination
Most other parameters are set according to the optimized fresh device with doping set to zero. To IE of the PCBM is kept constant to prevent changes to the hole blocking. The back contact is changed as well to keep a constant PCBM/metal injection barrier (a) V_{OC}, (b) FF.
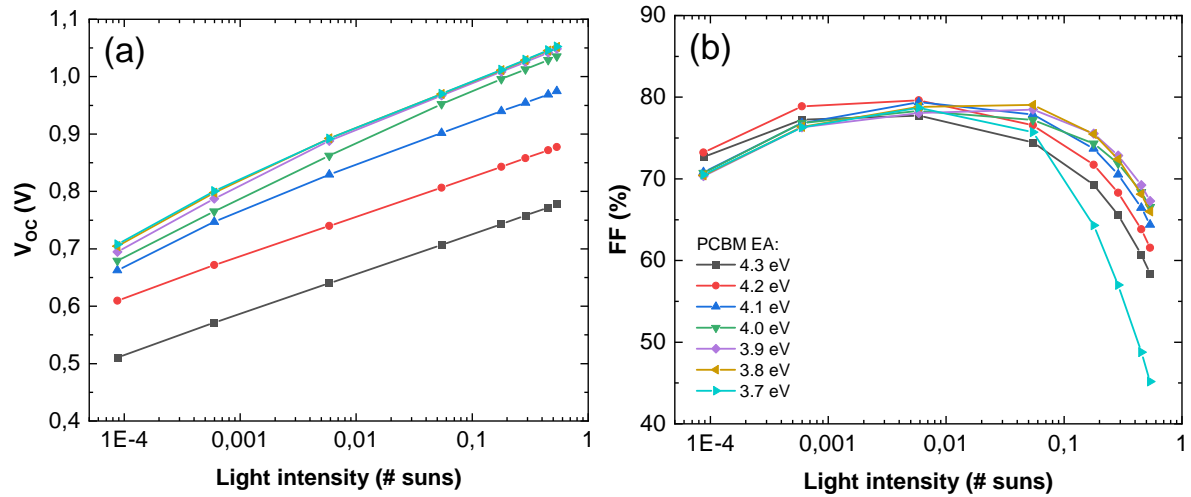
Figure B.7: Simulation sweep of the EA of the PCBM for ITO side illumination
Most other parameters are set according to the optimized fresh device with doping set to zero. To IE of the PCBM is kept constant to prevent changes to the hole blocking. The back contact is changed as well to keep a constant PCBM/metal injection barrier (a) V_{OC}, (b) FF.

B.4 Comparison measurement and simulation fresh devices
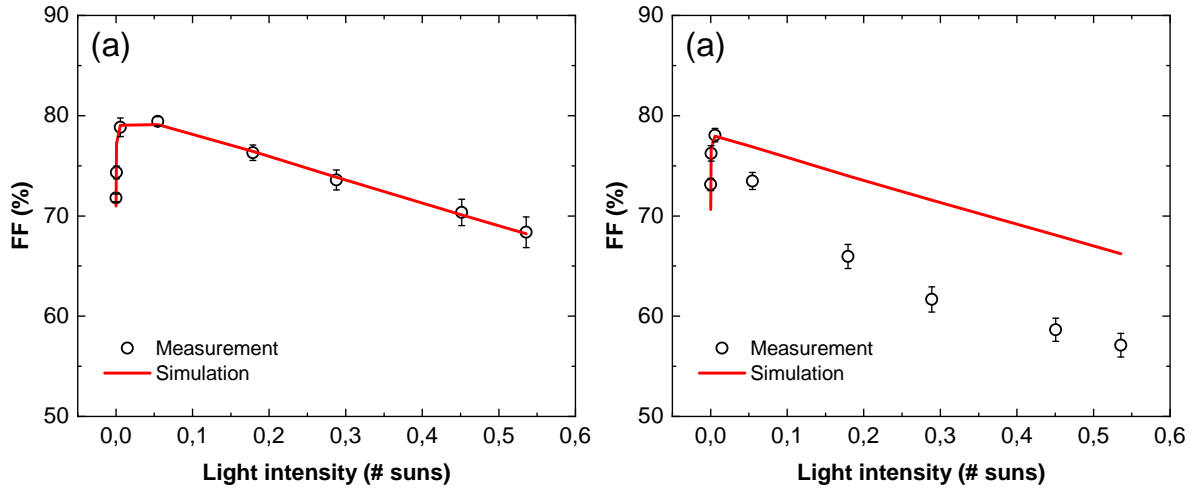
Figure B.8: FF comparison of the measurement and simulation for the fresh IBr device (a) Glass side illumination, (b) ITO side illumination
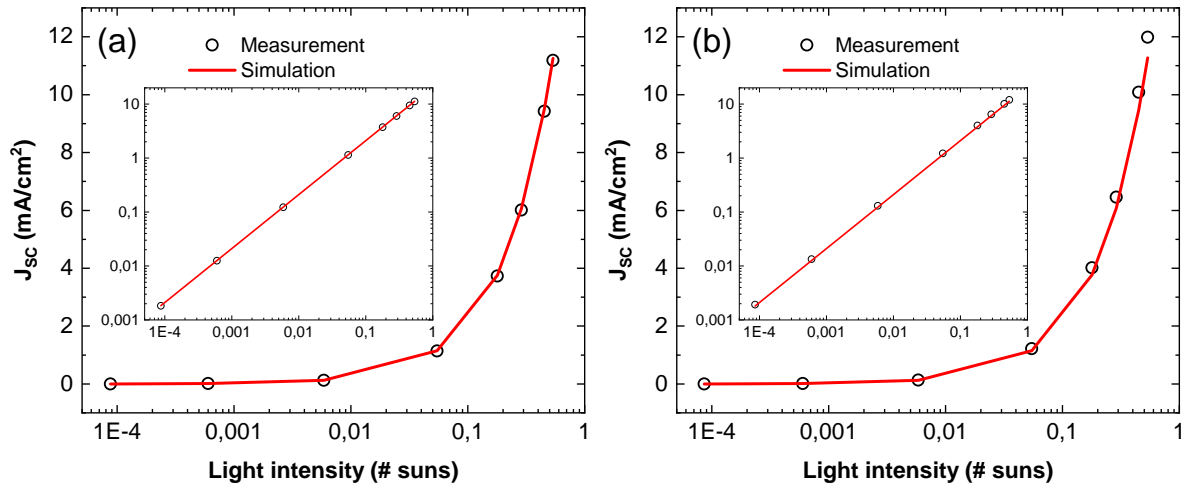
Figure B.9: J_{SC} **comparison of the measurement and simulation for the fresh IBr device** (a) Glass side illumination, (b) ITO side illumination
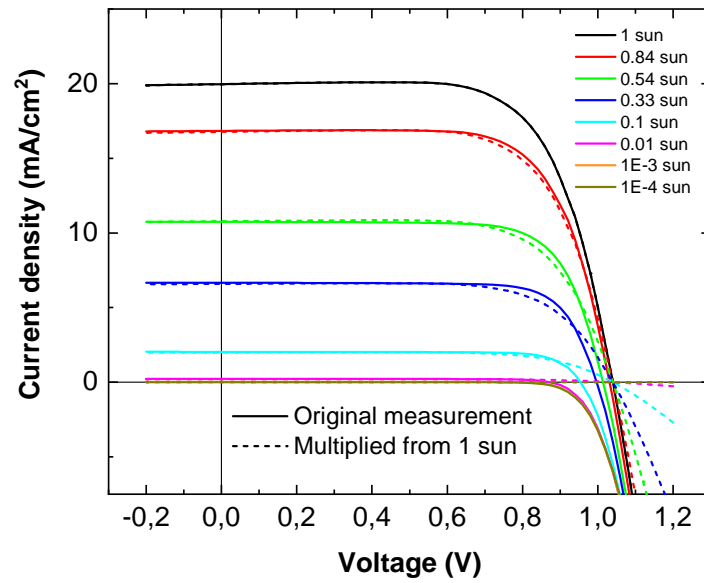
Figure B.10: Comparison light intensity J-V curves versus filter multiplication
The dashed lines are derived from multiplying the original 1 sun J-V measurement with the filter values.
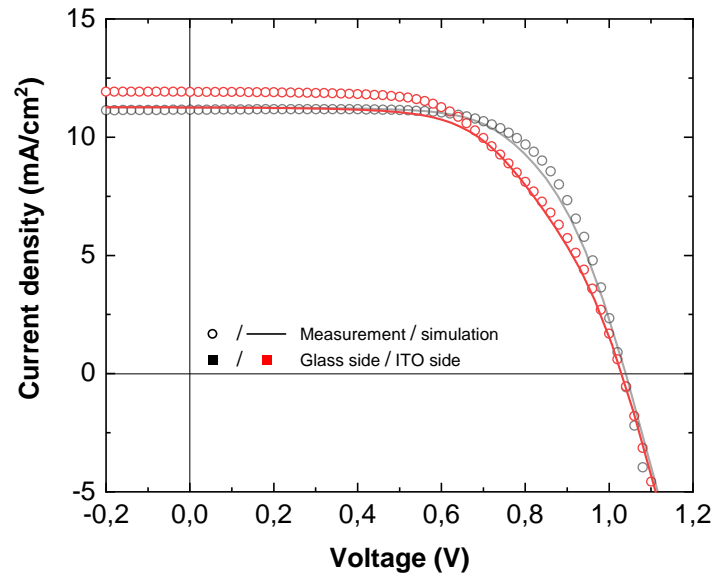
Figure B.11: Simulation of the J-V curve kink for ITO side illumination
Most parameters are set according to the optimized fresh device. The EA of the PTAA is set to 1.85 eV, PTAA/perovskite interface defect density is 2E+9 cm^{-3}, perovskite/PCBM interface defect density is 3E+9 cm^{-3} and the defect energy level of the PTAA/perovskite interface defects is set to 0.3 eV above VBM of the perovskite.

B.5 Measurements results aged devices
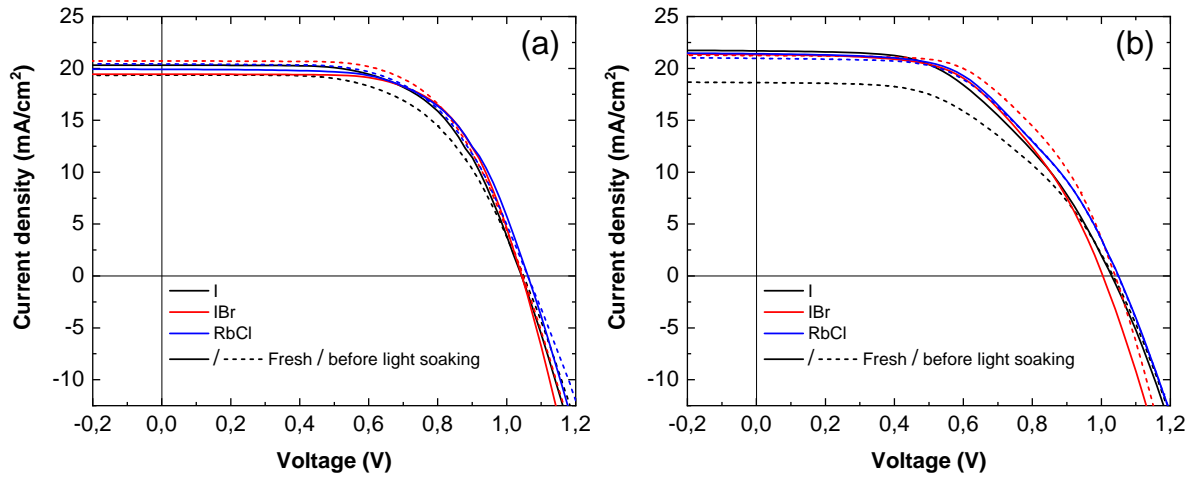
Figure B.12: J-V curve comparison of the fresh versus before light soaking
The samples are measured after approximately 1.5 months just before the light soaking period was started. Only one sample (= 4 devices) is measured and averaged per composition. (a) Measurement from glass side, (b) measurement from ITO side.
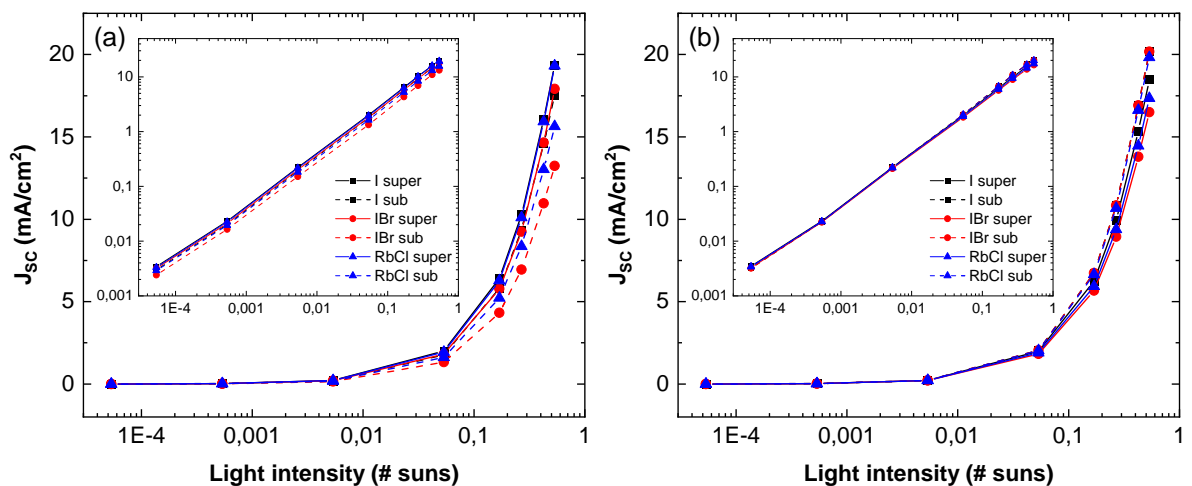
Figure B.13: Composition comparison of the J_{SC} during aging
The measurements are done from glass side. (a) After 1250 hours of light soaking, (b) After 2 to 3 months of storage
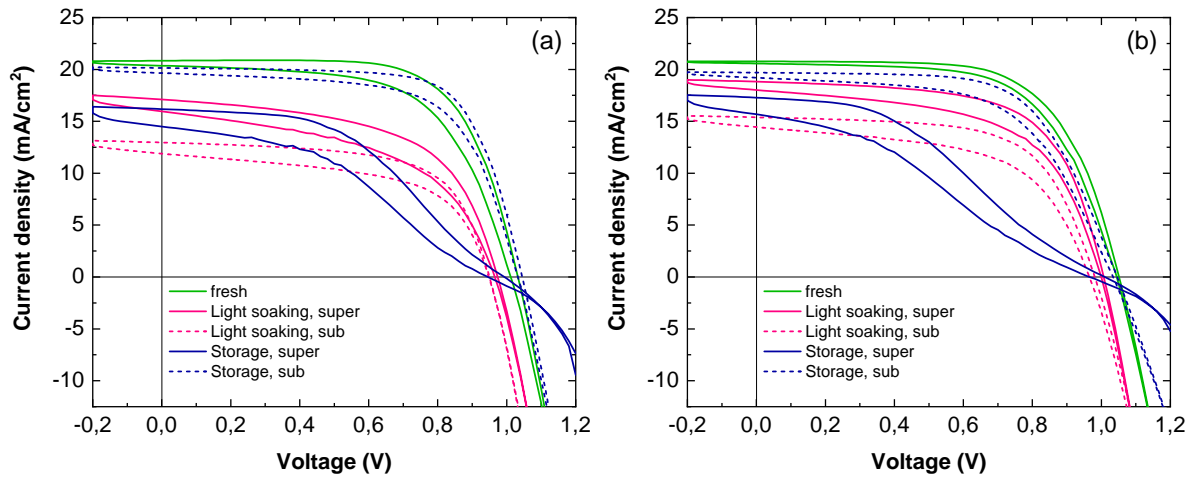
Figure B.14: The effect of aging on the J-V curves for glass side measurements
(a) IBr, (b) RbCl
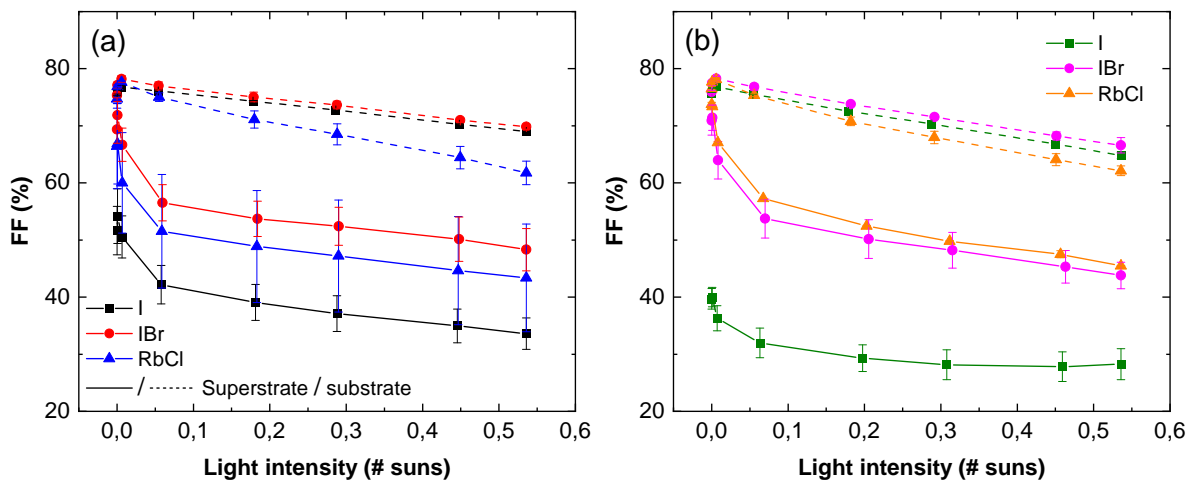
Figure B.15: Composition comparison of the FF on a linear scale after storage
(a) Glass side measurement, (b) ITO side measurement.

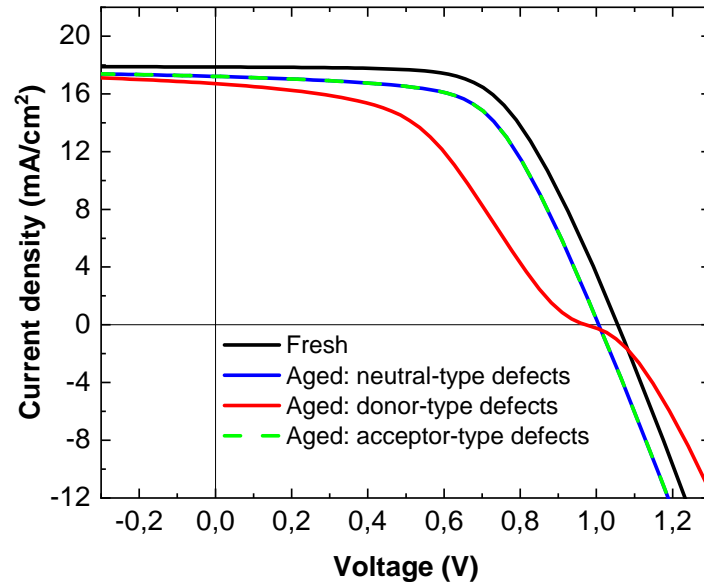## B.6 Simulation results aged devices

Figure B.16: Comparison of the J-V curves with different defect types
The fresh simulation vs aged simulation with different defect types at the PTAA/perovskite interface.
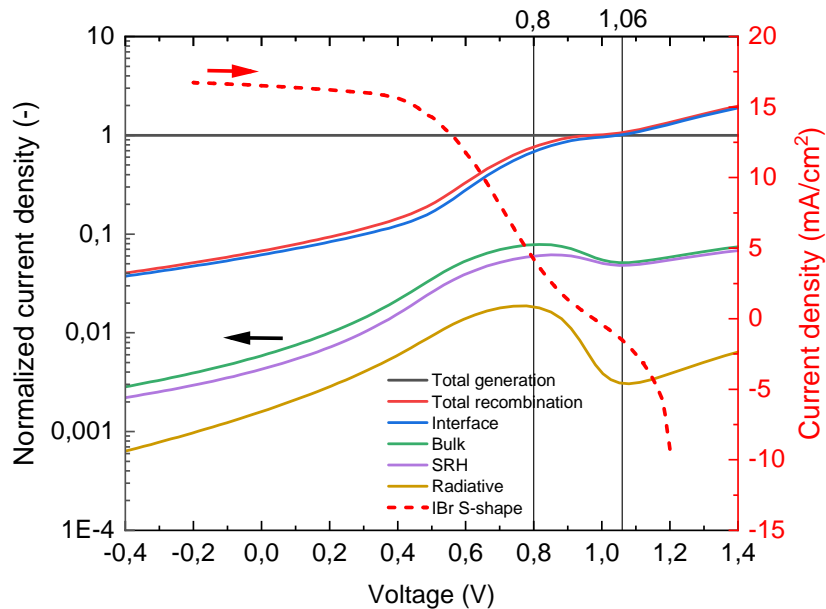

Figure B.17: Local decrease in bulk recombination
The inflection point of the J-V measurement falls within the region of local decrease of the bulk recombination.
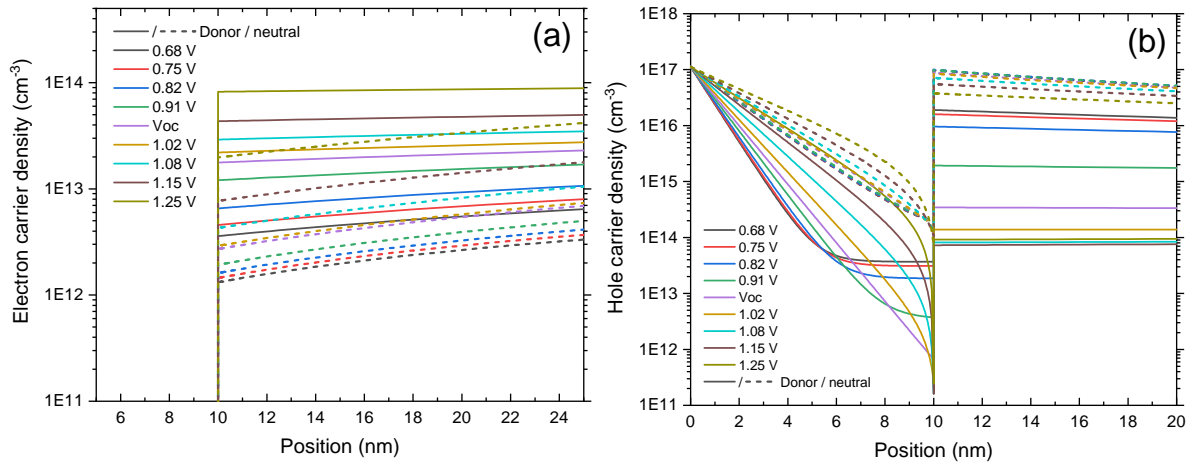
Figure B.18: Close-up of the free carrier density at the PTAA/perovskite interface
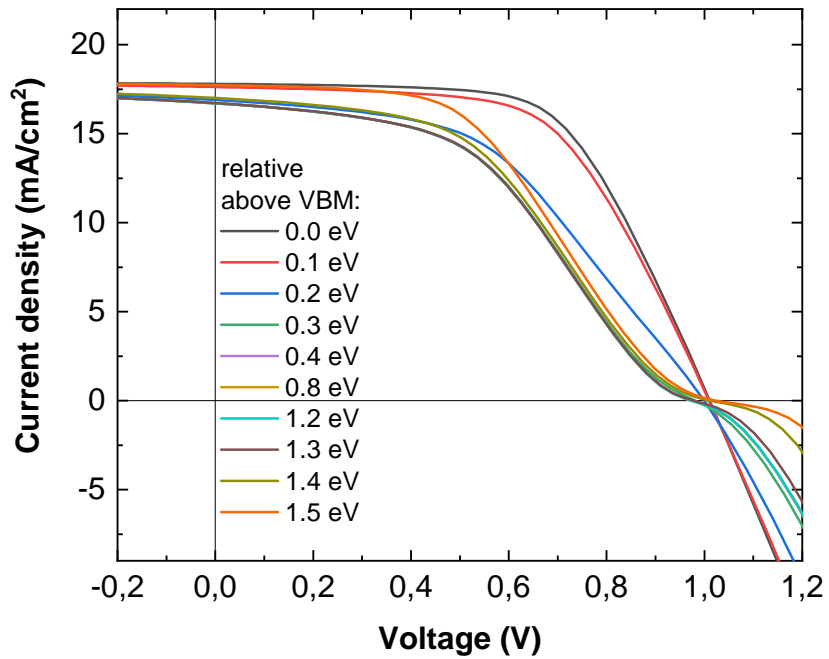(a) Electron carrier density, (b) Hole carrier density.

Figure B.19: Simulation sweep of the donor defect energy level
The other parameters are set to the optimized aged simulation.